UNIVERSIDADE DE SÃO PAULO
Escola de Engenharia de São Carlos

Development of enriched isogeometric Boundary Element Method formulations for the fracture and fatigue analysis in three-dimensional structures

Desenvolvimento de formulações enriquecidas do Método dos Elementos de Contorno isogeométrico para a análise da fratura e fadiga de estruturas tridimensionais

Matheus Rocha

Ph.D. Thesis – Programa de Pós-Graduação em Engenharia Civil (Engenharia de Estruturas) da Escola de Engenharia de São Carlos, Universidade de São Paulo

EESC · USP

Matheus Rocha

Development of enriched isogeometric Boundary Element Method formulations for the fracture and fatigue analysis in three-dimensional structures

Ph.D. thesis submitted to São Carlos School of Engineering, University of São Paulo (USP), in partial fulfillment of the requirements for the degree of Doctor in Science - Programa de Pós-Graduação em Engenharia Civil (Engenharia de Estruturas).

Supervisor: Prof. Edson Denner Leonel

VERSÃO CORRIGIDA

São Carlos

2025

AUTORIZO A REPRODUÇÃO TOTAL OU PARCIAL DESTE TRABALHO, POR QUALQUER MEIO CONVENCIONAL OU ELETRÔNICO, PARA FINS DE ESTUDO E PESQUISA, DESDE QUE CITADA A FONTE.

Ficha catalográfica elaborada pela Biblioteca Prof. Dr. Sérgio Rodrigues Fontes da EESC/USP com os dados inseridos pelo(a) autor(a).

Rocha, Matheus
R672d Development of enriched isogeometric Boundary Element Method formulations for the fracture and fatigue analysis in three-dimensional structures / Matheus Rocha; orientador Edson Denner Leonel. São Carlos, 2025.

Tese (Doutorado) - Programa de Pós-Graduação em Engenharia Civil (Engenharia de Estruturas) e Área de Concentração em Estruturas -- Escola de Engenharia de São Carlos da Universidade de São Paulo, 2025.

1. Boundary Element Method. 2. Enriched formulations. 3. Isogeometric analysis. 4. Crack growth. 5. Fatigue analysis. I. Título.

Eduardo Graziosi Silva - CRB - 8/8907

FOLHA DE JULGAMENTO

Candidato: Bacharel **MATHEUS ROCHA**.

Título da tese: "Desenvolvimento de formulações enriquecidas do Método dos Elementos de Contorno Isogeométrico para análises de fratura e fadiga em estruturas tridimensionais".

Data da defesa: 21/03/2025.

Comissão Julgadora	**Resultado**
Prof. Titular Edson Denner Leonel **(Orientador)** (Escola de Engenharia de São Carlos/EESC-USP)	APROVADO
Prof. Dr. Eder Lima de Albuquerque (Universidade de Brasilia/UnB)	APROVADO
Prof. Dr. Sérgio Gustavo Ferreira Cordeiro (Instituto Tecnológico de Aeronáutica/ITA)	APROVADO
Prof. Dr. Felício Bruzzi Barros (Universidade Federal de Minas Gerais/UFMG)	APROVADO
Prof. Dr. Fabio Carlos da Rocha (Universidade Federal de Sergipe/UFS)	APROVADO

Coordenador do Programa de Pós-Graduação em Engenharia Civil (Engenharia de Estruturas):
Prof Associado **Ricardo Carrazedo**

Presidente da Comissão de Pós-Graduação:
Prof. Titular **Carlos De Marqui Junior**

ACKNOWLEDGEMENTS

I would like first to thank God for His continuous protection in all moments of my life.

I would like to express my gratitude to my family, and especially to my parents, Sandra A. Pontes and Valdecy J. Rocha, for all their love, care, sacrifice, and encouragement throughout my academic and professional life. You have always believed in me, even in the hardest times.

I would like to acknowledge my supervisor, prof. Edson D. Leonel, for the academic support of this thesis. Prof. Edson is an outstanding researcher, and his serenity and patience were crucial for the development of this work. I also express my deep gratitude to Prof. Jon Trevelyan for the supervision of this work during and after my research internship at Durham University, and for receiving me so well. His contributions to this work and to my professional growth are invaluable. I extend the acknowledgments to my research group friends Aline L. Alves, Antonio Rodrigues Neto, Daniel V. C. Teles, Débora M. Guimarães, Deborah C. Nardi, Gabriel N. Queiroz, Georgia B. Bofill, Heider C. Andrade, Luís Philipe R. Almeida, Mário S. O. César Filho, and Ray C. S. Silva.

I would also like to thank the committee members, Prof. Sérgio G. F. Cordeiro and Prof. Éder L. Albuquerque, who attended my qualifying exam and Ph.D. defense, for their insights into this work, and Prof. Fábio C. Rocha and Prof. Felício B. Bruzzi for their participation in my Ph.D. defense.

I express my special thanks to Alexandre R. Ribeiro, for always bringing me joy, love, support, and hope.

I thank all my friends from São Carlos, for the conversations about the topics of this thesis, and also for the enjoyable times and support throughout these years. Special thanks to: Daniane C. C. V. Prataviera, Henrique B. Soares, Isabela D. Rodrigues, Lucas R. Ribeiro, Luiz Fernando H. Teodoro, Marcela Bassoli, Marina Naomi Furukawa, Murilo H. C. Bento, Patricia Tonon, Péricles R. P. Carvalho, Rafaela S. Silva, Tainá M. Borghi, and Thássia D. Z. Rufato, and also to the research group friends previously mentioned.

I also acknowledge my friends from my internship at Durham: Adolfo C. B. Souza, Bradley Sims, Eduardo R. Triboni, Felipe M. Nogueira, Jeferson L. S. Freitas, Paulo H. Gaem, Takudzwa Mutsvairo, Ted O'Hare, Sueli Anderson, and Vitor M. Ramos. Our fun times together helped me not miss Brazil so much and made the experience of living abroad unforgettable.

I thank all my friends from Vitória as well: André R. Kuster, Elidio R. Corona

Júnior, Isabela C. Thomazini, João P. L. Bastos, Lucas C. Baldotto, Lucas C. Pellanda, Thiago T. Turini, Yan Prado, and Yasmin C. C. Menezes. Thank you all for your partnership and the fun times we shared.

I acknowledge the Department of Structural Engineering at the São Carlos School of Engineering and the Department of Engineering at Durham University for the facilities that enabled this Ph.D. thesis to be developed.

This study was financed in part by the Coordenação de Aperfeiçoamento de Pessoal de Nível Superior, Brasil – CAPES, Finance Code 001. Additionally, I would like to gratefully acknowledge the financial support provided by the São Paulo Research Foundation (FAPESP) under grants #2019/18795-6 and #2022/00714-2.

AGRADECIMENTOS

Primeiramente agradeço a Deus pela proteção contínua em toda a minha vida.

À minha família, especialmente a meus pais, Sandra A. Pontes e Valdecy J. Rocha, pelo amor, carinho, sacrifício e incentivo durante todos os anos da vida escolar, acadêmica e profissional. Vocês sempre acreditaram em minha capacidade, mesmo nos momentos mais difícieis.

Agradeço ao meu orientador, prof. Edson D. Leonel, pelo suporte acadêmico durante o desenvolvimento desta tese. Além de excelente pesquisador, sua serenidade e paciência foram cruciais para o desenvolvimento deste trabalho. Agradeço ao prof. Jon Trevelyan pela orientação durante o estágio de pesquisa na Durham University, que me acolheu de forma exemplar. Suas contribuições para este trabalho e para minha formação profissional são inestimáveis. Estendo os agradecimentos aos amigos do grupo de pesquisa Aline L. Alves, Antonio Rodrigues Neto, Daniel V. C. Teles, Débora M. Guimarães, Deborah C. Nardi, Gabriel N. Queiroz, Georgia B. Bofill, Heider C. Andrade, Luís Philipe R. Almeida, Mário S. O. César Filho, e Ray C. S. Silva.

Aos profs. Sérgio G. F. Cordeiro e Éder L. Albuquerque, membros da banca qualificação e de defesa desta tese, pelas valorosas contribuições a este trabalho, e aos profs. Fábio C. Rocha e Felício B. Bruzzi, pela participação na banca de defesa desta tese.

Ao Alexandre R. Ribeiro, por todos os dias me trazer felicidade, amor, apoio e esperança.

A todos os meus amigos de São Carlos, pelas conversas valorosas a respeito dos temas desta tese, e também pelos momentos de descontração e apoio ao longo desses anos. Agradecimentos especiais a: Daniane C. C. V. Prataviera, Henrique B. Soares, Isabela D. Rodrigues, Lucas R. Ribeiro, Luiz Fernando H. Teodoro, Marcela Bassoli, Marina Naomi Furukawa, Murilo H. C. Bento, Patricia Tonon, Péricles R. P. Carvalho, Rafaela S. Silva, Tainá M. Borghi, e Thássia D. Z. Rufato, e também ao amigos do grupo de pesquisa previamente citados.

Agradeço também aos amigos do intercâmbio em Durham: Adolfo C. B. Souza, Bradley Sims, Eduardo R. Triboni, Felipe M. Nogueira, Jeferson L. S. Freitas, Paulo H. Gaem, Takudzwa Mutsvairo, Ted O'Hare, Sueli Anderson, e Vitor M. Ramos. Os momentos leves e divertidos que passamos juntos ajudaram a aliviar a saudade do Brasil e tornar a experiência de morar fora inesquecível.

Aos amigos de Vitória: André R. Kuster, Elidio R. Corona Júnior, Isabela C. Thomazini, João P. L. Bastos, Lucas C. Baldotto, Lucas C. Pellanda, Thiago T. Turini,

Yan Prado, e Yasmin C. C. Menezes, agradeço pela parceria e pelos momentos divertidos que compartilhamos.

Agradeço ao Departamento de Engenharia de Estruturas da Escola de Engenharia de São Carlos, e ao Departamento de Engenharia da Durham University, pela infraestrutura concedida.

A presente pesquisa foi realizada com apoio da Coordenação de Aperfeiçoamento de Pessoal de Nível Superior – Brasil (CAPES) – Código de Financiamento 001. Adicionalmente, esta pesquisa foi desenvolvida com auxílio da Fundação de Amparo à Pesquisa do Estado de São Paulo (FAPESP), processo nº 2019/18795-6 e nº 2022/00714-2.

ABSTRACT

ROCHA, M. **Development of enriched isogeometric Boundary Element Method formulations for the fracture and fatigue analysis in three-dimensional structures**. 2025. 188 p. Thesis (Ph.D.) - São Carlos School of Engineering, University of São Paulo, São Carlos, 2025.

The main objective of this doctoral thesis is the development of enriched formulations based on the Isogeometric Boundary Element Method (IGABEM) for three-dimensional fracture and fatigue analysis. The IGABEM is a suitable numerical approach due to its boundary-only discretisation, which allows the direct use of Computer-Aided Design (CAD) models, eliminating the need for the mesh generation task. This study utilises the Dual IGABEM to accommodate coincident geometries for opposing crack surfaces, and inherits the well-known advantages of the Non-Uniform Rational B-Splines (NURBS) basis as other isogeometric implementations. This study proposes an enrichment with the Heaviside function to represent the displacement discontinuity at external faces intersected by cracks. This proposition eliminates the need for conformal meshes along the intersection. Additional degrees of freedom emerge from this strategy, and since this study applies a collocation-based IGABEM, the supplementary equations do not arise naturally with the enrichment proposition. In this sense, two different strategies of supplementary equations recover a well-posed system. Then, another proposition involves the Williams' solution as enrichment functions to the displacement approximation. This function possesses the asymptotic behaviour typical of fracture mechanics problems, which is not part of the NURBS space. This expansion incorporates the displacement discontinuity when applied at external faces crossed by cracks. Additionally, enriching crack surfaces using this method enables the direct extraction of the Stress Intensity Factors (SIFs) as they become system unknowns. This eliminates the need for post-processing tasks, such as the J-integral. Moreover, introducing the $\sqrt{r}$ behaviour at the displacements approximation results in higher convergence rates when compared to standard IGABEM or Lagrangian BEM approaches. This study also performs a fatigue crack propagation analysis with the proposed eXtended Isogeometric Boundary Element Method (XIGABEM) formulations. The Williams' solution enrichment directly obtains the SIFs and the Heaviside function represents the displacement discontinuity modelling. The Paris-Erdogan Law determines the fatigue life assessment, while two different crack growth criteria define the crack advancement: the hoop stress and the Schollmann criterion. Additionally, this study proposes a new algorithm to define the new crack front position during the propagation analysis based on a least squares minimisation. Then, it becomes possible to represent changes in the crack front curvature during the crack growth. While the principal focus of this thesis is the development of enriched formulations of the IGABEM, incorporating trimmed surfaces into the method is a preliminary research into expanding the scope

of its geometric representation. This enables the numerical analysis of more complex geometries without rebuilding the original CAD model, which it allows for the study of industrial components. Results have demonstrated the viability of the trimmed surfaces in the IGABEM formulation, although for limited cases. Its generalisation requires further investigation about implementation details and suitable collocation schemes. In addition, several numerical applications demonstrate the robustness of the new XIGABEM for three-dimensional fracture and fatigue analysis. The results using the XIGABEM formulation agree with the reference solutions from analytical expressions or those from the literature. Moreover, the numerical results attest to the accuracy of the XIGABEM models with fewer degrees of freedom compared to the standard IGABEM or BEM.

Keywords: Boundary Element Method; enriched formulations; isogeometric analysis; crack growth; fatigue analysis.

RESUMO

ROCHA, M. **Desenvolvimento de formulações enriquecidas do Método dos Elementos de Contorno isogeométrico para a análise da fratura e fadiga de estruturas tridimensionais**. 2025. 188 p. Tese (Doutorado) - São Carlos School of Engineering, University of São Paulo, São Carlos, 2025.

O principal objetivo desta tese de doutorado é o desenvolvimento de formulações enriquecidas baseadas no Método dos Elementos de Contorno Isogeométrico (MECIG) para a análise da fratura e fadiga de sólidos tridimensionais. O MECIG se apresenta como uma abordagem numérica adequada devido à sua discretização exclusiva do contorno, o que permite a aplicação direta de modelos gerados via Computer-Aided Design (CAD), o que elimina a necessidade por geração de malha. Este estudo utiliza a formulação dual do MECIG para acomodar geometrias coincidentes das faces de fissura opostas, e também incorpora as vantagens conhecidas das funções Non-Uniform Rational B-Splines (NURBS) na implementação isogeométrica. Este estudo propõe o enriquecimento com a função Heaviside para representar a descontinuidade em deslocamento na face externa intersectada por fissuras. Esta proposição elimina a necessidade de malhas conformes ao longo da linha de intersecção. Graus de liberdade adicionais surgem dessa estratégia, e uma vez que este estudo aplica o MECIG por colocação, as equações adicionais não surgem naturalmente com a proposta de enriquecimento. Assim, duas estratégias diferentes para equações suplementares recuperam o sistema algébrico bem posto. Em seguida, outra proposição envolve a expansão de Williams como função de enriquecimento para a aproximação dos deslocamentos. Esta função possui o comportamento assintótico típico de problemas da mecânica da fratura, e que não fazem parte do espaço de aproximação das funções NURBS. Essa expansão incorpora a descontinuidade de deslocamentos quando aplicada a faces externas cortadas por fissuras. Adicionalmente, o enriquecimento de faces de fissura com este método permite a extração direta dos Fatores de Intensidade de Tensão (FITs), dado que eles se tornam incógnitas do sistema. Esse enriquecimento elimina a necessidade de etapas de pós-processamento, como Integral J. Destaca-se que a introdução do comportamento de $\sqrt{r}$ na aproximação dos deslocamentos resulta em maiores taxas de convergência quando comparado com o MECIG convencional ou com o MEC Lagrangiano. Este estudo também executa a análise de propagação de fissuras por fadiga com a formulação proposta do Método dos Elementos de Contorno Isogeométrico Estendido (MECIGE) O enriquecimento via solução de Williams obtém diretamente os FITs e a função Heaviside representa a modelagem da descontinuidade de deslocamentos. A Lei de Paris-Erdogan determina a vida útil à fadiga, enquanto que dois critérios de propagação de fissuras definem o avanço da frente: a máxima tensão circunferencial e o critério de Schollmann. Adicionalmente, este estudo propõe um novo algoritmo para

definição da posição da nova frente de fissura durante a análise de propagação baseada numa minimização por mínimos quadrados. Com isso, torna-se possível representar mudanças na curvatura da frente da fissura durante a propagação das fissuras. Enquanto o foco principal desta tese é o desenvolvimento de formulações enriquecidas do MECIG, a incorporação de superfícies aparadas ao método é um estudo preliminar com ênfase em expandir o escopo das suas representações geométricas. Isso permite a análise numérica de geometrias mais complexas sem reconstruir o modelo CAD original, o que possibilita o estudo de componentes industriais. Os resultados demonstraram a viabilidade do uso das superfícies aparadas na formulação do MECIG, embora para casos limitados. Sua generalização envolve investigações a respeito de detalhes de implementação e esquemas de colocação adequados. Adicionalmente, diversos exemplos numéricos demonstram a robustez da nova formulação do MECIGE para análise da fratura e fadiga de componentes tridimensionais. Os resultados com uso do MECIGE estão em concordância com resultados de referência obtidos por expressões analíticas ou por resultados da literatura. Destaca-se ainda que os resultados atestam a precisão dos modelos do MECIGE com uso de menos graus de liberdade quando comparados com as formulações do MECIG ou do MEC Lagrangiano.

Palavras-chave: Método dos Elementos de Contorno; formulações enriquecidas; análise isogeométrica; propagação de fissuras; análise de fadiga.

LIST OF FIGURES

Figure 1 – Arbitrary solid of the linear elasticity boundary value problem. 36
Figure 2 – Fictitious domain and boundary for the limiting process. 39
Figure 3 – Two-step algorithm to find the parametric coordinate of the trimming curve at the intersection with a knot span: ϱ definition. 48
Figure 4 – Ray casting algorithm for the detection of internal and external points to the trimming sets. 49
Figure 5 – Trimmed knot span types. 50
Figure 6 – Trimmed knot span ordering of vertices and edges. 50
Figure 7 – Influence of endpoints internal to trimmed knot span. 51
Figure 8 – Mappings required for Kim, Seo and Youn (2009) strategy. 51
Figure 9 – Polar mapping for trimmed knot spans. 53
Figure 10 – Pole choice in the polar integration strategy. 54
Figure 11 – Geometric meaning of $\hat{\rho}$. 54
Figure 12 – Collocation strategy for type 2 trimmed knot spans considering $p = q = 1$. 56
Figure 13 – Collocation strategy for type 3 trimmed knot spans considering $p = q = 1$. 57
Figure 14 – Cube with cylindrical hole: geometry and boundary conditions. 58
Figure 15 – CAD model of cube with cylindrical hole. 59
Figure 16 – Position of added collocation points in trimmed faces. 60
Figure 17 – Position of integration points for trimmed faces of cube with cylindrical hole. 60
Figure 18 – Total displacements of a cube with cylindrical hole under tensile loading. 61
Figure 19 – Relative L_2 norm of error for total displacements varying the number of integration points. 61
Figure 20 – Thick-walled quarter-torus geometry and boundary conditions. 62
Figure 21 – Thick-walled quarter-torus isogeometric mesh. 63
Figure 22 – Position of collocation points for Meshes A and B using the non-singular IGABEM approach with trimmed surfaces for a thick-walled quarter-torus. 64
Figure 23 – Relocated collocation points in the NURBS parametric space of the trimmed surfaces for a thick-walled quarter-torus. 64
Figure 24 – FE model reference model of the thick-walled quarter-torus. 65
Figure 25 – Total displacements: FE model. 65
Figure 26 – Total displacements: Mesh A. 66
Figure 27 – Total displacements: Mesh B. 66
Figure 28 – Total displacements: Mesh A in singular approach. 67
Figure 29 – Displacements along arch: FE and trimmed IGABEM models. 68
Figure 30 – Stress components along arch: FE and trimmed IGABEM models. . . . 69

Figure 31 – Shifted Heaviside function. 72
Figure 32 – Mid-points at each crack edge that search their correspondent external boundary face. 77
Figure 33 – Possible cases for entirely crossed knot-span, in which the crack is indicated by red and the knot-span sub-divisions are represented in dashed green. 78
Figure 34 – Knot-span subdivision for crack ending inside its domains. 79
Figure 35 – Subdivision for two different crack surfaces in the same knot-span. . . . 79
Figure 36 – Definition of auxiliary vectors for the calculation of $\mathscr{H}$. 80
Figure 37 – Geometry and boundary conditions of notched cube under split test. . 81
Figure 38 – Position of collocation points for meshes A, B and C of the notched cube. 81
Figure 39 – Crack position in each surface with $x_1 = 0.0$ and $x_1 = 10.0$. 83
Figure 40 – Deformed configuration of notched cube under split test: mesh C. . . . 84
Figure 41 – Relative L_2 norm of error in displacements for split test in notched cube. 85
Figure 42 – Geometry of cracked cylinder under split test. 86
Figure 43 – Isogeometric discretisation and placement of collocation points for split test in cracked cylinder. 87
Figure 44 – Deformed shape of cracked cylinder under split test. 88
Figure 45 – Geometry and boundary conditions of prism with initial crack. 89
Figure 46 – Isogeometric discretisation for prism with initial crack using the standard IGABEM. 90
Figure 47 – Knot spans reference model (mesh C) for prism with initial crack. . . . 91
Figure 48 – Isogeometric discretisation for prism with initial crack using the XIGA-BEM for strong discontinuities. 92
Figure 49 – Placement of collocation points of prism with initial crack for the XIGABEM analysis. 93
Figure 50 – Deformed shape of prism with initial crack: standard IGABEM vs XIGABEM. 94
Figure 51 – Strain energy comparison between the XIGABEM and the IGABEM models. 95
Figure 52 – Local coordinate system at the crossing between crack and external face. 98
Figure 53 – Local coordinate system for crack front enrichment. 101
Figure 54 – (a) Geometry and loading conditions for penny-shaped crack and (b) Control points position for penny-shaped crack mesh 107
Figure 55 – Deformed shape for penny shaped crack using (a) conventional IGABEM and (b) extended IGABEM 108
Figure 56 – Relative L_2 norm of error in displacements for in-plane penny-shaped crack. 109
Figure 57 – Condition number growth for in-plane penny-shaped crack. 109

Figure 58 – Stress Intensity Factors for penny-shaped crack inclined by $\pi/4$ rad. . . 110
Figure 59 – (a) Geometry of elliptical crack and (b) Mesh and control points for in-plane elliptical mesh. 112
Figure 60 – Relative L_2 norm of error in displacements for in-plane elliptical crack. 112
Figure 61 – Condition number growth for in-plane elliptical crack. 113
Figure 62 – Stress Intensity Factor K_I for in-plane elliptical crack. 113
Figure 63 – Stress Intensity Factors for elliptical crack inclined by $\pi/6$ rad. 115
Figure 64 – Geometry of prismatic block with edge crack. 116
Figure 65 – Mesh for prismatic block with edge crack for (a) XIGABEM analysis and (b) standard IGABEM approach. 117
Figure 66 – Deformed shape for each pure crack loading where standard IGABEM results are on the left-hand side while the XIGABEM responses are on the right-hand side. 118
Figure 67 – Relative L_2 norm of error in displacements for prismatic block with edge crack. 120
Figure 68 – Condition number growth for prismatic block with edge crack. 121
Figure 69 – Geometry and boundary conditions for prismatic specimen under uniform traction. 122
Figure 70 – Isogeometric mesh for prismatic block under uniform traction, in which (a) XIGABEM mesh with only the SIF enrichment, and (b) fully enriched model. 123
Figure 71 – Stress Intensity Factors along crack front, in which XIGABEM (a) is the model with only the crack front enrichment, XIGABEM (b) and (c) are the fully enriched models with Kosolov constant set as plane strain and plane stress, respectively. 124
Figure 72 – Local coordinate system for the crack front stresses. 130
Figure 73 – Definition of new crack position based on points and the corresponding new crack front. 131
Figure 74 – Averaging endpoints to guarantee C^0 continuity between NURBS surfaces. 133
Figure 75 – Control points position for each updated crack front for tangent alignment. 134
Figure 76 – New crack surface generation based on new crack front. 135
Figure 77 – Geometry and boundary conditions of elliptical crack immersed in prismatic solid. 137
Figure 78 – Isogeometric mesh and control points for elliptical crack. 138
Figure 79 – Elliptical crack growth: steps 1, 5 and 10. 139
Figure 80 – Deformed shape for each mesh in tenth propagation step. 139
Figure 81 – Fatigue life assessment of elliptical crack in in prismatic solid. 139
Figure 82 – Geometry and boundary conditions of inclined penny-shaped crack. . . 141

Figure 83 – Isogeometric mesh and control points position for inclined penny-shaped crack. 141
Figure 84 – Inclined penny-shaped crack configuration during fatigue growth by XI-GABEM considering (a) Hoop stress criterion, (b) Schollmann criterion, (c) Hoop stress criterion with $K_{III} = 0$, and (d) Schollmann criterion with $K_{III} = 0$. 142
Figure 85 – Inclined penny-shaped crack configuration from the hp-GFEM approach (Pereira; Duarte; Jiao, 2010), considering (a) Schollmann criterion and (b) Schollmann criterion with $K_{III} = 0$. 143
Figure 86 – SIF distribution along crack front at the last propagation step: Schollmann criterion and comparison against hp-GFEM results from Pereira, Duarte and Jiao (2010). 143
Figure 87 – SIF distribution along crack front at the last propagation step: Schollmann criterion considering $K_{III} = 0$ for propagation angle and comparison against hp-GFEM results from Pereira, Duarte and Jiao (2010). . 144
Figure 88 – SIF distribution along crack front at the last propagation step with the hoop stress criterion and the influence of K_{III} in the equivalent SIF. . . 145
Figure 89 – K_I distribution along crack front at steps 0, 7 and 14 for hoop stress criterion. 146
Figure 90 – K_{II} distribution along crack front at steps 0, 7 and 14 for hoop stress criterion. 146
Figure 91 – K_{III} distribution along crack front at steps 0, 7 and 14 for hoop stress criterion. 147
Figure 92 – K_I distribution along crack front at steps 0, 7 and 14 for Schollmann criterion. 147
Figure 93 – K_{II} distribution along crack front at steps 0, 7 and 14 for Schollmann criterion. 148
Figure 94 – K_{III} distribution along crack front at steps 0, 7 and 14 for Schollmann criterion. 148
Figure 95 – Fatigue life assessment of inclined penny-shaped crack. 149
Figure 96 – Geometry and boundary conditions of prism with edge crack under cyclic tensile load. 150
Figure 97 – Deformed shape of prism with edge crack under cyclic tensile load in all propagation steps. 152
Figure 98 – Prism with edge crack under cyclic tensile load: K_I through propagation steps. 153
Figure 99 – Prism with edge crack under cyclic tensile load: fatigue life. 153
Figure 100 – Geometry of hook with initial crack, dimensions in cm. 155
Figure 101 – Fatigue crack location in crane hook experiment (Kishore *et al.*, 2020). 156

Figure 102 – Isogeometric model of hook with crack. 156
Figure 103 – Collocation points position for the XIGABEM model of hook with crack. 157
Figure 104 – Deformed shape of a crane hook under cyclic loading when the load reaches its maximum value for different crack steps. 158
Figure 105 – Crack front evolution at the plane $x_1 = 2.5$ due to the cyclic loading on the hook. 159
Figure 106 – Stress Intensity Factors' distribution along crack front during fatigue propagation on hook. 160
Figure 107 – Evolution of K_I during fatigue propagation of a at the threaded region of a hook. 160
Figure 108 – Fatigue life assessment of hook under cyclic loading. 161
Figure 109 – B-Spline curve representation: control points, segments and knots . . . 180
Figure 110 – NURBS surface. 182
Figure 111 – Types of basis functions for trimmed surfaces. 183

LIST OF TABLES

Table 1 – Position of the control points of the trimming curve on the NURBS parametric space. 59
Table 2 – Control points and weights of trimming curves used in planar faces of the thick-walled quarter-torus. 63
Table 3 – Comparison between the relative L_2 norm of error in displacements and condition number for each strategy of supplementary equations in the split test of a cracked cylinder. 87
Table 4 – Number of collocation points for each reference mesh of prism with initial crack. 90
Table 5 – Average SIFs error for in-plane penny-shaped crack. 110
Table 6 – Relative error for SIFs in elliptical crack inclined by $\theta_i = \pi/6$. 115
Table 7 – Average values for SIFs in each pure mode loading case of prism with edge crack. 119
Table 8 – Material and fatigue properties of Ti-6Al-4V alloy. 137
Table 9 – Number of degrees of freedom at each propagation step. 138
Table 10 – Material and fatigue properties of inclined penny-shaped crack. 140
Table 11 – Average values for K_I in the last propagation step for Hoop stress criterion and for Schollmann criterion. 142
Table 12 – Control points and weights for the coarse mesh of the elliptical crack modelling of section 6.5.1. 185
Table 12 – Control points and weights for the coarse mesh of the elliptical crack modelling of section 6.5.1. 186
Table 13 – Connectivity of the elliptical crack model of section 6.5.1. 187

CONTENTS

1 INTRODUCTION 25
1.1 Scope and motivation 25
1.2 Objectives 32
1.3 Methodology 33
1.4 Outline 33

2 ISOGEOMETRIC BOUNDARY ELEMENT METHOD 35
2.1 Somigliana Identity and Kelvin Fundamental Solution 35
2.2 Limiting process: boundary integral equations 38
2.3 Dual Boundary Integral Equations 40
2.4 BEM algebraic system and IGABEM 41
2.5 Internal mechanical fields 45

3 TRIMMED SURFACES ON IGABEM 47
3.1 Identification of trimmed knot spans and basis functions 47
3.2 Numerical integration of trimmed knot spans 51
3.2.1 Kim, Seo and Youn (2009) strategy 51
3.2.2 Polar strategy 53
3.3 Collocation strategy for trimmed surfaces 56
3.4 Numerical applications 57
3.4.1 Cube with a cylindrical hole 57
3.4.2 Thick-walled quarter-torus 62
3.5 Challenges and limitations of trimmed surfaces on IGABEM 70

4 HEAVISIDE ENRICHMENT FOR DISPLACEMENT DISCONTINUITIES IN CROSSED SURFACES 71
4.1 Displacement field enrichment 71
4.2 Supplementary equations strategy 75
4.3 Implementation aspects 76
4.4 Numerical applications 79
4.4.1 Split test of notched cube 80
4.4.2 Split test of a cracked cylinder 86
4.4.3 Prism with initial crack 89
4.5 Partial conclusions 96

5 WILLIAMS SOLUTION-BASED ENRICHMENT STRATEGIES . . 97
5.1 Lateral face enrichment for $\sqrt{r_t}$ behaviour on intersected surfaces . 97

5.2 Crack front enrichment for the direct SIF extraction . . . 100
5.3 Regularisation of the singular enriched kernels for the Williams-based enrichment . . . 102
5.3.1 Partially cut faces: Williams-based enrichment . . . 102
5.3.2 Enrichment at the crack front for the direct extraction of SIFs . . . 104
5.4 Frenet-Serret frame for the rotation matrix and its derivative . . . 105
5.5 Numerical applications . . . 106
5.5.1 Penny-shaped crack under uniform traction . . . 106
5.5.2 Elliptical crack under uniform traction . . . 111
5.5.3 Prism with edge crack: pure mode analysis . . . 116
5.5.4 Prism with edge crack: uniform load . . . 122
5.6 Partial conclusions . . . 125

6 FATIGUE CRACK GROWTH MODELLING WITH THE XIGABEM 127
6.1 The Paris-Erdogan Law and fatigue life prediction . . . 127
6.2 Crack growth criteria . . . 128
6.2.1 Maximum hoop stress criterion . . . 129
6.2.2 Schollmann criterion . . . 129
6.3 Crack propagation framework in XIGABEM . . . 131
6.4 Modifications in the XIGABEM algebraic system . . . 135
6.5 Numerical applications . . . 136
6.5.1 Elliptical crack growth . . . 136
6.5.2 Inclined penny-shaped crack growth . . . 140
6.5.3 Crack growth analysis of prism with edge crack under cyclic tensile load . . . 150
6.5.4 Hook under cyclic loading . . . 154
6.6 Partial conclusions . . . 162

7 FINAL REMARKS . . . 163
7.1 Recommendations for future work . . . 165

REFERENCES . . . 167

APPENDIX A – B-SPLINES AND NURBS REPRESENTATION OF CURVES AND SURFACES . . . 179
A.1 B-Splines curves . . . 179
A.2 NURBS curves . . . 181
A.3 NURBS surfaces . . . 181
A.4 Trimmed NURBS . . . 182

APPENDIX B – GEOMETRICAL DATA OF ELLIPTICAL CRACK UNDER CRACK GROWTH 185

1 INTRODUCTION

This chapter presents the initial considerations of this Ph.D. research. Section 1.1 presents the scope and the main motivation of this study, while section 1.2 outlines the objectives to be accomplished. Section 1.3 presents the methodology applied to achieve the objectives of this Ph.D. and finally, the outline of this thesis is presented in section 1.4.

1.1 Scope and motivation

Understanding the collapse behaviour of solids is crucial to ensuring the proper performance of engineering components across various industrial sectors in modern society. In addition, preventing these unintended scenarios mitigates the high cost of failure, whether in terms of material losses or human lives. In this context, research in structural engineering focuses on developing theories that accurately represent the failure of solids. These theories ultimately predict and prevent failures during the design and inspection phases.

Fracture mechanics is a suitable approach between the existing theories to represent the mechanical behavior of solid near failure. This field assumes that the governing mechanism of collapse results from the presence of physical discontinuities, known as cracks, and their growth. In this theory, the mechanical analysis involves evaluating the influence of cracks in their discrete form within the solid's geometry. Therefore, fracture mechanics enables the consistent incorporation of cracks, the crack propagation phenomenon, and its effects on the mechanical behaviour of the solid.

In studying crack behaviour, Linear Elastic Fracture Mechanics (LEFM) provides a method of assessment for problems in which the fracture process zone (FPZ) is negligible. The assumption that the plastic region arising at a crack tip is small is often valid for brittle materials, hydraulic fracture, and for linear fatigue life cycle analysis, for instance. The crack stability criteria in the LEFM demand the computation of Stress Intensity Factors (SIFs) that characterise the complexity of the crack tip stress field. The SIFs define when the crack propagation occurs, and also is crucial part to define the crack propagation direction. Thus, their precise computation is an essential task in the analysis of a cracked component.

The failure of components and structures due to fatigue crack propagation is a significant concern in engineering, as it can occur under loading conditions below the ultimate bearing capacity. Examples such as the Liberty ships (Williams; Ellinger, 1949), multiple derailments in the 19th century, and the Aloha Flight 243 (National Transportation Safety Board, 1989) illustrate the dangers of fatigue crack propagation in

structural systems, underscoring the importance of their accurate prediction. In fracture mechanics, LEFM is valid to this failure mechanism, as the FPZ is negligible in fatigue life cycle analysis. Experimental observations of high-cycle fatigue reveal a relationship between crack growth rate and the number of loading cycles. Specifically, the Paris-Erdogan Law applies concepts from LEFM to relate the crack growth rate to SIFs. This allows for life cycle analysis of engineering components and their maintenance by assessing the current crack length during an inspection.

The need to comprehend the structural response of these components leads to theories that describe the corresponding mechanical problem. In this approach, the geometry, supports, loading conditions, and the material response determine the mechanical fields of the solid. To this end, partial differential equations relate these characteristics to the displacements, strains, and stresses. However, obtaining an analytical solution to these equations is a burdensome task, or even impractical, depending on the complexity of the solid's mechanical characteristics. To overcome these limitations, numerical methods provide a viable approach for determining the response of structural mechanics problems.

Numerical methods apply an algebraic treatment to a differential equation to establish a systematic procedure that yields an approximate solution. Consequently, this approach determines the displacements, stress and strain fields of a mechanical analysis, associating them with a finite number of degrees of freedom. This strategy expresses the mathematical representation of the problem in terms of the degrees of freedom. In addition, the geometric description involves parametric discretisation, eliminating the limitations associated with complex geometries. Specific mechanical models integrated into numerical methods accurately represent nonlinear boundary conditions and material responses, leading to an iterative solution process. Therefore, numerical methods are crucial for analysing structural components, as they enable the mechanical modelling of real-life engineering problems. In this context, some relevant numerical approaches merit attention: the Finite Element Method (FEM), the Generalised/eXtended Finite Element Method (G/XFEM), and the Boundary Element Method (BEM), as well as theories such as the peridynamics and the phase-field modelling.

The Finite Element Method (FEM) discretises the entire solid into nodes and elements. The equilibrium equations for the domain are discretised using the finite element formulation, incorporating the mechanical properties of each element. Applying the boundary conditions to the algebraic system yields the unknown displacement coefficients, while the mechanical fields are obtained through interpolating the nodal responses. This method has been widely successful in numerous engineering problems, particularly in elastostatics. Additionally, its application with techniques that incorporate physical and geometric nonlinearities is another advantage of the method. Several studies have used the FEM for the fatigue analysis of three-dimensional components (Lin; Smith, 1999a; Lin;

Smith, 1999b; Schöllmann; Fulland; Richard, 2003; Ural *et al.*, 2005).

However, the FEM for fracture mechanics problems has its limitations. The first issue arises from the singular nature of the stresses at the crack front, necessitating a fine mesh for accurate representation. Another disadvantage occurs in the crack propagation analysis, which demands a re-meshing task at each propagation step. Given these drawbacks, the G/XFEM emerges as a robust improvement of the FEM by enriching the displacement field to incorporate known a priori mechanical behaviour, overcoming these limitations. The introduction of the Williams solution (Oden; Duarte, 1996) and the discontinuous (Heaviside) (Moës; Dolbow; Belytschko, 1999) functions in the approximation space of the two-dimensional G/XFEM allows the crack to exist and propagate in a geometry completely independently of the FEM mesh, as demonstrated in the seminal work of Sukumar *et al.* (2000) for three-dimensional analysis. Based on these strategies, several applications of the G/XFEM were successful for fracture mechanics problems, such as in dynamic crack propagation (Duarte *et al.*, 2001), higher order functions in G/XFEM (Laborde *et al.*, 2005), crack initiation (Areias; Belytschko, 2005), among others (Duflot, 2008; Rabczuk; Bordas; Zi, 2010; Gupta; Duarte, 2014; Talebi; Silani; Rabczuk, 2015). Moreover, G/XFEM obtains optimal convergence in LEFM problems in both 2-D (Laborde *et al.*, 2005; Béchet *et al.*, 2005; Gupta *et al.*, 2013; Sanchez-Rivadeneira; Duarte, 2019; Bento; Proença; Duarte, 2022) and 3-D (Sanchez-Rivadeneira *et al.*, 2020; Sanchez-Rivadeneira; Duarte, 2020) applications. In addition, the G/XFEM is successful in representing 3-D fatigue propagation (Shi *et al.*, 2010; Rannou *et al.*, 2010; Pereira; Duarte; Jiao, 2010; Pathak; Singh; Singh, 2013; Garzon *et al.*, 2014; O'Hara *et al.*, 2016; Bergara *et al.*, 2017). However, it is important to use techniques such as these with caution because of the consequent ill-conditioning in the stiffness matrix caused by the enrichment contributions, which can compromise solution accuracy if not suitably treated.

Alternative numerical approaches have recently arise to successfully circumvent the problems of the FEM, such as peridynamics (Silling *et al.*, 2007; Liu; Hong, 2012; Breitenfeld, 2014; Sarego *et al.*, 2016; Hu; Madenci, 2017; Jung; Seok, 2017; Wang *et al.*, 2018; Nguyen; Oterkus; Oterkus, 2021) and phase-field models (Miehe; Hofacker; Welschinger, 2010; Ambati; Gerasimov; Lorenzis, 2015; Molnár; Gravouil, 2017; Lo *et al.*, 2019; Mesgarnejad; Imanian; Karma, 2019; Kristensen; Martínez-Pañeda, 2020; Carrara *et al.*, 2020; Ding *et al.*, 2024) for fracture and fatigue modelling. The comparison between these two methods performed by Diehl *et al.* (2022) highlights as advantages of both methods: ability to capture crack initiation, the dismissal of an additional criteria to describe crack growth and their applicability in multi-field fracture. While peridynamics presents an attractive approach in terms of capturing dynamic effects such as crack branching, it fails to capture some of the important physics, for example the propagation speed of an elastic wave. Moreover, the peridynamics approach can allow mechanical effects to propagate too quickly through media since mechanical interactions are instantaneous

over a finite horizon. In addition, these two methods are computationally expensive and, as a plausible consequence, there are few three-dimensional researches based on these two approaches.

An alternative method to domain-based methods is the BEM, which requires a boundary-only discretisation of the solid under analysis. This characteristic reduces the mesh dimension by one order, simplifying all mesh-related tasks. In three-dimensional problems, a parametrisation of the external surface is sufficient. Additionally, this significantly reduces the number of degrees of freedom compared to FEM due to the dimensional reduction. Furthermore, internal fields are determined using boundary integral equations in the post-processing step, rather than being interpolated from the nodal solution as in FEM. Therefore, internal displacements, strains, and stresses can be accurately obtained, provided the boundary response is sufficiently precise. Particularly, the Dual BEM formulation for fracture mechanics applies two linearly independent boundary equations, the Displacement Boundary Integral Equation (Somigliana, 1885) and its derivative, the Traction Boundary Integra Equation (Hong; Chen, 1988) at opposite crack faces to result in the Dual BEM (Portela; Aliabadi; Rooke, 1992). Due to the aforementioned characteristics, the BEM has been successfully explored for two-dimensional crack problems (Portela; Aliabadi; Rooke, 1993; Saleh; Aliabadi, 1995; Leonel; Venturini, 2010a; Price; Trevelyan, 2014; Li *et al.*, 2024), and also for three-dimensional applications (Mi; Aliabadi, 1992; Mi; Aliabadi, 1994; Cisilino; Aliabadi, 1999; Carter; Wawrzynek; Ingraffea, 2000; Yang; Mall; Ravi-Chandar, 2001; Cisilino; Aliabadi, 2004; Kolk; Kuhn, 2006; Cordeiro; Leonel, 2019; Feng *et al.*, 2020). However, there are some strong singularities and hyper-singularities that demand semi-analytical treatment, as presented in Guiggiani and Gigante (1990) and Guiggiani *et al.* (1992) for three-dimensional elasticity problems.

The advantages of BEM over FEM in fracture mechanics problems stem directly from the absence of a domain mesh. Firstly, the singular nature of the stress field near the crack front does not demand a fine mesh as it does in FEM. In addition, crack propagation is simplified, as the crack does not intersect any pre-existing volume mesh during the analysis. However, when the crack intersects the external boundary in three-dimensional analyses, a specific treatment is required during crack growth. In this situation, BEM requires re-meshing, though it remains simpler than in FEM.

The standard BEM formulation utilises Lagrange polynomials to approximate the geometry and mechanical fields. However, this parametrisation requires a large number of elements for curved surfaces, as standard polynomials have limited approximation capacity. Additionally, representing high gradients in numerical responses can be impractical with lower-order Lagrange functions, compromising the overall solution quality. To address these limitations, adopting an alternative set of basis functions in BEM can enhance the method's robustness by improving both geometry representation and numerical accuracy.

Among the available basis functions for interpolating geometry and mechanical fields, B-Splines, T-Splines, and especially Non-Uniform Rational B-Splines (NURBS) are well-suited for BEM for several reasons. Their primary advantage is their use as the geometric parametrisation in Computer-Aided Design (CAD) models, which are widely used in industry for three-dimensional modeling of engineering components, such as hooks and gears. Thus, importing these models into a boundary-only method that employs the same basis functions as the CAD model eliminates the need for mesh generation. This simultaneous use of basis functions for geometry and approximation fields, as in the CAD model, defines Isogeometric Analysis (IGA) (Hughes; Cottrell; Bazilevs, 2005). NURBS and T-Spline basis functions offer another advantage: as rational functions, they can exactly represent curved surfaces such as spheres and toroids. This results in a reduction in the number of parameters required for geometric parametrisation, and consequently, a reduction in the total number of degrees of freedom. Consequently, IGA-based formulations achieves higher accuracy with fewer degrees of freedom compared to the standard counterparts. Several authors have investigated the outcomes of the IGA coupled with the FEM (Bazilevs *et al.*, 2006b; Cottrell; Hughes; Reali, 2007; Bazilevs *et al.*, 2010), and its application to various engineering problems, such as fluid-structure interaction (Bazilevs *et al.*, 2008; Bazilevs *et al.*, 2006a), topology optimisation (Wall; Frenzel; Cyron, 2008), phase-field modelling (Borden *et al.*, 2014; Kiendl *et al.*, 2016; Nguyen-Thanh *et al.*, 2022) and the eXtended IGA (XIGA) approach (Benson *et al.*, 2010; Luycker *et al.*, 2011; Verhoosel *et al.*, 2011; Ghorashi; Valizadeh; Mohammadi, 2012; Ghorashi *et al.*, 2015; Nguyen-Thanh *et al.*, 2015; Fathi; Chen; Borst, 2020; Fathi; Borst, 2021; Fathi *et al.*, 2022) demonstrate the robustness of using IGA basis functions on Finite Element procedures. Additionally, collocation-based methods such as collocation-BEM exhibit improved robustness in IGA because the collocation points lie exactly on the boundary rather than on an approximation of it. Therefore, the substitution of the Lagrangian basis functions into NURBS results in the Isogeometric Boundary Element Method (IGABEM). The IGABEM started with the work of Politis *et al.* (2009) for two dimensional potential problems, and it was extended to 2-D linear elasticity problems by Simpson *et al.* (2012) and Simpson *et al.* (2013). Subsequently, the method demonstrated its robustness in a plethora of engineering problems, such as shape optimisation (Li; Qian, 2011; Sun *et al.*, 2018), fluid mechanics (Heltai; Arroyo; DeSimone, 2014), acoustics (Coox *et al.*, 2017; Chen *et al.*, 2018; Chen *et al.*, 2019; Shaaban *et al.*, 2020; Wu; Dong; Yang, 2020), and heat transfer (An *et al.*, 2018; Zang *et al.*, 2024).

Three-dimensional IGABEM for elastostatic analysis has been an emerging research topic, beginning with the use of unstructured T-Splines as basis functions by Scott *et al.* (2013), and followed by Lian, Simpson and Bordas (2013), Gu *et al.* (2015), Beer *et al.* (2017), Li *et al.* (2018), and Peres *et al.* (2024). Moreover, Peng *et al.* (2017a) pioneered the three-dimensional IGABEM formulation for linear elastic fracture mechanics and fatigue

propagation, focusing on cracks embedded in an infinite medium, while Cordeiro and Leonel (2018) applied the 3-D IGABEM to cracked engineering components. Subsequently, other studies (Sun; Dong, 2021; Sun; Dong, 2023; He; Peng; Ding, 2023) explored the advantages of the 3-D IGABEM formulation in crack growth analysis. However, the standard formulation induces non-physical displacements at the crack front, compromising both the convergence rate and displacement field accuracy. Additionally, in these studies, numerical modelling of cracks requires mesh alignment between the external boundary and the crack to properly represent the displacement discontinuity in this region. Then, this Ph.D. thesis addresses both issues through the enriched formulation of the 3-D IGABEM.

The use of enrichment functions in BEM is incipient, starting with Simpson and Trevelyan (2011b) and Simpson and Trevelyan (2011a) for two-dimensional applications. These studies applied the Partition of Unity concept to enrich the displacement field using the Williams solution-based strategy. This leads to accurate SIF solutions even with coarse models, outperforming standard BEM formulations. In addition, SIFs are incorporated into the solution vector, eliminating the need for post-processing tasks, such as J-integral and M-integral, for isotropic (Alatawi; Trevelyan, 2015) and anisotropic (Hattori; Alatawi; Trevelyan, 2017) media. Furthermore, the Heaviside enrichment function proposed by Andrade and Leonel (2020) in eXtended BEM (XBEM) eliminates the need for re-meshing when cracks intersect the external boundary in 2-D problems. Evidently, this intersection occurs between a point and a line, simplifying the re-meshing procedure. However, in three-dimensional problems, a line-surface intersection significantly increases the complexity of this enrichment function, as detailed in the present study. Moreover, the only study on 3D-XBEM (Alatawi, 2016) enables the direct extraction of SIFs using the Williams solution-based enrichment scheme at crack surfaces, where only planar cracks are analysed. Therefore, the development of enrichment functions for three-dimensional extended BEM formulations represents a novel contribution and is the main objective of the present work.

While enrichment strategies in the BEM framework have effectively enhanced the method, their use within IGABEM remains emergent, with few studies exploring this coupling. In acoustics, Peake, Trevelyan and Coates (2013) and Peake, Trevelyan and Coates (2015) pioneered the expansion of approximation fields, employing NURBS functions for 2-D and 3-D problems, respectively. Shaaban *et al.* (2020) subsequently applies the eXtended IGABEM (XIGABEM) formulation for shape optimisation in 2-D acoustic problems. In fracture mechanics, (Peng *et al.*, 2017b) extends the displacement field of the 2-D IGABEM using singular enrichment to enhance the mechanical response. Furthermore, Andrade, Trevelyan and Leonel (2022) directly extracts SIFs using XIGABEM in 2-D fatigue analysis of homogeneous media, while Andrade, Trevelyan and Leonel (2023) obtains SIFs and T-stresses for bi-materials from the solution vector through the XIGABEM approach.

Another aspect associated with IGA is the challenges that the standard NURBS surface parametrisation presents in representing holes and intricate details of complex geometries. This limitation stems from the definition of a NURBS surface as a tensor product of two univariate NURBS curves, resulting in large four-sided patches. This limits their ability to model surfaces with additional edges or internal cuts. Then, trimming operations resolve this issue, where a trimming curve defines the retained or removed portion within the parametric space of the NURBS surface. This is a standard procedure in CAD modelling, and its incorporation into numerical methods facilitates seamless coupling between CAD modeling and mechanical analysis. In the FEM framework, the seminal study of Kim, Seo and Youn (2009) promotes an IGA with trimmed surfaces, addressing a specific integration strategy for cut knot spans and the loss in accuracy from the trimming effect. Nagy and Benson (2015) subsequently refine solutions to these issues. In the IGABEM framework, Wang, Benson and Nagy (2015) apply the trimmed surfaces in a non-singular approach, in which the collocation points are placed outside the boundary. This alleviates requirements over the placement of these points, as collocation points retain validity even if their projections are on removed portions. Marussig *et al.* (2017) and Marussig, Hiemstra and Hughes (2018) present the singular formulation of the IGABEM with trimmed surfaces using Extended B-Splines and Truncated Hierarchical B-Splines to stabilise the set of basis functions by altering the standard NURBS approximation. The work of Peng and Lian (2022) performs a linear elastic fracture mechanics analysis using trimmed surfaces to model displacement discontinuities at lateral faces. In addition, the study of Beer (2025) proposes a global approach avoiding basis function trimming while ensuring continuous collocation points by creating an additional mapping that comprises only the valid region of the trimmed span. In this context, this study proposes the coupling between trimmed surfaces and IGABEM while retaining original NURBS basis functions.

The computational mechanics research group of the Department of Structural Engineering of the São Carlos School of Engineering (EESC) at the University of São Paulo (USP) has developed innovative contributions to the field of this thesis. In two-dimensional analyses, the numerical analysis of multi-cracked solids and their growth is present in Leonel and Venturini (2010a) and Leonel and Venturini (2011). The fracture process involving various material responses is also object of study using the BEM, such as quasi-brittle Leonel and Venturini (2010b), Oliveira and Leonel (2013), viscoelastic (Oliveira; Leonel, 2017), anisotropic Cordeiro and Leonel (2016), Cordeiro and Leonel (2020), and inhomogeneous materials under fatigue Andrade and Leonel (2019). In addition, the 2-D IGABEM formulation has been successfully applied to topology optimisation Oliveira, Andrade and Leonel (2020) and to quasi-brittle materials fracture analysis Nardi and Leonel (2024). Furthermore, three-dimensional BEM analysis has been conducted for LEFM (Cordeiro; Leonel, 2019) and cohesive crack growth (Rocha; Leonel, 2022; Almeida; Leonel, 2024a; Almeida; Leonel, 2024b; Almeida; Atroshchenko; Leonel, 2025). Enrichment

strategies have also been developed by the group in Andrade and Leonel (2020), Andrade, Trevelyan and Leonel (2022) and Andrade, Trevelyan and Leonel (2023) for isotropic and anisotropic materials using the XBEM and the XIGABEM. Finally, Cordeiro and Leonel (2018) is the first study of the research group addressing three-dimensional IGABEM formulations for fracture mechanics, while Neto and Leonel (2022) focuses on adaptive refinements for three-dimensional IGABEM with reinforcements and cracks. Thus, this thesis aligns with the research group developments, focusing on new topics in the same contexts of the previous researches.

1.2 Objectives

The main objective of this thesis is the proposal of enriched formulations for fracture and fatigue analyses of three-dimensional solids within the Isogeometric Boundary Element Method. Additionally, this study addresses the incorporation of trimmed CAD models into the IGABEM framework.

Initially, the incorporation of the trimmed surfaces into the 3-D IGABEM is developed. The main advantages of this topic are:

- Eliminating the need for mesh reconstruction from trimmed CAD models.
- Numerical analysis of more complex geometries than the ones generated with standard NURBS surfaces.

Subsequently, the Heaviside enrichment allows the representation of strong discontinuities along the external boundary intersected by cracks. The novel aspects associated with this development are:

- Eliminating the mesh alignment requirement along the crossed region.
- Dismissal of re-meshing procedures in crack growth analysis.

Next, the Williams solution-based enrichment scheme improves the 3-D IGABEM formulation by introducing an asymptotic behaviour next to the crack tip. Its main novelties are:

- Representing the $\sqrt{r}$ behaviour at lateral surfaces while capturing the strong discontinuity at the intersection between the boundary and a crack.
- Improvements in convergence rates in comparison to the standard IGABEM.
- Simplified extraction of SIFs, as they become enrichment parameters.

Finally, the fatigue crack propagation analysis using the aforementioned enrichment strategies is conducted. The novel features of this application are:

- Using the SIFs directly extracted from the Williams enrichment with the Paris-Erdogan Law to assess the component's life cycle
- A novel crack front advancement algorithm allows for capturing changes in the crack front curvature.
- Numerical analyses of three-dimensional crack configurations with two crack growth criteria, being the Schollmann criterion being applied for the first time with an IGABEM formulation.

1.3 Methodology

The numerical implementation of the formulations proposed in this Ph.D. thesis is developed within the computational code of Prof. Edson Leonel's research group, which originated with Cordeiro (2018) and was further expanded by Neto (2023). The programming language is Fortran 90, in which the 3-D formulation of the IGABEM had already been implemented before the development of this thesis. In this sense, all novel formulations presented in this thesis were implemented by the author. The validation of the proposed algorithms and formulations involves comparing the solutions of simple problems with analytical solutions, while more complex applications are verified against results from the literature. The computer used to run the code and obtain the results of this thesis is an AMD ®Ryzen 9 7900 processor (5.4 GHz, 12 cores) with 64 GB of RAM. The numerical code uses the OpenMP parallel directive to reduce computational time in critical tasks of the numerical analysis. The software Rhinoceros 6 (McNeel *et al.*, 2010) is responsible for generating the isogeometric geometry of all numerical applications.

1.4 Outline

The remainder of this thesis is organised as follows: Chapter 2 describes the IGABEM formulation for three-dimensional elastostatic problems. Chapter 3 presents the incorporation of trimmed surfaces into IGABEM. Subsequently, Chapter 4 contains the Heaviside enrichment function proposal for representing strong discontinuities along the external boundary intersected by cracks and its consequences for the numerical method. Next, the Williams solution-based enrichment strategy is presented in Chapter 5, for both the external boundary crossed by cracks, and for crack surfaces enabling the direct extraction of SIFs. In Chapter 6, the XIGABEM formulation is applied to fatigue crack propagation analysis of cracked solids under cyclical loading conditions. Finally, Chapter 7 summarises the main findings of this thesis and provides some recommendations for further investigation.

2 ISOGEOMETRIC BOUNDARY ELEMENT METHOD

This chapter presents the theoretical aspects of the IGABEM. The IGABEM for linear elasticity starts from the associated boundary value problem and the Somigliana Identity (Somigliana, 1885). This relation involves the three-dimensional elastostatic fundamental solutions. Furthermore, the limiting process over the Somigliana Identity results in the integral equations applied to points on the solid's boundary. Afterwards, this chapter presents the dual BEM approach, which allows the analysis of cracked solids. The next development is the isogeometric interpolation based on NURBS basis functions, and its impact on the numerical integration over the surface and the collocation strategy. The application of these tasks enables the generation of the algebraic system, which determines the unknown mechanical fields. From the numerical solution, the equations for the internal displacements and stresses are derived from the Somigliana Identity. Further details about the BEM and the IGABEM can be found in Aliabadi (2002) and Beer, Marussig and Duenser (2020), respectively. In addition, the numerical implementation of the three-dimensional IGABEM has been developed by this research group since the work of Cordeiro (2018).

2.1 Somigliana Identity and Kelvin Fundamental Solution

The linear elasticity boundary value problem considers a three-dimensional body with domain Ω and boundary Γ, subjected to body forces $\mathbf{b}$, as shown in fig. 1. The Neumann and Dirichlet prescribed boundary conditions are tractions $\overline{\mathbf{t}}$ over the boundary Γ_t and displacements $\overline{\mathbf{u}}$ over the boundary Γ_u, respectively, such that $\Gamma = \Gamma_u \cup \Gamma_t$ and $\Gamma_u \cap \Gamma_t = \emptyset$. In this problem, displacements and tractions are the unknown mechanical fields for Γ_t and Γ_u, respectively.

From the local equilibrium of an infinitesimal part of the solid, the equation for the balance of linear momentum is:

$$\sigma_{jk,j} + b_k = 0_k \tag{2.1}$$

in which σ_{jk} is the stress tensor. Solving it directly can be burdensome or even impractical. Alternatively, the application of the Weighted Residue Method on eq. (2.1) results in:

$$\int_\Omega \left(\sigma_{jk,j} + b_k\right) w_k \, d\Omega = 0 \tag{2.2}$$

where w_k is a weighting function. In the BEM, this function is the Kelvin Fundamental Solution (Kelvin, 1848), so that it becomes possible to eliminate the domain integral in further developments. This solution relates the displacements $U^*_{\ell k}$ and tractions $T^*_{\ell k}$ in the

Figure 1 – Arbitrary solid of the linear elasticity boundary value problem.

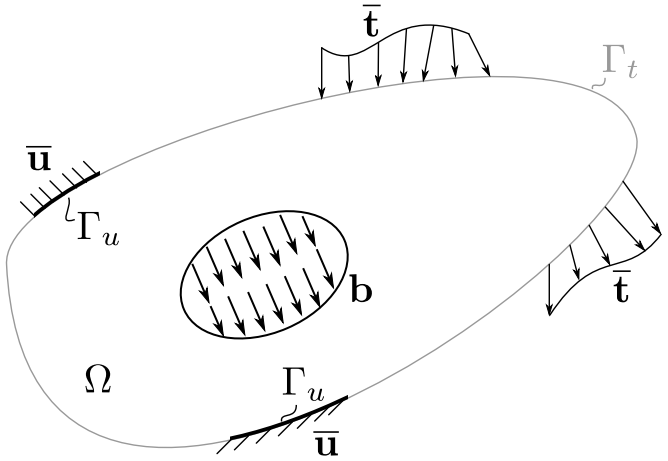

Source: The author.

k-direction at a given point $\mathbf{x}$ considering a unit force at the direction ℓ at the source point $\hat{\mathbf{x}}$ of an isotropic unbounded domain. The expressions for $U^*_{\ell k}$ and $T^*_{\ell k}$ are:

$$\begin{aligned} U^*_{\ell k}(\mathbf{x},\hat{\mathbf{x}}) &= \frac{1}{16\pi\mu\,(1-\nu)\,r}\left[(3-4\nu)\,\delta_{\ell k} + r_{,\ell} r_{,k}\right] \\ T^*_{\ell k}(\mathbf{x},\hat{\mathbf{x}}) &= \frac{-1}{8\pi\,(1-\nu)\,r^2}\left\{\frac{\partial r}{\partial \mathbf{n}}\left[(1-2\nu)\,\delta_{\ell k} + 3 r_{,\ell} r_{,k}\right] - (1-2\nu)\,(r_{,\ell} n_k + r_{,k} n_\ell)\right\} \end{aligned} \tag{2.3}$$

in which $\mathbf{r} = \mathbf{x} - \hat{\mathbf{x}}$ is the distance vector between the source point and the field point while $r = ||\mathbf{r}||$. The term $r_{,k} = \frac{r_k}{r}$ represents the derivatives of r with respect to the k direction, and $\mathbf{n}$ is the normal outward vector at the boundary field point. Additionally, $\mu = \frac{E}{2(1+\nu)}$, E and ν are the shear modulus, Young Modulus and Poisson ratio, respectively. Also, $\delta_{\ell k}$ is the Kronecker delta. The terms $(\mathbf{x},\hat{\mathbf{x}})$ will be omitted in all subsequent references to the fundamental solutions for brevity. By substituting eq. (2.3) into eq. (2.1) and integrating the first term by parts:

$$\int_\Omega \left(\sigma_{jk} U^*_{\ell k}\right)_{,j} d\Omega - \int_\Omega \sigma_{jk} U^*_{\ell k,j} d\Omega + \int_\Omega b_k U^*_{\ell k}\, d\Omega = 0_\ell \tag{2.4}$$

The application of the Divergence Theorem to the first integral of eq. (2.4) results in:

$$\int_\Gamma \sigma_{jk} U^*_{\ell k} n_j\, d\Gamma - \int_\Omega \sigma_{jk} U^*_{\ell k,j} d\Omega + \int_\Omega b_k U^*_{\ell k}\, d\Omega = 0_\ell \tag{2.5}$$

The application of the stress tensor symmetry ($\sigma_{jk} = \sigma_{kj}$) and the Cauchy formula ($t_k = \sigma_{kj} n_j$) in eq. (2.5) yields:

$$\int_\Gamma U^*_{\ell k} t_k\, d\Gamma - \int_\Omega \sigma_{kj} U^*_{\ell k,j} d\Omega + \int_\Omega b_k U^*_{\ell k}\, d\Omega = 0_\ell \tag{2.6}$$

From the linearised displacement-strain relation $\varepsilon^*_{\ell kj} = (\, U^*_{\ell k,j} + U^*_{\ell j,k})/2$, it follows that $\sigma_{kj} U^*_{\ell k,j} = \sigma_{kj} \varepsilon^*_{\ell kj}$ by considering the symmetry of the stress tensor. This change in eq. (2.6) culminates in:

$$\int_\Gamma U^*_{\ell k} t_k\, d\Gamma - \int_\Omega \sigma_{kj} \varepsilon^*_{\ell kj} d\Omega + \int_\Omega b_k U^*_{\ell k}\, d\Omega = 0_\ell \tag{2.7}$$

The generalised Hooke Law for isotropic materials states that $\sigma_{kj} = \mathbb{C}_{kjmn}\varepsilon_{mn}$. Due to the constitutive tensor symmetry, $\mathbb{C}_{kjmn} = \mathbb{C}_{mnkj}$. Then, $\sigma_{kj}\varepsilon^*_{\ell kj}$ is equivalent to $\mathbb{C}_{mnkj}\varepsilon^*_{\ell kj}\varepsilon_{mn}$. Analogously, these operations are also valid for the fundamental solutions, resulting in $\sigma^*_{\ell mn} = \mathbb{C}_{mnkj}\varepsilon^*_{\ell kj}$. These modifications transform the second term of eq. (2.7) into $\sigma^*_{\ell mn}\varepsilon_{mn}$. Since m and n are summation indices, they can be replaced by k and j, respectively. The application of all these operations modifies eq. (2.7) into:

$$\int_\Gamma U^*_{\ell k} t_k \, d\Gamma - \int_\Omega \sigma^*_{\ell kj}\varepsilon_{kj} \, d\Omega + \int_\Omega b_k U^*_{\ell k} \, d\Omega = 0_\ell \tag{2.8}$$

The manipulation of the linearised displacement-strain relation also leads to $\sigma^*_{\ell kj}\varepsilon_{kj} = \sigma^*_{\ell kj}u_{k,j}$, which then transforms the second integral of eq. (2.8) into:

$$\int_\Gamma U^*_{\ell k} t_k \, d\Gamma - \int_\Omega \sigma^*_{\ell kj} \, u_{k,j} \, d\Omega + \int_\Omega b_k U^*_{\ell k} \, d\Omega = 0_\ell \tag{2.9}$$

By integrating by parts and using the Divergence Theorem on the second integral, eq. (2.9) results:

$$\int_\Gamma U^*_{\ell k} t_k \, d\Gamma - \int_\Gamma T^*_{\ell k} u_k \, d\Gamma + \int_\Omega \sigma^*_{\ell jk,j} u_k d\Omega + \int_\Omega b_k U^*_{\ell k} \, d\Omega = 0_\ell \tag{2.10}$$

The development of the third integral follows from the local momentum with respect to the fundamental solution, $\sigma^*_{\ell jk,j} + b^*_{\ell k} = 0_{\ell k}$, or $\sigma^*_{\ell jk,j} = -b^*_{\ell k}$. Additionally, the body force in the fundamental problem relates to the Dirac delta as $b^*_{\ell k} = \delta_{\ell k}\Delta\left(\mathbf{x} - \hat{\mathbf{x}}\right)$. The substitution of the body force $b^*_{\ell k}$ into the third integral of eq. (2.10) enables the use of the sifting property of the Dirac delta, which makes this integral result in $-u_\ell(\hat{\mathbf{x}})$ and 0_ℓ for internal and external source points, respectively. When the source point is on the boundary, this integration process requires a limiting process, which is presented in section 2.2. These operations turn eq. (2.10) into the Somigliana Identity (Somigliana, 1885):

$$c_{\ell k}(\hat{\mathbf{x}})u_k(\hat{\mathbf{x}}) + \int_\Gamma T^*_{\ell k} u_k \, d\Gamma = \int_\Gamma U^*_{\ell k} t_k \, d\Gamma + \int_\Omega b_k U^*_{\ell k} \, d\Omega \tag{2.11}$$

in which $c_{\ell k}(\hat{\mathbf{x}})$ is the jump term whose value depends on the source point position. Internal source points have $c_{\ell k} = \delta_{\ell k}$, while $c_{\ell k} = 0_{\ell k}$ for the external counterparts. The Somigliana Identity relates the displacement of a point $\hat{\mathbf{x}}$ based on the known mechanical fields at the boundary. The remaining domain integral associated with the body forces can be evaluated in several forms, such as radial integration (Gao, 2002) or the Dual Reciprocity Theorem (Aliabadi, 2002). In this work, the body forces will be absent in the numerical analyses, which dismisses the assessment of the domain integral.

Obtaining of stresses and strains is also possible from the Somigliana Identity. The differentiation of the eq. (2.11) with respect to the source point position and the incorporation of the linearised displacement-strain relation yields the strains at the internal source point as:

$$\varepsilon_{\ell i}(\hat{\mathbf{x}}) + \int_\Gamma \hat{T}^*_{\ell ik} u_k \, d\Gamma = \int_\Gamma \hat{U}^*_{\ell ik} t_k \, d\Gamma \tag{2.12}$$

The stresses integral equation arises from the application of the Hooke Law in eq. (2.12) as:

$$\sigma_{\ell j}(\hat{\mathbf{x}}) + \int_\Gamma S^*_{k\ell j} u_k \, d\Gamma = \int_\Gamma D^*_{k\ell j} t_k \, d\Gamma \tag{2.13}$$

in which the fundamental solutions $D^*_{k\ell j}$ and $S^*_{k\ell j}$ are:

$$\begin{aligned} D^*_{k\ell j}(\mathbf{x},\hat{\mathbf{x}}) &= \frac{1}{8\pi(1-\nu)r^2}\left[(1-2\nu)(\delta_{k\ell}r_{,j}+\delta_{jk}r_{,\ell}-\delta_{\ell j}r_{,k})+3(r_{,\ell}r_{,j}r_{,k})\right] \\ S^*_{k\ell j}(\mathbf{x},\hat{\mathbf{x}}) &= \frac{\mu}{4\pi(1-\nu)r^3}\{3\frac{\partial r}{\partial \mathbf{n}}[(1-2\nu)\delta_{\ell j}r_{,k}+\nu(\delta_{\ell k}r_{,j}+\delta_{jk}r_{,\ell})-5r_{,\ell}r_{,j}r_{,k}] \\ &+3\nu(n_\ell r_{,j}r_{,k}+n_j r_{,\ell}r_{,k})+(1-2\nu)(3n_k r_{,\ell}r_{,j}+n_j\delta_{\ell k}+n_\ell\delta_{jk})-(1-4\nu)n_k\delta_{\ell j}\} \end{aligned} \tag{2.14}$$

Lastly, the substitution of the eq. (2.13) in the Cauchy formula ($t_j = \sigma_{\ell j}n_\ell$) results in:

$$t_j(\hat{\mathbf{x}}) + n_\ell(\hat{\mathbf{x}})\int_\Gamma S^*_{k\ell j}u_k\,d\Gamma = n_\ell(\hat{\mathbf{x}})\int_\Gamma D^*_{k\ell j}t_k\,d\Gamma \tag{2.15}$$

Equation (2.15) is linearly independent from eq. (2.11), which is crucial for the Dual BEM approach (Hong; Chen, 1988). This strategy is in section 2.3 for the numerical analysis of cracked solids.

In the linear elasticity boundary value problem, the unknowns are displacements and tractions at Γ_t and Γ_u, respectively. The Somigliana Identity allows finding these fields by choosing source points external to the boundary. However, this approach is highly dependent on the adopted distance between these points and the boundary. In addition, near-singular integrals arise when the source point is close to the external boundary, which jeopardises the accuracy of the response. Alternatively, placing the source points on the boundary leads to more stable results; however, strongly singular and hypersingular integrals appear as a consequence of the $O(1/r^\alpha), \alpha = 1,2,3$ nature of the fundamental solutions. Additionally, determining the jump term requires a limiting process analysis.

2.2 Limiting process: boundary integral equations

The Somigliana Identity and its traction equivalent are not yet valid for source points on the boundary of the solid. To overcome this issue, the limiting process involves taking an internal source point $\hat{\mathbf{x}}$ on the boundary Γ and expanding the surrounding boundary into an auxiliary semi-sphere centered in $\hat{\mathbf{x}}$ with radius ϵ, as illustrated in fig. 2. The addition of this fictitious additional domain and boundary results in $\hat{\mathbf{x}}$ to become an internal source point, in which eq. (2.11) and eq. (2.15) are now valid.

In this context, the addition of the fictitious domain and boundary on eq. (2.11) yields:

$$u_\ell(\hat{\mathbf{x}}) + \int_{\Gamma-\Gamma_\epsilon} T^*_{\ell k}u_k\,d\Gamma + \int_{\Gamma^+_\epsilon} T^*_{\ell k}u_k\,d\Gamma = \int_{\Gamma-\Gamma_\epsilon} U^*_{\ell k}t_k\,d\Gamma + \int_{\Gamma^+_\epsilon} U^*_{\ell k}t_k\,d\Gamma \tag{2.16}$$

The limiting process involves taking $\epsilon \to 0$ in the integrals of eq. (2.16) as:

$$\begin{aligned} u_\ell(\hat{\mathbf{x}}) &+ \lim_{\epsilon\to 0}\left(\int_{\Gamma-\Gamma_\epsilon} T^*_{\ell k}u_k\,d\Gamma\right) + \lim_{\epsilon\to 0}\left(\int_{\Gamma^+_\epsilon} T^*_{\ell k}u_k\,d\Gamma\right) \\ &= \lim_{\epsilon\to 0}\left(\int_{\Gamma-\Gamma_\epsilon} U^*_{\ell k}t_k\,d\Gamma\right) + \lim_{\epsilon\to 0}\left(\int_{\Gamma^+_\epsilon} U^*_{\ell k}t_k\,d\Gamma\right) \end{aligned} \tag{2.17}$$

The integral containing the kernel U^* and over $\Gamma - \Gamma_\epsilon$ is weakly-singular of order $O(r^{-1})$, and it is computed as an improper integral. The integral with the same kernel U^* but over Γ^+_ϵ is

Figure 2 – Fictitious domain and boundary for the limiting process.

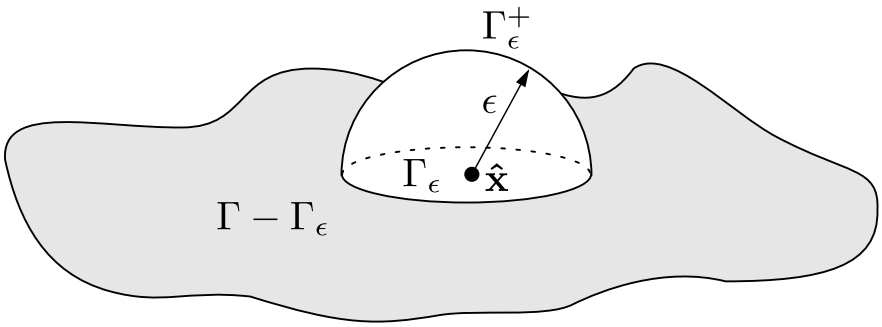

Source: Adapted from Rocha (2020)

0 when $\epsilon \to 0$. On the other hand, the integrals with the kernel T^* are strongly-singular ($O(r^{-2})$) in the limit, which demands the evaluation of $\lim_{\epsilon\to 0}\left(\int_{\Gamma-\Gamma_\epsilon} T^*_{\ell k} u_k \, d\Gamma\right)$ in the Cauchy Principal Value (CPV) sense. The remaining integral over Γ_ϵ^+ computation considers the displacement expansion in the the first term of the Taylor Series as $u_k = u_k - u_k(\hat{\mathbf{x}}) + u_k(\hat{\mathbf{x}})$. The incorporation of this expansion into the remaining integral results in:

$$\lim_{\epsilon\to 0}\left(\int_{\Gamma_\epsilon^+} T^*_{\ell k} u_k \, d\Gamma\right) = \lim_{\epsilon\to 0}\left[\int_{\Gamma_\epsilon^+} T^*_{\ell k}\left(u_k - u_k(\hat{\mathbf{x}})\right) \, d\Gamma\right] + \lim_{\epsilon\to 0}\left[\int_{\Gamma_\epsilon^+} T^*_{\ell k} u_k(\hat{\mathbf{x}}) \, d\Gamma\right] \tag{2.18}$$

The displacement continuity is responsible for the first integral being zero. The second integral can be rearranged as $u_k(\hat{\mathbf{x}}) \lim_{\epsilon\to 0}\left[\int_{\Gamma_\epsilon^+} T^*_{\ell k} \, d\Gamma\right]$ as $u_k(\hat{\mathbf{x}})$ is constant, it can be placed outside the integral. This integral yields a constant value, which results in the jump term $c_{\ell k}$. For source points on smooth boundaries having a unique value for the normal outward vector the jump term is $c_{\ell k} = 0.5\delta_{\ell k}$. In this sense, the jump term now comprises all three possible scenarios for the source point: internal, external, and on the boundary. By denoting the integration on the CPV sense of the term with kernel T^* by $\fint$, eq. (2.11) becomes the Displacement Boundary Integral Equation as:

$$c_{\ell k}(\hat{\mathbf{x}}) u_k(\hat{\mathbf{x}}) + \fint_\Gamma T^*_{\ell k} u_k \, d\Gamma = \int_\Gamma U^*_{\ell k} t_k \, d\Gamma \tag{2.19}$$

The limiting process can be applied at the stress boundary integral equation for internal points to obtain a linearly independent equation from eq. (2.19) over the boundary of the solid. Applying it to eq. (2.13) in a analogous manner to the displacement equation leads to:

$$\begin{aligned} \sigma_{\ell j}(\hat{\mathbf{x}}) + \lim_{\epsilon\to 0}\left(\int_{\Gamma-\Gamma_\epsilon} S^*_{k\ell j} u_k \, d\Gamma\right) + \lim_{\epsilon\to 0}\left(\int_{\Gamma_\epsilon^+} S^*_{k\ell j} u_k \, d\Gamma\right) \\ = \lim_{\epsilon\to 0}\left(\int_{\Gamma-\Gamma_\epsilon} D^*_{k\ell j} t_k \, d\Gamma\right) + \lim_{\epsilon\to 0}\left(\int_{\Gamma_\epsilon^+} D^*_{k\ell j} t_k \, d\Gamma\right) \end{aligned} \tag{2.20}$$

The integrals with the kernel D^* are strongly singular due to the nature of the kernel, which is of order $O(r^{-2})$. The integral with D^* and over $\Gamma - \Gamma_\epsilon$ is also improper, which demands the integration in the CPV sense. In addition, the other integral containing D^* requires regularisation, which involves expanding the traction field into the first term of its Taylor Series as $t_k = t_k - t_k(\hat{\mathbf{x}}) + t_k(\hat{\mathbf{x}})$. This allows rearranging this integral as:

$$\lim_{\epsilon\to 0}\left(\int_{\Gamma_\epsilon^+} D^*_{k\ell j} t_k \, d\Gamma\right) = \lim_{\epsilon\to 0}\left[\int_{\Gamma_\epsilon^+} D^*_{k\ell j}\left(t_k - t_k(\hat{\mathbf{x}})\right)\right] + t_k(\hat{\mathbf{x}}) \lim_{\epsilon\to 0}\left[\int_{\Gamma_\epsilon^+} D^*_{k\ell j} \, d\Gamma\right] \tag{2.21}$$

in which the first integral of eq. (2.21) is zero after taking the limit. $t_k(\hat{\mathbf{x}})$ is constant and is placed outside the second integral, while the limit of the remaining integral is a term that multiplies the stress tensor $\sigma_{\ell j}$, being $\rho_{\ell j}(\hat{\mathbf{x}})$.

Subsequently, the evaluation of the integrals with S^* takes place considering the hypersingular nature of this kernel ($O(r^{-3})$). The expansion of the displacement field into the second term of the Taylor Series as $u_k = u_k - u_k(\hat{\mathbf{x}}) + u_k(\hat{\mathbf{x}}) - u_{k,m}(\hat{\mathbf{x}})(x_m - \hat{x}_m) + u_{k,m}(\hat{\mathbf{x}})(x_m - \hat{x}_m)$ allows the regularisation of the term $\lim_{\epsilon\to 0}\left(\int_{\Gamma_\epsilon^+} S^*_{k\ell j} u_k \, d\Gamma\right)$. This substitution leads to:

$$\begin{aligned}\lim_{\epsilon\to 0}\left(\int_{\Gamma_\epsilon^+} S^*_{k\ell j} u_k \, d\Gamma\right) = \lim_{\epsilon\to 0}\left[\int_{\Gamma_\epsilon^+} S^*_{k\ell j}\left(u_k - u_k(\hat{\mathbf{x}}) - u_{k,m}(\hat{\mathbf{x}})(x_m - \hat{x}_m)\right) d\Gamma\right] \\ + u_k(\hat{\mathbf{x}}) \lim_{\epsilon\to 0}\left[\int_{\Gamma_\epsilon^+} S^*_{k\ell j} \, d\Gamma\right] + u_{k,m}(\hat{\mathbf{x}}) \lim_{\epsilon\to 0}\left[\int_{\Gamma_\epsilon^+} S^*_{k\ell j}(x_m - \hat{x}_m) \, d\Gamma\right]\end{aligned} \tag{2.22}$$

in which both $u_k(\hat{\mathbf{x}})$ and $u_{k,m}(\hat{\mathbf{x}})$ are constants and are placed outside their corresponding integrals. Taking the limit yields the first integral as zero and the third integral results in another term that multiplies the stress tensor $\sigma_{\ell j}$ as $\beta_{\ell j}$. Combining both $\rho_{\ell j}$ and $\beta_{\ell j}$ results in $-0.5\sigma_{\ell j}$ for a source point on a smooth boundary. Lastly, the conjoint analysis of the second integral and the first integral of eq. (2.20) allows for their evaluation in the Hadamard Finite Part (HPF) sense, denoted as:

$$\lim_{\epsilon\to 0}\left\{\int_{\Gamma-\Gamma_\epsilon} S^*_{k\ell j} u_k \, d\Gamma + u_k(\hat{\mathbf{x}}) \int_{\Gamma_\epsilon^+} S^*_{k\ell j} \, d\Gamma\right\} = \text{⨍}_\Gamma S^*_{k\ell j} u_k \, d\Gamma \tag{2.23}$$

in which ⨍ denotes the integration in the HPF sense. The limiting process for the stress boundary integral equation enables the definition of the jump term for source points also on the boundary as:

$$0.5\,\sigma_{\ell j}(\hat{\mathbf{x}}) + \text{⨍}_\Gamma S^*_{k\ell j} u_k \, d\Gamma = \text{⨍}_\Gamma D^*_{k\ell j} t_k \, d\Gamma \tag{2.24}$$

By applying the Cauchy formula to eq. (2.24) and using c to express the source point position, the Traction Boundary Integral Equation emerges as:

$$c(\hat{\mathbf{x}})\, t_j(\hat{\mathbf{x}}) + n_\ell(\hat{\mathbf{x}}) \text{⨍}_\Gamma S^*_{k\ell j} u_k \, d\Gamma = n_\ell(\hat{\mathbf{x}}) \text{⨍}_\Gamma D^*_{k\ell j} t_k \, d\Gamma \tag{2.25}$$

in which $c(\hat{\mathbf{x}})$ is 0, 0.5 and 1.0 for external, on the boundary, and internal source points.

In summary, the limiting process applied to both the Somigliana Identity and the stress BIEs results in two linearly independent BIEs that are valid for source points on the boundary. The imposition by collocation of these two equations for the opposite sides of a crack in cracked solids is the main idea of the Dual BEM.

2.3 Dual Boundary Integral Equations

In cracked solids, the crack surfaces coincide geometrically, which prohibits the collocation of the DBIE on both sides, as it results in an ill-posed system. This issue occurs because the fundamental kernels depend on the distance between the source point and the boundary, and placing two source points in the same position but in different crack surfaces will lead to the problem not identifying the presence of the crack in the analysis. To overcome this limitation,

Hong and Chen (1988) proposed the Dual BEM, in which a crack surface and and its opposite receive the DBIE and the TBIE, respectively. This strategy permits the accurate determination of the mechanical quantities at these surfaces and at the entire solid.

In this context, let the boundaries Γ_c^+ and Γ_c^- represent the opposite crack faces. The DBIE is responsible for representing the contribution of the source points $\hat{\mathbf{x}}^{c+}$ over Γ_c^+ as:

$$\frac{\delta_{\ell k}(\hat{\mathbf{x}}^{c+})}{2} u_k(\hat{\mathbf{x}}^+) + \frac{\delta_{\ell k}(\hat{\mathbf{x}}^{c-})}{2} u_k(\hat{\mathbf{x}}^-) + \cancel{\int_\Gamma} T^*_{\ell k} u_k \, d\Gamma = \int_\Gamma U^*_{\ell k} t_k \, d\Gamma \tag{2.26}$$

in which $\hat{\mathbf{x}}^{c-}$ is the source point over Γ_c^-. It is worth noting the presence of the jump term from $\hat{\mathbf{x}}^{c-}$, which arises from the limiting process that considers both crack surfaces in this analysis. The application of the TBIE over the source point on Γ_c^- also brings up a jump term from $\hat{\mathbf{x}}^{c+}$ as:

$$\frac{1}{2} t_j(\hat{\mathbf{x}}^{c-}) - \frac{1}{2} t_j(\hat{\mathbf{x}}^{c+}) + n_\ell(\hat{\mathbf{x}}^{c-}) \cancel{\int_\Gamma} S^*_{k\ell j} u_k \, d\Gamma = n_\ell(\hat{\mathbf{x}}^-) \cancel{\int_\Gamma} D^*_{k\ell j} t_k \, d\Gamma \tag{2.27}$$

Thus, the mechanical problem is entirely represented by applying eq. (2.19) on the external boundary, while eq. (2.26) and eq. (2.27) model the upper and lower crack surfaces. Then, the next task is to apply a discretisation strategy to promote the approximation of displacements and traction fields.

2.4 BEM algebraic system and IGABEM

Discretisation techniques allow the mechanical analysis of various solids with complex geometries. This strategy consists of interpolating the mechanical fields using a parametric representation, in which the quality of the numerical response is intrinsic to the ability of these approximations. In standard isoparametric approaches of the BEM, the same polynomial functions are responsible for interpolating both geometry and mechanical fields. In this sense, the choice of a better set of functions improves the overall accuracy, which reduces the refinement requirement and the amount of system unknowns. A suitable set of approximation functions is the NURBS function space due to its capacity to exactly represent curves and surfaces such as circles, spheres, and cylinders. Since CAD models normally apply NURBS functions for the geometry discretisation, their use for the mechanical fields leads to the isogeometric approach of the BEM (IGABEM). In this context, the parametrisation for the geometry, displacements, and tractions becomes:

$$\begin{aligned} x_k^\gamma(\xi_1, \xi_2) &= \phi_\alpha^\gamma(\xi_1, \xi_2) P_k^\beta \\ u_k^\gamma(\xi_1, \xi_2) &= \phi_\alpha^\gamma(\xi_1, \xi_2) d_k^\beta \\ t_k^\gamma(\xi_1, \xi_2) &= \phi_\alpha^\gamma(\xi_1, \xi_2) p_k^\beta \end{aligned} \tag{2.28}$$

in which ϕ_α^γ is the NURBS function shown in eq. (A.9) d_k^β and p_k^β are displacement and traction coefficients for the interpolation of these mechanical fields, and β is a global connectivity index associated with its local counterpart α of the NURBS patch γ. These parameters are directly related to their corresponding control points, so that they do not have a physical meaning but have appropriate units. Despite their lack of physical meaning, boundary values of displacement and traction components can be obtained from the direct application of eq. (2.28). However, this

characteristic raises concerns in the application of non-constant boundary conditions, for which a Least-Squares approximation is an alternative to this task (Peng, 2016).

The imposition of the NURBS discretisation on the BIEs leads to the discretised form of the BIEs. Besides, it is relevant to mention that the nomenclature of "source point" and "collocation point" is interchangeable in a collocation-based approach and only the latter will be applied in the remainder of this work. Then, by substituting eq. (2.28) for collocation points on the external boundary (eq. (2.19)) and on opposite crack faces (eq. (2.26)) and eq. (2.27)), the discretised BIEs are obtained as:

$$
\begin{aligned}
&\frac{\delta_{\ell k}}{2}\phi_{\alpha}^{\hat{\gamma}}(\hat{\mathbf{x}}^{eb})d_k^{\beta} + \sum_{\gamma=1}^{NS}\left[\fint_{\Gamma_\gamma} T_{\ell k}^{*}\phi_{\alpha}^{\gamma}\, d\Gamma\right] d_k^{\beta} = \sum_{\gamma=1}^{NS}\left[\int_{\Gamma_\gamma} U_{\ell k}^{*}\phi_{\alpha}^{\gamma}\, d\Gamma\right] p_k^{\beta} \\
&\frac{\delta_{\ell k}}{2}\phi_{\alpha}^{\hat{\gamma}}(\hat{\mathbf{x}}^{c+})d_k^{\beta} + \frac{\delta_{\ell k}}{2}\phi_{\alpha}^{\hat{\gamma}}(\hat{\mathbf{x}}^{c-})d_k^{\beta} + \\
&\sum_{\gamma=1}^{NS}\left[\int_{\Gamma_\gamma} T_{\ell k}^{*}\phi_{\alpha}^{\gamma}\, d\Gamma\right] d_k^{\beta} = \sum_{\gamma=1}^{NS}\left[\int_{\Gamma_\gamma} U_{\ell k}^{*}\phi_{\alpha}^{\gamma}\, d\Gamma\right] p_k^{\beta} \\
&\frac{1}{2}\,\phi_{\alpha}^{\hat{\gamma}}(\hat{\mathbf{x}}^{c-})p_k^{\beta} - \frac{1}{2}\phi_{\alpha}^{\hat{\gamma}}(\hat{\mathbf{x}}^{c+})\,p_k^{\beta} + \\
&n_\ell(\hat{\mathbf{x}}^{c-})\sum_{\gamma=1}^{NS}\left[\fint_{\Gamma} S_{k\ell j}^{*}\phi_{\alpha}^{\gamma}(\mathbf{x})\, d\Gamma\right] d_k^{\beta} = n_\ell(\hat{\mathbf{x}}^{c-})\sum_{\gamma=1}^{NS}\left[\fint_{\Gamma} D_{k\ell j}^{*}\phi_{\alpha}^{\gamma}\, d\Gamma\right] p_k^{\beta}
\end{aligned}
\tag{2.29}
$$

in which $\hat{\mathbf{x}}^{eb}$, $\hat{\mathbf{x}}^{c+}$ and $\hat{\mathbf{x}}^{c-}$ represent the collocation points on the external boundary, upper crack face and lower crack face, respectively. The coefficients d_k^{β} and p_k^{β} are constants and placed outside of the integrals. Additionally, the $\fint$ and $\fint\!\!\!\!\!\!=$ symbols represent the integration in the CPV and in the HPF sense, respectively, as mentioned in section 2.2.

The BIEs require numerical integration over the NURBS surfaces. The Gauss-Legendre quadrature is responsible for the non-singular numerical integration, in which a mapping occurs between the physical space and the integration space Λ such that $\{\hat{\xi}_1, \hat{\xi}_2 \in \Lambda \,|\, \Lambda = [-1,1]\times[-1,1]\}$. The NURBS parametric space requires two transformations, being the first between the physical space and the parametric space, as in eq. (2.28) and the NURBS functions are given in Appendix A. The second transformation maps a given NURBS parametric space whose knot span is $[\xi_1^i, \xi_1^{i+1}] \times [\xi_2^j, \xi_2^{j+1}]$ to the integration space as:

$$
\begin{aligned}
\xi_1 &= \frac{(\xi_1^{i+1} - \xi_1^{i})\,\hat{\xi}_1 + (\xi_1^{i+1} + \xi_1^{i})}{2} \\
\xi_2 &= \frac{(\xi_2^{j+1} - \xi_2^{j})\,\hat{\xi}_2 + (\xi_2^{j+1} + \xi_2^{j})}{2}
\end{aligned}
\tag{2.30}
$$

The correspondence between the physical space and the integration space for the boundary

mapping involves two Jacobians, J_1 and J_2, as:

$$\begin{aligned} d\Gamma &= J_1 J_2 d\Lambda = J d\Lambda \\ J_1 &= \left\| \frac{\partial \mathbf{r}}{\partial \xi_1} \times \frac{\partial \mathbf{r}}{\partial \xi_2} \right\| \\ J_2 &= \frac{(\xi_1^{i+1} - \xi_1^i)}{2} \frac{(\xi_2^{j+1} - \xi_2^j)}{2} \end{aligned} \tag{2.31}$$

in which J accounts for the total Jacobian of the transformation. The non-singular numerical integration occurs at all knot spans that do not contain the collocation point, while the integration of knot spans containing collocation points requires a different approach due to the strongly-singular or hyper-singular nature of the kernels. This study applies the Singularity Subtraction Technique (SST) (Guiggiani; Gigante, 1990; Guiggiani *et al.*, 1992) for its evaluation. This technique is based on a polar transformation around the singularity, followed by the expansion in Laurent series of the singular integrand and a semi-analytical approach in the circumferential direction. In addition, the integration in the HPF sense demands a C^1 continuity for the integrand in the vicinity of the collocation point. This study utilises the expanded terms for the application of the SST for three-dimensional IGABEM according to Cordeiro and Leonel (2018). In this sense, the boundary discretisation of the BIEs with NURBS surfaces shown in eq. (2.28) after the corresponding numerical integration results in:

$$\begin{aligned} \frac{\delta_{\ell k}}{2} \sum_{\alpha=1}^{n^\gamma} \phi_\alpha^{\hat{\gamma}}(\hat{\mathbf{x}}^{eb}) d_k^\beta + \sum_{\gamma=1}^{NS} \underline{\mathrm{T}}_{\ell k}^{*\,\alpha\gamma} d_k^\beta &= \sum_{\gamma=1}^{NS} \underline{\mathrm{U}}_{\ell k}^{*\,\alpha\gamma} p_k^\beta \\ \frac{\delta_{\ell k}}{2} \sum_{\alpha=1}^{n^\gamma} \phi_\alpha^{\hat{\gamma}+}(\hat{\mathbf{x}}^{c+}) d_k^\beta + \frac{\delta_{\ell k}}{2} \sum_{\alpha=1}^{n^\gamma} \phi_\alpha^{\hat{\gamma}-}(\hat{\mathbf{x}}^{c-}) d_k^\beta + \sum_{\gamma=1}^{NS} \underline{\mathrm{T}}_{\ell k}^{*\,\alpha\gamma} d_k^\beta &= \sum_{\gamma=1}^{NS} \underline{\mathrm{U}}_{\ell k}^{*\,\alpha\gamma} p_k^\beta \\ \frac{1}{2} \sum_{\alpha=1}^{n^\gamma} \phi_\alpha^{\hat{\gamma}-}(\hat{\mathbf{x}}^{c-}) p_j^\beta - \frac{1}{2} \sum_{\alpha=1}^{n^\gamma} \phi_\alpha^{\hat{\gamma}+}(\hat{\mathbf{x}}^{c+}) p_j^\beta & \\ + n_\ell(\hat{\mathbf{x}}^{c-}) \sum_{\gamma=1}^{NS} \underline{\mathrm{S}}_{k\ell j}^{*\,\alpha\gamma} d_k^\beta = n_\ell(\hat{\mathbf{x}}) \sum_{\gamma=1}^{NS} \underline{\mathrm{D}}_{k\ell j}^{*\,\alpha\gamma} p_k^\beta & \end{aligned} \tag{2.32}$$

in which $\hat{\mathbf{x}}$ represents position of the collocation point on the NURBS surface, n^γ represents the number of parameters in a surface γ, while NS stands for the total of NURBS surfaces in the discretisation. Additionally, the terms $\underline{\mathrm{T}}_{\ell k}^{*\,\alpha\gamma}$, $\underline{\mathrm{U}}_{\ell k}^{*\,\alpha\gamma}$, $\underline{\mathrm{S}}_{k\ell j}^{*\,\alpha\gamma}$, and $\underline{\mathrm{D}}_{k\ell j}^{*\,\alpha\gamma}$ represent the integration of the fundamental kernels along the knot spans as:

$$
\begin{aligned}
\underline{\mathrm{T}}^{*\,\alpha\gamma}_{\ell k} &= \sum_{\mathrm{ks}=1}^{n^{\gamma}_{\mathrm{ks}}} \int_{\Lambda} T^{*}_{\ell k} \phi^{\gamma}_{\alpha}\, J^{\mathrm{ks}}_{\gamma}\, d\Lambda \\
\underline{\mathrm{U}}^{*\,\alpha\gamma}_{\ell k} &= \sum_{\mathrm{ks}=1}^{n^{\gamma}_{\mathrm{ks}}} \int_{\Lambda} U^{*}_{\ell k} \phi^{\gamma}_{\alpha}\, J^{\mathrm{ks}}_{\gamma}\, d\Lambda \\
\underline{\mathrm{S}}^{*\,\alpha\gamma}_{k\ell j} &= \sum_{\mathrm{ks}=1}^{n^{\gamma}_{\mathrm{ks}}} \int_{\Lambda} S^{*}_{k\ell j} \phi^{\gamma}_{\alpha}\, J^{\mathrm{ks}}_{\gamma}\, d\Lambda \\
\underline{\mathrm{D}}^{*\,\alpha\gamma}_{k\ell j} &= \sum_{\mathrm{ks}=1}^{n^{\gamma}_{\mathrm{ks}}} \int_{\Lambda} D^{*}_{k\ell j} \phi^{\gamma}_{\alpha}\, J^{\mathrm{ks}}_{\gamma}\, d\Lambda
\end{aligned}
\tag{2.33}
$$

in which ks denotes the knot span, J^{ks}_{γ} refers to the corresponding Jacobian of the surface γ, and n^{γ}_{ks} indicates the number of knot spans in the patch γ.

The amount of displacement and traction coefficients in eq. (2.33) is $3N_d$ and $3N_p$, respectively, in which $N_d = N_p = N_{\mathrm{coeff}}$ when both fields share the same discretisation. Since the boundary conditions enable the determination of half of these coefficients, the other half remains unknown due to $\Gamma_u \cap \Gamma_p = \varnothing$. This implies that the elastostatic boundary value problem in its discretised form has $3\,N_{\mathrm{coeff}}$ unknowns distributed between $\mathbf{d}$ and $\mathbf{p}$. To obtain these coefficients, the required number of equations for constructing a well-posed algebraic system comes from the application of eq. (2.32) for N_{coeff} different collocation points, resulting in 3 different equations at each point. A suitable strategy for defining the placement of each $\hat{\mathbf{x}}$ on the boundary is the Greville Abscissae (Greville, 1964). In this sense, a given collocation point associated with a basis function α in a NURBS surface γ has its parametric coordinates $(\xi^{i}_{1}, \xi^{j}_{2})^{\alpha\gamma}$ as:

$$
\begin{aligned}
(\xi^{i}_{1})^{\alpha\gamma} &= \frac{\sum_{s=i+1}^{i+p} \xi^{s}_{1}}{p} \\
(\xi^{j}_{2})^{\alpha\gamma} &= \frac{\sum_{s=j+1}^{j+q} \xi^{s}_{2}}{q}
\end{aligned}
\tag{2.34}
$$

in which i and j refer to the indices of the uni-variate NURBS curve responsible for generating the surface and ξ^{s}_{1} and ξ^{s}_{2} are the knots from the knot vectors. In addition, the repositioning strategy replaces the collocation point when it lies on a surface edge or when either ξ^{s}_{1} or ξ^{s}_{2} are equal to a knot whose multiplicity causes C^0 continuity. This step ensures that all collocation points are on a smooth boundary, and guarantees the C^1 continuity required for all points lying on the crack surfaces. The replacement for a knot span $[\xi^{i}_{1}, \xi^{i+1}_{1}] \times [\xi^{j}_{2}, \xi^{j+1}_{2}]$ is performed by adjusting ξ^{s}_{1} or ξ^{s}_{2} as:

$$
\begin{aligned}
(\xi^{i\,\mathrm{alt}}_{1})^{\alpha\gamma} &= (\xi^{i}_{1})^{\alpha\gamma} \pm 0.1(\xi^{i+1}_{1} - \xi^{i}_{1}) \\
(\xi^{j\,\mathrm{alt}}_{2})^{\alpha\gamma} &= (\xi^{j}_{2})^{\alpha\gamma} \pm 0.1(\xi^{j+1}_{2} - \xi^{j}_{2})
\end{aligned}
\tag{2.35}
$$

in which the $\pm$ sign refers to forward or backward movement, which depends on the original position of the collocation point.

The application of eq. (2.32) to all collocation points, whose position comes from the

Greville Abscissae strategy, results in the IGABEM algebraic system:

$$\begin{bmatrix} \mathbf{H}^{\mathrm{eb}} \\ \mathbf{H}^{\mathrm{c}^+} \\ \mathbf{H}^{\mathrm{c}^-} \end{bmatrix} \begin{bmatrix} \mathbf{d}^{\mathrm{eb}} \\ \mathbf{d}^{\mathrm{c}^+} \\ \mathbf{d}^{\mathrm{c}^-} \end{bmatrix} = \begin{bmatrix} \mathbf{G}^{\mathrm{eb}} \\ \mathbf{G}^{\mathrm{c}^+} \\ \mathbf{G}^{\mathrm{c}^-} \end{bmatrix} \begin{bmatrix} \mathbf{p}^{\mathrm{eb}} \\ \mathbf{p}^{\mathrm{c}^+} \\ \mathbf{p}^{\mathrm{c}^-} \end{bmatrix} \tag{2.36}$$
$$\mathbf{Hd} = \mathbf{Gt}$$

in which $\mathbf{H}^{\mathrm{eb}}$, $\mathbf{H}^{\mathrm{c+}}$, $\mathbf{H}^{\mathrm{c\text{-}}}$, $\mathbf{G}^{\mathrm{eb}}$, $\mathbf{G}^{\mathrm{c+}}$, and $\mathbf{G}^{\mathrm{c\text{-}}}$ represent the influence factors of displacement and traction for a collocation point on the external boundary (eb), upper crack face (c+) or lower crack face (c-).

The boundary conditions application consists of assigning appropriate values to the displacement and traction coefficients in eq. (2.36) followed by a rearranging task of the algebraic system. Constant boundary conditions only require specifying their value for all coefficients of the corresponding NURBS surface. However, all other distributions require an intermediate operation, such as direct integration of the entire kernel using the analytical expression of the boundary condition, or a Least-Squares strategy to determine the best coefficients representing the known field. In this thesis, all applications either use constant boundary conditions or apply them using their analytical expressions in specific applications, as mentioned when applicable. The algebraic system of eq. (2.36) transforms into $\mathbf{Ax} = \mathbf{b}$ after incorporating the boundary conditions, in which $\mathbf{A}$ stores all influence factors, and is a dense and unsymmetrical matrix. The vector $\mathbf{x}$ comprises both unknown displacements and tractions coefficients, and $\mathbf{b}$ is the right-hand side vector containing the result of the boundary condition application.

2.5 Internal mechanical fields

After solving the algebraic system, the displacement and traction coefficients provide a complete mechanical description of the mechanical fields over the boundary of the solid. Subsequently, the BIEs for internal points (eq. (2.19) and eq. (2.24)) allow for the determination of displacements and stresses throughout the entire solid's domain. Their discretised form arises from a procedure analogous to that used in the IGABEM algebraic system determination. The main difference is the absence of strongly singular or hyper singular integration, which eliminates the need for their treatment due to the position of the internal source point. Thus, the compact form of the discretised Displacement BIE is:

$$u_k(\hat{\mathbf{x}}_i^{\mathrm{int}}) = \sum_{\gamma=1}^{NS} \underline{\mathrm{U}}_{\ell k}^{*\,\alpha\gamma} p_k^{\beta} - \sum_{\gamma=1}^{NS} \underline{\mathrm{T}}_{\ell k}^{*\,\alpha\gamma} d_k^{\beta} \tag{2.37}$$
$$\mathbf{u}^{\mathrm{int}} = \mathbf{G}^{\mathrm{int}}\mathbf{p} - \mathbf{H}^{\mathrm{int}}\mathbf{d}$$

in which $\underline{\mathrm{U}}_{\ell k}^{*\,\alpha\gamma}$ and $\underline{\mathrm{T}}_{\ell k}^{*\,\alpha\gamma}$ are defined in eq. (2.33) requiring no singularity treatment. In the matrix form, $\mathbf{H}^{\mathrm{int}}$ and $\mathbf{G}^{\mathrm{int}}$ are influence matrices of the displacement and traction coefficients, respectively.

By using the discretised form of the mechanical fields in eq. (2.24), the BIE for stresses

at an internal point becomes:

$$\begin{aligned} \sigma_{\ell j}\left(\hat{\mathbf{x}}_i^{\text{int}}\right) &= \sum_{\gamma=1}^{NS} \underline{\mathrm{D}}_{k\ell j}^{*\,\alpha\gamma} p_k^{\beta} - \sum_{\gamma=1}^{NS} \underline{\mathrm{S}}_{k\ell j}^{*\,\alpha\gamma} d_k^{\beta} \\ \sigma^{\text{int}} &= \mathbb{D}^{\text{int}}\mathbf{t} - \mathbb{S}^{\text{int}}\mathbf{u} \end{aligned} \tag{2.38}$$

in which the terms $\underline{\mathrm{D}}_{k\ell j}^{*\,\alpha\gamma}$ and $\underline{\mathrm{S}}_{k\ell j}^{*\,\alpha\gamma}$ correspond to the integration of eq. (2.33), and the tensors $\mathbb{D}^{\text{int}}$ and $\mathbb{S}^{\text{int}}$ store the computed values.

3 TRIMMED SURFACES ON IGABEM

This chapter presents the required adaptations of the three-dimensional IGABEM to account for geometries containing trimmed surfaces. Trimmed surfaces are standard NURBS surface under a Boolean subtraction operation to remove certain parts, leaving the desired shape. This operation is necessary in the context of NURBS parametrisation because NURBS surfaces often represent large portions of the boundary using a single tensor-product structure. Consequently, the trimming operation becomes a suitable approach to represent holes or geometric details without requiring multiple NURBS surfaces. Since these surfaces are common in CAD solid modelling, their use with the IGABEM enables numerical analysis of more complex components without the need for a mesh restructuring. In this context, incorporating trimmed surfaces to the IGABEM requires three steps. The first task is identifying the knot spans crossed by the trimming curves, and the corresponding effect on basis functions and control points of the original NURBS surface. Next, the numerical integration of trimmed knot spans requires a specific procedure since their arbitrary shape prevents the direct use of Gauss-Legendre quadrature. Lastly, trimming may remove portions that contain the original collocation points obtained through the Greville Abscissae strategy. To address this issue, an additional collocation strategy replaces the previous points with new points on trimmed knot spans. Two numerical applications demonstrate the ability of the IGABEM to solve three-dimensional problems with trimmed surfaces, as well as its challenges and limitations in its incorporation.

3.1 Identification of trimmed knot spans and basis functions

The identification task for incorporating trimmed surfaces into the IGABEM focuses on classifying knot spans and control points in complete, trimmed, or void, according to section A.4. In addition, the intersection of the trimming curve and the knot span of the NURBS surface in either parametric direction is crucial for defining the the shape of the trimmed knot span. To store this information, a specific procedure identifies both the parametric coordinate of the trimming curve and the corresponding NURBS surface pair in the knot span where the intersection occurs.

The first task in the identification scheme is to find the parametric coordinate of the trimming curve where the curve intersects a knot span edge. This search relies on a two-step algorithm, firstly performing an incremental scan along the trimming curve using its parametric coordinate $t_i = t_0 + i\delta$, with $\delta = (t_F - t_0)/n$ and n is the number of subdivisions. The pair of parametric coordinates at the NURBS surface $(\xi_1(t_i), \xi_2(t_i))$ corresponds to a position within each uni-variate knot vector. When the pair related to t_{i+1} is at a different knot span than the pair associated with t_i, it indicates that a crossing exists at a t_s such that $t_i \leq t_s \leq t_{i+1}$. An auxiliary variable $\varrho = 1, 2$ indicates the parametric direction in which the crossing occurs so that the value at ξ_ϱ is known. The second step is a local Newton-Raphson approach to determine $t = t_s$ such that the residual $E(t) = \xi_\varrho^S - \xi_\varrho(t)$ is zero. Figure 3 illustrates this algorithm, in which the crossing at both parametric directions depicts the possibilities for ϱ. By expanding the

residual $E(t)$ into a Taylor series around t and taking the first term, the increment Δt_k of the local Newton-Raphson iterative procedure is:

$$\Delta t_k = \frac{E(t_k)}{\left.\frac{\partial E}{\partial t}\right|_k} \tag{3.1}$$

in which the update of $t_{k+1} = t_k + \Delta t_k$ occurs until the residual is less than a prescribed tolerance. In addition, $\partial E/\partial t$ is the tangent vector component in the ϱ direction. Additionally, each knot span in which the local Newton-Raphson search for t_s occurs is classified as a trimmed knot span.

Figure 3 – Two-step algorithm to find the parametric coordinate of the trimming curve at the intersection with a knot span: ϱ definition.

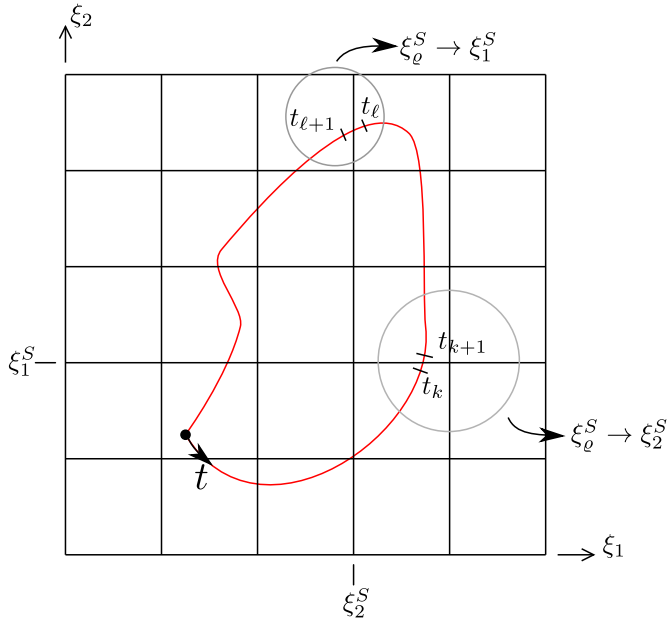

Source: The author.

Next, the ray casting algorithm is responsible for classifying points (ξ_1^{cl}, ξ_2^{cl}) as internal or external to the set of trimming curves. This strategy requires defining a crossing function f_{cross} which counts the number of crossings between a line segment and the trimming curve. The line segment originates at the point under classification (ξ_1^{cl}, ξ_2^{cl}) and extends across the trimming curve. An even number of crossings indicates that the point is external to the set, whereas it is internal if f_{cross} is odd. The function f_{cross} relates the parametric coordinate at the NURBS surface ξ_2 with the coordinate $\xi_2^L(\xi_1(t))$, in which the line segment equation defines ξ_2^L while $\xi_1(t)$ follows the interpolation of the trimming curve in terms of its parametric coordinate t. The expression for f_{cross} is:

$$f_{\text{cross}} = \xi_2(t) - \xi_2^L(\xi_1(t)) \Rightarrow f_{\text{cross}} = \xi_2(t) - \{m_L[\xi_1(t) - \xi_1^{cl}] + \xi_2^{cl}\} \tag{3.2}$$

in which $m_L = (\xi_2^P - \xi_2^{cl})/(\xi_1^P - \xi_1^{cl})$. Figure 4 illustrates the geometric components of the ray casting algorithm. The crossing function is zero when the line segment intersects the trimming curve. This allows scanning the trimming curve along the parametric coordinate t

using $\delta = (t_F - t_0)/n$ and $t_i = t_0 + i\delta$. Each sign change in f_{cross} indicates a crossing, implying that $f_{\text{cross}} = 0$ for t between t_i and t_{i+1}.

Figure 4 – Ray casting algorithm for the detection of internal and external points to the trimming sets.

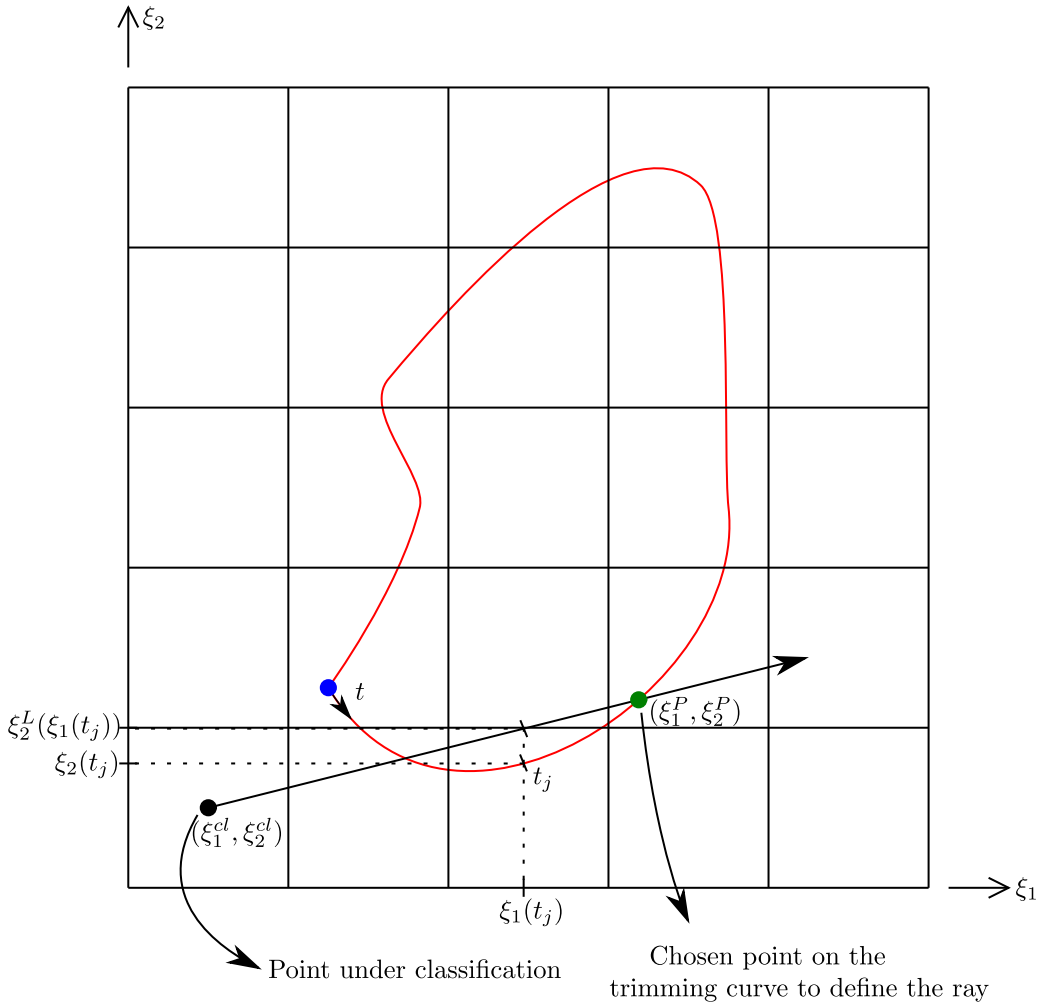

Source: The author.

The ray casting algorithm determines the position of the knot span and each of its vertices relative to the trimming set. The knot span definition as complete or void considers the relative position of its central point to a trimming set when it is not crossed by any curve. Complete knot spans are those external to inner trimming curves or internal to outer trimming curves. Conversely, void knot spans are internal to inner trimming curves or external to outer trimming curves. In addition, categorising vertices of a trimmed knot span is necessary to define its cell subdivision for plotting and numerical integration. It is worth mentioning that a single scanning along the trimming set is sufficient to classify all knot spans and vertices, which results in efficient analysis.

The classification of the vertices allows defining the shape of each trimmed knot span. Three possible scenarios exist for these vertices, as illustrated in fig. 5. Types 1, 2, and 3 have, respectively, 1, 2, and 3 original vertices in their final shapes, with three, four, or five sides.

Other vertices result from the intersections between the trimming curve and the knot span, with their parametric coordinates determined during the identification process. The ordering of the knot span vertices follows fig. 6 proceeding counter-clockwise from the bottom left corner in the parametric space. The positions of trimming curve endpoints influence the trimmed knot spans when they are not located on an trimmed knot span edge. Reshaping trimmed knot spans that include trimming curve endpoints accounts for an additional edge and vertex, as shown in fig. 7. Other specific cases, such as two different trimming curves or two endpoints on the same knot span, are not considered in this study. Expanding the types of trimmed knot spans is suggested for future work.

Figure 5 – Trimmed knot span types.

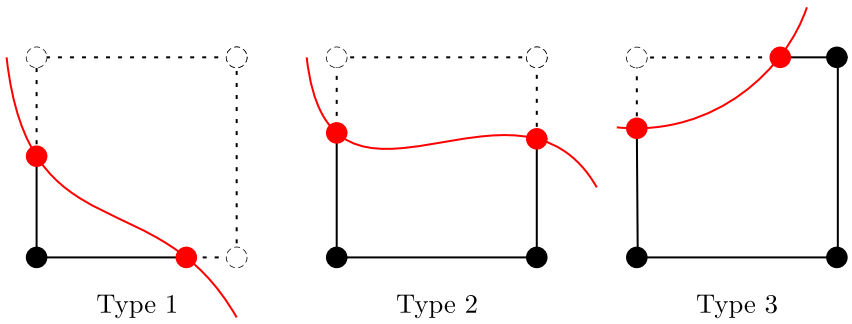

Source: The author.

Figure 6 – Trimmed knot span ordering of vertices and edges.

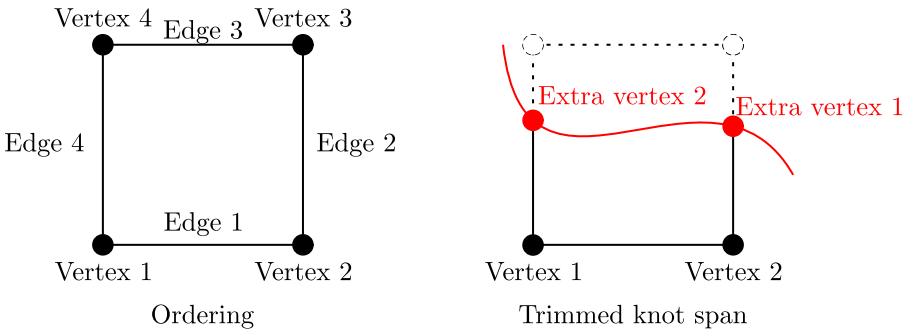

Source: The author.

The final identification task involves categorising control points and their associated basis functions as complete, trimmed, or void. Their classification relies on the type of knot spans within the support of the basis functions. Complete basis functions and control points have only complete knot spans in their support, while the void counterparts contain only void knot spans in it. Basis functions whose support includes a trimmed knot span are trimmed ones. After this step, void control points are dispensable from the interpolation, since their domain does not represent any portion of the solid.

Figure 7 – Influence of endpoints internal to trimmed knot span.

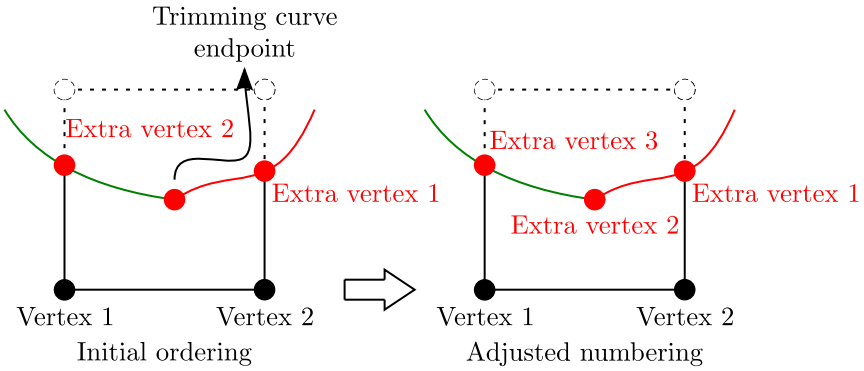

Source: The author.

3.2 Numerical integration of trimmed knot spans

The trimming operation on NURBS surfaces requires a specific approach for the numerical integration of the trimmed knot spans since the direct Gauss-Legendre quadrature does not account for curved sides in the standard transformation. This study adopts two different integration strategies: the Kim, Seo and Youn (2009) approach and a new polar strategy in the trimming context. Both strategies place the integration points at the same positions. However, the polar strategy is computationally simpler than Kim, Seo and Youn (2009) approach, particularly in evaluating singular integrals in IGABEM.

3.2.1 Kim, Seo and Youn (2009) strategy

The Kim, Seo and Youn (2009) integration strategy for trimmed knot spans adopts two supplementary mappings between the integration space and the NURBS parametric space, as illustrated in fig. 8. These two mappings incorporate the trimming curve geometry, ensuring an accurate representation of the trimmed knot span. This strategy requires subdividing the knot span into two types of triangular cells. Type A cells are triangles with one side formed by the trimming curve, whereas Type B cells are standard triangles.

Figure 8 – Mappings required for Kim, Seo and Youn (2009) strategy.

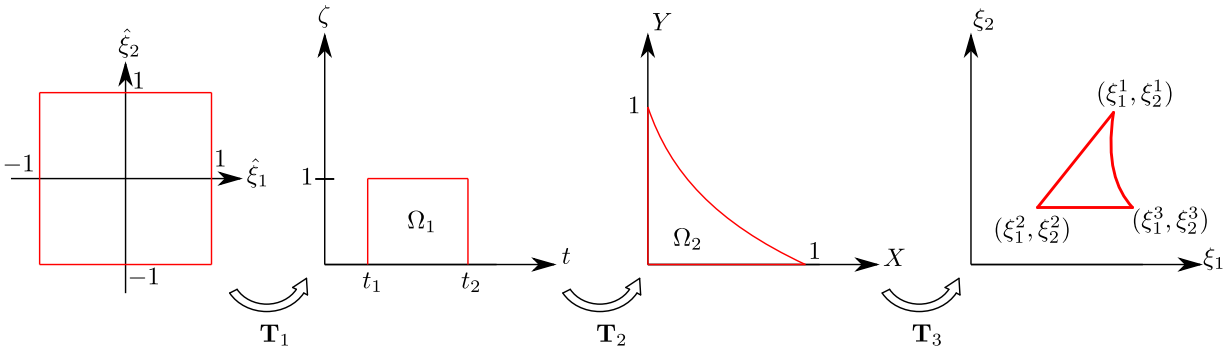

Source: The author.

The first mapping T_1 transforms a pair of coordinates in the integration space $(\hat{\xi_1}, \hat{\xi_2})$ to the first auxiliary rectangular space Ω_1 with $(t, \zeta) \in \Omega_1 = \{[t_1; t_2] \times [0; 1]\}$, in which t is the trimming curve parametric coordinate, and t_1 and t_2 denote its limits in the mapped cell. The expressions for this mapping are:

$$\begin{aligned} &\mathbf{T}_1 : \{\hat{\xi_1}, \hat{\xi_2}\} \to \{t, \zeta\} \\ &t = \frac{\hat{\xi_1}}{2}(t_2 - t_1) + \frac{1}{2}(t_2 + t_1) \\ &\zeta = \frac{\hat{\xi_2}}{2} + \frac{1}{2} \end{aligned} \tag{3.3}$$

The second mapping $\mathbf{T}_2$ transforms a pair from Ω_1 into the second auxiliary space Ω_2 in which both upper limits from Ω_1 collapse into a single point in Ω_2, converting a rectangle into a triangle. In addition, this mapping incorporates the trimming curve $\mathbf{C}(t)$ through $\boldsymbol{\psi} = \mathbf{T}_3^{-1}\mathbf{C}(t)$, in which $\mathbf{T}_3$ represents a third mapping that follows in sequence. Thus, $\mathbf{T}_2$ is:

$$\begin{aligned} &\mathbf{T}_2 : \{t, \zeta\} \to \{X, Y\} \\ &X = \psi_X(t)(1 - \zeta) \\ &Y = \psi_Y(t)(1 - \zeta) + \zeta \end{aligned} \tag{3.4}$$

in which ψ_X and ψ_Y are components of $\boldsymbol{\psi}$

$\mathbf{T}_3$ is then responsible for mapping from the auxiliary space Ω_2 to the NURBS parametric space. This transformation is analogous to the linear triangular finite element, in which the vertices in the NURBS space are (ξ_1^1, ξ_2^1), (ξ_1^2, ξ_2^2) and (ξ_1^3, ξ_2^3), being:

$$\begin{aligned} &\mathbf{T}_3 : \{X, Y\} \to \{\xi_1, \xi_2\} \\ &\xi_1 = Y\xi_1^1 + (1 - X - Y)\xi_1^2 + X\xi_1^3 \\ &\xi_2 = Y\xi_2^1 + (1 - X - Y)\xi_2^2 + X\xi_2^3 \end{aligned} \tag{3.5}$$

The integration of type B cells uses all the mappings for type A cells considering $t_1 = 0.0$ and $t_2 = 1.0$ in eq. (3.3), and $\psi_X(t) = t$ and $\psi_Y(t) = 0$ in eq. (3.4). These assumptions cause curved side of the type A cell to become a straight side.

The Jacobians of each transformation perform a role in the numerical integration. Similar to the definition in eq. (2.31), the Jacobian for a cell in the trimmed knot span is:

$$d\Gamma_\gamma = \left\| \frac{\partial \mathbf{r}}{\partial \hat{\xi}_1} \times \frac{\partial \mathbf{r}}{\partial \hat{\xi}_2} \right\| d\Lambda = \bar{J}_1^\gamma \bar{J}_2^\gamma \bar{J}_3^\gamma \left\| \frac{\partial \mathbf{r}}{\partial \xi_1} \times \frac{\partial \mathbf{r}}{\partial \xi_2} \right\| d\Lambda = \bar{J}_1^\gamma \bar{J}_2^\gamma \bar{J}_3^\gamma J_2^\gamma d\Lambda \tag{3.6}$$

in which $\bar{J}_1^\gamma$, $\bar{J}_2^\gamma$, and $\bar{J}_3^\gamma$ correspond to the mappings $\mathbf{T}_1$, $\mathbf{T}_2$ and $\mathbf{T}_3$ as:

$$\begin{aligned}
\bar{J}_1^\gamma &= \begin{vmatrix} \dfrac{\partial t}{\partial \hat{\xi}_1} & \dfrac{\partial \zeta}{\partial \hat{\xi}_1} \\ \dfrac{\partial t}{\partial \hat{\xi}_2} & \dfrac{\partial \zeta}{\partial \hat{\xi}_2} \end{vmatrix} = \begin{vmatrix} \dfrac{t_2 - t_1}{2} & 0 \\ 0 & \dfrac{1}{2} \end{vmatrix} \\
\bar{J}_2^\gamma &= \begin{vmatrix} \dfrac{\partial X}{\partial t} & \dfrac{\partial Y}{\partial t} \\ \dfrac{\partial X}{\partial \zeta} & \dfrac{\partial Y}{\partial \zeta} \end{vmatrix} = \begin{vmatrix} \dfrac{\partial \psi_X(t)}{\partial t}(1-\zeta) & \dfrac{\partial \psi_Y(t)}{\partial t}(1-\zeta) \\ -\psi_X(t) & -\psi_Y(t)+1 \end{vmatrix} \\
\bar{J}_3^\gamma &= \begin{vmatrix} \dfrac{\partial \xi_1}{\partial X} & \dfrac{\partial \xi_2}{\partial X} \\ \dfrac{\partial \xi_1}{\partial Y} & \dfrac{\partial \xi_2}{\partial Y} \end{vmatrix} = \begin{vmatrix} -\xi_1^2 + \xi_1^3 & -\xi_2^2 + \xi_2^3 \\ \xi_1^1 - \xi_1^2 & \xi_2^1 - \xi_2^2 \end{vmatrix}
\end{aligned} \tag{3.7}$$

3.2.2 Polar strategy

This study proposes a specific mapping with a polar strategy to address the presence of the trimming curve in the knot span. This proposition is suitable for the singular integration context in the IGABEM, in which a polar mapping already exists in the SST procedure. In this context, this strategy is responsible for the integration assessment of knot spans containing collocation points, and also non-singular integration. Figure 9 depicts the polar mapping transformations.

Figure 9 – Polar mapping for trimmed knot spans.

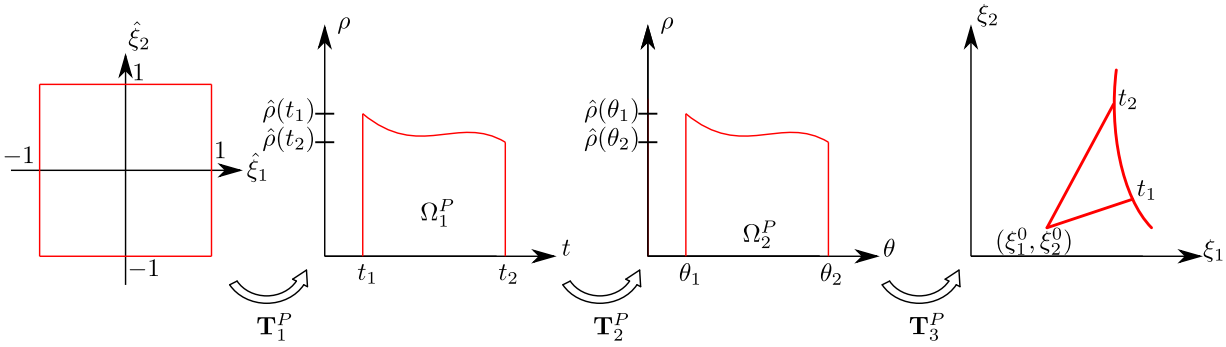

Source: The author.

The first step is defining the pole around which the integration is centred. In the SST context, the pole is the collocation point, whereas for regular integration assessment, it is a vertex opposite to the trimming curve, as illustrated in fig. 10. The strategy requires subdividing the trimmed knot span into triangles, depending on the pole position. When the opposite side is regular, all transformations remain valid by setting $t_1 = 0.0$, $t_2 = 1.0$ and assuming a linear correlation between its vertices.

The first transformation maps the integration space $\{\hat{\xi}_1, \hat{\xi}_2\} \in \Lambda \,|\, \Lambda = \{[-1;1] \times [-1;1]\}$

Figure 10 – Pole choice in the polar integration strategy.

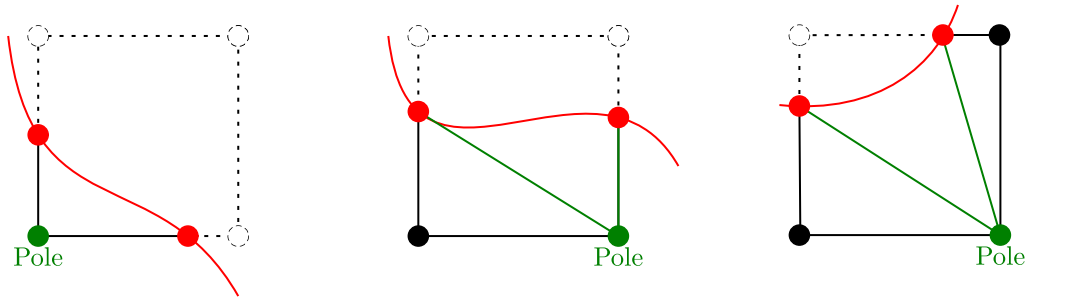

Type 1: pole is remaining vertex

Type 2: pole is vertex before the trimming curve in the ordering

Type 3: pole is opposite vertex to the trimming curve

Source: The author.

onto the first auxiliary space $\Omega_1^P = \{[t_1, t_2] \times [0, \hat{\rho}]\}$ using the $\mathbf{T}_1^P$ operation as:

$$\begin{aligned} &\mathbf{T}_1^P : (\hat{\xi}_1, \hat{\xi}_2) \to (t, \rho) \\ &t = \frac{(t_2 - t_1)\hat{\xi_2}}{2} + \frac{(t_2 + t_1)}{2} \\ &\rho = \frac{\hat{\rho}(t)\hat{\xi_1}}{2} + \frac{\hat{\rho}(t)}{2} \end{aligned} \tag{3.8}$$

in which for a given t on the trimming curve limit $\hat{\rho}(t)$ exists. This term represents the distance between the pole and the point on the trimming curve with parametric coordinate t. The geometric meaning of $\hat{\rho}(t)$ is illustrated in fig. 11, and its value is given by:

$$\hat{\rho}(t) = \sqrt{[\xi_1(t) - \xi_1^0]^2 + [\xi_2(t) - \xi_2^0]^2} \tag{3.9}$$

in which (ξ_1^0, ξ_2^0) denotes the pole.

Figure 11 – Geometric meaning of $\hat{\rho}$.

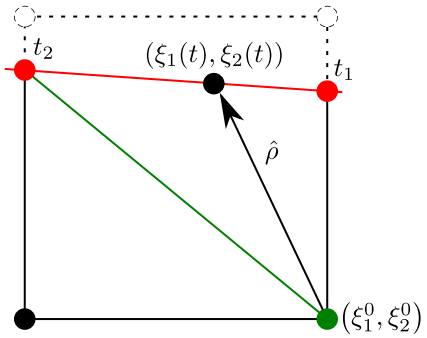

Source: The author.

Next, determining θ and its cosine and sine requires the pair of coordinates $(\xi_1(t), \xi_2(t))$

and the second transformation $\mathbf{T}_2^P$ operates its role as:

$$\begin{aligned} \mathbf{T}_2^P &: (t,\rho) \rightarrow (\theta,\rho) \\ \cos\theta &= \frac{\xi_1(t)-\xi_1^0}{\hat{\rho}(t)} \\ \sin\theta &= \frac{\xi_2(t)-\xi_2^0}{\hat{\rho}(t)} \\ \theta &= \arctan\left(\frac{\xi_2(t)-\xi_2^0}{\xi_1(t)-\xi^0}\right) \end{aligned} \tag{3.10}$$

The final transformation $\mathbf{T}_3^P$ computes the parametric coordinates on the NURBS surface from the radius ρ and the angle θ as:

$$\begin{aligned} \mathbf{T}_3^P &: (\theta,\rho) \rightarrow (\xi_1,\xi_2) \\ \xi_1(\rho,\theta) &= \xi_1^0 + \rho\cos\theta \\ \xi_2(\rho,\theta) &= \xi_2^0 + \rho\sin\theta \end{aligned} \tag{3.11}$$

Notably, the main difference between the proposed strategy and classical approaches is the inclusion of the transformations $\mathbf{T}_1^P$ and $\mathbf{T}_2^P$, which account for the trimming curve. In the context of numerical integration, the Jacobians of each transformation are:

$$\begin{aligned} \bar{J}_1^{P\gamma} &= \frac{\hat{\rho}(t)}{2}\frac{(t_2-t_1)}{2} \\ \bar{J}_2^{P\gamma} &= \frac{\mathrm{d}\theta}{\mathrm{d}t} \\ \bar{J}_3^{P\gamma} &= \rho \end{aligned} \tag{3.12}$$

and the complete transformation is:

$$d\Gamma_\gamma = \left\| \frac{\partial \mathbf{r}}{\partial \hat{\xi}_1} \times \frac{\partial \mathbf{r}}{\partial \hat{\xi}_2} \right\| d\Lambda = \bar{J}_1^{P\gamma}\bar{J}_2^{P\gamma}\bar{J}_3^{P\gamma} \left\| \frac{\partial \mathbf{r}}{\partial \xi_1} \times \frac{\partial \mathbf{r}}{\partial \xi_2} \right\| d\Lambda = \bar{J}_1^{P\gamma}\bar{J}_2^{P\gamma}\bar{J}_3^{P\gamma} J_2^{\gamma} d\Lambda \tag{3.13}$$

The differential relation of $\bar{J}_2^{P\gamma}$ from eq. (3.12) utilises a chain rule as:

$$\frac{\mathrm{d}\theta}{\mathrm{d}t} = \frac{\partial\theta}{\partial\xi_1}\frac{\partial\xi_1}{\partial t} + \frac{\partial\theta}{\partial\xi_2}\frac{\partial\xi_2}{\partial t} \tag{3.14}$$

in which the derivatives of θ with respect to ξ_1 and ξ_2 are:

$$\begin{aligned} \frac{\partial\theta}{\partial\xi_1} &= \frac{-1}{1+\left[\dfrac{\xi_2(t)-\xi_2^0}{\xi_1(t)-\xi_1^0}\right]^2}\frac{\xi_2(t)-\xi_2^0}{\left[\xi_1(t)-\xi_1^0\right]^2} = \frac{\xi_2^0-\xi_2(t)}{\left[\xi_1(t)-\xi_1^0\right]^2+\left[\xi_2(t)-\xi_2^0\right]^2} = \frac{\xi_2^0-\xi_2(t)}{\hat{\rho}(t)^2} \\ \frac{\partial\theta}{\partial\xi_1} &= \frac{-\sin\theta}{\hat{\rho}(t)} \\ \frac{\partial\theta}{\partial\xi_2} &= \frac{1}{1+\left[\dfrac{\xi_2(t)-\xi_2^0}{\xi_1(t)-\xi_1^0}\right]^2}\frac{1}{\xi_1(t)-\xi_1^0} = \frac{\xi_1(t)-\xi_1^0}{\left[\xi_1(t)-\xi_1^0\right]^2+\left[\xi_2(t)-\xi_2^0\right]^2} = \frac{\xi_1(t)-\xi_1^0}{\hat{\rho}(t)^2} \\ \frac{\partial\theta}{\partial\xi_2} &= \frac{\cos\theta}{\hat{\rho}(t)} \end{aligned} \tag{3.15}$$

while $\partial\xi_1/\partial t$ and $\partial\xi_2/\partial t$ are components of the trimming curve tangent vector.

3.3 Collocation strategy for trimmed surfaces

The collocation strategy for trimmed NURBS surfaces poses a challenge in IGABEM because the standard Greville Abscissae approach may position the collocation points on removed portions of the boundary of these surfaces. This requires an additional modification accounting for the contribution of these points. This topic is relevant as no studies have investigated the optimal position of these points for trimmed surfaces in IGABEM, and current collocation strategies remain limited to simple geometries. In this context, this study proposes a collocation strategy inspired by Peng and Lian (2022), in which the trimmed knot spans receive $(p+1)*(q+1)$ collocation points. Since Peng and Lian (2022) does not specify the rules for this positioning, this section details the placement strategy for these points.

Initially, the standard Greville Abscissae strategy distributes the collocation points onto the trimmed surfaces irrespective of the presence of trimming curves. Next, the points associated with void basis functions are removed from the analysis since their support no longer defines the boundary. Subsequently, the proposed strategy identifies collocation points at trimmed knot spans and assigns new collocation points to these spans to occupy their influence in the algebraic system.

Each trimmed knot span adopts a positioning approach depending on its type (1, 2 or 3, according to fig. 5). Type 1 trimmed knot spans have a triangular shape, in which the strategy distributes collocation points in the integration space $[-1,1]\times[-1,1]$ based on the Gauss points' position. The mapping proposed by Kim, Seo and Youn (2009) transforms their coordinates to obtain their parametric coordinates in the NURBS parametric space, according to fig. 8. The strategy for type 2 trimmed knot spans uniformly subdivides the side opposite the trimming curve and places equally spaced points along the line segment perpendicular to this side, as illustrated in fig. 12. For type 3 trimmed knot spans, the approach first subdivides the trimming curve uniformly. Then, it defines a perpendicular line segment starting from the subdivided trimming curve and distributes collocation points uniformly along this segment, according to fig. 13.

Figure 12 – Collocation strategy for type 2 trimmed knot spans considering $p=q=1$.

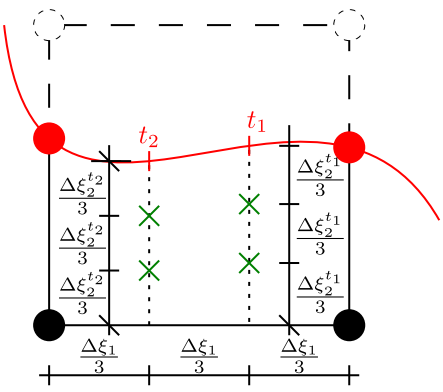

Source: The author.

The contribution of the BIEs applied to each new collocation point occupies the position

Figure 13 – Collocation strategy for type 3 trimmed knot spans considering $p = q = 1$.

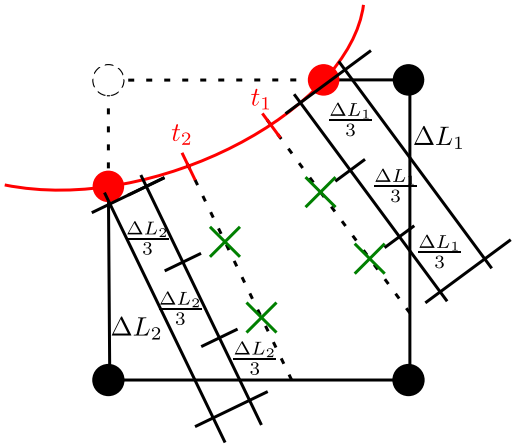

Source: The author.

of the removed collocation point of the corresponding trimmed knot span. This strategy utilises more points than the minimum necessary for the numerical analysis, which poses as a disadvantage that can be further explored in other studies. To accommodate the influence of the new collocation points while keeping a square system, the strategy assigns to each previous row the mean value of the contributions from the new points.

3.4 Numerical applications

This section presents two numerical applications using the IGABEM formulations for trimmed surfaces. The first application consists of a cube with a cylindrical hole, that has an analytical solution. The second application is a quarter of a toroidal shape under loading in one of its extremities and clamped in the other. These two analyses enable a critical view of the formulations in this chapter and their limitations.

3.4.1 Cube with a cylindrical hole

The first application involving trimmed surfaces in the IGABEM framework analyses the mechanical behavior of a cube with unit side and a cylindrical hole of radius $r = 0.15$. Figure 14 illustrates its geometry and boundary conditions. The prescribed displacements are $u_1 = 0.0$, $u_2 = 0.0$ and $u_3 = 0.0$ at the faces with constant coordinates $x_1 = 0.0$, $x_2 = 0.0$, and $x_3 = 0.0$, respectively. In addition, the face with $x_3 = 1.0$ has a traction $t_3 = 1.0$, which induces a uniform stress state along the x_3 direction. The analytical solution of this problem is:

$$\begin{aligned} u_1(x_1, x_2, x_3) &= \frac{-\nu x_1}{E} \\ u_2(x_1, x_2, x_3) &= \frac{-\nu x_2}{E} \\ u_3(x_1, x_2, x_3) &= \frac{x_3}{E} \end{aligned} \tag{3.16}$$

in which the material properties are $E = 1.0$ and $\nu = 0.3$. This allows evaluating the numerical response quality using the L_2 error norm at the boundary as:

$$||e||_{L_2} = \frac{\int_\Gamma (\mathbf{u}_{\text{num}} - \mathbf{u}_{\text{ex}}) \,.\, (\mathbf{u}_{\text{num}} - \mathbf{u}_{\text{ex}})^T \, \mathrm{d}\Gamma}{\int_\Gamma (\mathbf{u}_{\text{ex}} \mathbf{u}_{\text{ex}}^T) \, \mathrm{d}\Gamma} \tag{3.17}$$

in which $\mathbf{u}_{\text{num}}$ and $\mathbf{u}_{\text{ex}}$ represent the numerical and exact solutions for the displacements, respectively. The error assessment uses integration points positioned exactly as in the numerical evaluation of standard integrals, specifically those that do not include the SST scheme.

Figure 14 – Cube with cylindrical hole: geometry and boundary conditions.

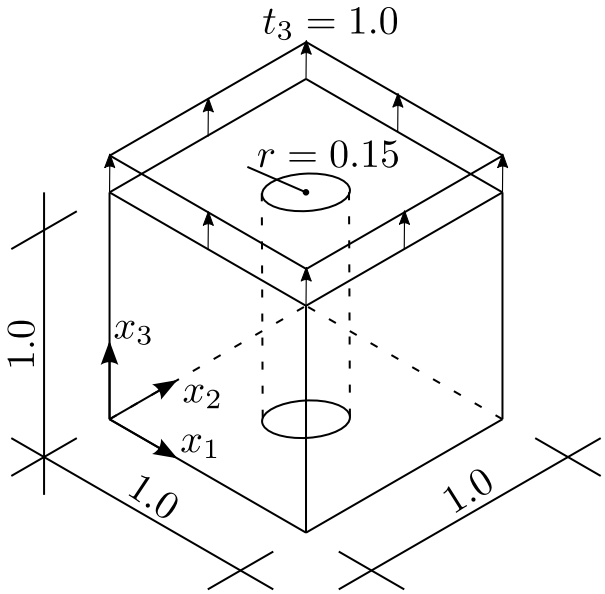

Source: The author.

The isogeometric mesh of this application has 10 NURBS surfaces, as depicted in fig. 15. Six faces define the cube geometry, while the other four faces parametrise the lateral faces of the hole. The upper ($x_3 = 1.0$) and the lower ($x_3 = 0.0$) faces contain a trimming curve of degree 2 that removes the internal region of the hole. The knot vector of these trimming curves is $\tau = \{0;\ 0;\ 0;\ 1/4;\ 1/2;\ 3/4;\ 1;\ 1;\ 1\}$ and table 1 presents the coordinates of the control points on the NURBS parametric space. These two faces use a single trimmed NURBS surface, instead of four surfaces in a standard IGABEM approach. All NURBS surfaces that represent the cube have degree 1 in both parametric directions and the corresponding knot vectors are $\Xi_1 = \Xi_2 = \{0.0; 0.0; 0.5; 1.0; 1.0\}$. The faces that represent the cylinder have degree 2 in the circumferential direction and degree 1 in the longitudinal direction, and the knot vectors are $\Xi_1 = \{0.0; 0.0; 0.0; 0.5; 1.0; 1.0; 1.0\}$ and $\Xi_2 = \{0.0; 0.0; 0.5; 1.0; 1.0\}$. It is worth mentioning that the linear and quadratic basis functions adopted for the mechanical fields approximation are capable of representing in an exact manner both the geometry and the expected response of this application. The IGABEM analysis with trimmed surfaces uses 116 collocation points, in which fig. 16 illustrates the placement of those associated with the upper and lower faces. The mapping strategies for the trimmed surfaces place the integration points according to fig. 17 using 20 integration points for each direction in the integration space. The subdivision of the NURBS parametric space into sub-triangles is noticeable, which is a characteristic of both mappings.

Figure 15 – CAD model of cube with cylindrical hole.

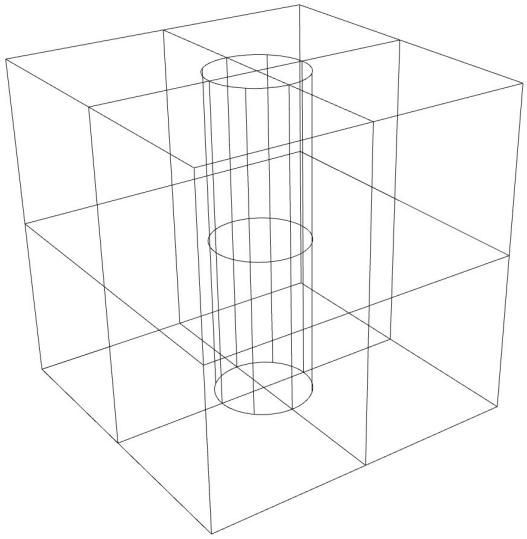

Source: The author.

Table 1 – Position of the control points of the trimming curve on the NURBS parametric space.

Number	ξ_1	ξ_2	w
1	0.65	0.50	1.0
2	0.65	0.35	$\frac{\sqrt{2}}{2}$
3	0.50	0.35	1.0
4	0.35	0.35	$\frac{\sqrt{2}}{2}$
5	0.35	0.50	1.0
6	0.35	0.65	$\frac{\sqrt{2}}{2}$
7	0.50	0.65	1.0
8	0.65	0.65	$\frac{\sqrt{2}}{2}$
9	0.65	0.50	1.0

Source: The author.

Figure 18 illustrates the total displacement field of this application. The response is in accordance with the expected uniform displacement, and also captures the Poisson effect in other directions. The convergence analysis of the relative L_2 norm of error for this application presented in fig. 19 involves varying the number of integration points, ranging from 5 to 30 in increments of 5. The error drops below 10^{-6} with 25 integration points or more, demonstrating the accuracy of the response. This number of integration points addresses the near-singular integrations of the IGABEM formulation.

Figure 16 – Position of added collocation points in trimmed faces.

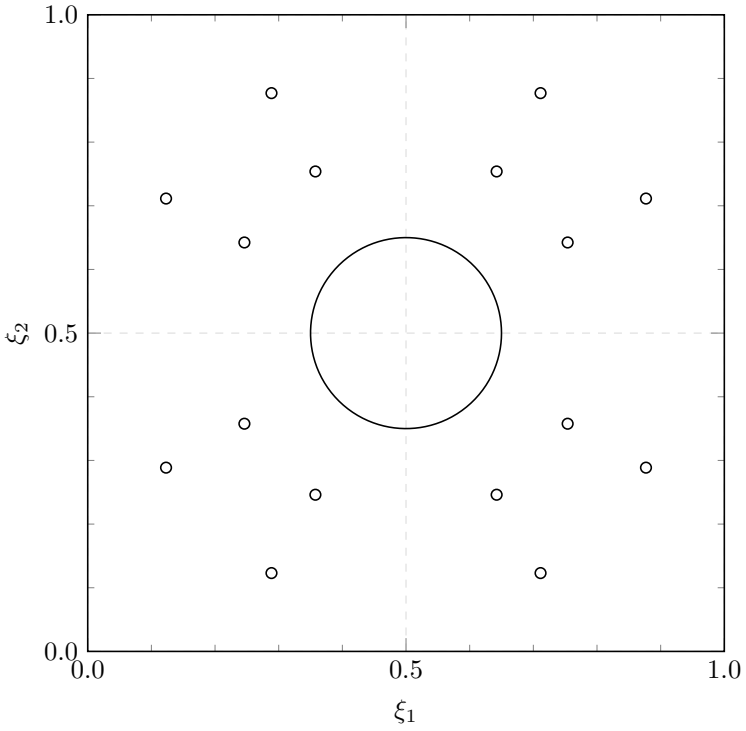

Source: The author.

Figure 17 – Position of integration points for trimmed faces of cube with cylindrical hole.

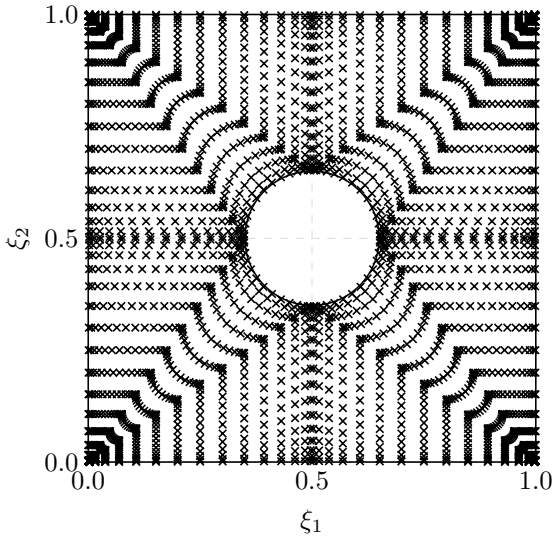

Source: The author.

Figure 18 – Total displacements of a cube with cylindrical hole under tensile loading.

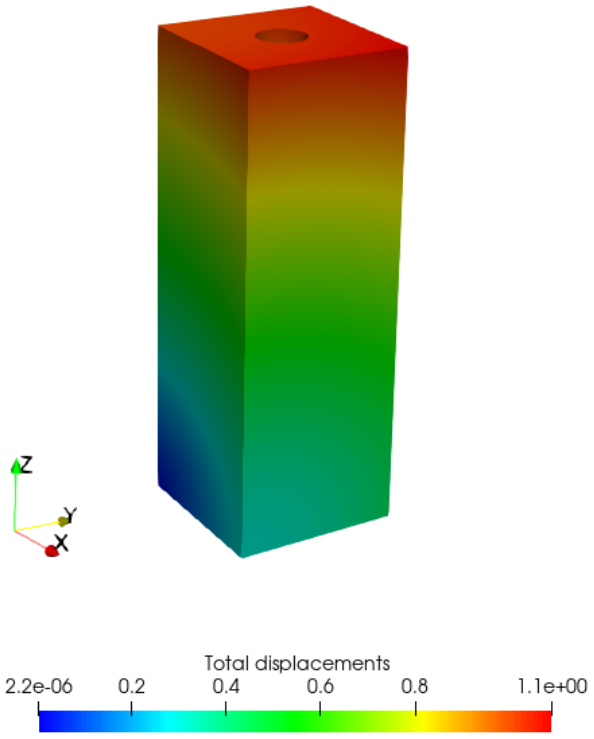

Source: The author.

Figure 19 – Relative L_2 norm of error for total displacements varying the number of integration points.

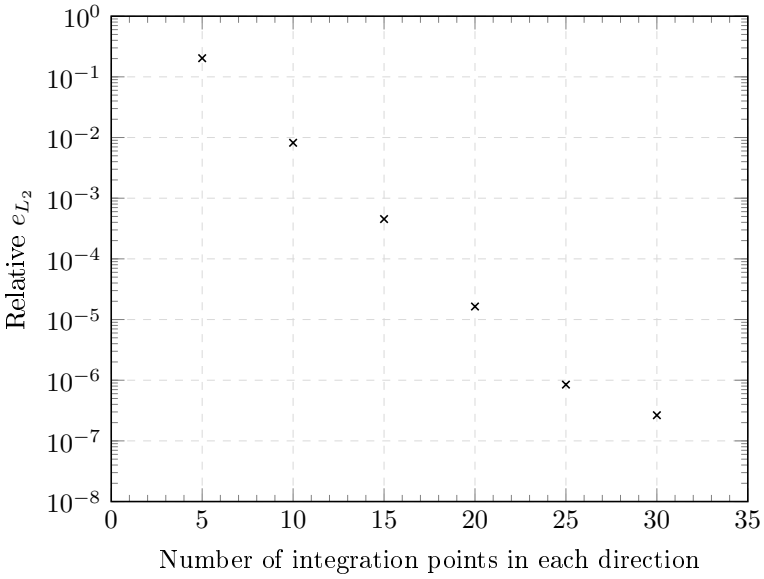

Source: The author.

3.4.2 Thick-walled quarter-torus

The second application using the IGABEM for a trimmed model is the mechanical analysis of a thick-walled tube whose geometry is a quarter-torus. Since standard Lagrangian interpolations cannot accurately represent this curved geometry with few parameters, the IGABEM approach is superior for determining the mechanical fields. In this context, fig. 20 illustrates the geometry and the boundary conditions of this analysis, in which the face with $x_1 = 0.0$ has the displacements restricted in all three directions and two uniform tractions, $t_1 = 1.0$ and $t_3 = 1.0$, are applied at the face $x_2 = 0.0$. The material properties are $E = 1000.0$ and $\nu = 0.3$. Notably, these loading conditions induce a three-dimensional response.

Figure 20 – Thick-walled quarter-torus geometry and boundary conditions.

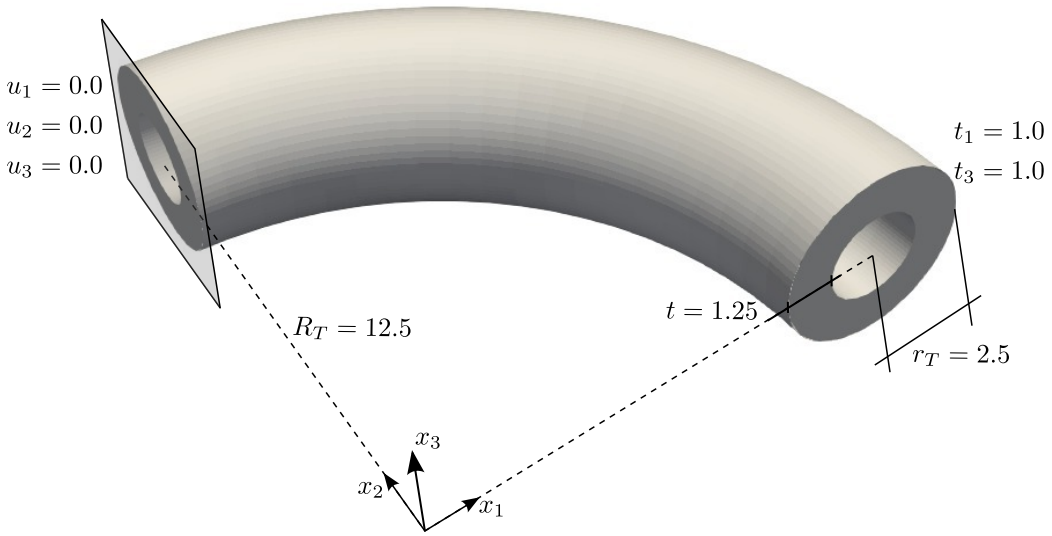

Source: The author.

The isogeometric model of this application comprises 10 NURBS surfaces, as illustrated in fig. 21, in which 8 faces form the laterals curved faces and 2 planar faces. The planar faces have degree 1 in both parametric directions, and their knot vectors are *knot* $\Xi_1 = \Xi_2 = \{0.0;\ 0.0;\ 0.25;\ 0.5;\ 0.75; 1.0; 1.0\}$. Two trimming curves cut the planar faces, in which the inner curve defines the hole, while the outer curve removes the unnecessary part. Table 2 presents the control points and weights of these curves in the NURBS parametric space. The control points 1 to 9 and 10 to 18 correspond to the inner and outer trimming curves, respectively. Thus, the numerical analysis considers both trimming types on the same surface. Other surfaces have degree 3 in the internal radial direction and degree 2 in the outer radial direction. The associated knot vectors are $\Xi_1 = \{0.0; 0.0; 0.0; 0.0; 0.11649028; 0.2399796; 0.36862; 0.5; 0.7600204; 0.883509724; 1.0; 1.0; 1.0; 1.0\}$ and $\Xi_2 = \{0.0;\ 0.0;\ 0.0;\ 1.0; 1.0;\ 1.0\}$ for the directions with degree 3 and 2, respectively. The resulting isogeometric model contains 314 collocation points, namely Mesh A. A refined model obtained by knot insertion in Mesh A produces a second model, Mesh B, with 2122 collocation points. This application also uses the non-singular version of the IGABEM for trimmed surfaces (Wang; Benson; Nagy, 2015), in which initially the Greville Abscissae strategy places the collocation points, and they are moved outside the boundary along the normal outward direction. This

adjustment is based on a percentage of the characteristic length of the knot span in the physical space, being the knot span area divided by the length of a diagonal mapped in the parametric space and measured in the physical space. In this application, this percentage is 10%, and fig. 22 illustrates the collocation point positions for both Meshes A and B. In addition, analyzing this application using the singular version of the IGABEM enables a comparison between these strategies. For this approach, fig. 23 depicts the placement of the additional collocation points on the trimmed surfaces for Mesh A.

Figure 21 – Thick-walled quarter-torus isogeometric mesh.

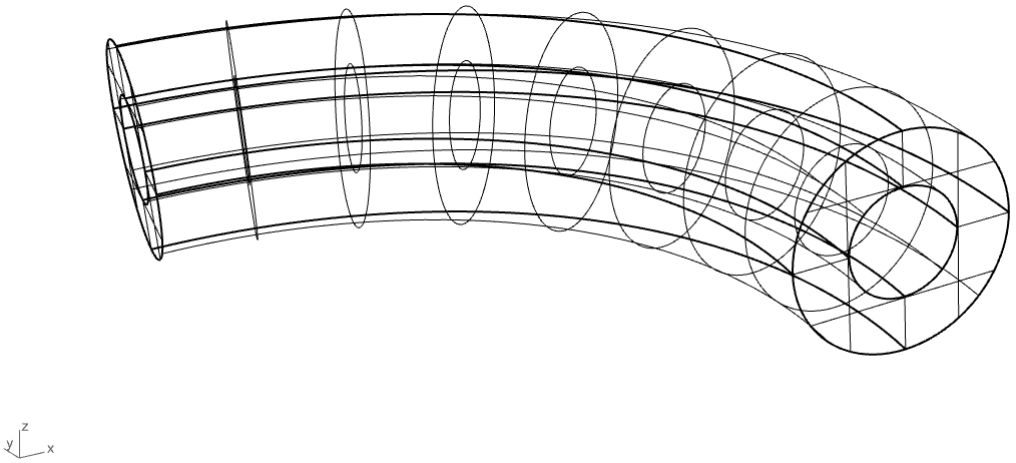

Source: The author.

Table 2 – Control points and weights of trimming curves used in planar faces of the thick-walled quarter-torus.

Number	ξ_1	ξ_2	w	Number	ξ_1	ξ_2	w
1	0.5	0.9901961	1.0	10	0.745098	0.5	1.0
2	0.009803922	0.9901961	$\frac{\sqrt{2}}{2}$	11	0.745098	0.254902	$\frac{\sqrt{2}}{2}$
3	0.009803922	0.5	1.0	12	0.5	0.254902	1.0
4	0.009803922	0.009803922	$\frac{\sqrt{2}}{2}$	13	0.254902	0.254902	$\frac{\sqrt{2}}{2}$
5	0.5	0.009803922	1.0	14	0.254902	0.5	1.0
6	0.9901961	0.009803922	$\frac{\sqrt{2}}{2}$	15	0.254902	0.745098	$\frac{\sqrt{2}}{2}$
7	0.9901961	0.5	1.0	16	0.5	0.745098	1.0
8	0.9901961	0.9901961	$\frac{\sqrt{2}}{2}$	17	0.745098	0.745098	$\frac{\sqrt{2}}{2}$
9	0.5	0.9901961	1.0	18	0.745098	0.5	1.0

Source: The author.

The validation of the results in this application involves a comparison of solutions between the trimmed IGABEM model and a Finite Element (FE) model using the ANSYS. The reference FE model has 76,622 nodes and 51,295 20-node three-dimensional quadratic elements (SOLID 186), in which fig. 24 illustrates its mesh.

Figure 22 – Position of collocation points for Meshes A and B using the non-singular IGABEM approach with trimmed surfaces for a thick-walled quarter-torus.

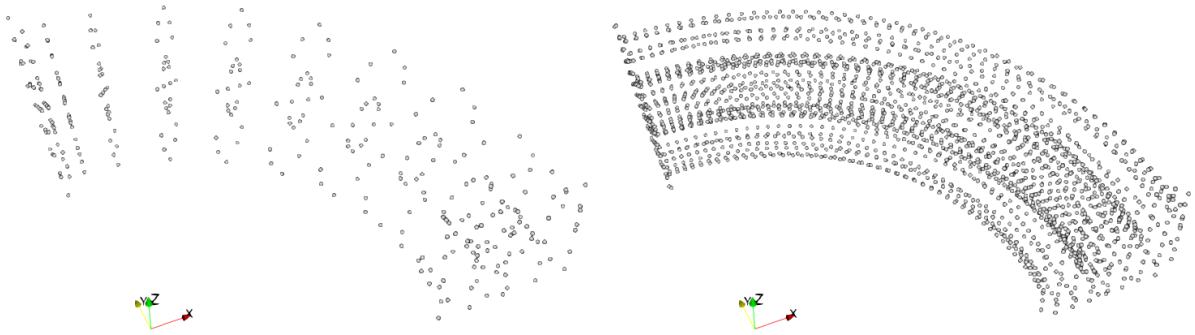

(a) Mesh A (b) Mesh B

Source: The author.

Figure 23 – Relocated collocation points in the NURBS parametric space of the trimmed surfaces for a thick-walled quarter-torus.

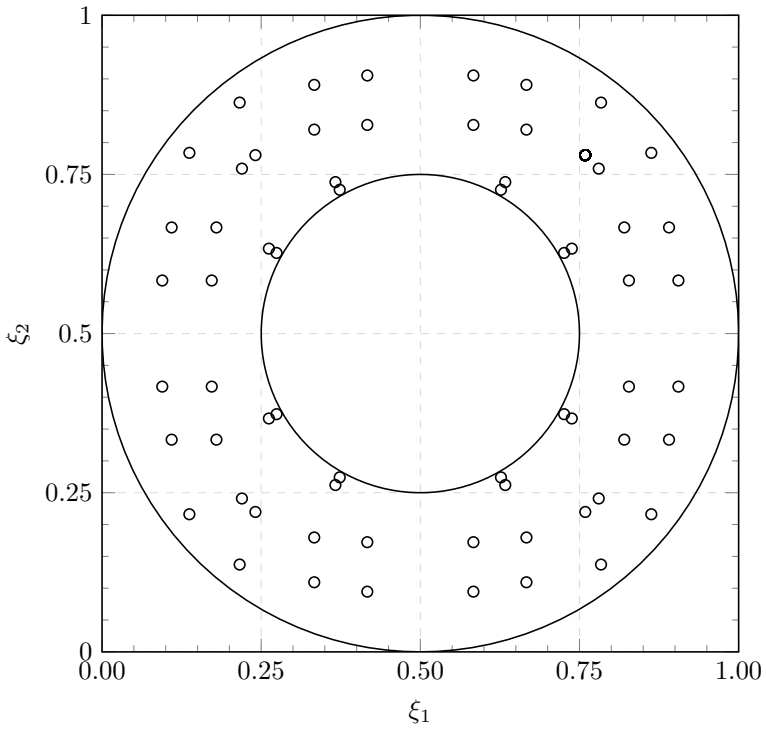

Source: The author.

Figure 25, fig. 26, and fig. 27 depict the mechanical response in terms of total displacements for the FE model, Mesh A, and Mesh B, respectively. Notably, the displacements of the reference and both trimmed non-singular IGABEM models agree, even for the coarsest one, which attests to the accuracy of the proposed strategies for considering two trimming curves at the same face. Figure 28 presents the total displacements of Mesh A considering the singular approach of the

Figure 24 – FE model reference model of the thick-walled quarter-torus.

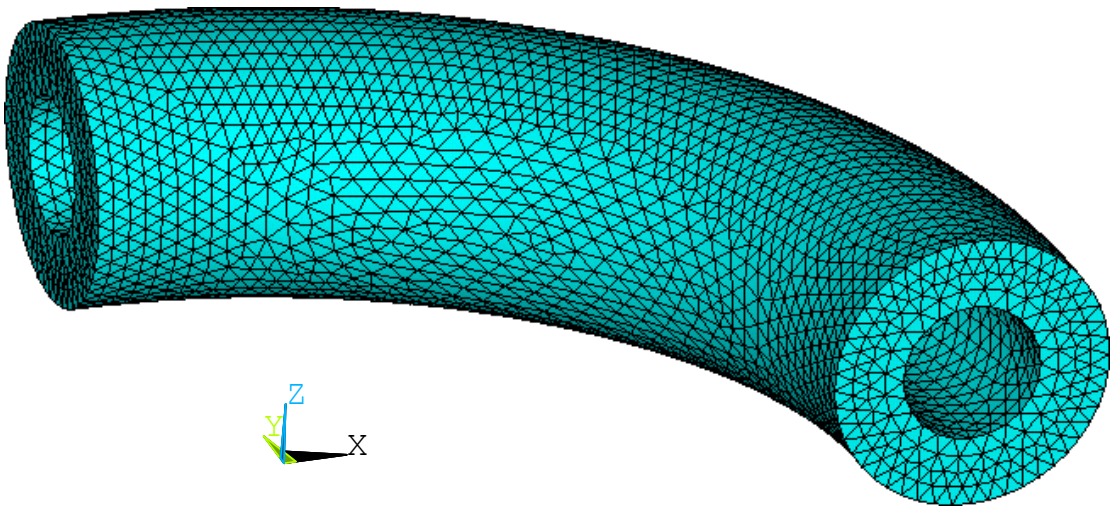

Source: The author.

trimmed IGABEM formulation, in which all collocation points lie on the boundary, with the adjustments proposed in section 3.3. The results demonstrate that this model slightly deviates from the reference solutions, which indicates that the repositioning strategy is not successful in the case of two trimming curves on the same face. The algebraic system for Mesh B in the singular approach does not produce reasonable results, suggesting that the current formulation lacks robustness in this case and requires further investigation.

Figure 25 – Total displacements: FE model.

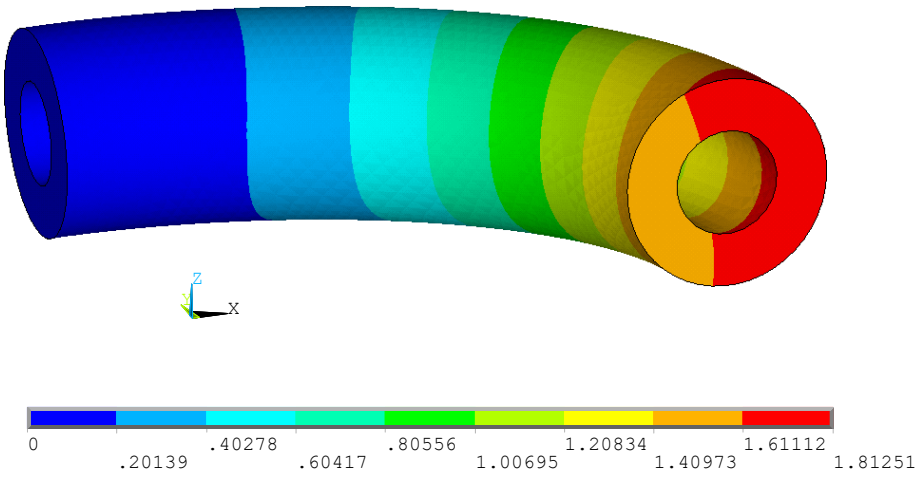

Source: The author.

Finally, fig. 29 and fig. 30 present a comparison of displacements and stress components along an arch with radius $r_A = 11.25$ at the x_3 coordinate, from (0.0; 11.25; 0.0) to (11.25; 0.0; 0.0). The responses of Meshes A and B in the nonsingular version of IGABEM with trimmed surfaces closely match the reference solution, confirming the capability of this version

Figure 26 – Total displacements: Mesh A.

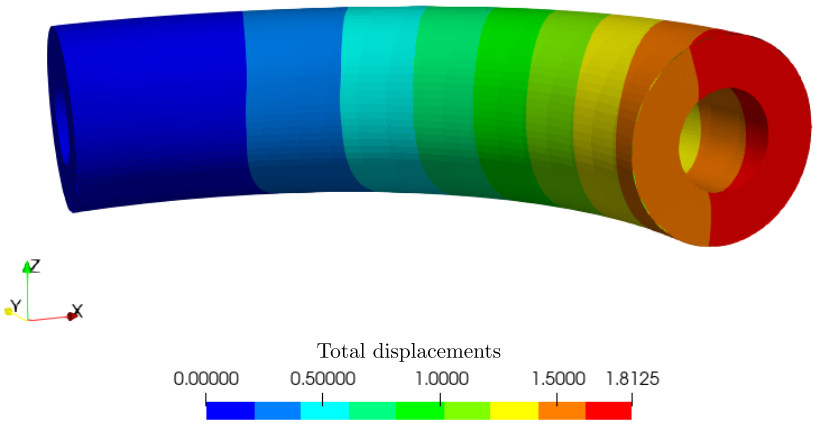

Source: The author.

Figure 27 – Total displacements: Mesh B.

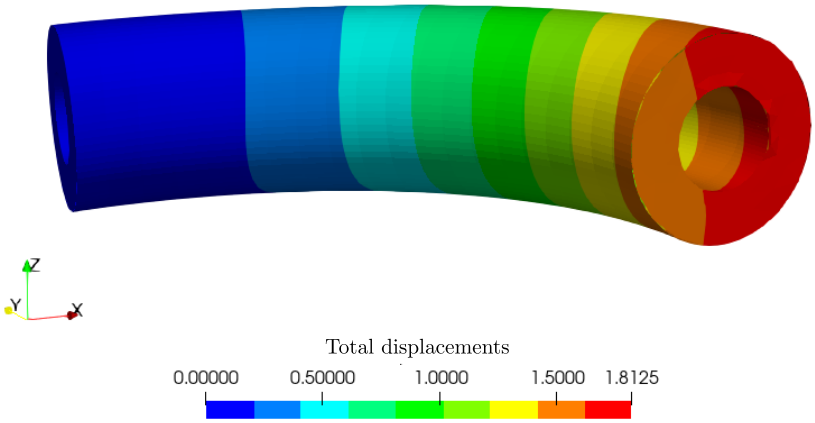

Source: The author.

of the trimmed IGABEM in capturing a purely three-dimensional response. The graphs also presents the results for the singular version of the IGABEM with trimmed surfaces. The results corroborate that this formulation has not been able to precisely capture the mechanical behaviour of this application in comparison to the non-singular version.

Figure 28 – Total displacements: Mesh A in singular approach.

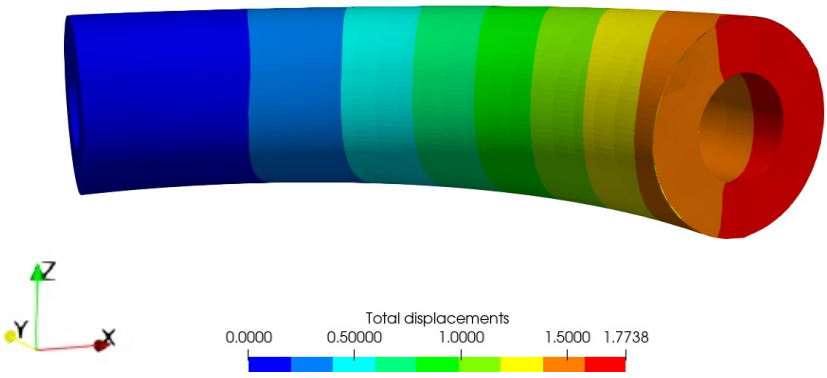

Source: The author.

Figure 29 – Displacements along arch: FE and trimmed IGABEM models.

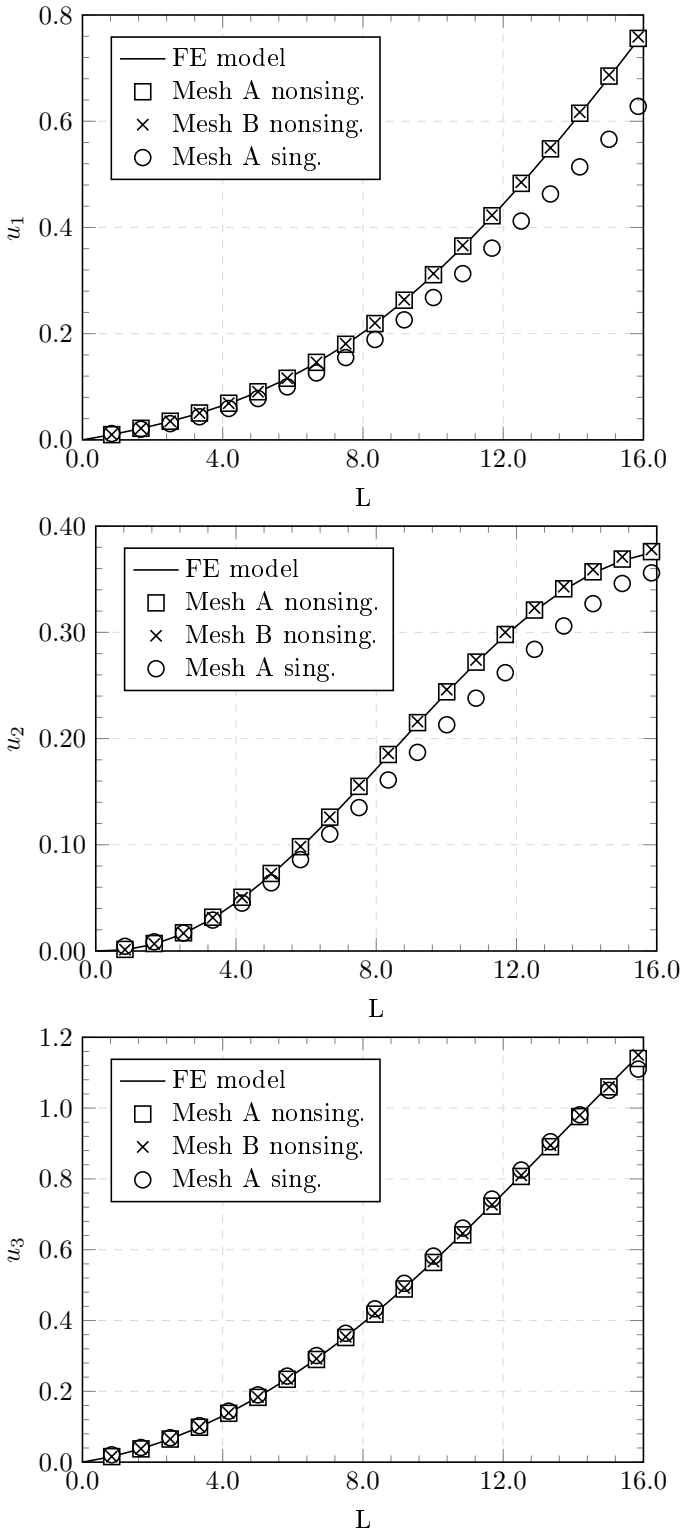

Source: The author.

Figure 30 – Stress components along arch: FE and trimmed IGABEM models.

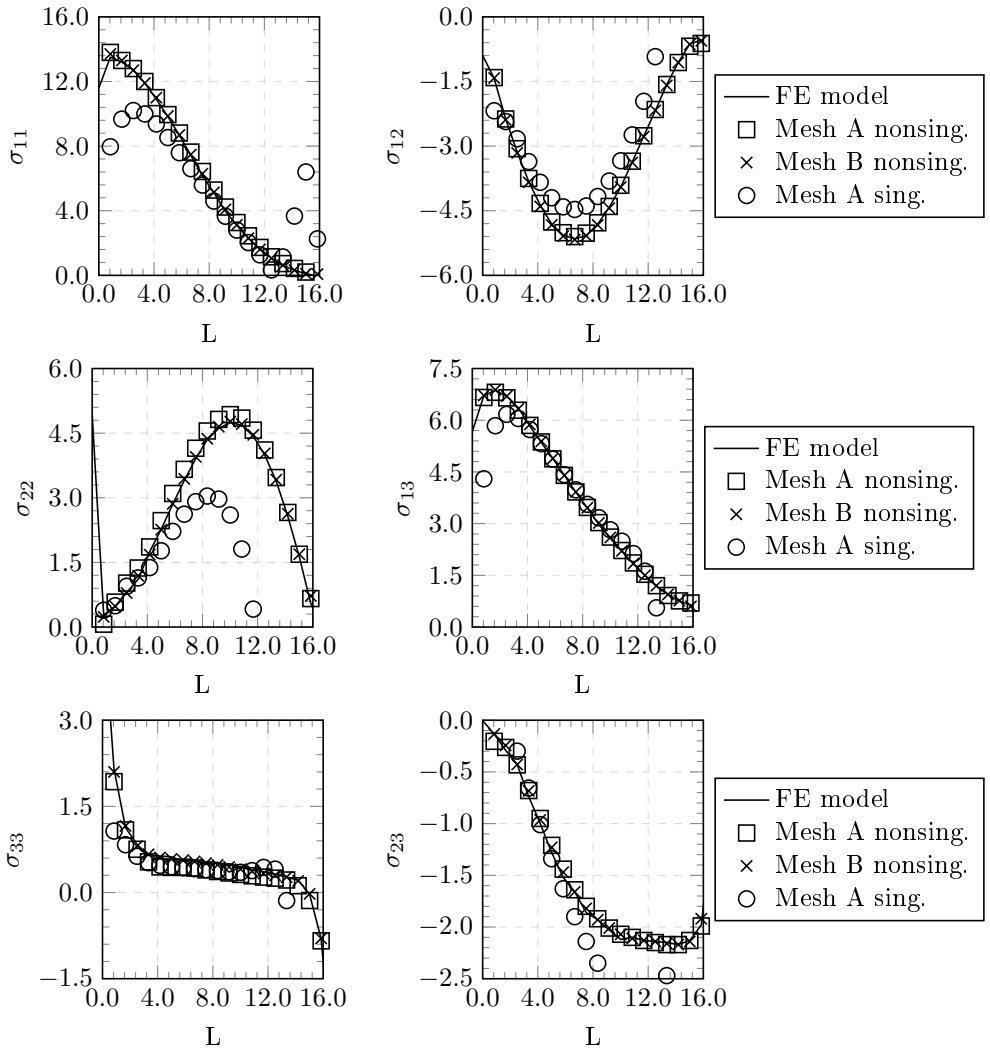

Source: The author.

3.5 Challenges and limitations of trimmed surfaces on IGABEM

This thesis performs a preliminary study on the incorporation of trimmed surfaces into the IGABEM for the elastic analysis of components. Based on the numerical applications presented, this task is successful for simple geometries, especially with the non-singular version of IGABEM. In this scenario, the numerical implementations for incorporating trimmed surfaces into the IGABEM allow a critical review of the method in this context. Particularly, the complexity in importing the geometry, the trimming effect, the need for additional collocation points in the system assembly, and the search for the best geometric placement of these points pose challenges for the general use of the trimmed IGABEM formulation. This section discusses each of these topics.

Firstly, the trimming operation on CAD models requires an identification step for its coupling with the IGABEM. This study considers the possibility of more than one trimming curve on the same set, in which each curve ends either inside a knot span or at its edges. When the endpoint lies inside a knot span, the need for several geometric adaptations in this region hinders its generalisation for more than one endpoint in the same knot span. However, this study does not consider two or more trimming curves at the same knot span, since it requires high complexity alterations in the numerical implementation.

The trimming effect is a matter of concern in IGA with trimmed surfaces. This phenomenon involves the direct exclusion of the support of a basis function in the trimming operation. Wang, Benson and Nagy (2015) discusses how this effect occurs when the remaining support is too small in comparison to its untrimmed size. This results in a significantly smaller contribution by orders of magnitude. Consequently, conditioning issues arise in the algebraic system of the trimmed IGABEM due to this effect.

The use of more collocation points than the minimum required by the formulation also affects the robustness of the trimmed IGABEM. Naturally, using this greater number of collocation points demands the numerical integration of the boundary, which impacts the computational cost of the method. In addition, the sub-optimal placement of these points also results in a lower overall quality of the numerical response, even when more points try to represent the altered knot spans. During the numerical tests, the further the points remain from the positions determined by the Greville Abscissae, the better the results are. In this context, this topic remains open and it and remains relevant for future investigation.

4 HEAVISIDE ENRICHMENT FOR DISPLACEMENT DISCONTINUITIES IN CROSSED SURFACES

This chapter presents the development of the enrichment formulation to introduce a discontinuity in the displacement field on the external boundary where cracks intersect. In standard IGABEM modelling, mesh generation must account for two NURBS surfaces sharing an edge aligned with the intersecting crack to capture the strong discontinuity along this edge. However, CAD model construction commonly represents the external boundary while neglecting its intersection with cracks. Moreover, for crack growth analysis it is impractical to discard and rebuild the NURBS surface parametrisation at each crack increment. In this context, this study proposes the enrichment of the displacement field by the Heaviside function to dismiss the re-meshing task required in the numerical analysis of cracked solids. This approach is novel in IGABEM since there are no other studies that incorporate this discontinuous behaviour at the external boundary triggered by the crack.

In this context, this chapter presents the displacement field enrichment and its implications on the algebraic system since they introduce new unknown coefficients in the approximation. Supplementary equations restore the square system, and this study proposes two distinct approaches to determine them. In addition, the enrichment scheme raises some implementation challenges such as identifying intersected knot spans and their numerical integration. Three numerical applications demonstrate the robustness and efficiency of the developed scheme, highlighting its capabilities within the context of fracture mechanics.

4.1 Displacement field enrichment

The enrichment strategy expands the standard isogeometric displacement approximation eq. (2.28) by introducing additional displacement coefficients $\overline{d}_k^\beta$ and its product with the Heaviside function $\mathscr{H}$ and the basis function as follows:

$$u_k^\gamma(\xi_1,\xi_2) = \sum_{\alpha=1}^{n^\gamma} \phi_\alpha^\gamma(\xi_1,\xi_2) d_k^\beta + \sum_{\alpha=1}^{n_{\mathscr{H}}^\gamma} \left[\mathscr{H}(\xi_1,\xi_2) - \mathscr{H}_\alpha\right] \phi_\alpha^{\gamma^{\mathscr{H}}} \overline{d}_k^\beta \tag{4.1}$$

in which $u_k^\gamma(\xi_1,\xi_2)$ represents for the displacement at the enriched NURBS surface $\gamma^{\mathscr{H}}$. The Heaviside function $\mathscr{H}$ assumes the value -1.0 before the crossing and 1.0 after it. In addition, $n_{\mathscr{H}}^\gamma$ represents the number of enriched functions in the patch γ. The term $\mathscr{H}_\alpha$ is the Heaviside function at the corresponding collocation point α and its subtraction from the enrichment function results in the shifting approach (Belytschko *et al.*, 2001). This proposition avoids the need for blending elements since the shifting removes the support at uncrossed knot spans.

Figure 31 illustrates the construction of an enriched basis function ϕ_4 of a NURBS surface of degree 2 in both parametric directions and knot vector $\Xi_1 = \Xi_2 = \{0.0; 0.0; 0.0; 1.0; 1.0; 1\}$. The collocation point of this basis function is at the parametric coordinates $(\xi_1, \xi_2) = (0.9; 0.1)$. The crack has a parametric equation of $\xi_2 = 0.44 * \xi_1 + 0.23$ to represent its intersection, in which the region $\xi_2 \leq 0.44 * \xi_1 + 0.23$ assumes $\mathscr{H} = -1.0$. In this context, fig. 31(a) represents

the standard basis function, fig. 31(b) is the function $\mathscr{H} - \mathscr{H}_4$ and fig. 31(c) illustrates the final enrichment function.

Figure 31 – Shifted Heaviside function.

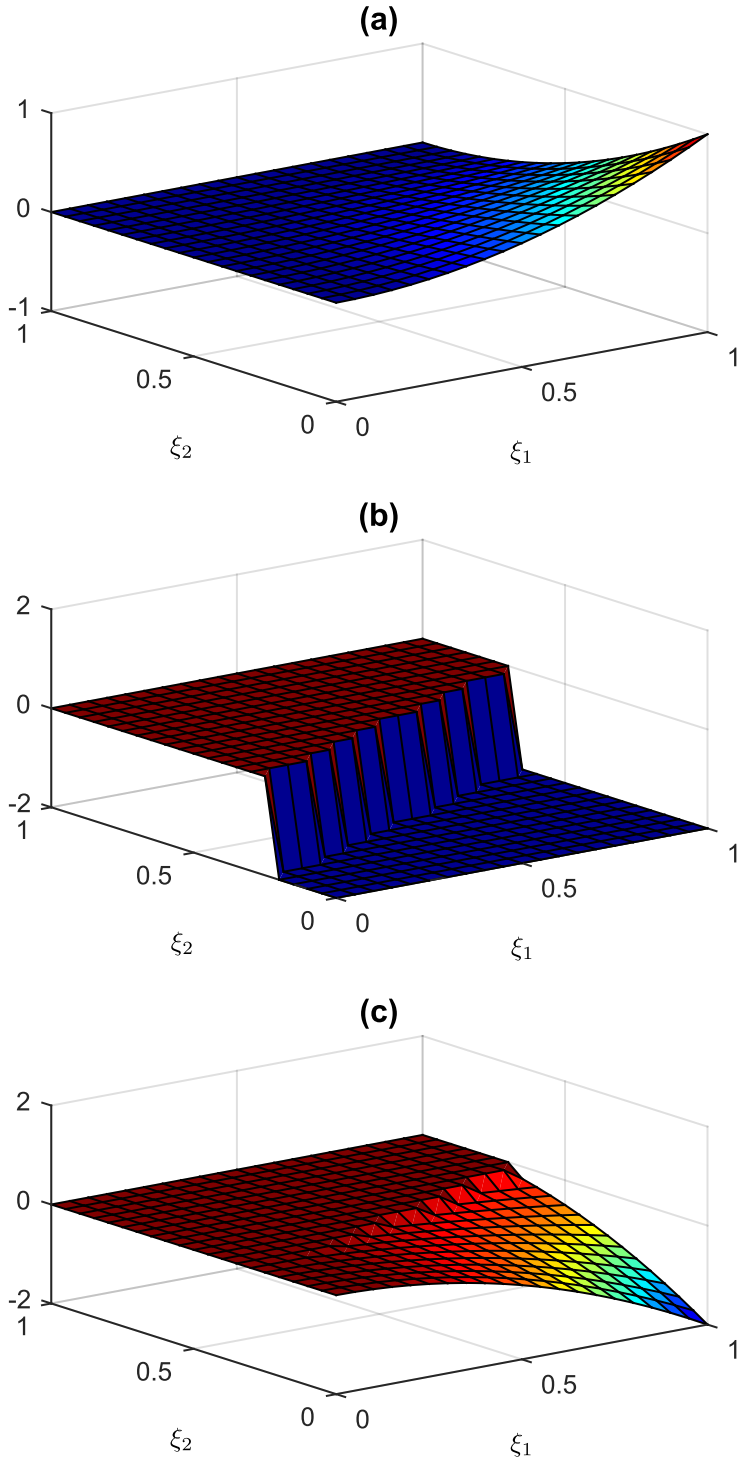

Source: The author.

The introduction of the expanded approximation for u_k^γ (eq. (4.1)) on the BIEs leads to the modified discretised equations:

$$c_{\ell k}(\hat{\mathbf{x}}^{eb})\sum_{\alpha=1}^{n^\gamma}\phi_\alpha^{\hat{\gamma}}(\hat{\mathbf{x}}^{eb})d_k^\beta+\sum_{\gamma=1}^{NS}\underline{\mathrm{T}}_{\ell k}^{*\alpha\gamma}d_k^\beta+\sum_{\gamma=1}^{NS}\underline{\mathrm{T}}_{\mathrm{h}\ell k}^{\alpha\gamma}\overline{d}_k^\beta=\sum_{\gamma=1}^{NS}\underline{\mathrm{U}}_{\ell k}^{*\alpha\gamma}p_k^\beta$$

$$\begin{aligned}c_{\ell k}(\hat{\mathbf{x}}^{c+})\sum_{\alpha=1}^{n^\gamma}\phi_\alpha^{\hat{\gamma}+}(\hat{\mathbf{x}}^{c+})d_k^\beta+c_{\ell k}(\hat{\mathbf{x}}^{c-})\sum_{\alpha=1}^{n^\gamma}\phi_\alpha^{\hat{\gamma}-}(\hat{\mathbf{x}}^{c-})d_k^\beta\\+\sum_{\gamma=1}^{NS}\underline{\mathrm{T}}_{\ell k}^{*\alpha\gamma}d_k^\beta+\sum_{\gamma=1}^{NS}\underline{\mathrm{T}}_{\mathrm{h}\ell k}^{\alpha\gamma}\overline{d}_k^\beta=\sum_{\gamma=1}^{NS}\underline{\mathrm{U}}_{\ell k}^{*\alpha\gamma}p_k^\beta\end{aligned}\tag{4.2}$$

$$\begin{aligned}\frac{1}{2}\sum_{\alpha=1}^{n^\gamma}\phi_\alpha^{\hat{\gamma}-}(\hat{\mathbf{x}}^{c-})p_j^\beta-\frac{1}{2}\sum_{\alpha=1}^{n^\gamma}\phi_\alpha^{\hat{\gamma}+}(\hat{\mathbf{x}}^{c+})p_j^\beta\\+n_\ell(\hat{\mathbf{x}}^{c-})\sum_{\gamma=1}^{NS}\underline{\mathrm{S}}_{k\ell j}^{\alpha\gamma}d_k^\beta+n_\ell(\hat{\mathbf{x}}^{c-})\sum_{\gamma=1}^{NS}\underline{\mathrm{S}}_{\mathrm{h}k\ell j}^{*\alpha\gamma}\overline{d}_k^\beta=n_\ell(\hat{\mathbf{x}}^{c-})\sum_{\gamma=1}^{NS}\underline{\mathrm{D}}_{k\ell j}^{*\alpha\gamma}p_k^\beta\end{aligned}$$

in which solely $\underline{\mathrm{T}}_{\mathrm{h}\ell k}^{\alpha\gamma}$ and $\underline{\mathrm{S}}_{\mathrm{h}k\ell j}^{*\alpha\gamma}$ emerge from enrichment function influence, being:

$$\begin{aligned}\underline{\mathrm{T}}_{\mathrm{h}\ell k}^{\alpha\gamma}&=\sum_{\mathrm{ks}=1}^{n_{\mathrm{ks}}^\gamma}\sum_{\alpha=1}^{n_{\mathscr{H}}^\gamma}\int_\Lambda T_{\ell k}^*\phi_\alpha^{\gamma^{\mathscr{H}}}\,(\mathscr{H}-\mathscr{H}_\alpha)\,J_\gamma^{\mathrm{ks}}\,d\Lambda\\\underline{\mathrm{S}}_{\mathrm{h}k\ell j}^{*\alpha\gamma}&=\sum_{\mathrm{ks}=1}^{n_{\mathrm{ks}}^\gamma}\sum_{\alpha=1}^{n_{\mathscr{H}}^\gamma}\int_\Lambda S_{k\ell j}^*\phi_\alpha^{\gamma^{\mathscr{H}}}\,(\mathscr{H}-\mathscr{H}_\alpha)\,J_\gamma^{\mathrm{ks}}\,d\Lambda\end{aligned}\tag{4.3}$$

The shifting procedure results in having an enrichment function being zero at the collocation point. This removes the requirement for the SST on new integral. Consequently, the SST for the S^* kernel does not require the first derivative of the enrichment function, which constitutes an advantage of this approach compared against the use of unshifted enrichment functions. Additionally, the influence of the Heaviside enrichment on the jump term cancels out as a consequence of the shifting procedure.

Another aspect of the integration of the kernels in eq. (4.3) is its discontinuous nature over the crossed knot-span. In this case, as standard for the GFEM/XFEM (Béchet *et al.*, 2005),its accuracy depends on an element subdivision scheme to correctly account for each continuous contribution. The generation of a cell-based subdivision and integration follow the ideas for the trimmed knot spans in the trimmed IGABEM. In addition, the polar integration strategy computes the influence for both the enrichment term and the standard IGABEM contributions in intersected knot spans.

The definition of the enriched basis functions is directly related to the number of added degrees of freedom. The set $\phi_\alpha^{\gamma^{\mathscr{H}}}$ consists of all non-null basis functions of each knot-span crossed by the crack. The implementation details associated to this task in the isogeometric context are presented in section 4.3. A key complication is that the introduction of the unknowns $\overline{d}_k^\beta$ does not naturally come with additional equations, which leads to an ill-posed system containing an insufficient number of equations. Strategies to obtain the auxiliary equations required for

this, and other enrichment strategies of this study, are presented in section 4.2. All terms arising from a standard IGABEM analysis are still present in the augmented system, highlighting the straightforward introduction of enrichment in pre-existing IGABEM codes.

4.2 Supplementary equations strategy

The enrichment strategy for strong discontinuities introduces new unknowns to the algebraic system. Unlike Galerkin-based schemes, the collocation-based IGABEM does not provide additional equations as a natural consequence of the enrichment. To recover a well-posed square system, the XIGABEM requires alternative strategies to obtain these supplementary equations. This study proposes two approaches to determining them in the context of the Heaviside enrichment for strong discontinuities.

The first approach relies on an L_2 projection of the relative displacement between the intersected external boundary and the crack surfaces. This strategy is analogous to the scheme proposed by (Peng; Lian, 2022) for applying boundary condition at trimmed surfaces. By considering a functional $J(u_k^{\gamma^{\mathscr{H}}} - u_k^c)$ as the L_2 norm of the displacement error along the intersection, its minimisation leads to:

$$\begin{aligned} J(u_k^{\gamma^{\mathscr{H}}} - u_k^c) &:= ||u_k^{\gamma^{\mathscr{H}}} - u_k^c||^2_{L_2(\Gamma)} \\ &= \int_s (u_k^{\gamma^{\mathscr{H}}} - u_k^c)(u_k^{\gamma^{\mathscr{H}}} - u_k^c) ds \end{aligned} \tag{4.4}$$

in which the integration occurs along the line defined by the crack front that introduces the displacement jump at the external boundary. $u_k^{\gamma^{\mathscr{H}}}$ represents the displacement at the external boundary at the corresponding side of the crack front whose displacement is u_k^{c+} or u_k^{c-}, depending on the crack surface. This integral is zero for any vector $(\delta u_k^{\gamma^{\mathscr{H}}} - \delta u_k^c)$ orthogonal to $(u_k^{\gamma^{\mathscr{H}}} - u_k^c)$, being:

$$\begin{aligned} \int_s (u_k^{\gamma^{\mathscr{H}}} - u_k^c)(\delta u_k^{\gamma^{\mathscr{H}}} - \delta u_k^c) ds = 0 \\ \Rightarrow \int_s \left[\phi_\alpha^{\gamma^{\mathscr{H}}}(s) d_k^\beta + (\mathscr{H}(s) - \mathscr{H}_\alpha)\, \phi_\alpha^{\gamma^{\mathscr{H}}} \overline{d}_k^\beta) - \phi_\alpha^{\gamma(c)}(s) d_k^\beta \right] \\ \left[\phi_\alpha^{\gamma^{\mathscr{H}}}(s) \delta d_k^\beta + (\mathscr{H}(s) - \mathscr{H}_\alpha)\, \phi_\alpha^{\gamma^{\mathscr{H}}} \delta \overline{d}_k^\beta - (\phi_\alpha^{\gamma(c)}(s) \delta d_k^\beta) \right] ds = 0 \end{aligned} \tag{4.5}$$

The integral must be zero for any arbitrary δd_k^β, $\delta \overline{d}_k^\beta$, and δd_k^β. This generates more equations than the number of additional parameters. Considering that the equations generated from $\delta \overline{d}_k^\beta$ results in the exact number of enriched parameters, this leads to the supplementary equations of this strategy as:

$$\int_s \left[\phi_\alpha^{\gamma^{\mathscr{H}}}(s) d_k^{\beta)} + (\mathscr{H}(s) - \mathscr{H}_\alpha)\, \phi_\alpha^{\gamma^{\mathscr{H}}} \overline{d}_k^\beta - \phi_\alpha^{\gamma(c)}(s) d_k^{\beta)} \right] \left[(\mathscr{H}(s) - \mathscr{H}_\alpha)\, \phi_\alpha^{\gamma^{\mathscr{H}}} \right] ds = 0 \tag{4.6}$$

The second strategy consists of applying the TBIE on the collocation points whose basis functions are enriched. Since these points already have the DBIE used from the standard IGABEM approach, these points receive both types of equations at the same time. The linear independence of these BIEs leads to a non redundant set of equations. Additional collocation points are also a feasible approach (Simpson; Trevelyan, 2011b), but using the TBIE dismisses the need for an optimal placement for additional collocation points.

However, since the SST of the TBIE requires Hölder continuity at the collocation point (C^1 continuous at the singular point for the S^* kernel), degree 1 NURBS surfaces face an issue for

receiving this BIE. The Greville Abscissae strategy positions these points where basis functions may be C^0, which prevents the sole use of the SST for the precise evaluation of the SST integrals. To circumvent this limitation, the rigid body motion approach (Brebbia, 1978) computes the missing contribution. This strategy considers a solid with traction-free boundaries, inducing a constant displacement u_k^{RBM} field. Furthermore, the XIGABEM additional paramaters vanish under this condition as no relative displacement occurs. In this situation, the TBIE reduces to:

$$\left(n_\ell(\hat{\mathbf{x}}) \sum_{\gamma=1}^{NS} \underline{\mathrm{S}}_{k\ell j}^{*\,\alpha\gamma} \right) u_k^{\mathrm{RBM}} = 0_k \tag{4.7}$$

Since eq. (4.7) is valid for arbitrary u_k^{RBM}, the associated coefficient term multiplying it must be zero. Thus, introducing this condition into the TBIE generates the missing contribution of the S^*-kernel integration as:

$$\begin{aligned} &\left(-n_\ell(\hat{\mathbf{x}}) \sum_{\gamma=1}^{NS} \underline{\mathrm{S}}_{k\ell j}^{*\,\alpha\gamma} \right) \sum_{\alpha=1}^{n^\gamma} \phi_\alpha^{\hat{\gamma}}(\hat{\mathbf{x}}) d_k^\beta + c_{\ell k}(\hat{\mathbf{x}}) \sum_{\alpha=1}^{n^\gamma} \phi_\alpha^{\hat{\gamma}}(\hat{\mathbf{x}}) p_k^\beta \\ &+ n_\ell(\hat{\mathbf{x}}) \sum_{\gamma=1}^{NS} \underline{\mathrm{S}}_{k\ell j}^{\alpha\gamma} d_k^\beta + n_\ell(\hat{\mathbf{x}}) \sum_{\gamma=1}^{NS} \underline{\mathrm{S}}_{\mathrm{h}k\ell j}^{*\,\alpha\gamma} \overline{d}_k^\beta = n_\ell(\hat{\mathbf{x}}) \sum_{\gamma=1}^{NS} \underline{\mathrm{D}}_{k\ell j}^{*\,\alpha\gamma} p_k^\beta \end{aligned} \tag{4.8}$$

and is specific to $p = 1$ or $q = 1$ NURBS surfaces in the XIGABEM scheme. The algebraic system incorporates the correction term obtained by eq. (4.7) after the integration of the boundary.

The XIGABEM algebraic system stores the standard IGABEM contribution, eq. (2.36), and the new parameters arising from the enrichment strategy. The system expands to accommodate the influence factors from the integration of the kernels associated with the additional parameters and the supplementary equations. Thus, the XIGABEM matrix with the Heaviside enrichment becomes:

$$\begin{bmatrix} \mathbf{H} & \mathbf{H}_{\mathrm{h}} \\ \mathbf{\Phi}^{\mathrm{T}} & \mathbf{\Phi}_{\mathrm{h}}^{\mathrm{T}} \end{bmatrix} \left\{ \begin{array}{c} \mathbf{d} \\ \overline{\mathbf{d}} \end{array} \right\} = \begin{bmatrix} \mathbf{G} \\ \mathbf{G}_{\mathrm{h}}^{\mathrm{T}} \end{bmatrix} \left\{ \begin{array}{c} \mathbf{p} \end{array} \right\} \tag{4.9}$$

in which $\mathbf{H}$ and $\mathbf{G}$ are the standard IGABEM matrices, while $\mathbf{d}$ and $\mathbf{p}$ represent displacement and traction coefficients, respectively. The subscript h denotes the contribution from the Heaviside enrichment for the strong discontinuities in the external boundary. $\mathbf{\Phi}^{\mathrm{T}}$, $\mathbf{\Phi}_{\mathrm{h}}^{\mathrm{T}}$, and $\mathbf{G}_{\mathrm{h}}^{\mathrm{T}}$ contain terms derived from the supplementary equations. Notably, for the L_2 projection strategy, the matrix $\mathbf{G}_{\mathrm{h}}^{\mathrm{T}}$ vanishes.

4.3 Implementation aspects

This section presents the implementation details of the Heaviside enrichment on the IGABEM formulation. All the required tasks occur before the system assembly, and they are responsible for defining geometrical aspects of the crack intersection at the external boundary. These pre-processing tasks are similar to the techniques required by the trimmed IGABEM approach.

Initially, the algorithm detects which sides of the upper crack face (modelled with the DBIE) intersect the external boundary. Using the physical coordinates of the side's midpoint, an

Figure 32 – Mid-points at each crack edge that search their correspondent external boundary face.

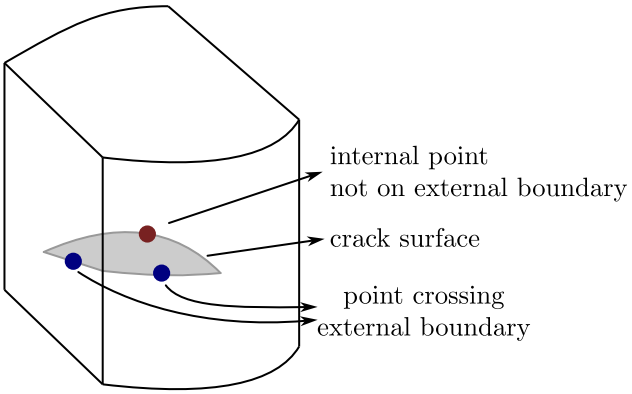

Source: The author.

iterative Newton-Raphson scheme computes the corresponding parametric coordinates at each NURBS surface candidate. If the point on this candidate surface belongs to an edge, this surface does not receive the enrichment since the strong discontinuity is already present. Otherwise, the NURBS surface requires enriching to account for the displacement jump induced by the crack. After finding the enriched NURBS surface, the algorithm searches for its corresponding lower crack face (with the TBIE). Figure 32 illustrates this initial search for crossings.

The crack edge projection to the enriched NURBS surface enables further geometric analysis. This representation involves finding an equivalent NURBS curve mapped onto the intersected NURBS surface parametric space. This curve has the same degree and knot vector as the crack edge, and each new control point inherits the weight of its corresponding control point from the univariate edge NURBS curve. Computing the corresponding control points requires sampling anchor points with parametric coordinate t_s on the crossing crack edge. For each point, the NURBS interpolation over the crack edge determines its physical coordinates and then an iterative Newton-Raphson scheme calculates the parametric coordinates $(\xi_1(t_s), \xi_2(t_s))$ of the anchor point in the intersected NURBS surface. Subsequently, by computing the basis functions $\phi^k(t_s)$ from the corresponding crack edge that crosses the NURBS surface, the search for the control points $(\underset{\sim}{\xi}{}^s_1, \underset{\sim}{\xi}{}^s_2)$ of the projected NURBS curve becomes:

$$\begin{aligned} \sum_{k=1}^{n} \phi^k(t_s) \underset{\sim}{\xi}{}^s_1 &= \xi_1(t_s) \\ \sum_{k=1}^{n} \phi^k(t_s) \underset{\sim}{\xi}{}^s_2 &= \xi_2(t_s) \end{aligned} \tag{4.10}$$

The search for the points where the projected NURBS edge crosses the knot spans occurs in an analogous manner as the trimming curves intersection with the knot span edges. The two step algorithm subdivides the projected NURBS curve, and for each subdivision whose edges do not belong to the same knot span the algorithm of eq. (3.1) finds the parametric coordinate for the crossing.

The numerical integration of the intersected knot spans requires a sub-cell approach to

account separately for the contribution of each term arising from the kernels of the enrichment strategy due to its discontinuous nature. The intersection between the crack surface and the knot spans allows the definition of each sub-cell, again in a similar fashion to the trimmed IGABEM procedure. This enables the use of the polar integration strategy presented in section 3.2.2. There are six possible cases for the generation of the sub-cells in entirely crossed knot-spans, which are shown in fig. 33. In addition, when the crack ends inside a knot-span there are four possible sub-cell configurations within the Heaviside enrichment, illustrated by fig. 34. It is worth noting that in the case of a partial crossing, the Heaviside function assumes null values after the crack tip. Furthermore, it is possible that two different crack surfaces share a connection inside a knot-span. In this situation, fig. 35 presents three general cases of sub-division, in which the local knot-span connectivity is rotated to fit into these cases. The first NURBS curve always crosses the lower edge and the second NURBS curve can cross either the right, upper or left corner. This scenario is more common in the crack growth analysis in chapter 6.

Figure 33 – Possible cases for entirely crossed knot-span, in which the crack is indicated by red and the knot-span sub-divisions are represented in dashed green.

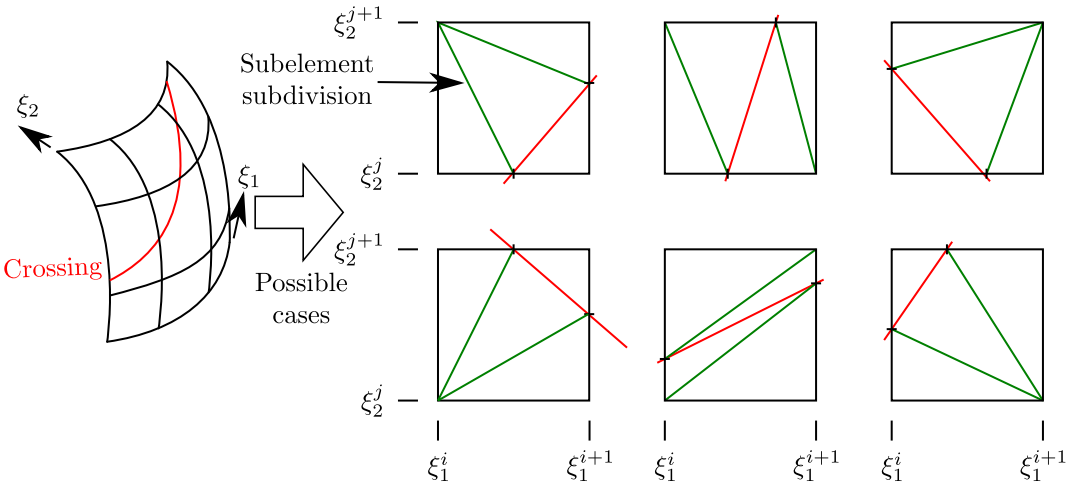

Source: The author.

The Heaviside function $\mathscr{H}$ assumes a constant value over each sub-cell, which allows its calculation just once for the cell. This eliminates the need for its evaluation at each Gauss point, accelerating the integration procedure for the associated enriched kernel. Determining $\mathscr{H}$ involves the sign of the dot product between the vector extending from a crack endpoint into the sub-cell interior (fig. 36) and the normal outward vector of the upper crack face. Obtaining $\mathscr{H}_\alpha$ of each collocation point follows the $\mathscr{H}$ value of the corresponding cell, or adopts a similar approach when the collocation point is outside any crossed cell.

The visualisation of the numerical results uses a plotting-specific mesh to properly represent the strong discontinuity at the enriched NURBS surfaces. Gmsh software processes the the sub-cells and generates a plotting mesh for them, ensuring that the model displays results consistent with the physical behaviour.

Figure 34 – Knot-span subdivision for crack ending inside its domains.

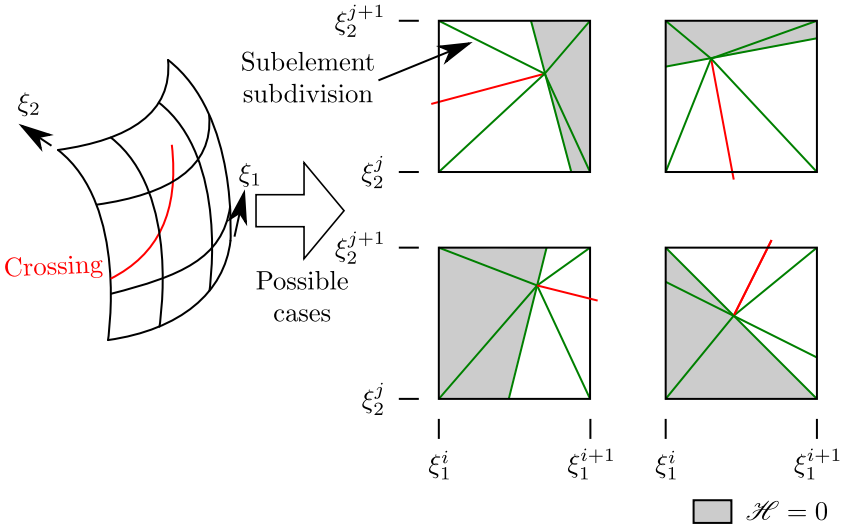

Source: The author.

Figure 35 – Subdivision for two different crack surfaces in the same knot-span.

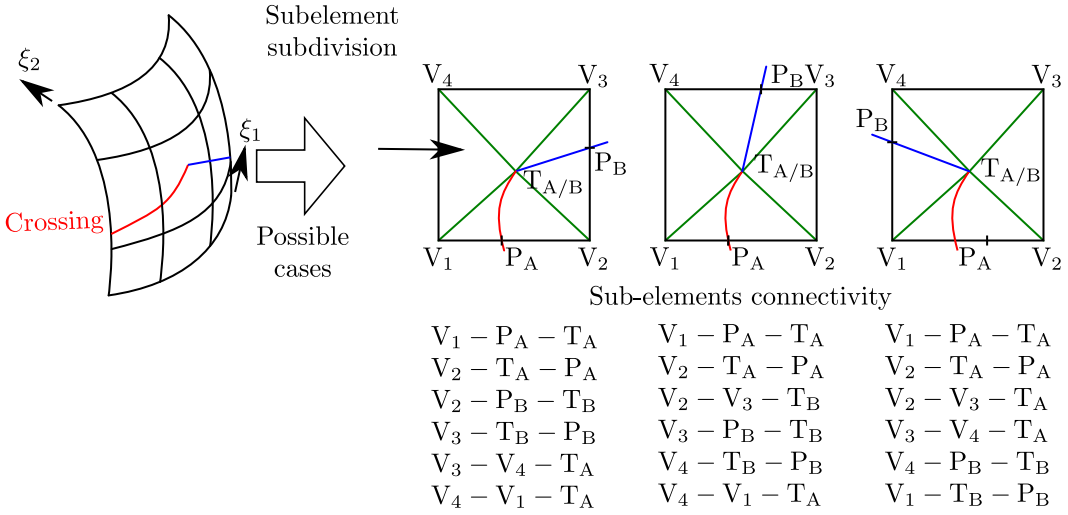

Sub-elements connectivity

$V_1 - P_A - T_A$	$V_1 - P_A - T_A$	$V_1 - P_A - T_A$
$V_2 - T_A - P_A$	$V_2 - T_A - P_A$	$V_2 - T_A - P_A$
$V_2 - P_B - T_B$	$V_2 - V_3 - T_B$	$V_2 - V_3 - T_A$
$V_3 - T_B - P_B$	$V_3 - P_B - T_B$	$V_3 - V_4 - T_A$
$V_3 - V_4 - T_A$	$V_4 - T_B - P_B$	$V_4 - P_B - T_B$
$V_4 - V_1 - T_A$	$V_4 - V_1 - T_A$	$V_1 - T_B - P_B$

Source: The author.

4.4 Numerical applications

This section presents three numerical applications in which the enrichment strategy captures strong discontinuities induced by cracks, eliminating the need for conformal meshes. The first application is a cube with an initial notch and subjected to rigid body motion in each portion. Next, the second numerical example addresses the mechanical analysis of a cylinder with an initial crack, in which the isogeometric formulation exactly represents its geometry with degree 2 NURBS surfaces. Lastly, the numerical analysis of a cracked prism under tensile loading examines the accuracy of the XIGABEM for strong discontinuities within the context of fracture mechanics.

Figure 36 – Definition of auxiliary vectors for the calculation of $\mathscr{H}$.

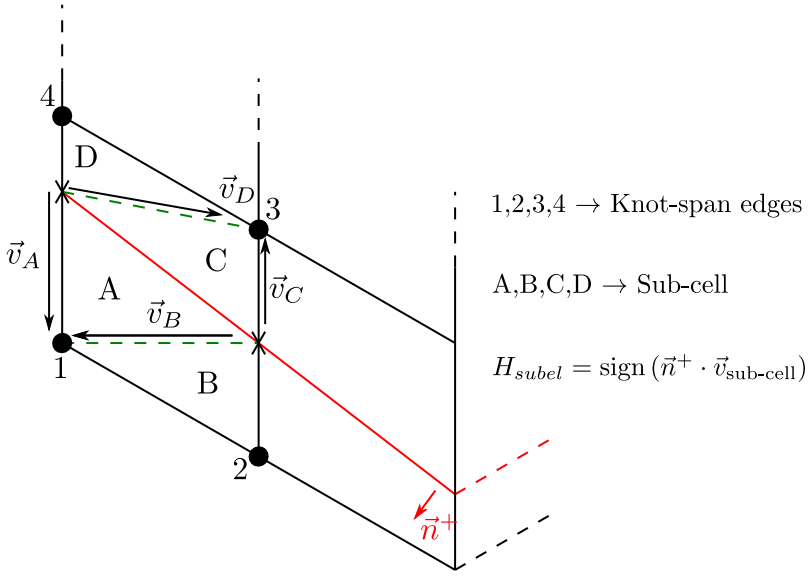

Source: The author.

4.4.1 Split test of notched cube

The first numerical application of the XIGABEM formulation for strong discontinuities consists of a cube with a side length of 10.0 (length units) and a notch, as illustrated in fig. 37. The boundary conditions are $u_1 = u_2 = u_3 = -1.0$ at the face with $x_3 = 0.0$ and $u_1 = u_2 = u_3 = 1.0$ at the face with $x_3 = 10.0$. These prescribed displacements induce rigid body motion in each portion of the cube, requiring the enrichment parameters to correctly model a displacement discontinuity along the crack. Since this is a simple mechanical case, it allows the analysis of different crack configurations and their effects on numerical integration and precision of the response. The crack angle varies from 0.0° to 30.0° in increments of 10.0°, and its centre of rotation is at $x_3 = 6.0$. The material properties are $E = 1000.0$ and $\nu = 0.0$.

The isogeometric discretisation adopts three meshes, in which 6 NURBS surfaces of degree 1 define the external faces of the cube and 2 NURBS surfaces of degree 2 model the crack surfaces. Figure 38 illustrates the collocation points placement for meshes A, B and C, in which Mesh A is the coarsest, mesh B has intermediate refinement level and mesh C is the finest one. The number of collocation points for each mesh is 126, 222, and 686, respectively, regardless of the crack angle, as the discontinuity and external meshes remain decoupled in the XIGABEM approach. In this application, the strategy for the additional equations is the minimisation of the relative displacement between the crack and the external boundary.

This application analyses the influence of different crack angles on the formulation's ability to represent the displacement jump at the external boundary. In this context, Figure 39 illustrates the intersection between the knot spans and the crack, which tests all possible sub-cells. In addition, fig. 40 illustrates the deformed configuration for each crack angle. The results indicate agreement between the numerical and theoretical responses, regardless of the angle. It is emphasised that the discontinuity lies across the central part of the patch, so that some

Figure 37 – Geometry and boundary conditions of notched cube under split test.

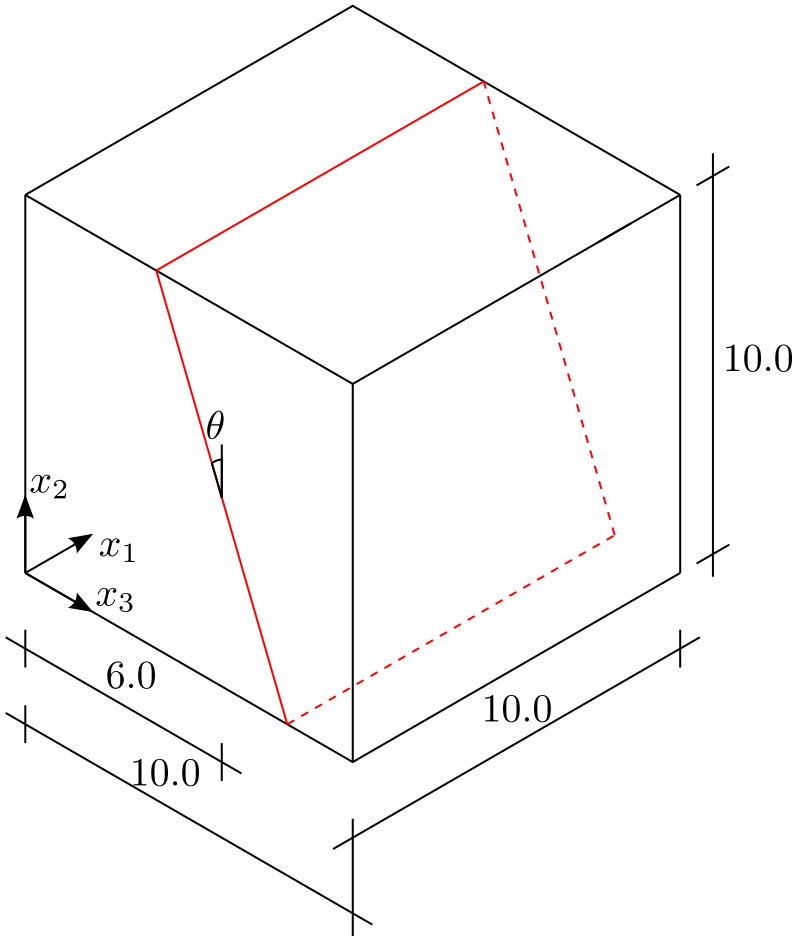

Source: The author.

Figure 38 – Position of collocation points for meshes A, B and C of the notched cube.

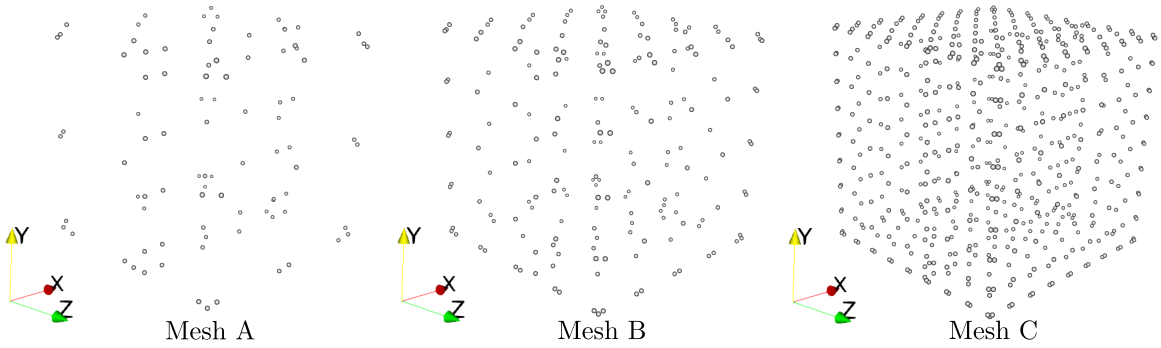

Source: The author.

elements are split into two parts in the deformed geometry. The plane of the discontinuity is not represented in the meshing, but is entirely produced using the Heaviside enrichment.

The relative L_2 norm of error in displacements allows the analysis of the numerical response quality in this application since it has an analytical solution. Figure 41 presents this error measurement for all meshes and angles examined in terms of the relative L_2 norm of

displacements. All errors remain below 10^{-6} for Mesh A, indicating a suitable response even for a coarse mesh. Meshes B and C exhibit errors similar to Mesh A, further attesting to the formulation's accuracy in this application. Another notable aspect is the error behaviour when the angle varies in the same mesh. This occurs due to variations in sub-cell shapes and their distortion depending on the cut. Nevertheless, this variation does not affect the overall response quality, attesting to the success of the strong discontinuity insertion in the XIGABEM approach in capturing the split in this application.

Figure 39 – Crack position in each surface with $x_1 = 0.0$ and $x_1 = 10.0$.

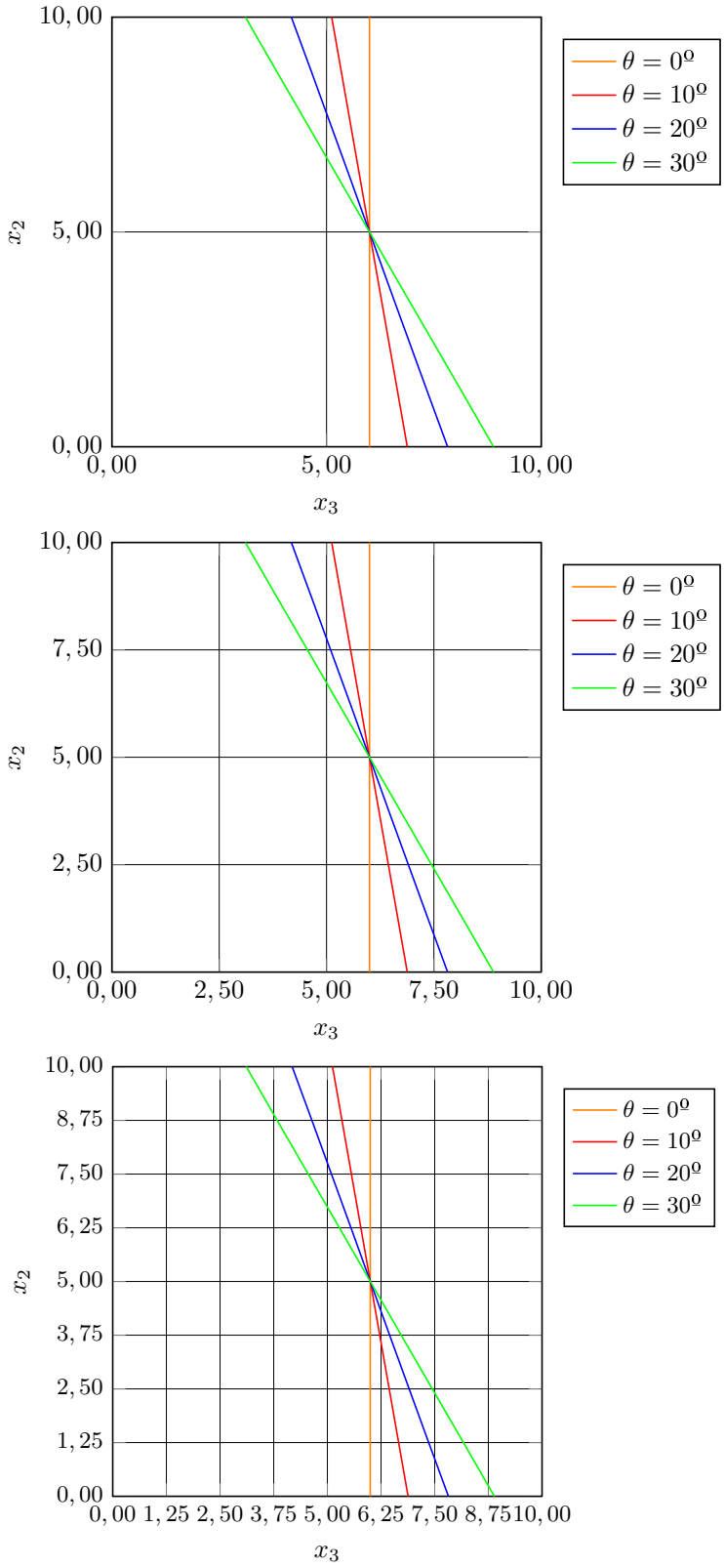

Source: The author.

Figure 40 – Deformed configuration of notched cube under split test: mesh C.

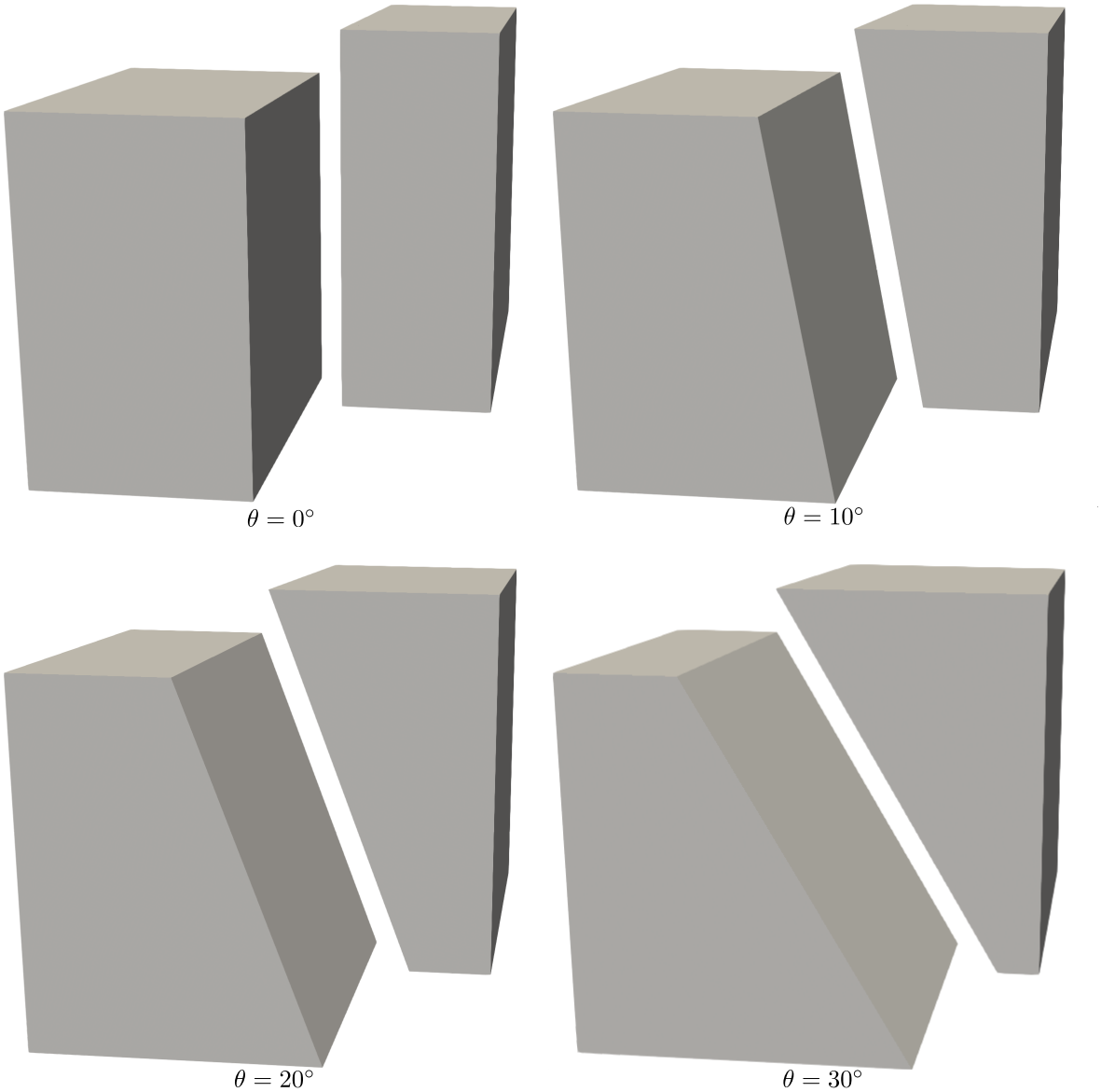

Source: The author.

Figure 41 – Relative L_2 norm of error in displacements for split test in notched cube.

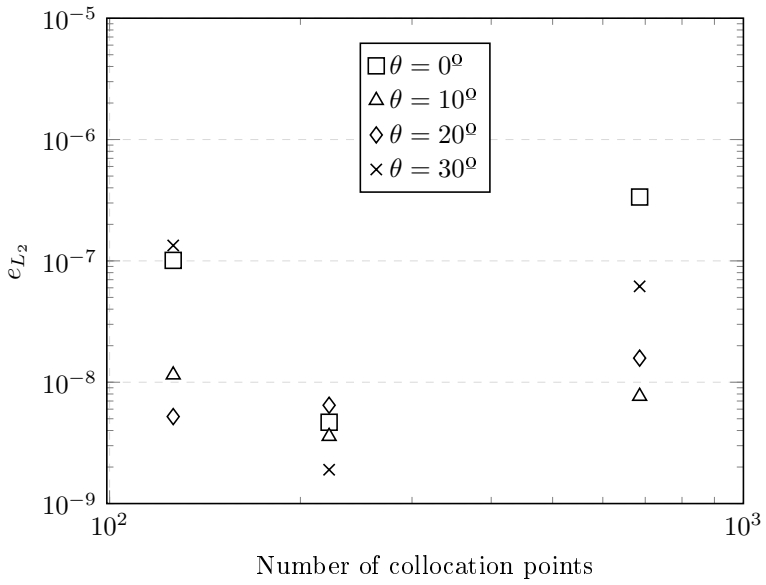

Source: The author.

4.4.2 Split test of a cracked cylinder

The second application of the XIGABEM formulation for strong discontinuities involves a split test of a cracked cylinder with radius $R = 10.0$, height $H = 10.0$ and a circular crack at $x_3 = 1.1$, as shown in fig. 42. The advantage of using an isogeometric description lies in its exact representation of the cylinder via a simple degree-two NURBS surface, in contrast to the impossibility of the Lagrangian description in performing this role in an exact manner. The boundary conditions inducing the split between the portions are $u_1 = u_2 = u_3 = 1.0$ at the upper face ($x_3 = 5.0$) and $u_1 = u_2 = u_3 = -1.0$ at the lower face ($x_3 = -5.0$). The material properties are $E = 1000.0$ and $\nu = 0.0$ for the Young Modulus and Poisson ratio, respectively.

Figure 42 – Geometry of cracked cylinder under split test.

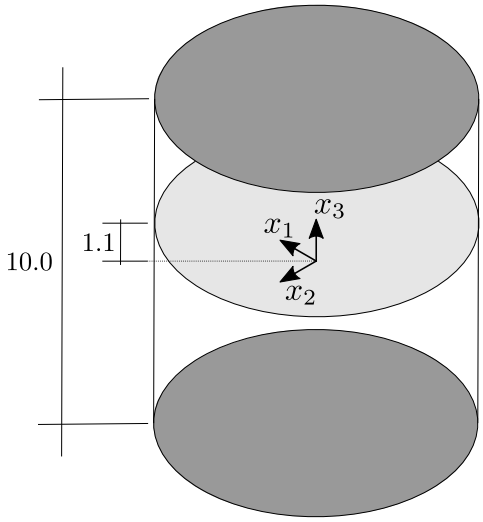

Source: The author.

The isogeometric discretisation utilises a mesh with a total of 24 NURBS surfaces, as depicted in fig. 43a. Each circular face has 5 NURBS surfaces with degree 2 in both parametric directions. The modelling of the lateral parts of the cylinder use four NURBS surfaces of degree 1 in the longitudinal and degree 2 in the circumferential directions. This parametrisation leads to a XIGABEM model with 236 collocation points, whose placement is illustrated in fig. 43b.

The deformed shape presented in fig. 44 demonstrates that the XIGABEM formulation successfully captures the split between portions using the enrichment strategy through the use of TBIE as supplementary equations. In addition, section 4.4.2 contains the relative L_2 norm of error in displacements for this application and the condition number for both strategies used to recover the square system. In both scenarios the error is less than 2×10^{-8}, which attests to the formulation's robustness in addressing a cut curved NURBS surface. Furthermore, the condition number comparison indicates that the choice of strategy does not significantly alter its effects on the algebraic system. Thus, both strategies emerge as viable alternatives to resolve the rank deficient system issue initially generated by the enrichment approach.

Figure 43 – Isogeometric discretisation and placement of collocation points for split test in cracked cylinder.

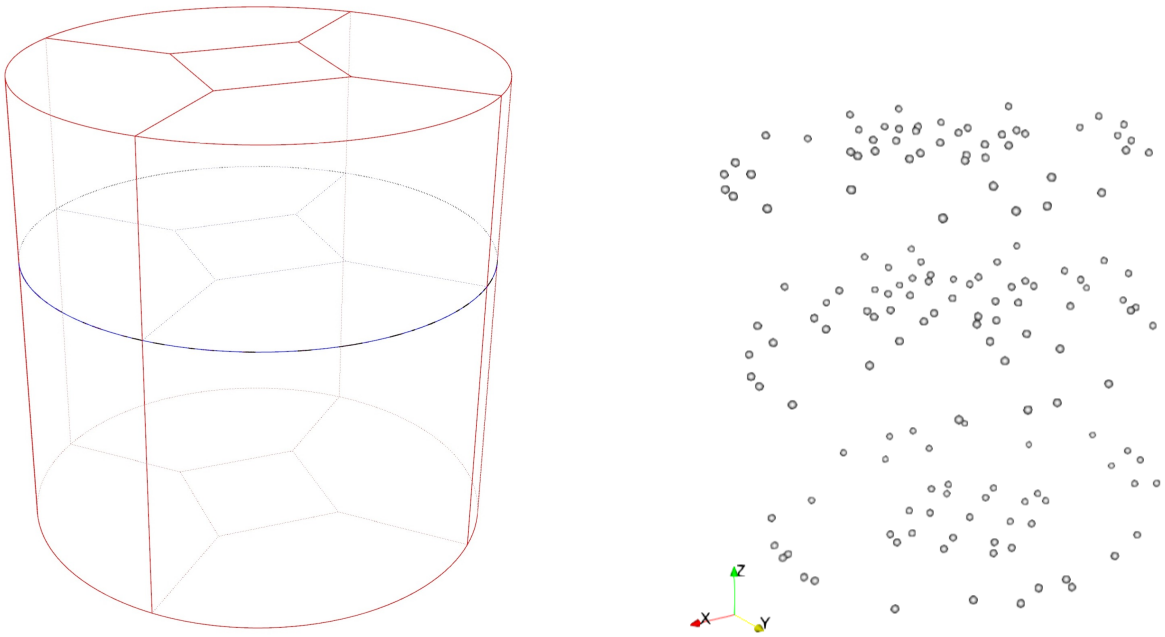

(a) (b)

Source: The author.

Table 3 – Comparison between the relative L_2 norm of error in displacements and condition number for each strategy of supplementary equations in the split test of a cracked cylinder.

Strategy	$\|\|e\|\|_{L_2}$	Condition Number
TBIE collocation points	$1.47\text{x}10^{-8}$	$1.15\text{x}10^{9}$
Weak form compatibility	$1.37\text{x}10^{-8}$	$4.43\text{x}10^{9}$

Figure 44 – Deformed shape of cracked cylinder under split test.

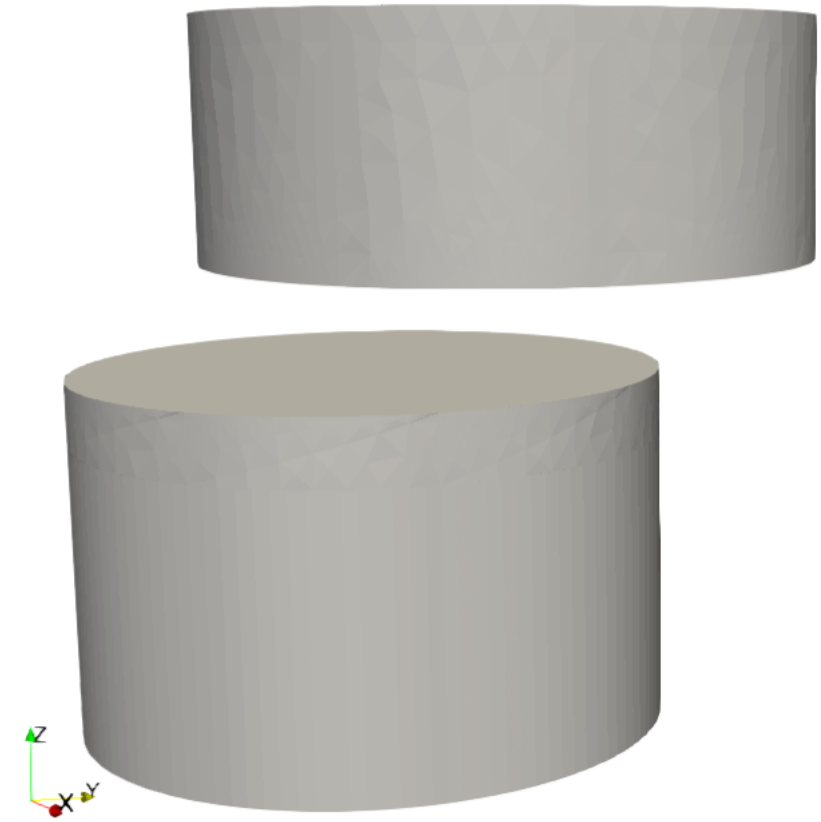

Source: The author.

4.4.3 Prism with initial crack

The third application of the XIGABEM for strong discontinuities, which eliminates the re-meshing task, consists of a cracked prism subjected to a uniform traction $p_3 = 1.0$ and $p_3 = -1.0$ at the upper and lower faces, respectively. The prescribed displacements at the centre of the back face ($x_1 = 10.0$, $0.0 \leq x_2 \leq 10.0$, $9.0 \leq x_3 \leq 11.0$) prevent rigid body motion by enforcing $u_1 = u_2 = u_3 = 0.0$. Figure 45 depicts its geometry and boundary conditions, where the crack angle takes four different values in this analysis: $\theta = 0.0°$, $\theta = 15.0°$, $\theta = 30.0°$, and $\theta = 45.0°$. These inclinations necessitate an essentially three-dimensional formulation for determining its mechanical fields. In addition, the material properties are $E = 100.0$ and $\nu = 0.0$ for the Young modulus and the Poisson ratio.

Figure 45 – Geometry and boundary conditions of prism with initial crack.

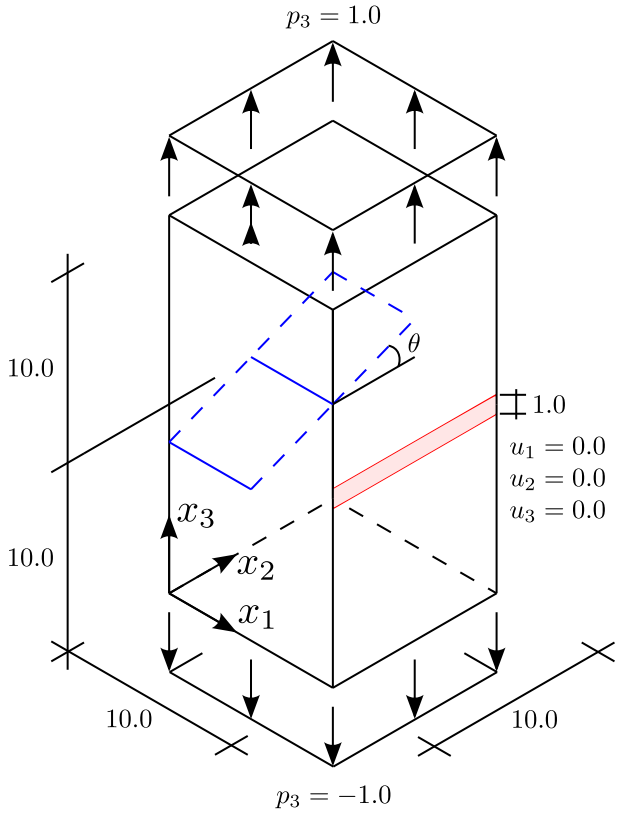

Source: The author.

The reference solution is a standard IGABEM numerical analysis based on a discretisation with 15 NURBS surfaces, as illustrated in fig. 46 for $\theta = 0.0°$. The crack surfaces have degree 2 in both parametric directions, whereas all other faces use NURBS surfaces of degree 1. Notably, the standard IGABEM modelling requires conformal meshing for all intersected faces, which is required for all angles under study. Additionally, this analysis uses three different meshes for each crack angle, where meshes A, B, and C correspond to the coarsest, intermediate, and finest meshes, respectively. Table 4 presents the number of collocation points for each mesh and each crack angle. Furthermore, fig. 47 illustrates the knot spans of Mesh C for each inclination, where a slight distortion occurs in the knot spans of the frontal face.

Figure 46 – Isogeometric discretisation for prism with initial crack using the standard IGABEM.

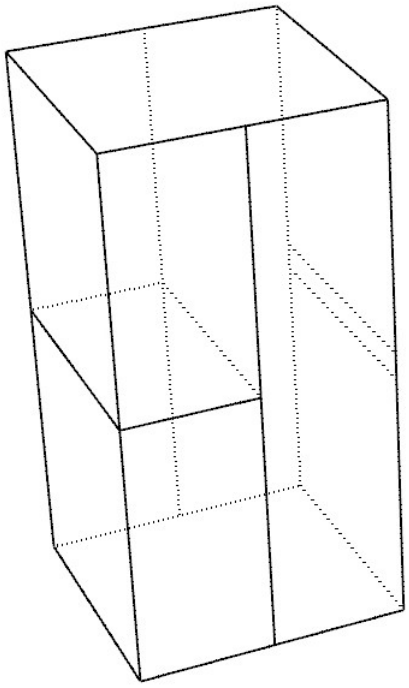

Source: The author.

Table 4 – Number of collocation points for each reference mesh of prism with initial crack.

Angle	Mesh A	Mesh B	Mesh C
$\theta = 0°$	363	1121	3351
$\theta = 15°$	375	1007	3351
$\theta = 30°$	375	1007	3351
$\theta = 45°$	375	1121	3885

Source: The author.

The XIGABEM model uses 10 NURBS surfaces for the numerical modelling, where 8 surfaces represent the external boundary and are degree 1 in both parametric directions, while the crack surfaces have degree 2. Figure 48 depicts the discretisation for this XIGABEM model. The external boundary does not vary with the crack inclination, as the enrichment strategy removes the need for mesh alignment. The XIGABEM formulation enforces displacement expansion at the lateral faces ($x_2 = 0.0$ and $x_2 = 10.0$), as well as at the front face ($x_1 = 0.0$). In this context, meshes A, B, and C have 349, 869 and 3301 collocation points, respectively. The placement of these points for $\theta = 30°$ is illustrated in fig. 49. Notably, the XIGABEM approach is superior to the standard IGABEM counterpart in this analysis, as it only requires a single discretisation of the external boundary regardless of the crack angle.

Figure 50 illustrates the total displacement field for both the reference and the enriched models magnified by 5 times, for all inclination angles in Mesh C. This comparison confirms

Figure 47 – Knot spans reference model (mesh C) for prism with initial crack.

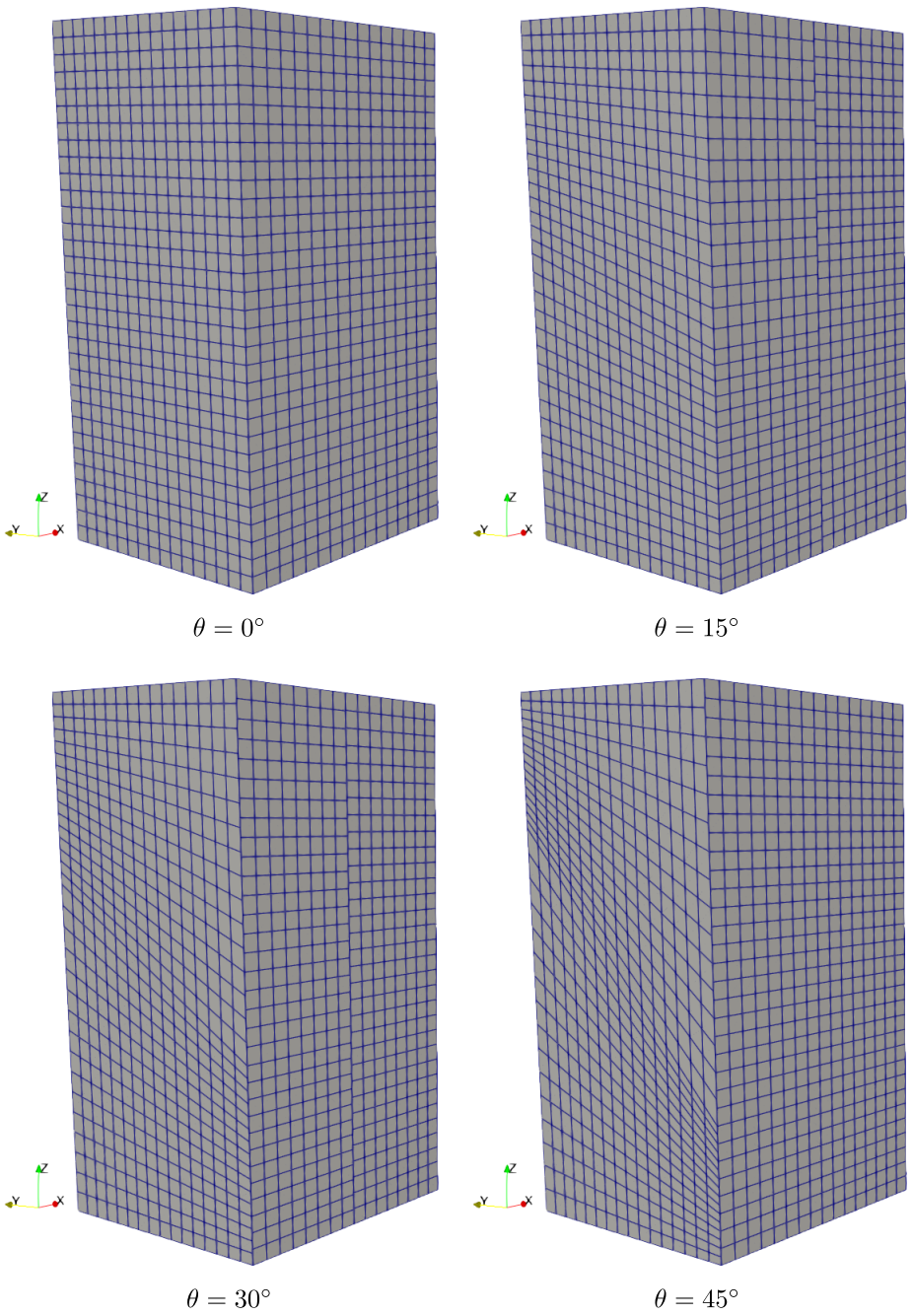

Source: The author.

the expected mechanical behaviour of the XIGABEM formulation, while the introduction of the Heaviside function in three different faces results in the displacement jump induced by the crack. In addition, the displacement values are consistent, corroborating the robustness of XIGABEM.

The strain energy comparison illustrated in fig. 51 allows the assessment of the accuracy of XIGABEM in this application. In this case, the strain energy is equal to the external work done at the upper and lower faces of the prism. Each enriched model yields values similar to its equivalent IGABEM model, with a relative difference of approximately 10^{-3} for Mesh C. The XIGABEM approach achieves results comparable to the standard IGABEM while using fewer

Figure 48 – Isogeometric discretisation for prism with initial crack using the XIGABEM for strong discontinuities.

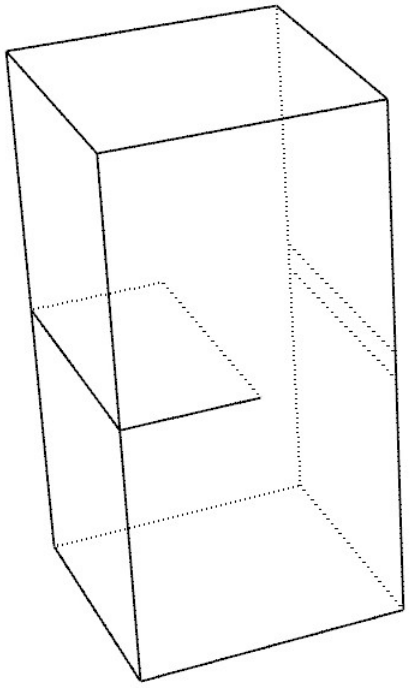

Source: The author.

collocation points, which is another advantage of this formulation, in addition to eliminating the need for mesh alignment.

Figure 49 – Placement of collocation points of prism with initial crack for the XIGABEM analysis.

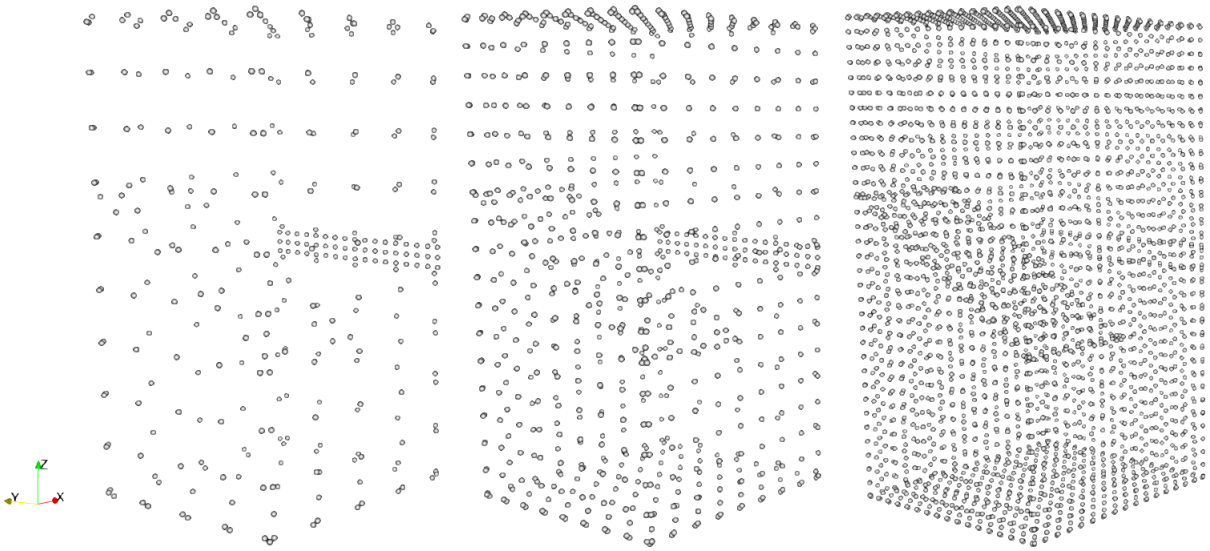

Mesh A Mesh B Mesh C

Source: The author.

Figure 50 – Deformed shape of prism with initial crack: standard IGABEM vs XIGABEM.

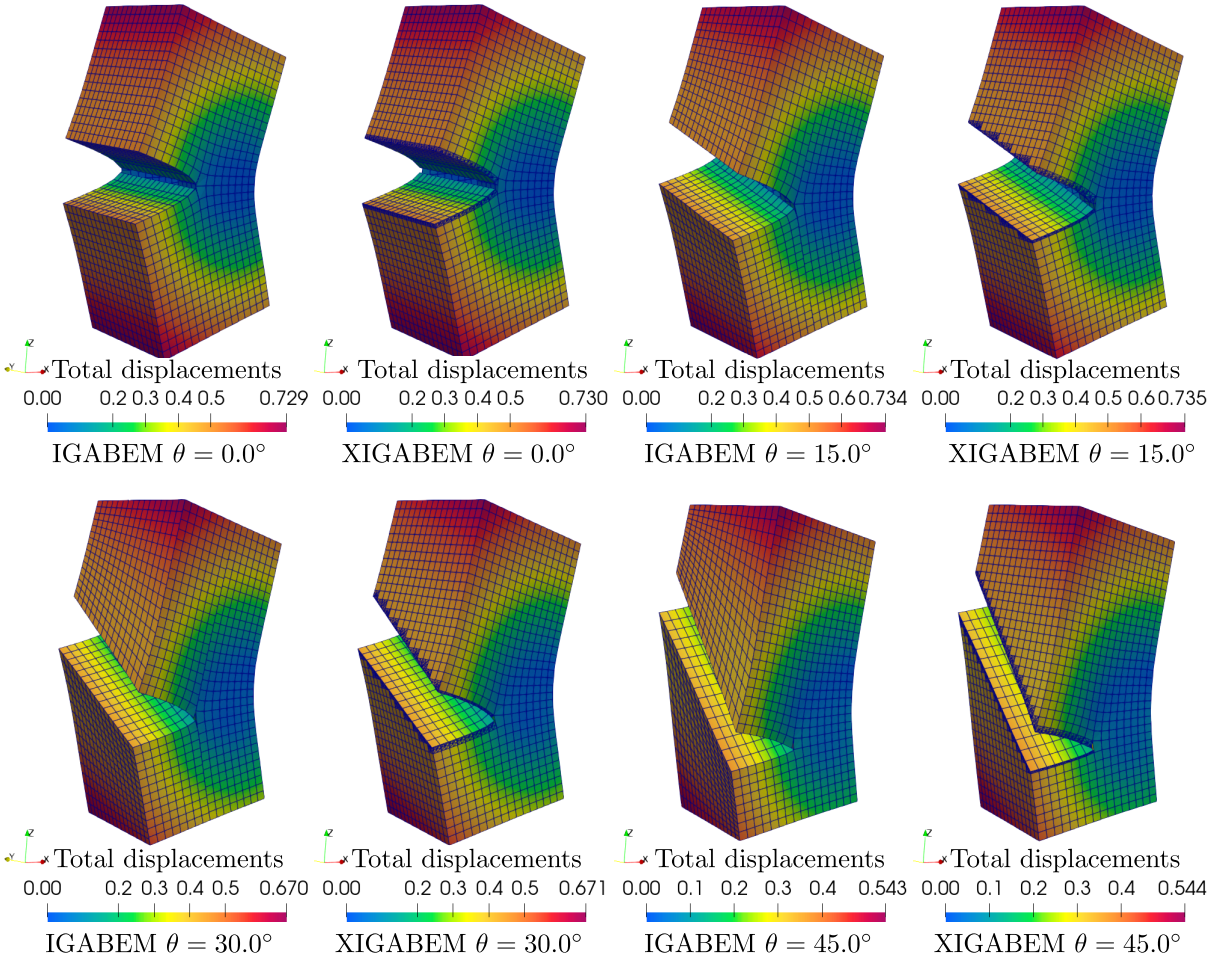

Source: The author.

Figure 51 – Strain energy comparison between the XIGABEM and the IGABEM models.

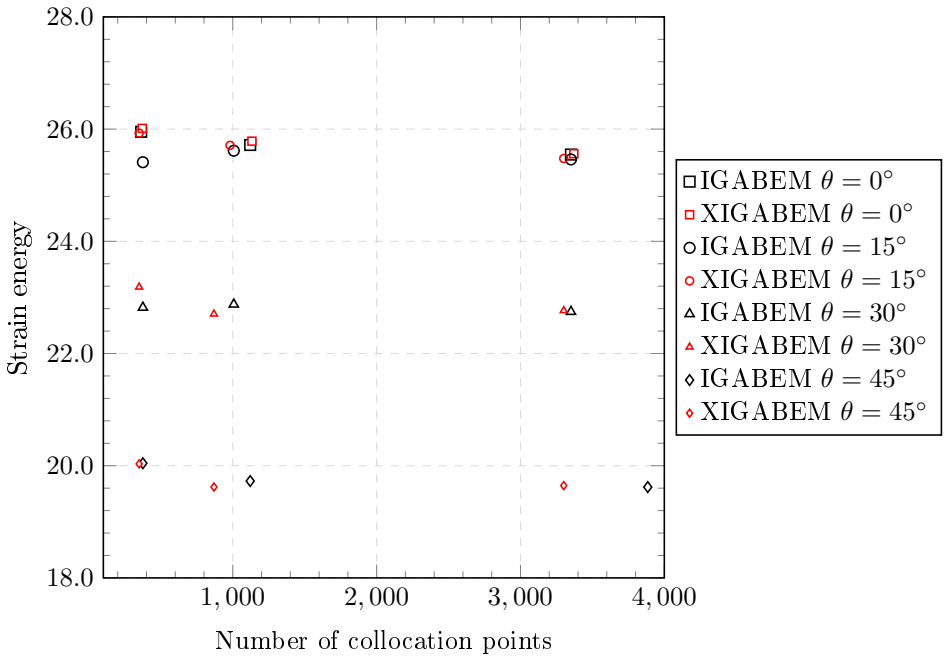

Source: The author.

4.5 Partial conclusions

The first enrichment proposition of this thesis consists of the Heaviside enrichment presented in this chapter. Its main purpose is to represent the discontinuous displacement at the crossing between the external boundary and cracks. Consequently, this enrichment eliminates the need for mesh alignment at the intersection, which allows the direct use of the original CAD model in the fracture analysis. The displacement approximation of surfaces intersected by cracks receives an enrichment term with the Heaviside function. The shifted enrichment removes blending elements and does not introduce SST treatment for the arising kernels. In this context, the enrichment approach introduces additional parameters to quantify the displacement jump along the intersected surface. As a consequence, the addition of unknowns requires new equations to recover a square system. This study proposes two different strategies for this task. The first scheme consists of a minimisation of the relative displacement between the intersected surface and the crack surface, measured in terms of an L_2 error. The second strategy uses the Traction Boundary Integral Equation at the same position as the collocation points whose basis functions were enriched. Several implementation aspects are important for the success of the incorporation of this enrichment scheme into existing IGABEM codes. Particularly, the detection of the intersection between the crack and the external boundary is necessary to define the sub-regions in which the Heaviside function assumes different values. The numerical integration of these sub-cells considers a polar strategy previously used for trimmed knot spans. Numerical results demonstrate the ability of the Heaviside enrichment function for representing the displacement discontinuity induced by the crack, while reducing the number of degrees of freedom. In this context, the XIGABEM formulation successfully eliminates the need of conformal meshes in the numerical analysis of three-dimensional cracked solids.

5 WILLIAMS SOLUTION-BASED ENRICHMENT STRATEGIES

The enrichment strategy using the Heaviside function from chapter 4 successfully introduces displacement discontinuities at the external boundary when intersected by cracks. However, An asymptotic behaviour occurs near the crack front that neither the standard IGABEM nor the XIGABEM with the Heaviside enrichment can represent. To address this limitation, this chapter proposes incorporating the first term of the Williams solution expansion as an enrichment function for the displacement field. This strategy enables accurate capture of the $\sqrt{r_t}$ asymptotic behaviour induced by cracks (being r_t the distance between the point and the crack tip), which is consistent with LEFM. In addition, this enrichment introduces the displacement jump on faces on the external boundary that are crossed by cracks. In addition, it enables the direct extraction of the SIFs when applied to crack surfaces.

This chapter begins with the displacement expansion based on Williams solution for faces in the external boundary that are crossed by cracks, its effects on the algebraic system, and the strategy for obtaining the supplementary equations. Subsequently, the approach for enriching crack surfaces is explained, as well as its impact on the BIEs and the strategy to restore a well-posed algebraic system. Since the IGABEM requires the treatment of the singular integrals, the next section presents the regularisation of the enriched kernels using the SST. Additionally, the Frenet-Serret frame (Frenet, 1852; Serret, 1851) defines the rotation matrix and its derivatives in the isogeometric framework. Four numerical applications demonstrate the robustness and accuracy of this proposition, achieving higher convergence rates while requiring fewer collocation points compared to the BEM and the standard IGABEM.

5.1 Lateral face enrichment for $\sqrt{r_t}$ behaviour on intersected surfaces

Edge cracks present an enormous challenge for boundary-based methods, because of the requirement of aligned meshes between the external boundary and crack surfaces. In addition, the displacements over the crack surface exhibit a classical $\sqrt{r_t}$ behaviour found in LEFM, with r being the distance from the crack front. Standard NURBS basis functions and the Heaviside enrichment cannot precisely capture this for the external boundary partially cut by the crack, which leads to a sub-optimal convergence. In this context, this study proposes a displacement field enrichment for partially cut surfaces based on the leading order term of the Williams expansion (Williams, 1957). This expansion leads to the augmented displacement field as:

$$u_k^{\gamma^{\mathscr{T}}}(\xi_1,\xi_2) = \sum_{\alpha=1}^{n^\gamma} \phi_\alpha^\gamma(\xi_1,\xi_2) d_k^\beta + \sum_{\alpha=1}^{n^\gamma} \phi_\alpha^\gamma(\xi_1,\xi_2) R_{kq} \psi_{qM}^\gamma \hat{d}_M^\beta \tag{5.1}$$

in which the additional unknowns $\hat{d}_M^\beta$ represent the magnitudes related to the enrichment function ψ_{qM}^γ. R_{kq} is a rotation matrix from the local coordinate system at the crack front, where ψ_{qM}^γ is defined, to the global coordinate system, according to fig. 52. The Williams-based enrichment function, ψ_{qM}^γ, is:

Figure 52 – Local coordinate system at the crossing between crack and external face.

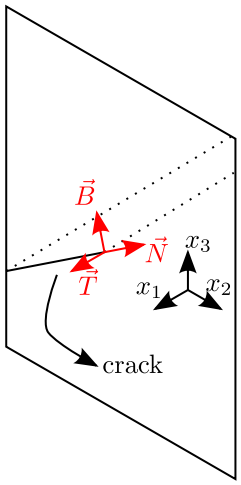

Source: The author.

$$
\begin{aligned}
\psi_{qM} &= \begin{bmatrix} \psi_{nI} & \psi_{nII} & \psi_{nIII} \\ \psi_{bI} & \psi_{bII} & \psi_{bIII} \\ \psi_{tI} & \psi_{tII} & \psi_{tIII} \end{bmatrix} \\
\psi_{nI} &= \frac{1}{2\mu}\sqrt{\frac{r_t}{2\pi}}\cos\left(\frac{\theta_t}{2}\right)\left[\kappa - 1 + 2\sin^2\left(\frac{\theta_t}{2}\right)\right] \\
\psi_{nII} &= \frac{1}{2\mu}\sqrt{\frac{r_t}{2\pi}}\sin\left(\frac{\theta_t}{2}\right)\left[\kappa + 1 + 2\cos^2\left(\frac{\theta_t}{2}\right)\right] \\
\psi_{bI} &= \frac{1}{2\mu}\sqrt{\frac{r_t}{2\pi}}\sin\left(\frac{\theta_t}{2}\right)\left[\kappa + 1 - 2\cos^2\left(\frac{\theta_t}{2}\right)\right] \\
\psi_{bII} &= -\frac{1}{2\mu}\sqrt{\frac{r_t}{2\pi}}\cos\left(\frac{\theta_t}{2}\right)\left[\kappa - 1 - 2\sin^2\left(\frac{\theta_t}{2}\right)\right] \\
\psi_{tIII} &= \frac{1}{2\mu}\sqrt{\frac{r_t}{2\pi}}4\sin\left(\frac{\theta_t}{2}\right) \\
\psi_{tI} &= \psi_{tII} = \psi_{nIII} = \psi_{bIII} = 0
\end{aligned}
\tag{5.2}
$$

in which r_t is the distance to the crack tip, θ_t is the angle between the tangent vector in the local coordinate system and the vector $\mathbf{r_t}$, as defined using the Frenet-Serret frame (Kühnel, 2015). κ is the Kolosov constant, being $\kappa = 3 - 4\nu$ for plane-strain and $\kappa = \frac{3-\nu}{1+\nu}$ for plane-stress, and $\mu = \frac{E}{2(1+\nu)}$ is the shear modulus. This proposition is similar to the Oden-Duarte (Duarte; Babuška; Oden, 2000; Oden; Duarte, 1996) enrichment, but with the major difference that here all enrichment functions are combined based on the rotation matrix to become a single function multiplying each additional unknown.

In this study a Williams-based enrichment is applied to NURBS basis functions on the partially cut surface, which justifies the use of ϕ_α^γ on both standard and enriched terms of the eq. (5.1). Then, the substitution of the expanded displacements in eq. (5.1) on the BIEs results in a similar equation to that in the standard IGABEM, eq. (2.32), but with an additional kernel, as:

$$
\begin{aligned}
c_{\ell k}(\hat{\mathbf{x}}) \sum_{\alpha=1}^{n^\gamma} \phi_\alpha^{\hat{\gamma}}(\hat{\mathbf{x}}) d_k^\beta + c_{\ell k}(\hat{\mathbf{x}}) \sum_{\alpha=1}^{n^\gamma} \phi_\alpha^{\hat{\gamma}}(\hat{\mathbf{x}}) R_{kq}(\hat{\mathbf{x}}) \psi_{qM}^\gamma(\hat{\mathbf{x}}) \hat{d}_M^\beta \\
+ \sum_{\gamma=1}^{NS} \underline{\mathrm{T}}_{\ell k}^{*\alpha\gamma} d_k^\beta + \sum_{\gamma=1}^{NS} \underline{\mathrm{T}}_{\mathrm{t}\ell M}^{\alpha\gamma} \hat{d}_M^\beta = \sum_{\gamma=1}^{NS} \underline{\mathrm{U}}_{\ell k}^{*\alpha\gamma} p_k^\beta \\
\frac{1}{2} \sum_{\alpha=1}^{n^\gamma} \phi_\alpha^{\hat{\gamma}}(\hat{\mathbf{x}}) p_j^\beta + \frac{1}{2} \sum_{\alpha=1}^{n^\gamma} \phi_\alpha^{\hat{\gamma}}(\hat{\mathbf{x}}) R_{jq}(\hat{\mathbf{x}}) \psi_{qM}^\gamma(\hat{\mathbf{x}}) \hat{p}_M^\beta \\
+ n_\ell(\hat{\mathbf{x}}) \sum_{\gamma=1}^{NS} \underline{\mathrm{S}}_{k\ell j}^{\alpha\gamma} d_k^\beta + n_\ell(\hat{\mathbf{x}}) \sum_{\gamma=1}^{NS} \underline{\mathrm{S}}_{\mathrm{t}M\ell j}^{*\alpha\gamma} \hat{d}_M^\beta = n_\ell(\hat{\mathbf{x}}) \sum_{\gamma=1}^{NS} \underline{\mathrm{D}}_{k\ell j}^{*\alpha\gamma} p_k^\beta
\end{aligned}
\tag{5.3}
$$

in which $\underline{\mathrm{T}}_{\mathrm{t}\ell k}^{\alpha\gamma}$ and $\underline{\mathrm{S}}_{\mathrm{t}k\ell j}^{*\alpha\gamma}$ are new kernels originated from the Williams-based enrichment, being:

$$
\begin{aligned}
\underline{\mathrm{T}}_{\mathrm{t}\ell M}^{\alpha\gamma} &= \sum_{\mathrm{ks}=1}^{n_{\mathrm{ks}}^\gamma} \sum_{\alpha=1}^{n^\gamma} \int_\Lambda T_{\ell k}^* \phi_\alpha^\gamma R_{kq} \psi_{qM}^\gamma \, J_\gamma^{\mathrm{ks}} \, d\Lambda \\
\underline{\mathrm{S}}_{\mathrm{t}M\ell j}^{*\alpha\gamma} &= \sum_{\mathrm{ks}=1}^{n_{\mathrm{ks}}^\gamma} \sum_{\alpha=1}^{n^\gamma} \int_\Lambda S_{k\ell j}^* \phi_\alpha^\gamma R_{kq} \psi_{qM}^\gamma \, J_\gamma^{\mathrm{ks}} \, d\Lambda
\end{aligned}
\tag{5.4}
$$

Analogously to the Heaviside enrichment, the Williams-based expansion of the displacements does not change the standard IGABEM coefficients, which are retained in the BEM matrices, while introducing additional parameters to the discretisation. Thus, it shares the capability of being directly incorporated into existing IGABEM computational codes. Additional equations are necessary due to the addition of new unknowns, similarly to the Heaviside enrichment, and this applies the TBIE on the collocation points associated with the enriched basis functions. Another similarity comes from the discontinuous nature of the term $\sin\frac{\theta}{2}$, requiring integration over a cell-based subdivision, as detailed in section 4.3. In this context, the matrix form of the XIGABEM algebraic system with the Williams enrichment for partially cut faces is similar to the XIGABEM with strong discontinuities in the displacement field (eq. (4.9)) as:

$$
\begin{bmatrix} \mathbf{H} & \mathbf{H}_{\mathrm{t}} \\ \mathbf{H}^{\mathrm{T}} & \mathbf{H}_{\mathrm{t}}^{\mathrm{T}} \end{bmatrix} \left\{ \begin{array}{c} \mathbf{d} \\ \hat{\mathbf{d}} \end{array} \right\} = \begin{bmatrix} \mathbf{G} \\ \mathbf{G}^{\mathrm{T}} \end{bmatrix} \left\{ \begin{array}{c} \mathbf{p} \end{array} \right\}
\tag{5.5}
$$

in which the new matrices $\mathbf{H}^{\mathrm{T}}$, $\mathbf{H}_{\mathrm{t}}^{\mathrm{T}}$, and $\mathbf{G}^{\mathrm{T}}$ correspond to the influence coefficients arising from the application of the TBIE on the collocation points associated with the enriched basis functions. The vector $\hat{\mathbf{d}}$ stores the additional enrichment parameters.

In this study, the main focus is the first development of the extended IGABEM for 3D fracture mechanics and the calculation of SIFs from the crack front enrichment depicted in section 5.2. A simple unshifted Williams enrichment is applied on the partially crossed faces. Since the shifting approach has not been applied for the Williams solution enrichment, singularities arise and they must be treated accordingly by using the SST, as detailed in section 5.3. Then, derivatives of both ψ_{qM} and R_{kq} are required with respect to the parent coordinate space, where integration is carried out.

5.2 Crack front enrichment for the direct SIF extraction

The enrichment strategy for the introduction of SIFs as additional unknowns consists of using the Williams-based enrichment function (eq. (5.2)) on the crack surfaces. In addition, these parameters are interpolated by uni-directional NURBS basis functions over the crack front, which leads to the following enriched displacement field for the crack surface:

$$u_k^{\gamma^{+/-}}(\xi_1,\xi_2) = \sum_{\alpha=1}^{n^\gamma} \phi_\alpha^{\gamma^{+/-}}(\xi_1,\xi_2) d_k^\beta + \sum_{s=1}^{n_K^\gamma} \tilde{\phi}_s^{\mathrm{cf}}(t) R_{kq}^{\mathrm{cf}} \psi_{qM}^{\bar{\gamma}^{\mathrm{cf}}} \tilde{K}_M^{s\,\mathrm{cf}} \tag{5.6}$$

in which $\tilde{\phi}_s^{\mathrm{cf}}(t)$ is the uni-directional NURBS basis functions over the crack front cf that interpolates the SIFs coefficients $\tilde{K}_M^{s\,\mathrm{cf}}$. This set of basis functions comes from the corresponding univariate NURBS curve in the crack front that generates the crack surface $\gamma^{+/-}$. Thus, each crack front introduces n_K^γ additional unknowns related to the distribution of SIFs along the front. The incorporation of eq. (5.6) in the BIEs yields to:

$$\begin{aligned} &c_{\ell k}(\hat{\mathbf{x}}) \sum_{\alpha=1}^{n^\gamma} \phi_\alpha^{\hat{\gamma}}(\hat{\mathbf{x}}) d_k^\beta + c_{\ell k}(\hat{\mathbf{x}}) \sum_{s=1}^{n_K^\gamma} \tilde{\phi}_s^{\mathrm{cf}}(t(\hat{\mathbf{x}})) R_{kq}^{\mathrm{cf}}(\hat{\mathbf{x}}) \psi_{qM}^{\bar{\gamma}^{\mathrm{cf}}}(\hat{\mathbf{x}}) \tilde{K}_M^{s\,\mathrm{cf}} \\ &\quad + \sum_{\gamma=1}^{NS} \underline{\mathrm{T}}_{\ell k}^{*\alpha\gamma} d_k^\beta + \sum_{\gamma=1}^{NS} \underline{\mathrm{T}}_{\mathrm{s}\ell M}^{s\,\mathrm{cf}} \tilde{K}_M^{s\,\mathrm{cf}} = \sum_{\gamma=1}^{NS} \underline{\mathrm{U}}_{\ell k}^{*\,\alpha\gamma} p_k^\beta \\ &\frac{1}{2} \sum_{\alpha=1}^{n^\gamma} \phi_\alpha^{\hat{\gamma}}(\hat{\mathbf{x}}) p_j^\beta + \frac{1}{2} \sum_{s=1}^{n_K^\gamma} \tilde{\phi}_s^{\mathrm{cf}}(t(\hat{\mathbf{x}})) R_{jq}^{\mathrm{cf}}(\hat{\mathbf{x}}) \psi_{qM}^{\bar{\gamma}^{\mathrm{cf}}}(\hat{\mathbf{x}}) \tilde{K}_M^{s\,\mathrm{cf}} \\ &+ n_\ell(\hat{\mathbf{x}}) \sum_{\gamma=1}^{NS} \underline{\mathrm{S}}_{k\ell j}^{*\alpha\gamma} d_k^\beta + n_\ell(\hat{\mathbf{x}}) \sum_{\gamma=1}^{NS} \underline{\mathrm{S}}_{\mathrm{s}M\ell j}^{s\,\mathrm{cf}} \tilde{K}_M^{s\,\mathrm{cf}} = n_\ell(\hat{\mathbf{x}}) \sum_{\gamma=1}^{NS} \underline{\mathrm{D}}_{k\ell j}^{*\,\alpha\gamma} p_k^\beta \end{aligned} \tag{5.7}$$

in which, analogously to both Heaviside and Williams-based enrichment, a new kernel arises in each BIE as:

$$\begin{aligned} \underline{\mathrm{T}}_{\mathrm{s}\ell M}^{s\,\mathrm{cf}} &= \sum_{\mathrm{ks}=1}^{n_{\mathrm{ks}}^{\gamma(\mathrm{cf})}} \sum_{s=1}^{n_K^\gamma} \int_\Lambda T_{\ell k}^* \tilde{\phi}_s^{\mathrm{cf}} R_{kq}^{\mathrm{cf}} \psi_{qM}^{\gamma(\mathrm{cf})} J_{\gamma(\mathrm{cf})}^{\mathrm{ks}} \, d\Lambda \\ \underline{\mathrm{S}}_{\mathrm{s}M\ell j}^{s\,\mathrm{cf}} &= \sum_{\mathrm{ks}=1}^{n_{\mathrm{ks}}^{\gamma(\mathrm{cf})}} \sum_{s=1}^{n_K^\gamma} \int_\Lambda S_{k\ell j}^* \tilde{\phi}_s^{\mathrm{cf}} R_{kq}^{\mathrm{cf}} \psi_{qM}^{\gamma(\mathrm{cf})} J_{\gamma(\mathrm{cf})}^{\mathrm{ks}} \, d\Lambda \end{aligned} \tag{5.8}$$

This integration takes place at the enriched crack surface. The kernels make use of the uni-directional coordinate t for the crack front projection at each Gauss point, which is obtained by a point projection algorithm (Piegl; Tiller, 1996).

Special care must be taken in the rotation matrix definition. For a crack front, fig. 53 defines the local coordinate system of the Williams solution, which may change depending on the crack geometry. This thesis applies the Frenet-Serret frame (Frenet, 1852; Serret, 1851) to accurately determine both the rotation matrix and its derivatives based on the crack front NURBS parametrisation, as shown in section 5.4. For flat cracks, the rotation matrix is simplified

Figure 53 – Local coordinate system for crack front enrichment.

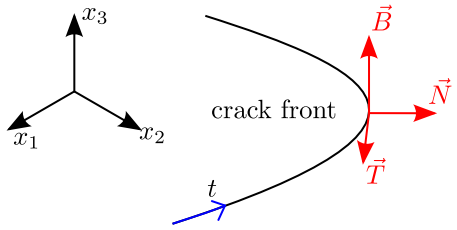

Source: The author.

by having $\vec{T}$ parallel to the crack front, $\vec{N}$ aligned to the normal outward vector of the upper crack surface (which receives the DBIE), with $\vec{B} = \vec{T} \times \vec{N}$.

Besides allowing a direct determination of the SIFs, and thereby precluding post-processing tasks, this strategy also introduces the $\sqrt{r_t}$ behaviour in the formulation, giving rise to accuracy improvements. The enrichment is applied over the entire crack surface, instead of solely at the portion closest to the crack front. Extending the enrichment over the whole crack surface gives rise to no additional degrees of freedom.

In this matter, it is worth mentioning the differences between the approach herein and the special crack tip element successfully proposed by Li, Mear and Xiao (1998) in the Symmetric Galerkin BEM approach. Their study proposed a different set of basis functions containing the $\sqrt{r_t}$ behaviour for the crack front elements, which culminates in a change in the construction of the H and G influence matrices. On the other hand, the present study allows the direct introduction of the SIF parameters without changes in the existing H and G matrices from IGABEM.

For the direct SIF enrichment scheme applied on the crack surfaces, the additional equations are obtained by considering displacement compatibility at the crack front taken by minimising a functional. This procedure is analogous to the first strategy for the supplementary equations in the Heaviside enrichment context (section 4.2). Both upper and lower crack faces are expected to experience identical displacement at the crack front. However, the discontinuous BEM approach for fracture mechanics cannot guarantee this behaviour. In two-dimensional analysis, it has been shown that a 'tying equation' enforcing displacement continuity at a crack tip is a simple approach to provide an additional equation, but it is also advantageous in that the unknowns $\tilde{K}_M^{s\,\mathrm{cf}}$ from eq. (5.6) become good approximations to the SIFs (Alatawi; Trevelyan, 2015; Andrade; Leonel, 2020). In the three-dimensional scope that is the focus of the current work, the crack front is a curve, and a weak-form strategy is presented to enforce compatibility as:

$$\int_{\Gamma_s^{\mathrm{cf}}} \left[\phi_\alpha^{\bar{\gamma}^+}(\xi_1,\xi_2) d_k^{\beta^+} - \phi_\alpha^{\bar{\gamma}^-}(\xi_1,\xi_2) d_k^{\beta^-} \right] \tilde{\phi}_s^{\mathrm{cf}}(t) dt = 0_k \tag{5.9}$$

in which Γ_s^{cf} is the line describing the crack front. $\tilde{\phi}_s^{\mathrm{cf}}$ is the weighting function chosen for this weak-form compatibility; here it is the NURBS function that interpolates the SIFs. The matrix form of the algebraic system with the Williams-based enrichment for the crack front is:

$$\begin{bmatrix} \mathbf{H} & \mathbf{H}_{\mathrm{s}} \\ \mathbf{\Phi}_{\mathrm{s}} & \mathbf{0} \end{bmatrix} \begin{Bmatrix} \mathbf{d} \\ \tilde{\mathbf{K}} \end{Bmatrix} = \begin{bmatrix} \mathbf{G} \\ \mathbf{0} \end{bmatrix} \begin{Bmatrix} \mathbf{p} \end{Bmatrix} \tag{5.10}$$

in which the sub-matrix $\mathbf{H}_{\mathrm{s}}$ contains the contributions from the new XIGABEM integrals, $\mathbf{\Phi}_{\mathrm{s}}$ corresponds to the coefficients from the compatibility equations eq. (5.9) and $\tilde{\mathbf{K}}$ contains the new enrichment parameters. The boundary condition application results in an algebraic system in its form $\mathbf{Ax} = \mathbf{b}$, and a standard solver computes all the unknowns of the vector $\mathbf{x}$.

The construction of the enrichment space results in the terms $\tilde{\mathbf{K}}$, arising in the solution vector $\mathbf{x}$, being direct approximation factors of the SIFs as:

$$K(t^{\mathrm{cf}}) = \sum_{s=1}^{n_K^{\gamma}} \tilde{\phi}_s^{\mathrm{cf}}(t) \tilde{K}_M^{s\,\mathrm{cf}} \tag{5.11}$$

thus dismissing a post-processing task that can be computationally demanding, such as the J-integral, or approximated techniques such as the Displacement Extrapolation Technique.

5.3 Regularisation of the singular enriched kernels for the Williams-based enrichment

Boundary integral equations have singular kernels due to the nature of the fundamental solutions. The method adopted for their regularisation is based on the Singularity Subtraction Technique (Guiggiani; Gigante, 1990; Guiggiani *et al.*, 1992). In the XIGABEM context, the new kernels introduced by the expansion of the displacement field for each enrichment strategy herein proposed also inherit this singular behaviour. Thus, SST must be also applied to them, and this is performed by an analogous procedure that consists of considering the augmented basis function as the basis function in the SST. For the Displacement BIE, the strongly singular kernel becomes regular by the expansion in a Taylor Series around the collocation point, which results in evaluating the augmented kernels directly at this position, without requiring any derivatives. On the other hand, the Traction BIE has a hypersingular kernel of order $O(r^{-3})$, which requires the expansion of the basis functions in a Taylor Series to its second term as $\mathbf{\Phi} = \mathbf{\Phi^0}(\hat{\mathbf{x}}) + \rho\mathbf{\Phi^1}(\hat{\mathbf{x}}) + O(\rho^2)$. It is important to mention that the components of $\mathbf{\Phi^1}$ are:

$$\phi_\alpha^1 = \frac{\partial \phi_\alpha}{\partial \hat{\xi}_1}\Big|_{\xi_1(\hat{\mathbf{x}}),\xi_2(\hat{\mathbf{x}})} \cos(\theta) + \frac{\partial \phi_\alpha}{\partial \hat{\xi}_2}\Big|_{\xi_1(\hat{\mathbf{x}}),\xi_2(\hat{\mathbf{x}})} \sin(\theta) \tag{5.12}$$

in which θ is the angular value associated to the polar coordinate transformation of the SST. In the context of new kernels, their regularisation takes place by the proper expansion of the enriched basis function in Taylor Series and its further incorporation in the SST expressions. Then, the SST of the arising kernels solely requires the substitution of the standard basis functions and their first derivative by the new augmented basis functions utilised. Therefore, expanding eq. (5.12) for each enrichment strategy applied in this study is sufficient for SST process.

5.3.1 Partially cut faces: Williams-based enrichment

For partially cut faces, the $\underline{\mathrm{S}}_{\mathrm{t}k\ell j}^{s\,\mathrm{cf}}$ kernels of eq. (5.4) require regularisation of their $O(r^{-3})$ hypersingular nature. The corresponding augmented basis functions are:

$$\phi^t_{\alpha M} = \phi^\gamma_\alpha R_{kq} \psi^\gamma_{qM} \tag{5.13}$$

and these require expansion in a Taylor series in polar coordinates for the SST, as:

$$\begin{aligned}
\frac{\partial \phi^t_{\alpha M}}{\partial \hat{\xi}_1} &= \frac{\partial \phi^\gamma_\alpha}{\partial \hat{\xi}_1} R_{kq} \psi^\gamma_{qM} + \phi^\gamma_\alpha \frac{\partial R_{kq}}{\partial \hat{\xi}_1} \psi^\gamma_{qM} + \phi^\gamma_\alpha R_{kq} \frac{\partial \psi^\gamma_{qM}}{\partial \hat{\xi}_1} \\
\frac{\partial \phi^t_{\alpha M}}{\partial \hat{\xi}_2} &= \frac{\partial \phi^\gamma_\alpha}{\partial \hat{\xi}_2} R_{kq} \psi^\gamma_{qM} + \phi^\gamma_\alpha \frac{\partial R_{kq}}{\partial \hat{\xi}_2} \psi^\gamma_{qM} + \phi^\gamma_\alpha R_{kq} \frac{\partial \psi^\gamma_{qM}}{\partial \hat{\xi}_2}
\end{aligned} \tag{5.14}$$

in which, for this enrichment, $\frac{\partial R_{kq}}{\partial \hat{\xi}_1} = \frac{\partial R_{kq}}{\partial \hat{\xi}_2} = 0$ since the local coordinate system is fixed at the crack tip. The derivatives of the NURBS basis function are well known from the standard IGABEM, while the derivatives of the enrichment function require further development. Initially, a chain rule enables the derivative in the NURBS parametric space as:

$$\begin{aligned}
\frac{\partial \psi^\gamma_{qM}}{\partial \hat{\xi}_1} &= \frac{\partial \psi^\gamma_{qM}}{\partial \xi_1} \frac{\partial \xi_1}{\partial \hat{\xi}_1} + \frac{\partial \psi^\gamma_{qM}}{\partial \xi_2} \frac{\partial \xi_2}{\partial \hat{\xi}_1} \\
\frac{\partial \psi^\gamma_{qM}}{\partial \hat{\xi}_2} &= \frac{\partial \psi^\gamma_{qM}}{\partial \xi_1} \frac{\partial \xi_1}{\partial \hat{\xi}_2} + \frac{\partial \psi^\gamma_{qM}}{\partial \xi_2} \frac{\partial \xi_2}{\partial \hat{\xi}_2}
\end{aligned} \tag{5.15}$$

but due to the relationship between the parametric space and the Gaussian space, $\frac{\partial \xi_1}{\partial \hat{\xi}_2} = \frac{\partial \xi_2}{\partial \hat{\xi}_1} = 0$. In addition, the Williams-based enrichment function is written in polar coordinates centred at the crack tip. This requires a sequential chain rule for both r_t and θ_t coordinates to obtain the derivatives in the Gaussian space, as:

$$\frac{\partial \psi^\gamma_{qM}}{\partial \hat{\xi}_j} = \frac{\partial \psi^\gamma_{qM}}{\partial r} \frac{\partial r_t}{\partial \xi_j} \frac{\partial \xi_j}{\partial \hat{\xi}_j} + \frac{\partial \psi^\gamma_{qM}}{\partial \theta_t} \frac{\partial \theta_t}{\partial \xi_j} \frac{\partial \xi_j}{\partial \hat{\xi}_j} \tag{5.16}$$

for the evaluation of the derivative in respect to the Gaussian coordinate in the j direction and $\frac{\partial \xi_j}{\partial \hat{\xi}_j}$ comes from eq. (2.31). Furthermore, the derivatives of the Williams enrichment function with respect to the polar coordinates are:

$$\begin{aligned}
\frac{\partial \psi_{qM}}{\partial r_t} &= \frac{1}{2\sqrt{r_t}} \psi_{qM} \\
\frac{\partial \psi_{nI}}{\partial \theta_t} &= \frac{1}{2\mu} \sqrt{\frac{r_t}{2\pi}} \left\{ -\frac{1}{2} \sin\left(\frac{\theta_t}{2}\right) \left[\kappa - 1 + 2\sin^2\left(\frac{\theta_t}{2}\right) \right] + \cos\left(\frac{\theta_t}{2}\right) \sin\theta_t \right\} \\
\frac{\partial \psi_{nII}}{\partial \theta_t} &= \frac{1}{2\mu} \sqrt{\frac{r_t}{2\pi}} \left\{ \frac{1}{2} \cos\left(\frac{\theta_t}{2}\right) \left[\kappa + 1 + 2\cos^2\left(\frac{\theta_t}{2}\right) \right] - \sin\left(\frac{\theta_t}{2}\right) \sin\theta_t \right\} \\
\frac{\partial \psi_{bI}}{\partial \theta_t} &= \frac{1}{2\mu} \sqrt{\frac{r_t}{2\pi}} \left\{ \frac{1}{2} \cos\left(\frac{\theta_t}{2}\right) \left[\kappa + 1 - 2\cos^2\left(\frac{\theta_t}{2}\right) \right] + \sin\left(\frac{\theta_t}{2}\right) \sin\theta_t \right\} \\
\frac{\partial \psi_{bII}}{\partial \theta_t} &= \frac{1}{2\mu} \sqrt{\frac{r_t}{2\pi}} \left\{ \frac{1}{2} \sin\left(\frac{\theta_t}{2}\right) \left[\kappa - 1 - 2\sin^2\left(\frac{\theta_t}{2}\right) \right] + \cos\left(\frac{\theta_t}{2}\right) \sin\theta_t \right\} \\
\frac{\partial \psi_{tIII}}{\partial \theta_t} &= \frac{1}{\mu} \sqrt{\frac{r_t}{2\pi}} \cos\left(\frac{\theta_t}{2}\right)
\end{aligned} \tag{5.17}$$

Lastly, r_t and θ_t are determined based on the position of the crack tip $\mathbf{x}^{\mathrm{ct}}$ as:

$$
\begin{aligned}
r_t &= ||\vec{r_t}|| = \sqrt{\sum_{k=1}^{3}(x_k - x_k^{\mathrm{ct}})^2} \\
\theta_t &= \mathrm{sign}\left[(\vec{N} \times \vec{r_t}) \cdot \vec{T}\right] \arccos\left(\frac{\vec{N} \cdot \vec{r_t}}{r_t}\right)
\end{aligned}
\tag{5.18}
$$

in which $\vec{N}$ is the vector parallel to the crack and $\vec{T}$ is the tangent vector, both at the crack tip and obtained by the Frenet-Serret frame. Then, their derivatives in respect to the parametric coordinates are:

$$
\begin{aligned}
\frac{\partial r_t}{\partial \xi_j} &= \frac{1}{r_t}\sum_{k=1}^{3}(x_k - x_k^{\mathrm{ct}})\sum_{\alpha=1}^{m}\frac{\partial \phi_\alpha}{\partial \xi_j}P_k^\alpha = \frac{1}{r_t}\sum_{k=1}^{3}(x_k - x_k^{\mathrm{ct}})\frac{\partial \vec{r_t}}{\partial \xi_j} \\
\frac{\partial \theta_t}{\partial \xi_j} &= \frac{-\mathrm{sign}\left[(\vec{N} \times \vec{r_t}) \cdot \vec{T}\right]}{\sqrt{1 - \left(\frac{\vec{N} \cdot \vec{r_t}}{r_t}\right)^2}} \frac{\vec{N} \cdot \frac{\partial \vec{r_t}}{\partial \xi_j} - \left(\vec{N} \cdot \vec{r_t}\frac{\partial r_t}{\partial \xi_j}\right)}{(r_t)^2}
\end{aligned}
\tag{5.19}
$$

5.3.2 Enrichment at the crack front for the direct extraction of SIFs

For the enrichment at the crack front that directly provides the SIFs as unknowns of the XIGABEM system, the local coordinate system is no longer constant over the enriched patch. Additionally, there is a uni-directional function at the crack front to interpolate the additional parameters that are proxies for the SIFs. In the context of regularising the kernels from eq. (5.8), the corresponding augmented basis function is:

$$
\phi_{skM}^{\mathrm{cf}} = \tilde{\phi}_s^{\mathrm{cf}}(t) R_{kq} \psi_{qM}^{\gamma} \tag{5.20}
$$

and, for the SST, its first derivative in the Gaussian coordinate direction j becomes:

$$
\frac{\partial \phi_{skM}^{\mathrm{cf}}}{\partial \hat{\xi}_j} = \frac{\partial \tilde{\phi}_s^{\mathrm{cf}}}{\partial \hat{\xi}_j} R_{kq} \psi_{qM}^{\gamma} + \tilde{\phi}_s^{\mathrm{cf}} \frac{\partial R_{kq}}{\partial \hat{\xi}_j} \psi_{qM}^{\gamma} + \tilde{\phi}_s^{\mathrm{cf}} R_{kq} \frac{\partial \psi_{qM}^{\gamma}}{\partial \hat{\xi}_j} \tag{5.21}
$$

in which both $\tilde{\phi}_s^{\mathrm{cf}}$ and R_{kq} are functions of the uni-direction parametric coordinate t at the crack front. This requires a chain rule in terms of this coordinate as:

$$
\begin{aligned}
\frac{\partial \tilde{\phi}_s^{\mathrm{cf}}}{\partial \hat{\xi}_j} &= \frac{d\tilde{\phi}_s^{\mathrm{cf}}}{dt}\frac{\partial v}{\partial \xi_j}\frac{\partial \xi_j}{\partial \hat{\xi}_j} \\
\frac{\partial R_{kq}}{\partial \hat{\xi}_j} &= \frac{dR_{kq}}{dt}\frac{\partial v}{\partial \xi_j}\frac{\partial \xi_j}{\partial \hat{\xi}_j}
\end{aligned}
\tag{5.22}
$$

The terms $\frac{d\tilde{\phi}_s^{\mathrm{cf}}}{dt}$ and $\frac{dR_{kq}}{dt}$ are the first derivatives of the uni-directional NURBS function and the rotation matrix at the crack front, respectively. In addition, the expression for $\frac{\partial t}{\partial \xi_j}$ derives from the orthogonality between the vector $\vec{r_t}$ and the tangent vector $\vec{T}$ at the crack front ($\vec{r_t} \cdot \vec{T} = 0$). It is worth mentioning that, for this enrichment, eq. (5.18) is valid by using x_k^{ct} as

$x_k^{\mathrm{cf}}(t)$ and $\theta_t = \pm\pi$ depending on whether it is a upper or lower crack surface. Then, the first variation of $\vec{r_t} \cdot \vec{T} = 0$ becomes:

$$\begin{gathered} \delta(\vec{r_t} \cdot \vec{T}) = 0 \Rightarrow \delta\vec{r_t} \cdot \vec{T} + \vec{r_t} \cdot \delta\vec{T} \\ \left(\frac{\partial \vec{r_t}}{\partial \xi_1}\delta\xi_1 + \frac{\partial \vec{r_t}}{\partial \xi_2}\delta\xi_2 + \frac{\partial \vec{r_t}}{\partial t}\delta t\right)\vec{T} + \vec{r_t}\frac{\partial \vec{T}}{\partial t}\delta t = 0 \end{gathered} \tag{5.23}$$

Assuming that $t = t(\xi_1, \xi_2)$, it is possible to write its perturbation in an implicit form as:

$$\delta t = \frac{\partial t}{\partial \xi_1}\delta\xi_1 + \frac{\partial t}{\partial \xi_2}\delta\xi_2 \tag{5.24}$$

which may be substituted into eq. (5.23) to give:

$$\left[\frac{\partial \vec{r_t}}{\partial \xi_1}\delta\xi_1 + \frac{\partial \vec{r_t}}{\partial \xi_2}\delta\xi_2 + \frac{\partial \vec{r_t}}{\partial t}\left(\frac{\partial t}{\partial \xi_1}\delta\xi_1 + \frac{\partial t}{\partial \xi_2}\delta\xi_2\right)\right]\vec{T} + \vec{r_t}\frac{\partial \vec{T}}{\partial t}\left(\frac{\partial t}{\partial \xi_1}\delta\xi_1 + \frac{\partial t}{\partial \xi_2}\delta\xi_2\right) = 0 \tag{5.25}$$

Equation (5.25) holds for any arbitrary $\delta\xi_i$, $i = 1, 2$. Then, its rearrangement results in:

$$\frac{\partial t}{\partial \xi_i} = \frac{-\dfrac{\partial \vec{r_t}}{\partial \xi_i} \cdot \vec{T}}{\dfrac{\partial \vec{r_t}}{\partial t} \cdot \vec{T} + \vec{r_t} \cdot \dfrac{\partial \vec{T}}{\partial t}} \tag{5.26}$$

5.4 Frenet-Serret frame for the rotation matrix and its derivative

The Frenet-Serret frame relates the rotation matrix and its first derivative with the curve parameterisation, and also the curvature $\kappa(t)$ and torsion $\tau(t)$ properties. In this context, the definition of the rotation system R_{kq} from the tangent vector $\vec{T}$, the normal vector $\vec{N}$ and the bi-normal vector $\vec{B}$ is:

$$\mathbf{R} = \begin{bmatrix} \vec{N} & \vec{B} & \vec{T} \end{bmatrix} \tag{5.27}$$

in which each vector comes from the position $\vec{x}$ in the NURBS curve as:

$$\begin{aligned} \vec{N} &= \frac{\vec{x}' \times (\vec{x}'' \times \vec{x}')}{||\vec{x}'||\,||\vec{x}'' \times \vec{x}'||} \\ \vec{B} &= \frac{\vec{x}' \times \vec{x}''}{||\vec{x}' \times \vec{x}''||} \\ \vec{T} &= \frac{\vec{x}'}{||\vec{x}'||} \end{aligned} \tag{5.28}$$

in which $\vec{x}' = \frac{d\vec{x}}{dt}$ and $\vec{x}'' = \frac{d^2\vec{x}}{dt^2}$. The first derivative assumes its form in terms of the rotation matrix $\mathbf{R}$ as:

$$\frac{d\mathbf{R}}{dt} = ||\vec{x}'||\begin{bmatrix} \vec{N} & \vec{B} & \vec{T} \end{bmatrix}\begin{bmatrix} 0 & -\tau(t) & \kappa(t) \\ \tau(t) & 0 & 0 \\ -\kappa(t) & 0 & 0 \end{bmatrix} \tag{5.29}$$

Finally, the curvature $\kappa(t)$ and torsion $\tau(t)$ are:

$$\begin{aligned}\kappa(t) &= \frac{||\vec{x}'' \times \vec{x}'''||}{||\vec{x}'||^3} \\ \tau(t) &= \frac{\vec{x}' \cdot (\vec{x}'' \times \vec{x}''')}{||\vec{x}' \times \vec{x}''||^3}\end{aligned} \tag{5.30}$$

with $\vec{x}''' = \frac{d^3\vec{x}}{dt^3}$ as the third derivative of the NURBS curve with respect to the parametric coordinate.

5.5 Numerical applications

In this section, four numerical applications demonstrate the effectiveness of the XIGABEM formulation using the Williams solution-based enrichment function. The first two applications are a penny-shaped crack and an elliptical crack under remote tension. Their shapes justify the isogeometric framework, in which NURBS curves of degree 2 can exactly represent their geometry. Both in-plane and inclined cases are analysed, inducing a mixed-mode response where all SIFs vary according to analytical solutions. The last two applications address a prism with an edge crack under two different loading cases: a pure mode I/II/III loading and a uniform traction load. While the third application has an analytical solution, the fourth is compared with numerical results from the BEM and the IGABEM.

5.5.1 Penny-shaped crack under uniform traction

The first application of the XIGABEM formulation with the Williams-based solution as enrichment function is a penny-shaped circular crack with radius $R = 1.0$ embedded in an infinite domain, subjected to a remote uniaxial stress $\sigma_0 = 1.0$, according to fig. 54(a). Since the Dual BEM formulation herein applied requires the discretisation of the external boundary, the crack is located inside a cube of side $200R$. The material properties are $E = 1.0$ and $\nu = 0.0$. It is noteworthy that the proper choice of the local coordinate system performs a major role for the crack front enrichment scheme when its front is curved. Thus, this application allows the evaluation of the Frenet-Serret frame, especially for mixed mode I/II/III problems. In addition, the analysis of both in-plane and inclined cracks allows the evaluation of a pure mode I and a mixed mode I/II/III in a problem whose enrichment function does not match with the analytical solution. For the pure mode I problem, both SIFs and the u_2 displacement at the crack have a reference solution (Tada; Paris; Irwin, 2000) as:

$$\begin{aligned}u_2(x_1, x_2, x_3) &= \frac{-2n_2(1-\nu)\sigma_0}{\pi\mu}\sqrt{R^2 - (x_1^2 + x_3^2)} \\ K_I &= \frac{2\sigma_0}{\pi}\sqrt{\pi R} \\ K_{II} &= K_{III} = 0\end{aligned} \tag{5.31}$$

in which σ_0 is the remote traction applied and n_2 is the normal outward vector at each crack surface. For the crack inclined through an angle θ_i, the corresponding SIFs are:

$$
\begin{aligned}
K_I &= \frac{2\sigma_0}{\pi}\sqrt{\pi R}\cos^2\theta_c \\
K_{II} &= \frac{4\sigma_0}{\pi(2-\nu)}\sqrt{\pi R}\cos\theta_i \sin\theta_i \cos\theta_c \\
K_{III} &= \frac{4\sigma_0(1-\nu)}{\pi(2-\nu)}\sqrt{\pi R}\cos\theta_i \sin\theta_i \sin\theta_c
\end{aligned}
\tag{5.32}
$$

in which θ_c is the angle of the crack front position taken in the crack plane.

Figure 54 – (a) Geometry and loading conditions for penny-shaped crack and (b) Control points position for penny-shaped crack mesh

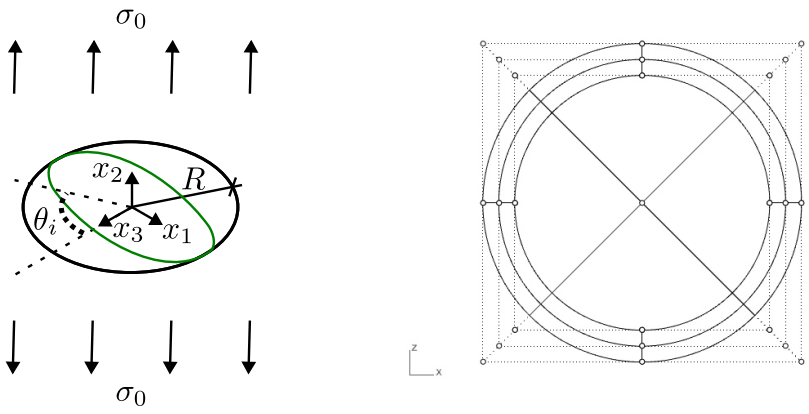

(a) (b)

Source: The author.

The discretisation adopted for this application consists of an external boundary composed of 6 NURBS surfaces with degree $p = q = 1$ Constant boundary conditions are responsible for representing the uniform stress state in the far field, in which the bottom face ($x_2 = -100.0$) has nil displacements in all directions and there is a traction $t_2 = 1.0$ applied over the top face ($x_2 = 100.0$). For the crack faces, five $p = q = 2$ degree NURBS surfaces describe each face, as illustrated in fig. 54(b). Each of the four patches that compose the circular crown receive the crack front enrichment, while the central circle remains with only the NURBS basis functions. The circular crown length is set as $R/5$, based on the analysis performed with the Displacement Fitting Technique (Cordeiro; Leonel, 2018), and the crack front increment chosen by Peng *et al.* (2017a) in their penny-shaped crack growth analysis. In addition, a Lagrangian BEM analysis considers a 9-node quadrilateral quadratic element to compare the XIGABEM and IGABEM results against the conventional BEM.

The in-plane crack deformed shape presented in fig. 55 compares the responses from the extended IGABEM approach and the standard IGABEM for the most refined mesh. A jump in the displacement field at the crack front is evident in the standard formulation, in contrast to the XIGABEM results. For the standard formulation, as previously obtained by Peng *et al.* (2017a), the major contribution for the error is at the crack front. The absence of a displacement jump in the XIGABEM solution is a direct consequence of the tying equations.

Figure 55 – Deformed shape for penny shaped crack using (a) conventional IGABEM and (b) extended IGABEM

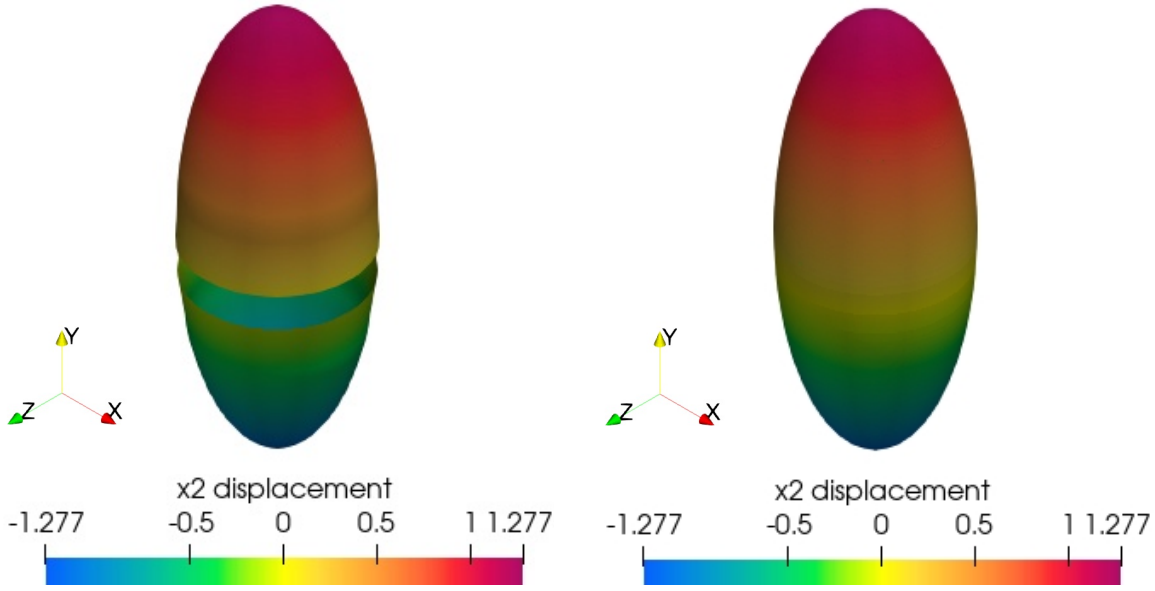

(a) Conventional IGABEM (a) Extended IGABEM

Source: The author.

The convergence analysis in the relative L_2 norm of displacement error presented in fig. 56 demonstrates the improvements in the convergence rate for the XIGABEM responses against the standard IGABEM and the Lagrangian BEM. By adding a small number of degrees of freedom, in addition to directly returning the SIFs, there is both a reduction in the relative L_2 norm of displacement error and an increase in the convergence rate. These outcomes are associated to the asymptotic behaviour introduced by the enrichment, as well as the tying at the crack front. Optimal convergence for collocation methods in the BEM context still has open questions (Sauter; Schwab, 2011; Marussig; Hiemstra; Hughes, 2018), but for a smooth problem, Marussig, Hiemstra and Hughes (2018) achieved convergence rates of $\mathcal{O}(N^{-p})$ in the L_2 norm, with N being the number of degrees of freedom. For fracture mechanics, this behaviour does not hold, as can be seen in Peng *et al.* (2017a) and the standard IGABEM simulations used for comparison in fig. 56 of the present study. On the other hand the XIGABEM approach described herein delivers improved convergence rates over standard IGABEM, both for smooth solutions (Marussig; Hiemstra; Hughes, 2018) and for fracture problems.

As widely presented in the literature for the GFEM/XFEM, enrichment strategies can cause an increase in the condition number, which has the potential to become problematic for the system solution. Based on the condition number growth shown in fig. 57, it is noteworthy that the extended IGABEM formulation for the crack front enrichment improves the overall conditioning when compared against its standard version, instead of worsening it.

Table 5 shows the average relative error for all SIFs to be in excellent agreement with the reference solution, being below 5.10^{-3} for K_1. Additionally, K_2 and K_3 are below 4.10^{-10}

Figure 56 – Relative L_2 norm of error in displacements for in-plane penny-shaped crack.

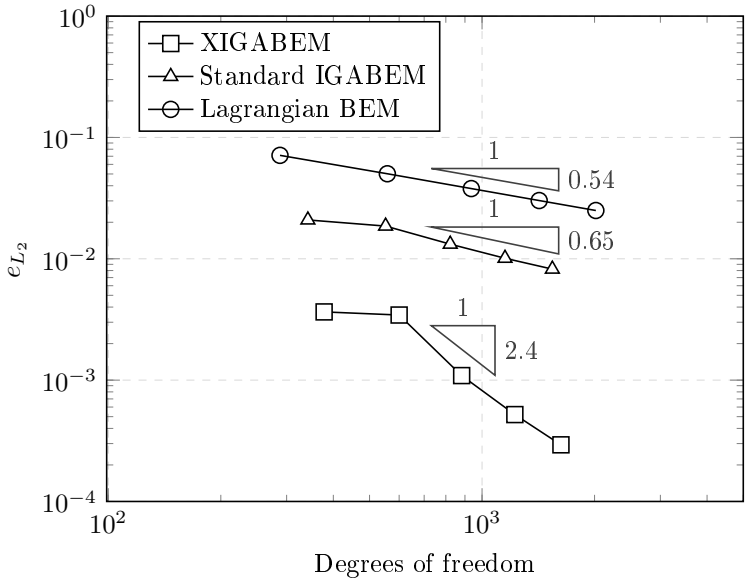

Source: The author.

Figure 57 – Condition number growth for in-plane penny-shaped crack.

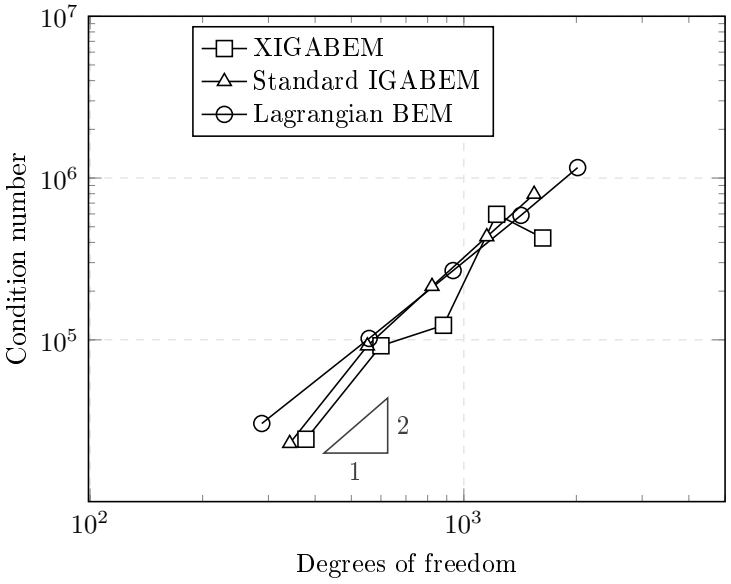

Source: The author.

Figure 58 – Stress Intensity Factors for penny-shaped crack inclined by $\pi/4$ rad.

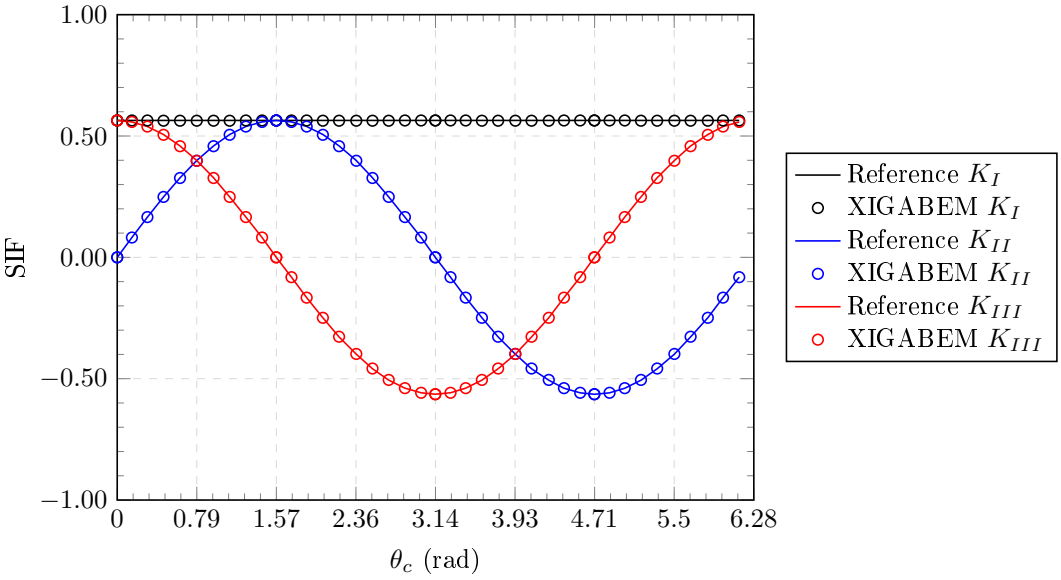

Source: The author.

for all meshes except the most refined one, in which the effect of near-singular integrals on the evaluation of the BIEs kernels start to influence the overall precision. These results can be improved by an enhanced integration scheme for those integrals, but this is beyond the scope of this study.

Table 5 – Average SIFs error for in-plane penny-shaped crack.

Degrees of freedom	avg. error in K_1	avg. error in K_2	avg. error in K_3
378	4.689e-03	-2.47e-11	-3.00e-13
600	2.936e-03	-4.11e-11	3.67e-12
882	2.267e-03	3.85e-10	-1.59e-12
1224	1.776e-03	-5.09e-12	4.59e-11
1626	1.432e-03	4.04e-07	-1.22e-11

Source: The author.

The numerical analysis for an inclined penny-shaped crack permits the proposed formulation accuracy assessment in the mixed-mode fracture response. For $\theta_i = \pi/4$, fig. 58 shows the SIFs for the most refined mesh. It is noticed that all SIFs vary in agreement with the reference solutions, with relative errors below $2.03e-3$. Additionally, the relative L_2 norm of error in displacements converges in a faster rate than the SIFs, mainly associated to the correction of the non-physical displacements at the crack front given by the IGABEM formulation. In summary, it is evident that the XIGABEM formulation for a circular crack obtains highly accurate results with an increase of only a few degrees of freedom in comparison to standard approach.

5.5.2 Elliptical crack under uniform traction

An elliptical crack embedded in an infinite domain and subjected to a far-field uniaxial stress $\sigma_0 = 1.0$ is the second application considered for the XIGABEM formulation with the Williams based enrichment. The crack has semi-major and semi-minor axis dimensions $a = 10.0$ and $b = 5.0$, respectively, as depicted in fig. 59(a). Similarly to section 5.5.1, the truncated domain that represents an infinite medium is a cube with side $20a$. In this application, the mechanical properties are $E = 1.0$ and $\nu = 0.3$. Besides encompassing all the characteristics of section 5.5.1 in respect to the definition of the local coordinate system, K_1 is no longer constant, which constitutes an important behaviour to capture by the enrichment scheme. The analytical solution for this case, which also considers the inclination angle θ_i, is (Tada; Paris; Irwin, 2000):

$$\begin{aligned}
K_I &= \frac{\sigma_0}{2}(1 + 2\cos 2\theta_i)\frac{\sqrt{b\pi}f(\theta_c)}{E(k)} \\
K_{II} &= \frac{\sigma_0}{2}(\sin 2\theta_i)\frac{\sqrt{b\pi}k^2 b/a\cos\theta_c}{f(\theta_c)B(k)} \\
K_{III} &= \frac{\sigma_0}{2}(\sin 2\theta_i)\frac{\sqrt{b\pi}k^2(1-\nu)\sin\theta_c}{f(\theta_c)B(k)} \\
k^2 &= 1 - \left(\frac{b}{a}\right)^2 \\
f(\theta_c) &= \left[\sin^2\theta_c + \left(\frac{b}{a}\right)^2\cos^2\theta_c\right]^{1/4} \\
B(k) &= (k^2 - \nu)E(k) + \nu\left(\frac{b}{a}\right)^2 K(k) \\
K(k) &= \int_0^{\pi/2} \frac{1}{\sqrt{1 - k^2\sin^2\theta_c}} d\theta_c \\
E(k) &= \int_0^{\pi/2} \sqrt{1 - k^2\sin^2\theta_c}\, d\theta_c
\end{aligned} \tag{5.33}$$

in which $\theta_i = 0$ for an in-plane situation. Particularly, for the in-plane case, the u_2 displacements are:

$$u_2(x_1, 0, x_3) = \frac{2(1-\nu)\sigma_0}{\mu}\frac{b}{E(k)}\sqrt{1 - \frac{x_1^2}{a^2} - \frac{x_3^2}{b^2}} \tag{5.34}$$

The crack mesh consists of 5 bi-quadratic NURBS surfaces for each face, in which the internal ellipse is scaled by 80% from the total crack size, as shown in fig. 59(b). In addition, the external boundary mesh has 6 bi-linear NURBS surfaces. For the convergence study, a knot-insertion strategy is used to increase uniformly in each parametric direction the number of basis functions only at the crack surfaces.

The convergence analysis in fig. 60 demonstrates again an increase in the order of convergence rate for the XIGABEM in comparison to the standard formulation. However, for the most refined mesh, the near-singular integral precision starts to have a mild effect on the solution accuracy. In addition, fig. 61 shows that the condition number remains similar to the standard formulation. Moreover, the SIFs directly obtained as degrees of freedom, presented in fig. 62, are

Figure 59 – (a) Geometry of elliptical crack and (b) Mesh and control points for in-plane elliptical mesh.

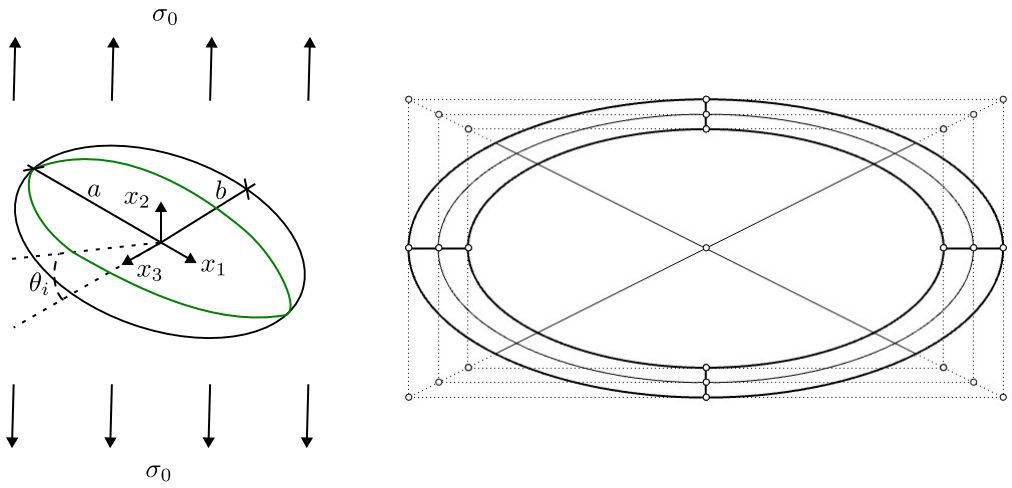

(a) (b)

Source: The author.

Figure 60 – Relative L_2 norm of error in displacements for in-plane elliptical crack.

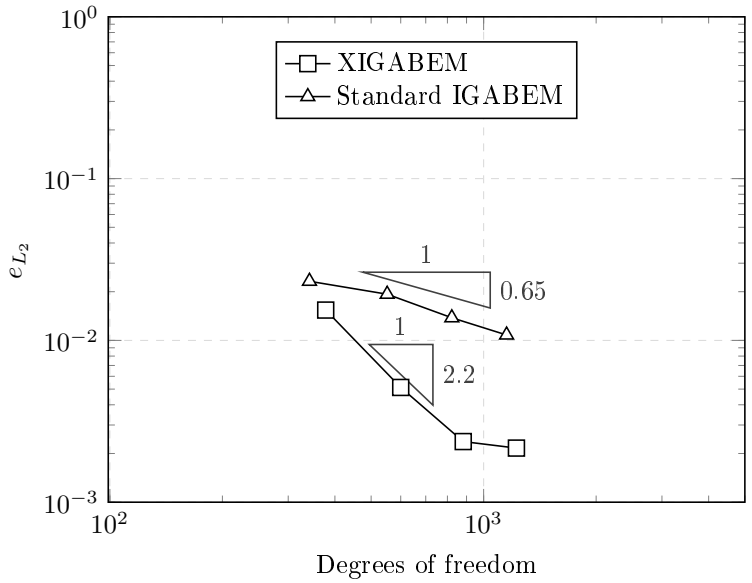

Source: The author.

in accordance with the analytical solutions for the in-plane case. Thus, the enrichment scheme is also capable of capturing the trigonometrical variation for all three SIFs of this application.

The elliptical crack inclined through angle $\theta_i = \pi/6$ permits an analysis of a complex crack geometry in a mixed-mode loading case. The extracted SIFs are depicted in fig. 63, in which again the formulation precisely captures the expected behaviour for all three SIFs. In addition, table 6 compares the SIFs relative errors with Peng *et al.* (2017a), when the analytical SIF is non-nil. The enriched formulation provides lower errors for both cases in all SIFs. Specifically, for

Figure 61 – Condition number growth for in-plane elliptical crack.

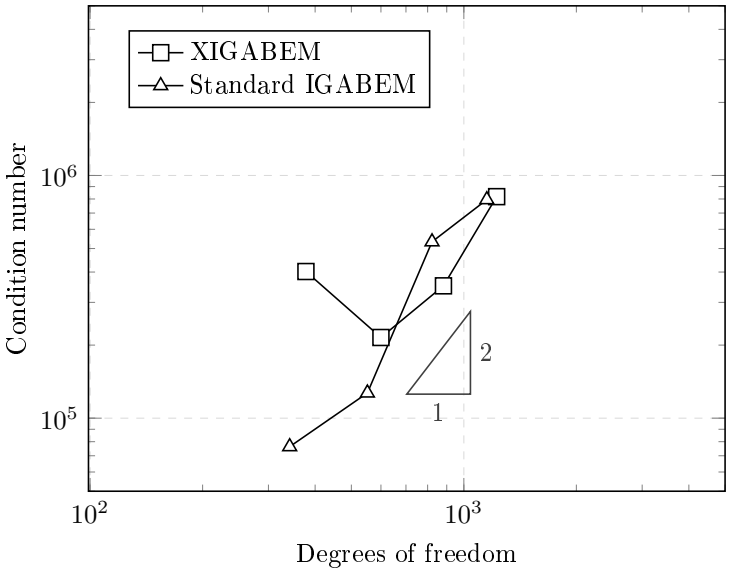

Source: The author.

Figure 62 – Stress Intensity Factor K_I for in-plane elliptical crack.

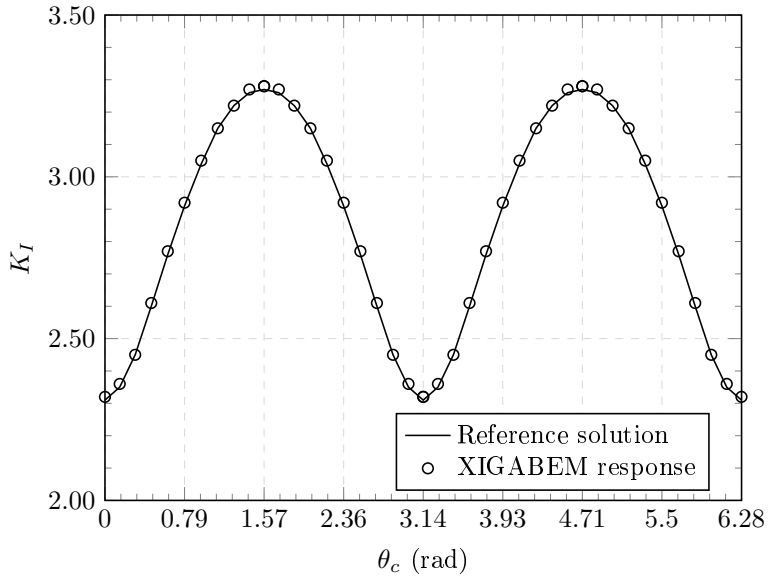

Source: The author.

K_I and K_{III}, an improvement of one order of magnitude is found in the relative error.

Table 6 – Relative error for SIFs in elliptical crack inclined by $\theta_i = \pi/6$.

		VCCI (Peng *et al.*, 2017a)	M-integral (Peng *et al.*, 2017a)	XIGABEM
$\theta_c = 0$	K_I	4.65e-02	1.53e-02	5.53e-04
	K_{II}	4.14e-02	1.28e-02	4.83e-03
	K_{III}	-	-	-
$\theta_c = \pi/2$	K_I	8.28e-03	2.21e-02	1.89e-03
	K_{II}	-	-	-
	K_{III}	6.88e-03	5.96e-02	1.77e-03

Source: The author.

Figure 63 – Stress Intensity Factors for elliptical crack inclined by $\pi/6$ rad.

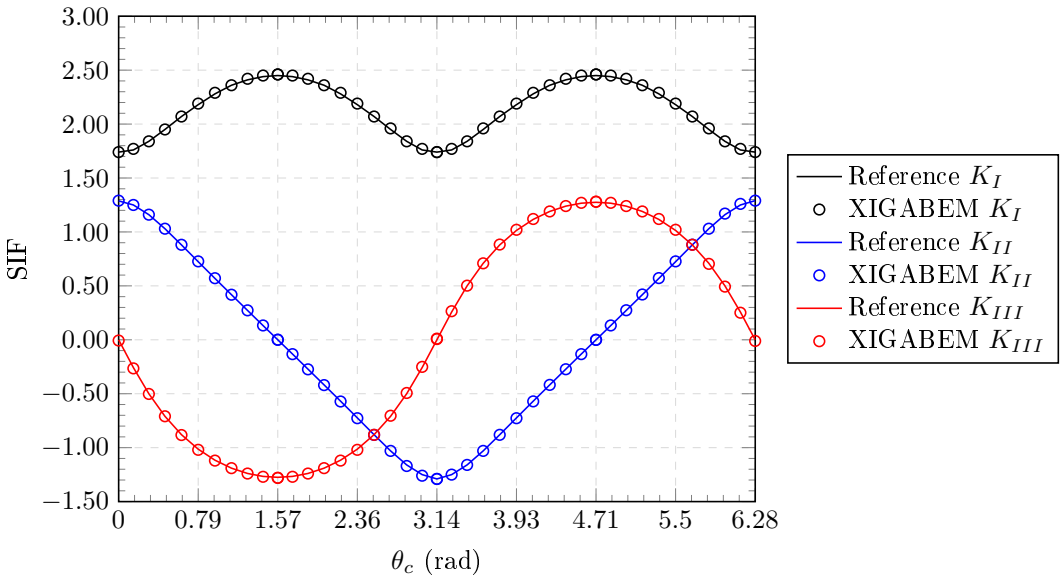

Source: The author.

Figure 64 – Geometry of prismatic block with edge crack.

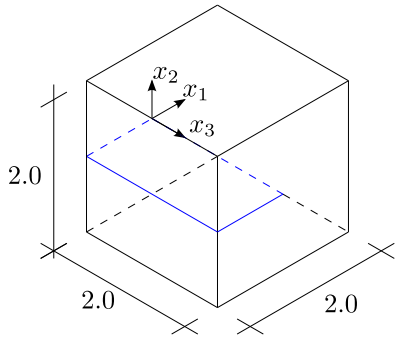

Source: The author.

5.5.3 Prism with edge crack: pure mode analysis

This application consists of a finite prismatic solid with a centred crack of geometry defined in fig. 64 and of material properties $E = 1.0$ and $\nu = 0.0$. The boundary conditions involve the pure mode behaviour, allowing the use of known analytical solutions as appropriate in order to elicit information about the numerical performance of the XIGABEM formulation. The upper face ($-1.0 \leq x_1 \leq 1.0$, $x_2 = 1.0$, $0.0 \leq x_3 \leq 2.0$), lower face ($-1.0 \leq x_1 \leq 1.0$, $x_2 = -1.0$, $0.0 \leq x_3 \leq 2.0$), front face ($x_1 = 1.0$, $-1.0 \leq x_2 \leq 1.0$, $0.0 \leq x_3 \leq 2.0$) and back faces ($x_1 = -1.0$, $-1.0 \leq x_2 \leq 1.0$, $0.0 \leq x_3 \leq 2.0$,) receive displacement boundary conditions, while all other faces in the external boundary have prescribed traction. Since the analytical solutions are known for each opening mode (Williams, 1957), they are directly applied as boundary conditions in the BIEs, as described in section 2.4. The displacement and stress values for this application are:

$$\begin{Bmatrix} u_1 \\ u_2 \\ u_3 \end{Bmatrix} = \frac{1}{2\mu}\sqrt{\frac{r_t}{2\pi}} \begin{bmatrix} \cos\left(\frac{\theta_t}{2}\right)(\kappa - \cos\theta_t) & \sin\left(\frac{\theta_t}{2}\right)(\kappa + 2 + \cos\theta_t) & 0 \\ \sin\left(\frac{\theta_t}{2}\right)(\kappa - \cos\theta_t) & -\cos\left(\frac{\theta_t}{2}\right)(\kappa - 2 + \cos\theta_t) & 0 \\ 0 & 0 & 4\sin\left(\frac{\theta_t}{2}\right) \end{bmatrix} \begin{Bmatrix} K_I \\ K_{II} \\ K_{III} \end{Bmatrix}$$

$$\begin{Bmatrix} \sigma_{11} \\ \sigma_{22} \\ \sigma_{33} \\ \sigma_{12} \\ \sigma_{13} \\ \sigma_{23} \end{Bmatrix} = \frac{1}{\sqrt{2\pi r_t}} \left\{ \begin{Bmatrix} \cos\left(\frac{\theta_t}{2}\right)\left[1 - \sin\left(\frac{\theta_t}{2}\right)\sin\left(\frac{3\theta_t}{2}\right)\right] \\ \cos\left(\frac{\theta_t}{2}\right)\left[1 + \sin\left(\frac{\theta_t}{2}\right)\sin\left(\frac{3\theta_t}{2}\right)\right] \\ 2\nu\cos\left(\frac{\theta_t}{2}\right) \\ \sin\left(\frac{\theta_t}{2}\right)\cos\left(\frac{\theta_t}{2}\right)\cos\left(\frac{3\theta_t}{2}\right) \\ 0 \\ 0 \end{Bmatrix} K_I \right.$$

$$+ \begin{Bmatrix} -\sin\left(\frac{\theta_t}{2}\right)\left[2 + \cos\left(\frac{\theta_t}{2}\right)\sin\left(\frac{3\theta_t}{2}\right)\right] \\ \sin\left(\frac{\theta_t}{2}\right)\cos\left(\frac{\theta_t}{2}\right)\cos\left(\frac{3\theta_t}{2}\right) \\ -2\nu\sin\left(\frac{\theta_t}{2}\right) \\ \cos\left(\frac{\theta_t}{2}\right)\left[1 - \sin\left(\frac{\theta_t}{2}\right)\sin\left(\frac{3\theta_t}{2}\right)\right] \\ 0 \\ 0 \end{Bmatrix} K_{II} + \left. \begin{Bmatrix} 0 \\ 0 \\ 0 \\ 0 \\ \cos\theta_t\sin\left(\frac{\theta_t}{2}\right) - \sin\theta_t\cos\left(\frac{\theta_t}{2}\right) \\ \sin\theta_t\sin\left(\frac{\theta_t}{2}\right) + \cos\theta_t\cos\left(\frac{\theta_t}{2}\right) \end{Bmatrix} K_{III} \right\} \tag{5.35}$$

Figure 65 – Mesh for prismatic block with edge crack for (a) XIGABEM analysis and (b) standard IGABEM approach.

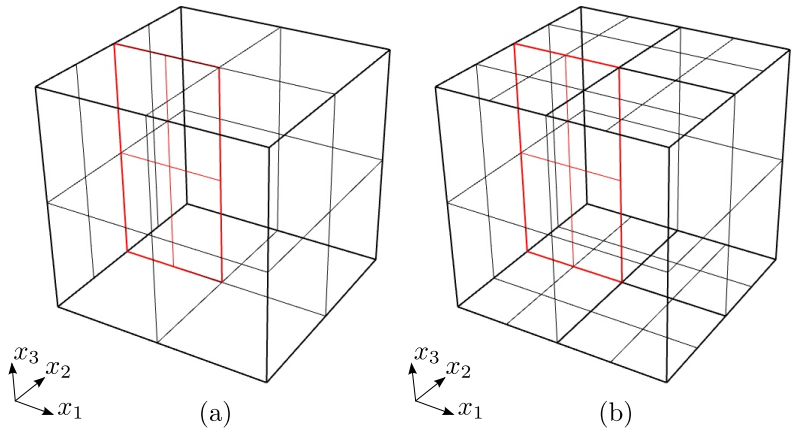

Source: The author.

The numerical analysis via XIGABEM is performed on a NURBS mesh with 9 patches, in which 7 patches define the external boundary and 2 patches represent the opposing crack faces. Figure 65(a) presents the extended IGABEM mesh. It should be noted that the lateral faces do not align with the crack faces, since the Williams-based enrichment functions capture the discontinuous solution independently of the mesh. The upper and lower crack faces receive the crack front enrichment, which allows the direct determination of the SIFs. To compare the convergence rate of the XIGABEM against the standard IGABEM formulation, the numerical responses for the conventional IGABEM method utilises a mesh containing 15 NURBS patches, as shown in fig. 65(b). The increased number of patches derives from the need for mesh alignment at the intersections between the external boundary and the crack on lateral faces.

This application considers each crack opening mode separately so that it is possible to evaluate the influence of all terms from the enrichment functions. The boundary conditions for the pure mode $M = I, II, III$ utilise eq. (5.35) with $K_M = 1.0$ and 0.0 for other K's. Figure 66 presents the deformed shape for each crack opening mode for both XIGABEM and standard IGABEM formulations. Discontinuous displacements are evident at the lateral faces in the IGABEM model, since multiple discontinuously defined NURBS patches represent these faces, and therefore no continuity between them is imposed. This is naturally circumvented by the extended IGABEM approach, because it does not require mesh alignment, and this can be seen in the results with continuity maintained over the face. Further, unlike in the standard IGABEM, the effect of the tying equations enforces displacement continuity over the crack front in the enriched XIGABEM scheme.

The convergence analysis shown in fig. 67 presents the error comparison for both XIGABEM and IGABEM approaches for each crack mode. For all modes, the standard IGABEM convergence rate is around 0.6, explained by the square-root nature of the fracture mechanics solution that is not captured by the NURBS basis functions (neither in the crack faces nor in the lateral faces). On the other hand, this behaviour is injected into the extended IGABEM approximation, which results in better convergence for all three modes when compared against

Figure 66 – Deformed shape for each pure crack loading where standard IGABEM results are on the left-hand side while the XIGABEM responses are on the right-hand side.

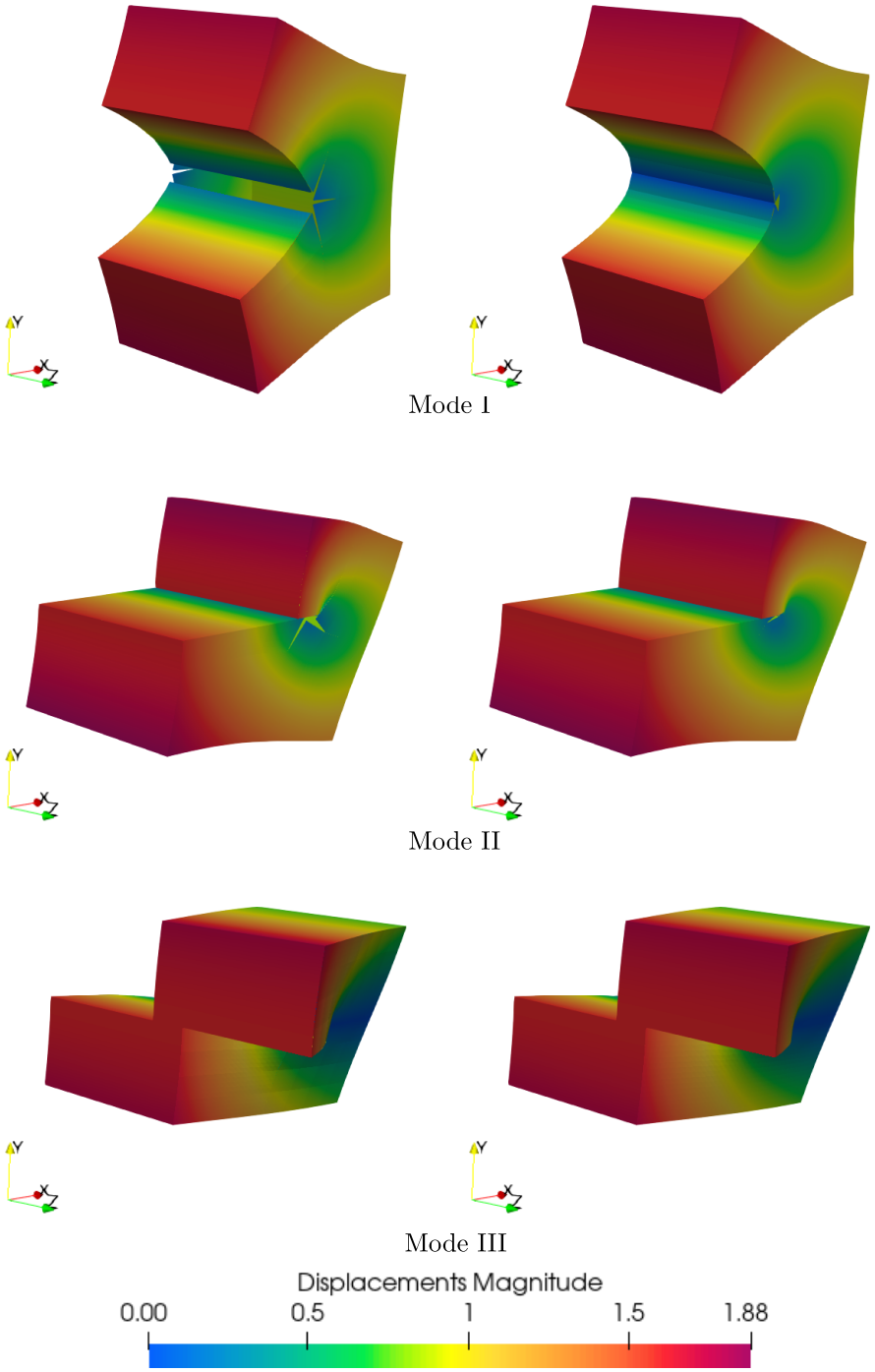

Source: The author.

Table 7 – Average values for SIFs in each pure mode loading case of prism with edge crack.

	Degrees of freedom	avg. $\|K_I\|$	avg. $\|K_{II}\|$	avg. $\|K_{III}\|$
Mode I	639	1.00057	5.84e-07	2.66e-06
	1275	0.99979	9.66e-06	2.95e-05
	2175	0.99991	9.17e-06	1.96e-05
Mode II	639	7.06e-07	1.00125	1.70e-02
	1275	7.55e-05	1.00050	2.21e-03
	2175	8.36e-07	1.00032	1.39e-04
Mode III	639	7.19e-07	7.06e-04	0.99579
	1275	1.51e-03	7.92e-04	1.00228
	2175	6.81e-06	2.74e-04	0.99991

Source: The author.

the standard formulation. It is evident from fig. 67 that different convergence rates are found for the different modes. It is noticeable that some caution is needed in interpreting convergence rates for XIGABEM, since the important square root behaviour is included in the coarsest models, but not improved in later refinements which add only the smooth NURBS basis functions. In addition, fig. 68 presents the comparison of the condition number of the $\mathbf{A}$ matrix for both XIGABEM and IGABEM approaches. For each approach, the condition number is the same for all modes, since a change in the boundary conditions only affects the right-hand side vector. Through this analysis, it can be seen that the enrichment strategies cause a consequent increase in the condition number. Nevertheless, the degree of ill-conditioning for the XIGABEM in this application is mild and does not jeopardise the accuracy of the system solution.

The SIF results obtained directly from the XIGABEM solution vector $\mathbf{x}$ are presented in table 7. The SIF presentation considers the average value for the absolute SIFs along the crack front for all crack opening modes. All SIFs match closely with the expected value for each pure mode loading, and the errors reduce with mesh refinement. For all cases, the most refined mesh provides the associated SIF for its pure mode loading with errors below 4.10^{-4}. This provides evidence that the proposed formulation is capable of delivering SIFs to high accuracy without the requirement for post-processing tasks, as J-Integral.

Figure 67 – Relative L_2 norm of error in displacements for prismatic block with edge crack.

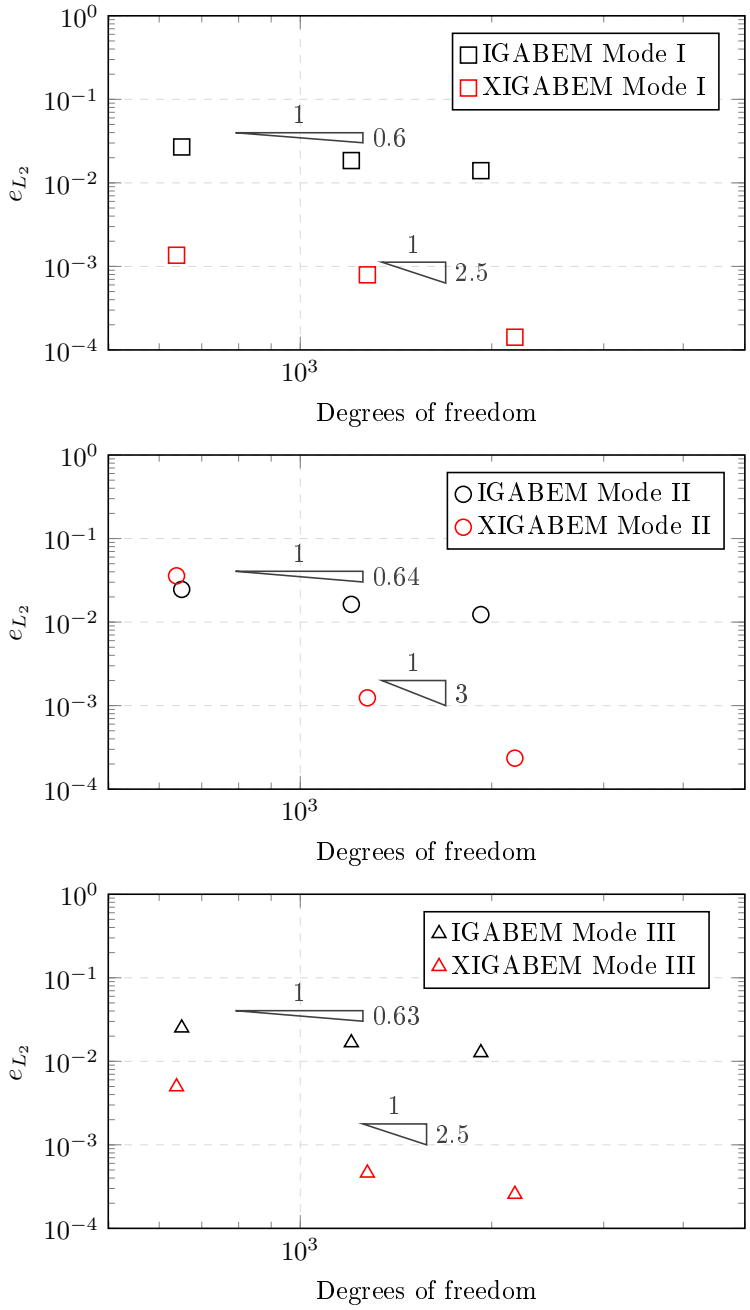

Source: The author.

Figure 68 – Condition number growth for prismatic block with edge crack.

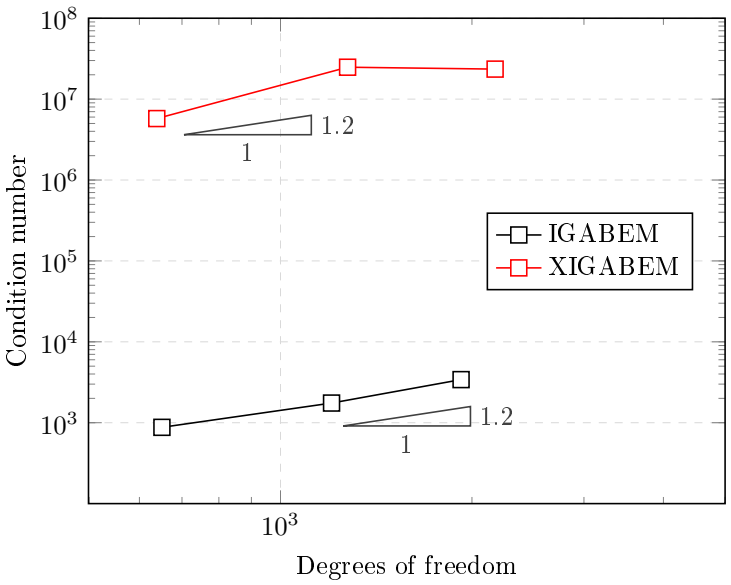

Source: The author.

5.5.4 Prism with edge crack: uniform load

The fourth application of the XIGABEM formulation with the Williams solution as enrichment function deals with the numerical analysis of a finite prismatic block under uniform traction $\sigma_0 = 1.0$ at its ends. Figure 69 presents its geometry and boundary conditions, in which the displacements in the highlighted region are responsible for preventing rigid body motion. The material properties are: Young modulus $E = 1000.0$ and Poisson ratio $\nu = 0.3$. This application does not have an analytical response, which requires its comparison against reference solutions obtained by other authors using different numerical methods. Also, it is reasonable to expect plane-strain behaviour at the middle of the crack front $z = 3.75$, at which the correspondent K_I is (Tada; Paris; Irwin, 2000):

$$\begin{aligned} K_I &= \sigma_0 \sqrt{\pi a} F(a/b) \\ F(a/b) &= 1.122 - 0.231 \left(\frac{a}{b}\right) + 10.550 \left(\frac{a}{b}\right)^2 - 21.710 \left(\frac{a}{b}\right)^3 + 30.382 \left(\frac{a}{b}\right)^4 \end{aligned} \tag{5.36}$$

Figure 69 – Geometry and boundary conditions for prismatic specimen under uniform traction.

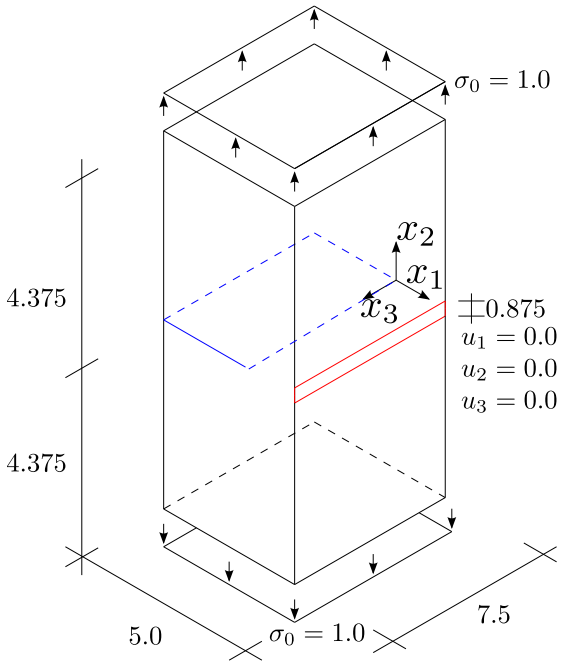

Source: The author.

Initially, the crack surfaces are given only the SIF enrichment, and the corresponding mesh presented in fig. 70(a) consists of 17 NURBS surfaces, of degree $p = q = 1$ for the external boundary and $p = q = 2$ for the crack surfaces. In this mesh, all surfaces must align with the crack, which places additional demands on the CAD model to satisfy this requirement. Additionally, the fully enriched analysis considers the SIF enrichment on the crack faces, the Williams-based enrichment on the lateral faces and the Heaviside enrichment on the fully cut face, which reduces the amount of NURBS surfaces to 10, as depicted in fig. 70(b). Again, the NURBS

basis functions are of degree $p = q = 1$ on the external boundary faces and $p = q = 2$ on the crack faces. In this application there is a plane-stress/plane-strain transition at the crack front close to the lateral faces. In order to study this behaviour, and therefore the influence of the Kolosov constant on the results, for the fully enriched model two different analyses consider the Kolosov constant prescribed for plane-stress and plane-strain scenarios. Therefore, three different models are compared against reference solutions using IGABEM by Cordeiro and Leonel (2018) and Lagrangian BEM by Mi and Aliabadi (1992), and against the 2-D plane-strain solution eq. (5.36). It is relevant to mention that the 2-D equivalent solution for this problem does not hold for the entire crack front. However, the aforementioned references have shown that it becomes a suitable comparison close to the crack front centre, where the plane-strain behaviour is more prominent.

Figure 70 – Isogeometric mesh for prismatic block under uniform traction, in which (a) XIGABEM mesh with only the SIF enrichment, and (b) fully enriched model.

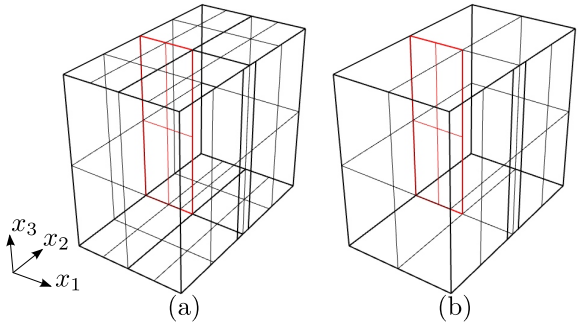

Source: The author.

The number of degrees of freedom for each analysis are 3,996 and 2,787 for the model with only SIF enrichment and for the fully enriched model, respectively. In addition, the models of Cordeiro and Leonel (2018) comprise 3,273 and 5,121 degrees of freedom for two different refinement levels, while Mi and Aliabadi (1992) do not provide their model sizes. The normalised K_I comparison in fig. 71 demonstrates that the crack front enrichment is capable of directly determining the SIF for all scenarios in broad agreement with other results in the literature. At the crack front coordinate $z = 3.75$, the XIGABEM model with only crack front enrichment has a relative difference in K_I of 2.0% in comparison to the 2-D plane-strain solution, while the fully enriched models give rise to discrepancies of 0.52% and 0.96% when using plane-strain and plane-stress Kolosov constants at the Williams-based enrichment, respectively. Therefore, it is noticeable that capturing the square-root behaviour over the lateral faces improves the SIF determination. On the other hand, it is interesting that the Kolosov parameter being considered as plane-stress on lateral faces forces the overall K_I variation to be lower than the plane-strain case. Still, both situations lead to an accurate result in comparison to other numerical methods and the handbook two-dimensional solution. Moreover, the fully enriched models deliver higher accuracy than the standard IGABEM model with 3,273 degrees of freedom, whose difference was 1.93%. It must be noticed that the present study and Cordeiro and Leonel (2018) utilised $\nu = 0.3$ while Mi and Aliabadi (1992) used $\nu = \frac{1}{3}$. The numerical analysis of this application with XIGABEM has obtained up to only 0.5% difference in SIF at the centre of the crack. In

Figure 71 – Stress Intensity Factors along crack front, in which XIGABEM (a) is the model with only the crack front enrichment, XIGABEM (b) and (c) are the fully enriched models with Kosolov constant set as plane strain and plane stress, respectively.

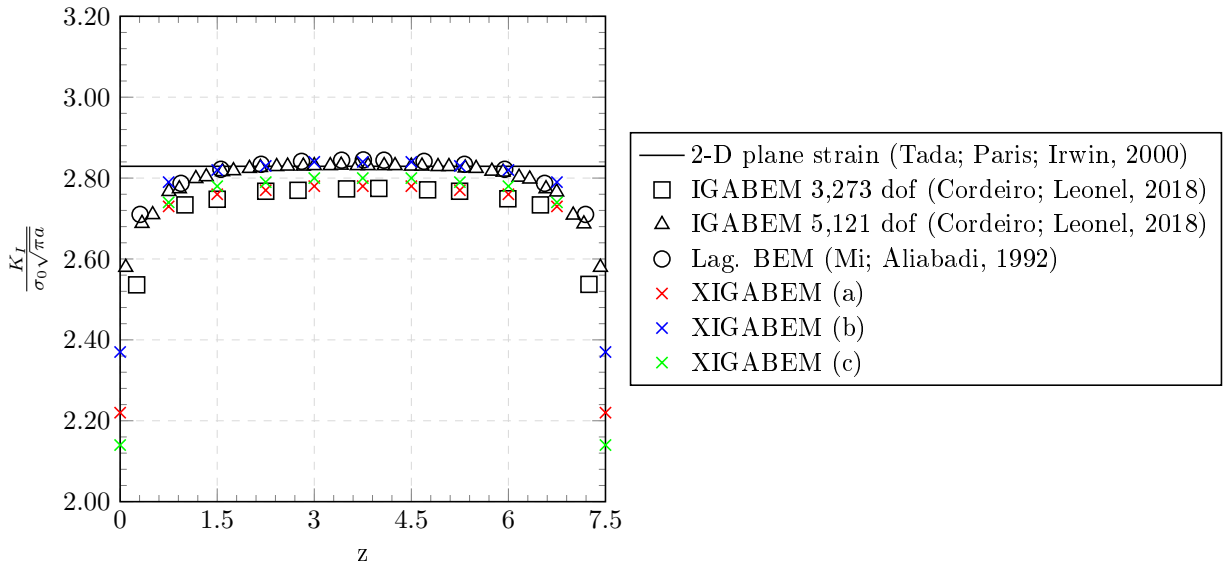

Source: The author.

summary, it is possible to obtain higher accuracy from coarser models, providing evidence of a gain in solution accuracy available using the extended IGABEM approach.

5.6 Partial conclusions

In this chapter, the Williams solution-based enrichment scheme allows the representation of the asymptotic behaviour of displacements near the crack front. Two different approaches consider the Williams solution: one on boundary faces partially cut by the crack, and another over the crack surfaces themselves. For the boundary faces, besides incorporating a behaviour that was not captured by the standard NURBS functions, this strategy precludes the need for a re-meshing task on this face. In addition, the Williams-based enrichment for crack faces introduces the Stress Intensity Factors directly as system unknowns, obtained in the solution vector, which removes a post-processing task for their determination. For the SIF enrichment, a tying constraint equation is responsible for obtaining the supplementary equations to recover a square algebraic system. As a consequence of the enrichment strategy, additional singular kernels arise, in which their correct treatment requires the derivatives of the enrichment functions for its use in the SST. Additionally, the correct representation of the local coordinate system of the crack front and its derivatives involves the Frenet-Serret frame, which is a suitable strategy for parametric curves. Numerical results have demonstrated the superior performance of the XIGABEM in comparison to both IGABEM and BEM, by analysing both planar and inclined cracks with different shapes, as well as a prismatic block with an edge crack.

6 FATIGUE CRACK GROWTH MODELLING WITH THE XIGABEM

Fatigue crack growth analysis with the LEFM is suitable for high-cycle loading scenarios. In this situation, the load amplitude is small enough not to cause material inelastic behaviour for a small amount of loading cycles, but it causes degradation through crack growth throughout the component life cycle. For LEFM to be admissible, it is assumed that the inelastic process zone ahead of the crack is negligible in size in comparison to the crack length and to the solid dimensions. The life prediction analysis then relies on empirical laws that relate the crack growth rate to the variation of the stress intensity factors over the load cycle. Because of its simplicity, the Paris-Erdogan Law is commonly applied for this type of problem, and is adopted in this study. It is noted that other crack growth laws may be applied if desired. In this context, the XIGABEM formulation presented in chapter 5 emerges as a suitable approach for fatigue crack growth analysis with the Paris-Erdogan Law. This law requires the SIFs for life cycle analysis, and these parameters are directly obtained from the Williams-based enrichment scheme. Consequently, crack growth analysis takes place immediately after solving the mechanical problem via IGABEM, without the need for any intermediate step to determine the SIFs.

This chapter initially presents the Paris-Erdogan Law and its application to predict the fatigue life of a cracked component under low-cycle repetitive load. Next, two crack growth criteria are presented: the hoop-stress (Erdogan; Sih, 1963) and Schollmann (Schöllmann *et al.*, 2002) criteria. Subsequently, this chapter details all modifications required within the XIGABEM framework to account for the crack propagation phenomenon. Finally, three numerical applications compare the responses from XIGABEM against reference solutions from the literature.

6.1 The Paris-Erdogan Law and fatigue life prediction

The Paris-Erdogan Law relates empirically the crack growth rate da/dN and the SIF range ΔK as:

$$\frac{da}{dN} = C(\Delta K)^m \tag{6.1}$$

in which C and m are material parameters for fatigue crack growth, whose determination relies on experimental studies. In a fully three-dimensional case, ΔK accounts for the equivalent SIF during a load cycle, which is a combination of the SIF of each mode. The crack growth criterion choice defines the equivalent SIF ΔK_{eq}. This study compares the use of two criteria: the hoop stress criterion (Erdogan; Sih, 1963) and the Schollmann criterion (Schöllmann *et al.*, 2002). The expressions for both the ΔK_{eq} and the propagation angle are present in section 6.2. It is worth mentioning that the power m in the SIF amplitude ΔK can significantly amplify the errors in the life cycle prediction when SIFs are not properly assessed. This requires high accuracy in the SIF determination, which is an advantage of the XIGABEM formulation developed in this thesis.

The classical approach for determining the required amount of cycles for the crack to grow from a length a to a length $a + \Delta a$ uses a constant approximation for the equivalent SIF

variation so that $\Delta K_{eq} = K_{eq}(a + \Delta a) - K_{eq}(a)$, which goes directly on eq. (6.1). Alternatively, this study uses the linear SIF approximation for the development of the eq. (6.1), firstly proposed by Andrade and Leonel (2019). The study of Cordeiro and Leonel (2019) applied this strategy for the three-dimensional BEM in a mixed-mode crack growth analysis, in which results have shown its advantages over the classical approach. In this context, the approximation of the equivalent SIF between the crack lengths a and $a + \Delta a$ is:

$$\Delta K_{eq} = \beta a + \gamma \tag{6.2}$$

in which β and γ are constants of the linear form as:

$$\begin{aligned} \beta &= \frac{\Delta K_{eq}(a + \Delta a) - \Delta K_{eq}(a)}{\Delta a} \\ \gamma &= \Delta K_{eq}(a) - \beta a \end{aligned} \tag{6.3}$$

The substitution of the eq. (6.2) in the Paris-Erdogan Law, eq. (6.1), and its integration result in:

$$\begin{aligned} &dN = \frac{da}{C(\Delta \bar{K}_{eq})^m} \Rightarrow \\ &N(a + \Delta a) - N(a) = \Delta N = \int_a^{a+\Delta a} \frac{1}{C[\Delta K_{eq}(a)]^m} da \Rightarrow \\ &\Delta N = \frac{1}{C} \int_a^{a+\Delta a} (\beta a + \gamma)^{-m} da \Rightarrow \\ &\Delta N = \frac{1}{C} \left[\frac{(\beta a + \gamma)^{1-m}}{(1-m)\beta} \right]_a^{a+\Delta a} \Rightarrow \\ &\Delta N = \frac{\Delta a \{ [\Delta K_{eq}(a + \Delta a)]^{1-m} - [\Delta K_{eq}(a)]^{1-m} \}}{C(1-m)[\Delta K_{eq}(a + \Delta a) - \Delta K_{eq}(a)]} \end{aligned} \tag{6.4}$$

in which ΔN stands for the increment in the number of cycles in the crack advancement from a to $a + \Delta a$. Cordeiro and Leonel (2019) have shown that this alternative formulation allows for the use of higher crack growth steps Δa in comparison to the classical approach. This enables a reduction in the computational cost by reducing the mesh density in crack growth analysis .

Finally, the total number of cycles of loading and unloading becomes the sum of each ΔN of all propagation steps of the analysis. In a computational assessment of the life cycle, the maximum increment $\Delta a_{\max}$ occurs at the crack front location with maximum $\Delta K_{eq}^{\max}$. The advancement for each point $\mathbf{x}_i$ at the crack front considers a weighting factor based on the Paris-Erdogan Law in a discrete manner as:

$$\Delta a(\mathbf{x}_i) = \Delta a_{\max} \left(\frac{\Delta K_{eq}(\mathbf{x}_i)}{\Delta K_{eq}^{\max}} \right)^m \tag{6.5}$$

in which $\Delta K_{eq}^{\max}$ is the maximum $\Delta K_{eq}(\mathbf{x}_i)$ at the crack front for the current propagation step.

6.2 Crack growth criteria

The crack growth criterion is responsible for defining the crack propagation angle θ_p associated with the local coordinate system at the crack front to define the new crack front

location. Several studies have proposed techniques to define the proper crack path considering the mechanical response, the type of loading and the thermodynamics of the fracture process. For the LEFM in particular, either a global or local energy balance may be capable of describing this phenomenon. Both techniques rely on the SIFs to represent the stress state at the crack front, which in this work are directly defined with the solution of the boundary value problem for each crack increment. In this study, the choice of the maximum hoop stress criterion (Erdogan; Sih, 1963) stems from its use in previous studies of three-dimensional IGABEM crack propagation (Peng *et al.*, 2017a; Sun; Dong, 2021; Sun; Dong, 2023). However, since the maximum hoop stress criterion does not consider the Mode III in the crack propagation angle, the Schollmann criterion (Schöllmann *et al.*, 2002) incorporates its effects on the crack growth process. This study presents a fully three-dimensional criterion that allows for the correct computing of the crack front angle. The brittle failure of the material occurs when $K_{eq} \geq K_{Ic}$, in which K_{Ic} is the material toughness for both criteria. It is noteworthy that the fatigue crack growth only occurs if $K_{eq} \geq K_{Ith}$, in which K_{Ith} is the threshold for the fatigue phenomenon.

6.2.1 Maximum hoop stress criterion

The maximum hoop stress criterion seeks the direction in which the hoop stress is maximised for a given loading scenario. This occurs for an angle θ_p so that:

$$\theta_p = 2 \arctan \left[\frac{-2(K_{II}/K_I)}{1 + \sqrt{1 + 8(K_{II}/K_I)^2}} \right] \tag{6.6}$$

and the equivalent SIF K_{eq} that incorporates the mode III effects according to Gerstle (1986) is:

$$K_{eq} = \sqrt{K_I^2 + K_{II}^2 + (1+\nu)K_{III}^2} \tag{6.7}$$

While the K_{eq} contains the influence of mode III through K_{III}, the crack propagation angle does not take this mode into account. Thus, mixed-mode fracture problems having a non-zero mode III component may not be properly represented by this criterion.

6.2.2 Schollmann criterion

The Schollmann criterion (Schöllmann *et al.*, 2002) defines the propagation angle such that it maximises the principal stress $\sigma_1^{'}$ in the local coordinate system defined on the crack front. The principal stress value is:

$$\sigma_1^{'} = \frac{\sigma_\theta + \sigma_{\bar{x}3}}{2} + \frac{\sqrt{(\sigma_\theta + \sigma_{\bar{x}3})^2 + 4(\tau_{\theta\bar{x}3})^2}}{2} \tag{6.8}$$

in which all stress variables are written according to a local coordinate system at the crack front, as shown in fig. 72. By assuming that the component $\sigma_{\bar{x}3}$ does not affect the propagation angle, the Schollmann criterion takes $\sigma_{\bar{x}3} = 0$. Then, the equivalent SIF is:

Figure 72 – Local coordinate system for the crack front stresses.

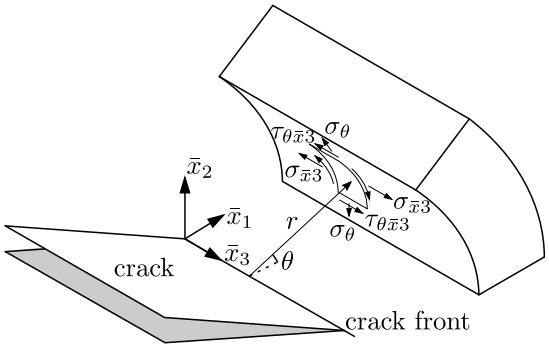

Source: The author.

$$K_{eq} = \frac{1}{2}\cos\left(\frac{\theta_p}{2}\right)\left\{K_I\cos^2\left(\frac{\theta_p}{2}\right) - \frac{3}{2}K_{II}\left(\sin\theta_p\right) + \sqrt{\left[K_I\cos^2\left(\frac{\theta_p}{2}\right) - \frac{3}{2}K_{II}\left(\sin\theta_p\right)\right]^2 + 4K_{III}^2}\right\} \tag{6.9}$$

and the equation for the propagation angle θ_p is:

$$\begin{aligned}
\Theta &= \frac{1}{8\sqrt{2\pi r}}\left\{\frac{-K_I\bar{S}}{2} - K_{II}\bar{C}_1 + \frac{1}{2}\left[2\left[\left(K_I\bar{C}_2 - K_{II}\bar{S}\right) - K_{II}\bar{C}_1\right]\left[\frac{-K_I\bar{S}}{2} - K_{II}\bar{C}_1\right]\right.\right. \\
&\left.\left. -16K_{III}^2\sin\left(\theta_p\right)\right]\left[\left[K_I\bar{C}_2 - K_{II}\bar{S}\right]^2 + 64K_{III}^2\cos^2\left(\frac{\theta_p}{2}\right)\right]^{-\frac{1}{2}}\right\} = 0 \\
\bar{C}_1 &= \frac{3}{2}\cos\left(\frac{\theta_p}{2}\right) + \frac{9}{2}\cos\left(\frac{3\theta_p}{2}\right) \\
\bar{C}_2 &= 3\cos\left(\frac{\theta_p}{2}\right) + \cos\left(\frac{3\theta_p}{2}\right) \\
\bar{S} &= 3\sin\left(\frac{\theta_p}{2}\right) + 3\sin\left(\frac{3\theta_p}{2}\right)
\end{aligned} \tag{6.10}$$

There is no analytical solution for the eq. (6.10), but θ_p may be determined numerically. This study applies the Golden Section algorithm to determine the propagation angle. In addition, the Schollmann criterion defines the twist angle ψ_p as:

$$\psi_p = \frac{1}{2}\arctan\left[\frac{2\tau_{\theta\bar{x}3}(\theta_p)}{\sigma_\theta(\theta_p) - \sigma_{\bar{x}3}(\theta_p)}\right] \tag{6.11}$$

The twist angle influence on the XFEM (Pereira; Duarte; Jiao, 2010) and in the BEM (Cordeiro; Leonel, 2019) relies on a crack front equivalent element. Both studies considered a linear approximation for this element, while in this study NURBS curves represent the crack front. There is therefore no natural equivalence for these strategies. In this study a zero twisting angle is assumed for simplicity; its influence on the crack front propagation within XIGABEM is suggested as a possible avenue for future work.

Figure 73 – Definition of new crack position based on points and the corresponding new crack front.

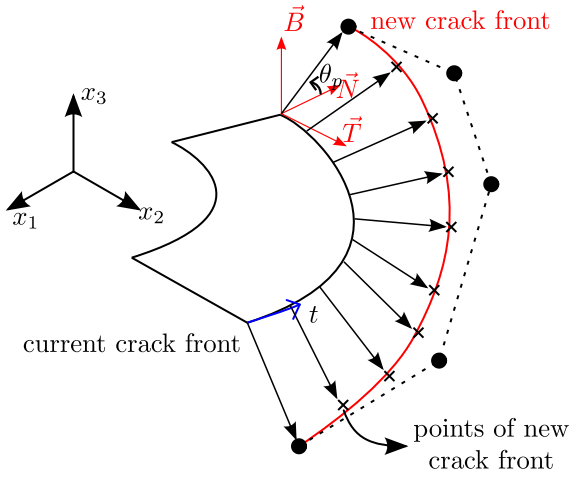

Source: The author.

6.3 Crack propagation framework in XIGABEM

In a crack growth framework within the XIGABEM, the definition of the propagation angle and the increment for the crack front takes place considering the solution of the boundary value problem for the previous geometry. Then, in a numerical framework, a new set of points defining the crack front are the starting point to determine a parametric curve that best represent them. Previous studies (Peng *et al.*, 2017a; Sun; Dong, 2021) for the crack growth in IGABEM applied a crack front updating algorithm proposed by LaGreca, Daniel and Bac (2004). This framework involves the movement of the existing control points that defined the previous crack front so that they best fit the new crack front points. However, this strategy does not allow the NURBS weights to be adjusted during the crack growth procedure, which leads to a sub-optimal representation of the crack front during its advance. In the current work, a least-squares fitting defines the new crack front based on an isogeometric representation with NURBS curves, as in Carlson (2009).

The new procedure for the crack front updating using the IGABEM considers initially that the previous knot span and degree of the NURBS crack front remains the same for the new crack front. The sample points $\tilde{C}_k^{ij}$ define the coordinate in the k direction of the updated front, and these come from a point-wise propagation of a uniformly spaced set of points whose parametric coordinate are t_j^i on the NURBS curve i that defined the growing crack front. The algorithm considers a crack propagation for multiple crack surfaces simultaneously. Figure 73 illustrates this sampling procedure and the definition of the new point based on Δa and θ_p.

The least-squares fitting algorithm proceeds by writing a minimisation problem for the squared distance of the sampled point $\tilde{C}_k^{ij}$:

$$\begin{aligned} &\min F = \mathbf{f}^T\mathbf{f} \\ &f_\ell = C_k(t_j^i, \mathbf{P}^i, \mathbf{w}^i) - \tilde{C}_k^{ij} \end{aligned} \tag{6.12}$$

in which $\mathbf{P}^i$ and $\mathbf{w}^i$ are the control points and weights of the optimised NURBS curve, while ℓ is a global connectivity index related to the indices i, j, and k. These two sets of variables are the output of this analysis. By applying the Gauss-Newton method and its truncation in the first term, the eq. (6.12) becomes:

$$\mathbf{J}^T\mathbf{J}\boldsymbol{\Delta}\mathbf{x} = -\mathbf{J}^T\mathbf{f} \tag{6.13}$$

in which the vector $\boldsymbol{\Delta}\mathbf{x} = \{\boldsymbol{\Delta}\mathbf{P} \;\; \boldsymbol{\Delta}\mathbf{w}\}^T$ stores the increments in each of the optimising variables (control points and weights), and the Jacobian $\mathbf{J}$ is:

$$\mathbf{J} = [\mathbf{J}_P \;\; \mathbf{J}_w] \tag{6.14}$$

corresponding to the first derivative of the vector $\mathbf{f}$ with respect to $\mathbf{P}^i$ and $\mathbf{w}^i$, for $\mathbf{J}_P$ and $\mathbf{J}_w$, respectively. Their expressions are present in Carlson (2009), which involves the intermediate matrix B_{P^i}:

$$B_{P^i} = \begin{pmatrix} \dfrac{\partial f_\ell}{\partial P^i} & 0 \\ 0 & \dfrac{\partial f_\ell}{\partial P^i} \end{pmatrix} \tag{6.15}$$

in which the partial derivative with respect to the control point is:

$$\frac{\partial f_\ell}{\partial P^i} = \phi_i \tag{6.16}$$

in which ϕ_i is the corresponding basis function of the control point P^i. The Jacobian $\mathbf{J}_P$ is:

$$\mathbf{J}_P = \begin{pmatrix} B_{P^1}(t_1) & B_{P^2}(t_1) & \cdots & B_{P^n}(t_1) \\ B_{P^1}(t_2) & B_{P^2}(t_2) & \cdots & B_{P^n}(t_2) \\ \vdots & \vdots & \ddots & \vdots \\ B_{P^1}(t_m) & B_{P^2}(t_m) & \cdots & B_{P^n}(t_m) \end{pmatrix} \tag{6.17}$$

in which m denotes the total of sampled points in the NURBS curve, and n is the total of control points of this curve. The Jacobian matrix $\mathbf{J}_w$ involves the partial derivative with respect to the weights, being:

$$\mathbf{J}_w = \begin{pmatrix} \dfrac{\partial f_\ell(t_1)}{\partial w_1} & \dfrac{\partial f_\ell(t_1)}{\partial w_2} & \cdots & \dfrac{f_\ell(t_1)}{\partial w_n} \\ \dfrac{\partial f_\ell(t_2)}{\partial w_1} & \dfrac{\partial f_\ell(t_2)}{\partial w_2} & \cdots & \dfrac{f_\ell(t_2)}{\partial w_n} \\ \vdots & \vdots & \ddots & \vdots \\ \dfrac{\partial f_\ell(t_m)}{\partial w_1} & \dfrac{\partial f_\ell(t_m)}{\partial w_2} & \cdots & \dfrac{f_\ell(t_m)}{\partial w_n} \end{pmatrix} \tag{6.18}$$

$$\frac{\partial f_\ell}{\partial w_i} = \frac{\left(\sum_{i=1}^n N_i w_i\right) N_i P_k^i - N_i \left(\sum_{i=1}^n N_i w_i P_k^i\right)}{\left(\sum_{i=1}^n N_i w_i\right)^2}$$

It is worth mentioning that the first and the last control points of each NURBS curve are fixed based on the propagation angle and crack increment of the end points. When a NURBS curve endpoint shares its position with an endpoint of another NURBS curve, their corresponding

Figure 74 – Averaging endpoints to guarantee C^0 continuity between NURBS surfaces.

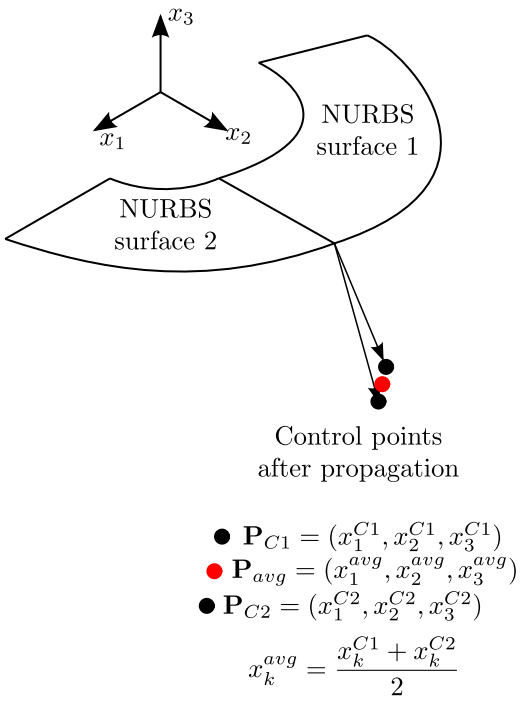

Source: The author.

control point is taken as the average of the resulting point from the propagation of each patch separately, as shown in fig. 74. This guarantees a C^0 continuity when multiple NURBS surfaces, and therefore multiple NURBS curves, describe a single crack front.

After finding the set of control points and weights that best approximates the new crack front, the enrichment nature requires also tangential and normal alignments between the junctions of each NURBS curve. For problems with multi-patch NURBS surfaces representing the crack surface, the optimisation for the crack growth update does not guarantee continuity for the local coordinate system at these points. This is an issue because this continuity is a requirement for the set of the enrichment functions herein applied. To circumvent it, a gradient descent algorithm promotes the alignment between the tangents and the normal outward vectors at each endpoint. The tangent vector at the end points is aligned with the vector between the first and second control points, for the initial point, or between the penultimate and last control points, for the final point, as illustrated in fig. 75.

Following the definition of fig. 75, let $\vec{A} = \mathbf{P}^A - \mathbf{P}^e$ be the vector between the endpoint $\mathbf{P}^e$ and the point $\mathbf{P}^A$ from the NURBS curve c_m, while $\vec{B} = \mathbf{P}^B - \mathbf{P}^e$ is the vector from $\mathbf{P}^e$ to the $\mathbf{P}^B$ on the neighbouring NURBS curve c_n. The tangent alignment comes from a collinearity condition as:

$$g_1 = 1 - \left| \frac{\vec{A}.\vec{B}}{||\vec{A}||.||\vec{B}||} \right| = 0 \tag{6.19}$$

in which both $\vec{A}$ and $\vec{B}$ are functions only of the second/penultimate control points of the curves c_m and c_n. The gradient descent strategy updates the control points $\mathbf{P}^A$ and $\mathbf{P}^B$ as:

Figure 75 – Control points position for each updated crack front for tangent alignment.

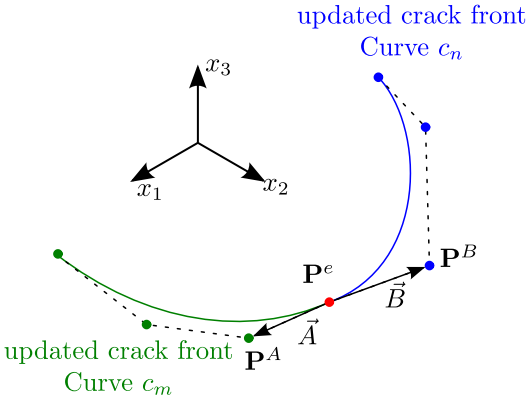

Source: The author.

$$\left\{ \begin{array}{c} \mathbf{P}^A \\ \mathbf{P}^B \end{array} \right\}^{k+1} = \left\{ \begin{array}{c} \mathbf{P}^A \\ \mathbf{P}^B \end{array} \right\}^{k} - \alpha_{GD} \left\{ \begin{array}{c} \dfrac{\partial g_1}{\partial \mathbf{P}^A} \\ \dfrac{\partial g_1}{\partial \mathbf{P}^B} \end{array} \right\}^{k} \tag{6.20}$$

in which the partial derivatives are:

$$\begin{aligned} \frac{\partial g_1}{\partial P_\ell^A} &= -\frac{\text{sign}(\vec{A}.\vec{B})B_\ell||\vec{A}||||\vec{B}|| - \dfrac{(\vec{A}.\vec{B})(P_\ell^A - P_\ell^e)||\vec{B}||}{||\vec{A}||}}{(||\vec{A}||\,||\vec{B}||)^2} \\ \frac{\partial g_1}{\partial P_\ell^B} &= -\frac{\text{sign}(\vec{A}.\vec{B})A_\ell||\vec{A}||||\vec{B}|| - \dfrac{(\vec{A}.\vec{B})(P_\ell^B - P_\ell^e)||\vec{A}||}{||\vec{B}||}}{(||\vec{A}||\,||\vec{B}||)^2} \end{aligned} \tag{6.21}$$

In the incremental procedure, the stopping criterion is based on the scalar g_1 associated with the tangent alignment condition. α_{GD} is a parameter set in the beginning of the analysis that considers the influence of the gradient during the iterative process. The alignment conditions are applied sequentially, in which firstly the tangent alignment occurs, and its result is the input data for the normal alignment. The normal outward alignment condition stems from using the inner product of the normal outward vector from each neighbouring NURBS curve as:

$$g_2 = 1 - |\vec{N}^m.\vec{N}^n| = 0 \tag{6.22}$$

in which $\vec{N}^m$ and $\vec{N}^n$ are the normal vectors at the shared point of the curves c_m and c_n. The gradient descent method for the outward normal vectors occurs in a similar fashion as eq. (6.20), but updating all control points of each NURBS curve

$$\left\{ \begin{array}{c} \mathbf{P}^m \\ \mathbf{P}^n \end{array} \right\}^{k+1} = \left\{ \begin{array}{c} \mathbf{P}^m \\ \mathbf{P}^n \end{array} \right\}^{k} - \alpha_{GD} \left\{ \begin{array}{c} \dfrac{\partial g_2}{\partial \mathbf{P}^m} \\ \dfrac{\partial g_2}{\partial \mathbf{P}^n} \end{array} \right\}^{k} \tag{6.23}$$

and the partial derivatives associated with the normal outward alignment are:

Figure 76 – New crack surface generation based on new crack front.

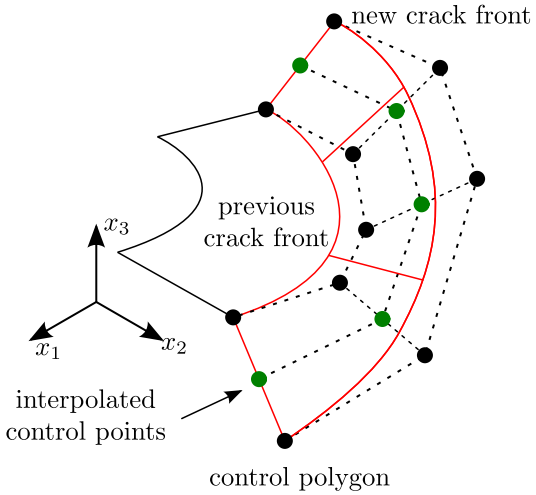

Source: The author.

$$\frac{\partial g_2}{\partial P_\ell^m} = \text{sign}(g_2) \sum_{k=1}^{3} \left(\frac{\partial N_k^m}{\partial P_\ell^m} N_k^n \right)$$
$$\frac{\partial g_2}{\partial P_\ell^n} = \text{sign}(g_2) \sum_{k=1}^{3} \left(\frac{\partial N_k^n}{\partial P_\ell^n} N_k^n \right) \tag{6.24}$$

in which a finite difference strategy computes the partial derivatives of the normal outward vector due to their complex analytical determination.

6.4 Modifications in the XIGABEM algebraic system

The fatigue crack propagation analysis with XIGABEM requires an incremental simulation, in which for each propagation step a new set of isogeometric surfaces represents the updated crack front. The generation of these new crack surfaces relies on the connection between the previous and the updated crack front as illustrated in fig. 76. The perpendicular direction receives the same knot vector as the previous surface. The new control points of this surface are found from a direct interpolation between the control points of the previous and new fronts.

The Greville Abscissae strategy generates the collocation points on the new surfaces, and application of the relevant boundary integral equations at these points requires integration over all the existing domain. In addition, the integration over the new portion of the boundary, formed by the latest crack surface increment(s), is also required for the pre-existing collocation points. In this stage, additional rows and columns arise in the algebraic system, the rows referring to the new collocation points and the columns to the displacement and traction coefficients for the new surfaces. It is important to recall that the remainder of the algebraic system is unaffected by the introduction of new crack surface elements.

After the definition of the new crack front, the determination of the enrichment terms occurs simultaneously to the integration of the corresponding new surfaces. With the definition

of the new crack front, all enrichment terms from the previous step are removed from the system, and previously enriched elements return to the standard (unenriched) IGABEM description.

When the crack intersects the external boundary, its growth also affects these faces. This study applies only the Heaviside enrichment to these faces for simplicity, while future work may consider applying the Williams-based solution. In this case, enriched basis functions with unchanged support remain unaltered, ensuring that their influence on the algebraic system is preserved from the previous propagation step to the next. This yields a computational gain by removing the need for recomputing the influence of this enrichment. In addition, the crack growth modifies the support of some enriched basis functions, and their corresponding contribution is removed and recomputed. Another possibility is the need to enrich basis functions that were not previously enriched, whose contributions will be computed during the integration from new collocation points and the existing boundary. The strategy for supplementary equations in this case is the minimisation of the L_2 error between the displacements at the crack edge and those at the intersected face.

6.5 Numerical applications

This section presents four numerical applications of the XIGABEM formulation for fatigue crack growth simulation. The first application considers an elliptical crack in a prism, where the loading conditions induce a pure mode I growth. Its elliptical shape becomes circular during crack propagation. The second application addresses an inclined penny-shaped crack under traction fatigue load, leading to a mixed-mode I/II/III propagation. The third application is a prism with an edge crack that evaluates the algorithm's ability to represent crack growth as the crack intersects the external boundary. The fourth application comprises a numerical analysis of a hook under cyclic loading, in which the isogeometric formulation deals with a complex geometry for both the external boundary and the initial crack, as well as with its change of curvature during the crack growth propagation.

6.5.1 Elliptical crack growth

The first application of the fatigue crack growth analysis with the XIGABEM involves the fatigue analysis of an elliptical shaped crack immersed in a prismatic solid. The geometry and boundary conditions are presented in fig. 77, in which the crack centre is at the coordinates $(0, 0, 0)$. A uniformly distributed traction varying from $\sigma_2^{\min} = 0$MPa to $\sigma_2^{\max} = 200$MPa is applied on the upper face, while the lower face is clamped. The material is a Ti-6Al-4V alloy, whose properties are given in table 8. The Paris constants provided assume units of ΔK and da/dN to be MPa mm$^{0.5}$ and mm/cycle. The numerical modelling of the elliptical crack considers 5 bi-quadratic ($p = q = 2$) NURBS surfaces modelling each crack surface, as in fig. 78, i.e. 10 NURBS surfaces are used for both crack sides. The inner elliptical surface has dimensions equivalent to 80% of the elliptical crack. The complex K_I variation along the crack front affects the crack propagation increment by triggering eq. (6.5). This application has been studied by Ilie and Ince (2022), in which a finite element analysis obtained results that approximate well

their proposed reference solution for the crack front advancement. The fatigue analysis stops after 10 increments, with a maximum increment of $\Delta a_{\max} = 0.6$mm.

Figure 77 – Geometry and boundary conditions of elliptical crack immersed in prismatic solid.

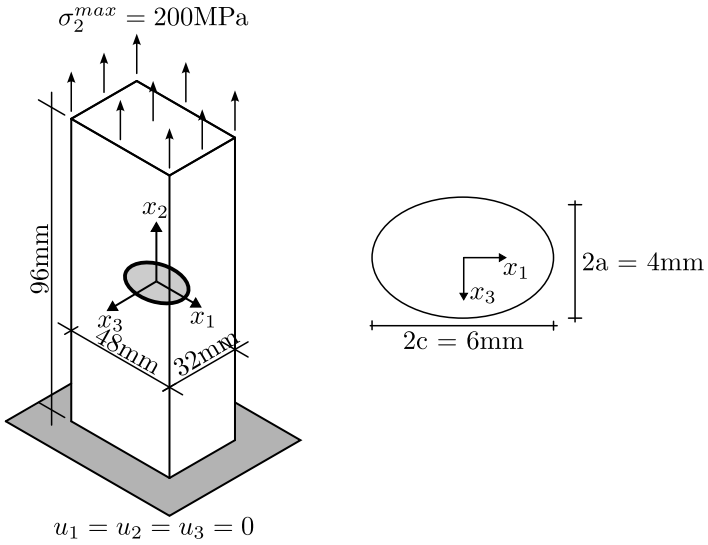

Source: The author.

Table 8 – Material and fatigue properties of Ti-6Al-4V alloy.

Young Modulus	$E = 115$GPa
Poisson's ratio	$\nu = 0.3$
Paris constant	$C = 1.77.10^{-14}$
Paris exponent	$m = 3.667$

Source: The author.

Three isogeometric meshes are used to test the performance of the proposed XIGABEM algorithm for the propagation of the elliptical crack under the given cyclical load. The coarse mesh, namely mesh 1 and shown in fig. 78, has its control points, weights and knot vectors given in the Appendix B. The uniform knot insertion refinement in both directions of mesh 1 generates the finer meshes 2 and 3. Meshes 1, 2 and 3 have 114, 184 and 274 collocation points, respectively, for the initial crack. The Schollmann criterion is adopted for the determination of the crack propagation angle; however, since the in-plane elliptical crack has a pure mode I response, there is no significant difference between the two criteria used in this study. In addition, table 9 presents the number of degrees of freedom in each propagation step, which highlights the XIGABEM ability of representing a curved problem with a small number of degrees of freedom.

The crack configuration for Mesh 2, in the first step, the fifth step and the last step, are shown in fig. 79. In addition, fig. 80 presents the deformed shape amplified by a factor of 1000 for each mesh in their last propagation step. As expected for this geometry during crack growth, the crack geometry transforms from its initial elliptical shape into a circular shape. Additionally, the XIGABEM formulation promotes the tying between the upper and lower crack faces, and

Figure 78 – Isogeometric mesh and control points for elliptical crack.

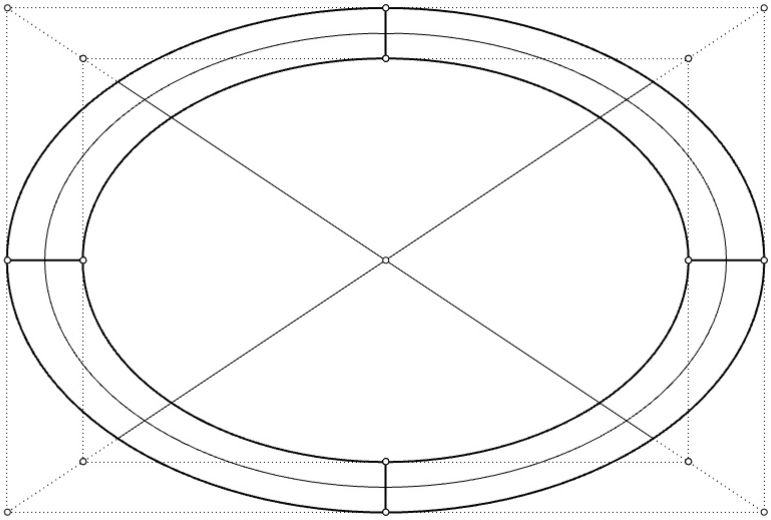

Source: The author.

Table 9 – Number of degrees of freedom at each propagation step.

	Number of degrees of freedom		
step	Mesh 1	Mesh 2	Mesh 3
0	378	600	882
1	594	888	1362
2	810	1176	1842
3	1026	1464	2322
4	1242	1752	2802
5	1458	2040	3282
6	1674	2328	3762
7	1890	2616	4242
8	2106	2904	4722
9	2322	3192	5202
10	2538	3480	5682

Source: The author.

this reduces the error in this region. Also, all three meshes give rise to a similar displacement field, which demonstrates the ability of the XIGABEM formulation to capture the response well even using coarse meshes. Moreover, the fatigue life cycle assessment for the elliptical crack in fig. 81 demonstrates a convergence pattern for the required amount of cycles, and this response agrees with the reference solution of Ilie and Ince (2022).

Figure 79 – Elliptical crack growth: steps 1, 5 and 10.

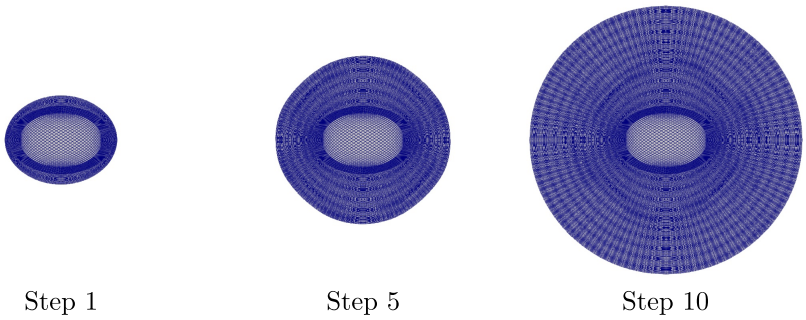

Source: The author.

Figure 80 – Deformed shape for each mesh in tenth propagation step.

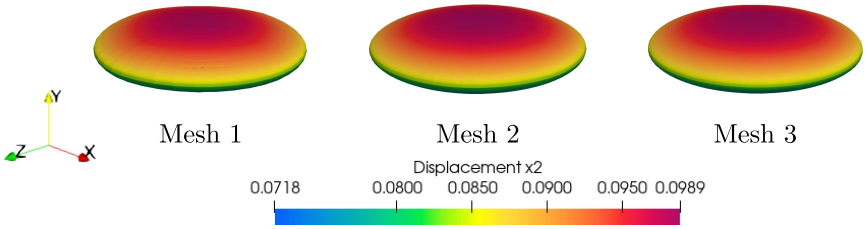

Source: The author.

Figure 81 – Fatigue life assessment of elliptical crack in in prismatic solid.

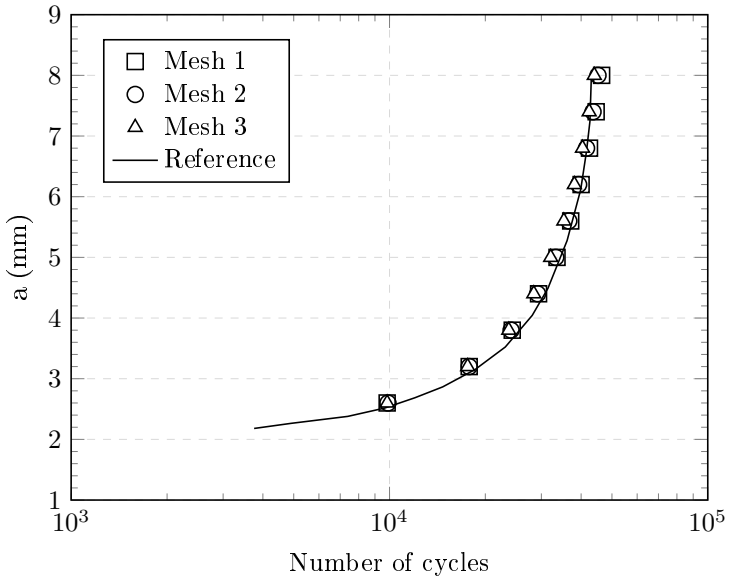

Source: The author.

6.5.2 Inclined penny-shaped crack growth

The second numerical application of the XIGABEM formulation for the fatigue crack growth assessment consists of an inclined penny-shaped crack as shown in fig. 82. The crack has radius $R = 0.1$m, is located centrally in a cube of side $a = 2.0$m, and is inclined by an angle $\pi/4$ rad. The isogeometric mesh for the crack geometry contains 5 NURBS surfaces of degree $p = q = 2$ for each crack surface, i.e. a total of 10 NURBS surfaces is used for the crack. The central portion of the crack is circular with a radius $R_{int} = 0.08$m while the annular outer portion of the crack is modelled using 4 NURBS surfaces, as shown in fig. 83. For the numerical analysis, this geometrical mesh undergoes two knot insertions in each parametric direction, which results in a total of 274 collocation points. In the face in which $x_1 = -1.0$, the prescribed displacement is $u_1 = 0.0$, while lower face $x_2 = -1.0$ has $u_2 = 0.0$ and the face with $x_3 = -1.0$ contains $u_3 = 0.0$ as an enforced displacement. The upper face $x_2 = 1.0$ is subjected to a load varying cyclically between $\sigma_2^{\min} = 0$MPa and $\sigma_2^{\max} = 1$MPa. Continuity between each crack surface is not naturally enforced in a multi-patch discretisation, which justifies the local adjustment for tangent and normal outward vectors. The loading condition results in a fully mixed mode I/II/III response due to the crack inclination. Pereira, Duarte and Jiao (2010) analysed this geometry with the hp-generalised FEM approach, in which the Schollmann criterion defined the crack growth direction for the crack. The material and fatigue properties are presented in table 10, in which the Paris constants assumed the units used for ΔK and da/dN to be MPa mm$^{0.5}$ and mm/cycle. The fatigue analysis terminates after 20 propagation steps. The proportion between the initial crack and the final crack configuration from the results obtained by Pereira, Duarte and Jiao (2010) indicates that those authors applied a $\Delta a_{\max}$ of 0.1m rather than the value of 0.002m stated in their description. Our parameters adopted in this study are tuned to allow a direct comparison of the end state of the crack against the Pereira, Duarte and Jiao (2010) results. The hoop stress criterion and the Schollmann criterion are both tested for defining the crack evolution. In addition, these two criteria are compared using K_{III} in their equations (as expected) and taking $K_{III} = 0$ for the crack propagation angle and equivalent SIF, in an attempt to compare with Pereira, Duarte and Jiao (2010). This application has a reference solution (Tada; Paris; Irwin, 2000) for the LEFM case, according to eq. (5.32).

Table 10 – Material and fatigue properties of inclined penny-shaped crack.

Young Modulus	$E = 1000$MPa
Poisson's ratio	$\nu = 0.3$
Paris constant	$C = 1.5463.10^{-11}$
Paris exponent	$m = 2.1$
Maximum increment	$\Delta a_{\max} = 0.0185$m

Source: The author.

The crack configurations for the initial geometry, and for the seventh, fourteenth and twentieth steps are presented in fig. 84, considering both hoop stress and Schollmann criteria and the presence or absence of K_{III} in the propagation analysis. Figure 85 shows the final crack configuration reproduced from Pereira, Duarte and Jiao (2010). Both geometries are similar

Figure 82 – Geometry and boundary conditions of inclined penny-shaped crack.

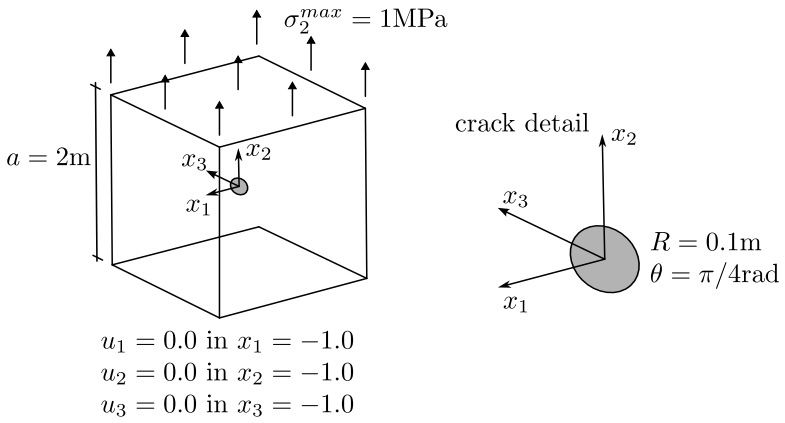

Source: The author.

Figure 83 – Isogeometric mesh and control points position for inclined penny-shaped crack.

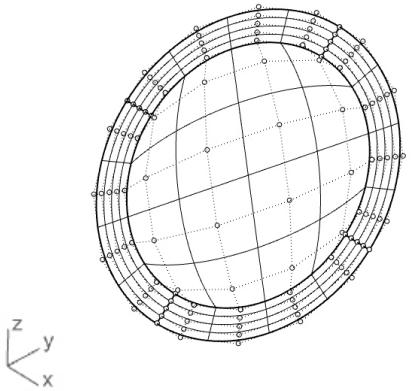

Source: The author.

when comparing all four scenarios obtained by XIGABEM with the reference response with the Schollmann criterion. As expected, the crack grows in a manner leading towards a pure mode I configuration with Schollmann criterion, as also found in the reference solution. However, the hoop stress criterion with and without K_{III} influence and the Schollmann criterion without K_{III} also lead to a similar crack configuration to that predicted using the Schollmann criterion considering K_{III} effects. This suggests that the choice between these two criteria for this application does not significantly alter the final response. This contrasts with Pereira, Duarte and Jiao (2010), who found their crack configuration when $K_{III} = 0$ not to reach a fully in-plane, circular geometry at the end of the analysis; the XIGABEM response is similar for all four different scenarios in the present study. In addition, the number of degrees of freedom at the last propagation step for the XIGABEM response is 8082, demonstrating the ability of XIGABEM to obtain accurate solutions for cracked problems with a small number of degrees of freedom.

The SIF comparison between the results obtained by the XIGABEM and the solution from Pereira, Duarte and Jiao (2010) for the final propagation step and using the Schollmann criterion is shown in fig. 86. In addition, the average value for K_I and the coefficient of variation (standard deviation divided by the mean value) for each case and the Pereira, Duarte and Jiao

Figure 84 – Inclined penny-shaped crack configuration during fatigue growth by XIGA-BEM considering (a) Hoop stress criterion, (b) Schollmann criterion, (c) Hoop stress criterion with $K_{III} = 0$, and (d) Schollmann criterion with $K_{III} = 0$.

step 7 step 14 step 20

(a) Hoop stress criterion

step 7 step 14 step 20

(b) Schollmann criterion

step 7 step 14 step 20

(c) Hoop stress criterion with $K_{III} = 0$ in K_{eq}

step 7 step 14 step 20

(d) Schollmann criterion with $K_{III} = 0$ in θ_c

Source: The author.

Table 11 – Average values for K_I in the last propagation step for Hoop stress criterion and for Schollmann criterion.

	avg. K_I (MPa$\sqrt{\text{m}}$)	Coefficient of Variation
Pereira, Duarte and Jiao (2010)	0.7316	0.40%
Hoop stress criterion	0.7511	0.84%
Schollmann criterion	0.7541	0.66%
Hoop stress criterion $K_{III} = 0$ in K_{eq}	0.7505	0.41%
Schollmann criterion $K_{III} = 0$ in θ_c	0.7491	0.38%

Source: The author.

(2010) solution in its last propagation step are presented in table 11. The discrepancy between the results and the reference solution may be associated to the absence of the crack front torsion angle in the definition of the new crack front in comparison to the hp-GFEM approach. Still, both strategies result in approximately constant K_I along the crack front, which is further evidence that the crack has evolved to a circular shape in a plane perpendicular to the applied load. In addition, the K_{II} and K_{III} values have reduced to negligible values by the last propagation step.

Figure 85 – Inclined penny-shaped crack configuration from the hp-GFEM approach (Pereira; Duarte; Jiao, 2010), considering (a) Schollmann criterion and (b) Schollmann criterion with $K_{III} = 0$.

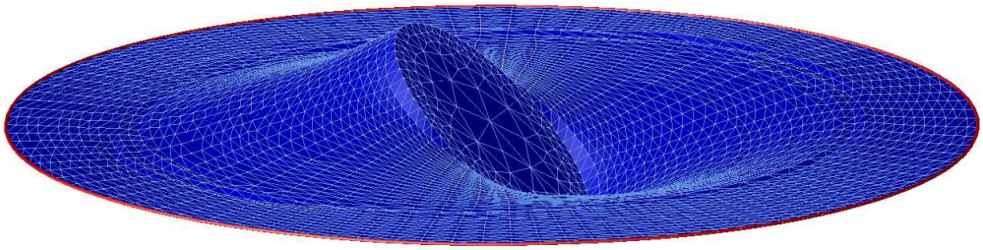

(a) Schollmann criterion - hp-GFEM

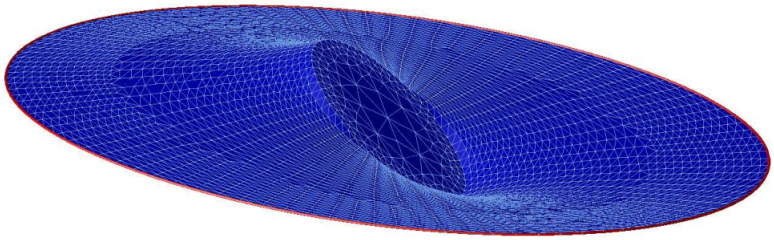

(b) Schollmann criterion with $K_{III} = 0$ - hp-GFEM

Source: The author.

Figure 86 – SIF distribution along crack front at the last propagation step: Schollmann criterion and comparison against hp-GFEM results from Pereira, Duarte and Jiao (2010).

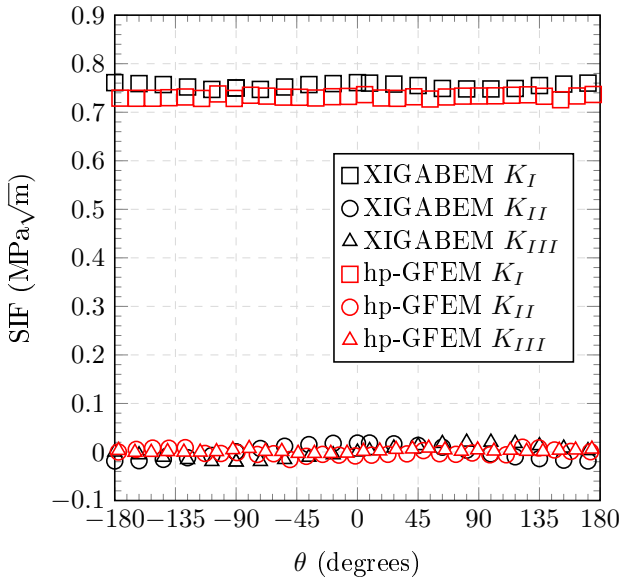

Source: The author.

Figure 87 – SIF distribution along crack front at the last propagation step: Schollmann criterion considering $K_{III} = 0$ for propagation angle and comparison against hp-GFEM results from Pereira, Duarte and Jiao (2010).

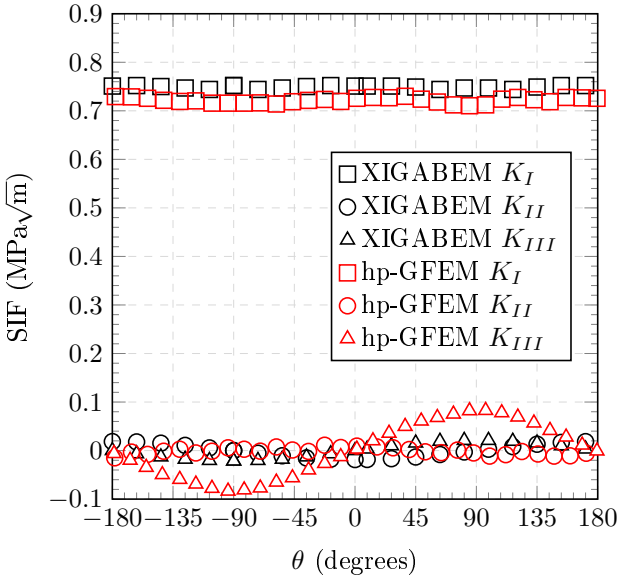

Source: The author.

Figure 87 compares the SIFs between the XIGABEM approach and the hp-GFEM approach (Pereira; Duarte; Jiao, 2010) with the Schollmann criterion using $K_{III} = 0$ during propagation, and for the last propagation step. The most important result for this problem, i.e. K_I, is largely unaffected by taking $K_{III} = 0$. The XIGABEM results for K_{II} and K_{III} are also very similar to the case in which K_{III} is not taken to be zero for the calculation of the propagation angle. Accordingly, the XIGABEM formulation was capable of achieving a pure mode I response, while the oscillation in the hp-GFEM results of Pereira, Duarte and Jiao (2010) is consistent with the final geometry of the crack not having reached a plane perpendicular to the applied load. Also, fig. 88 presents the SIFs for the last step using the hoop stress criterion, with K_{III} and without K_{III} effects on the equivalent SIF, respectively. Similarly, in these two cases, the SIF distribution matches that found with the Schollmann criterion (both with and without K_{III} effects on the propagation angle), which indicates that for the XIGABEM formulation the adoption of either of these two criteria will lead to similar responses.

Figure 89, fig. 90 and fig. 91 present the evolution of each SIF during propagation using the hoop stress criterion, while fig. 92, fig. 93 and fig. 94 correspond to the SIF evolution using the Schollmann criterion. Additionally, these graphs present the SIF variation of the initial configuration (step 0) along the crack front and its comparison with the reference solution given by eq. (5.32). Based on the comparison for the initial geometry, the XIGABEM response agrees with the reference response, as also previously found in section 5.5.1 for a crack with different dimensions. In addition, the SIF evolution is of great interest for the scientific community as it provides benchmark responses. Based on their evolution, it is evident that the pure mode I behaviour, in which the crack has evolved to lie in a plane perpendicular to the applied load, has

Figure 88 – SIF distribution along crack front at the last propagation step with the hoop stress criterion and the influence of K_{III} in the equivalent SIF.

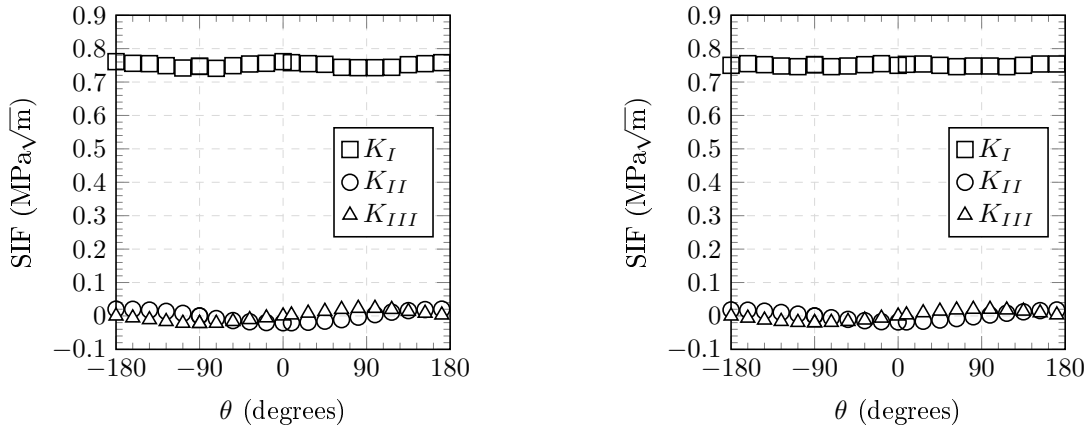

(a) $K_{III} \neq 0$ for K_{eq} (b) $K_{III} = 0$ for K_{eq}

Source: The author.

developed by step 14, since K_{II} and K_{III} have reduced to values close to zero in this step; they do not reduce further from step 14 to step 20. The crack configuration in fig. 84 justifies this claim, due to the planar circular shape the crack assumes in the step 14.

Furthermore, fig. 95 presents the required number of cycles for the crack growth for all four analysed cases. For the initial steps, there is a noticeable difference in the required number of cycles for a given increment for each criterion. This effect tends to reduce throughout the analysis, while the crack pursues a pure mode I response. At the final stages, all four analysis strategies predict similar numbers of cycles, which is consistent with the similarity in the SIF distribution during crack propagation.

Figure 89 – K_I distribution along crack front at steps 0, 7 and 14 for hoop stress criterion.

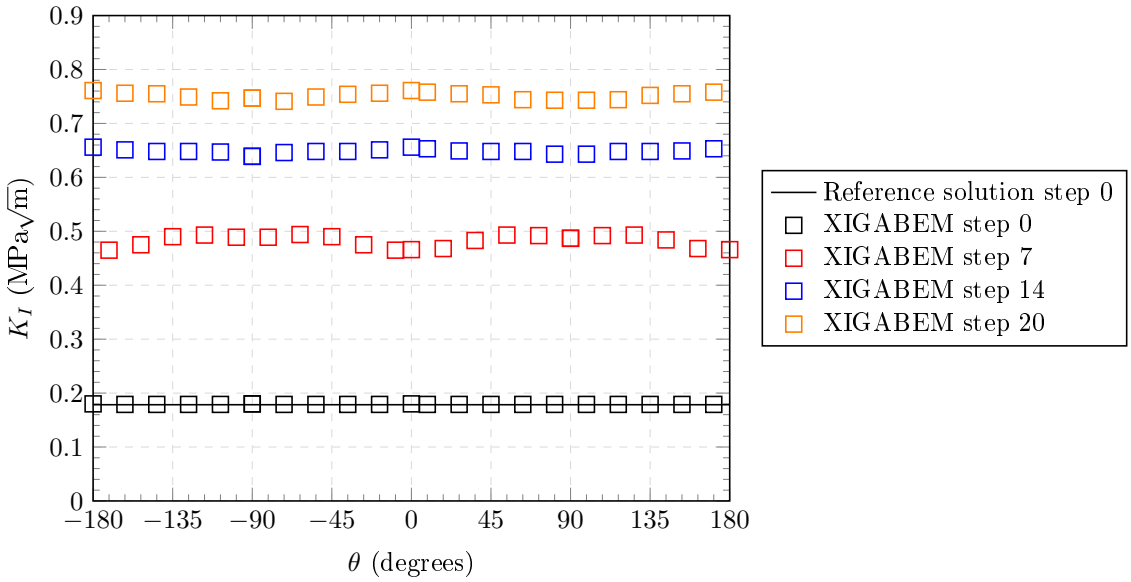

Source: The author.

Figure 90 – K_{II} distribution along crack front at steps 0, 7 and 14 for hoop stress criterion.

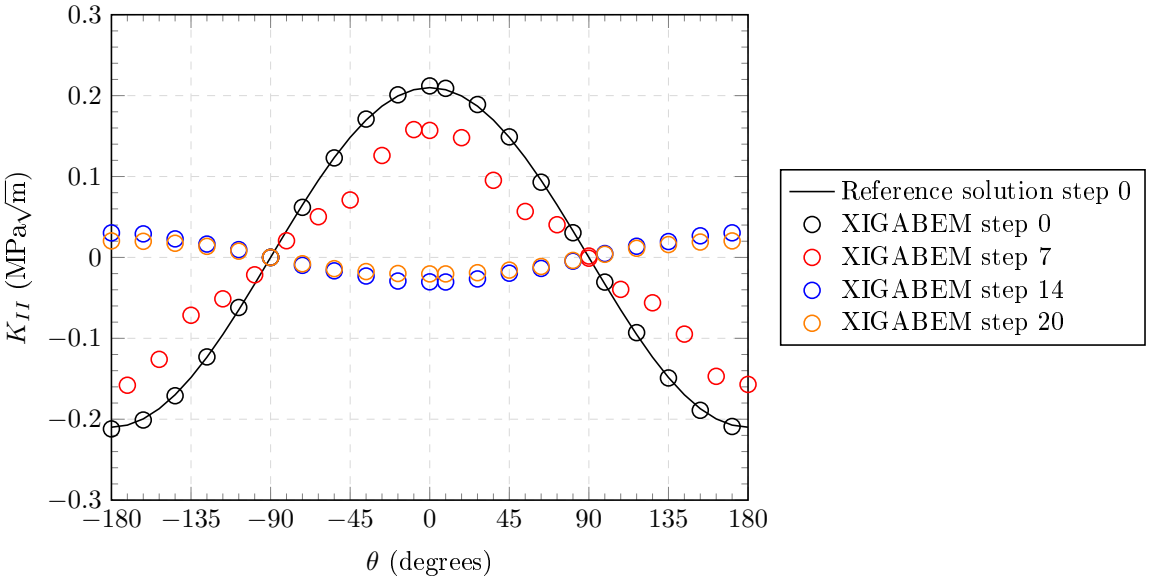

Source: The author.

Figure 91 – K_{III} distribution along crack front at steps 0, 7 and 14 for hoop stress criterion.

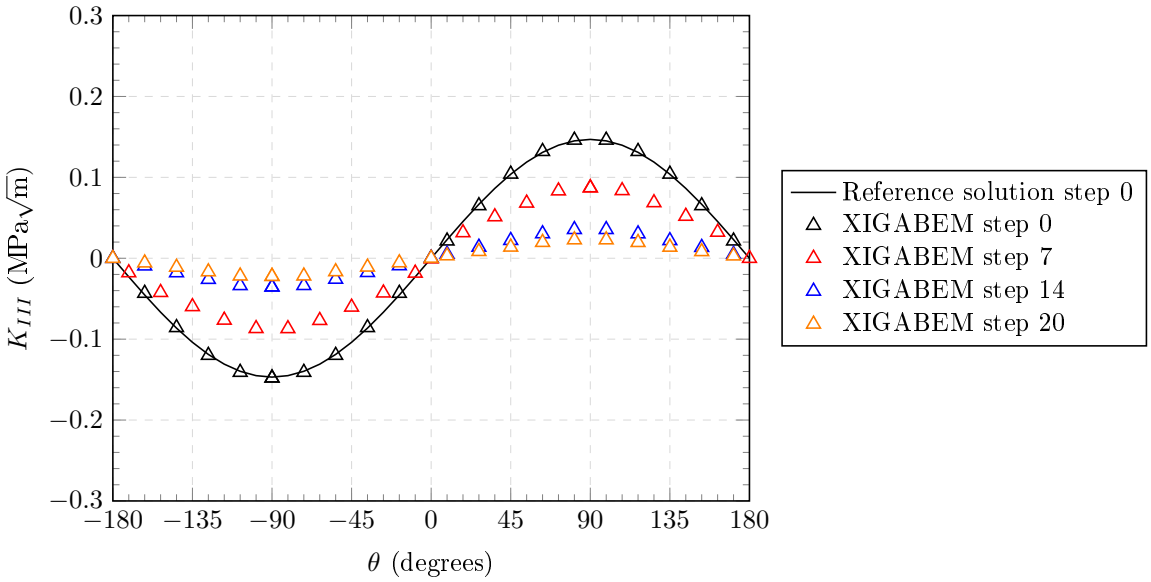

Source: The author.

Figure 92 – K_I distribution along crack front at steps 0, 7 and 14 for Schollmann criterion.

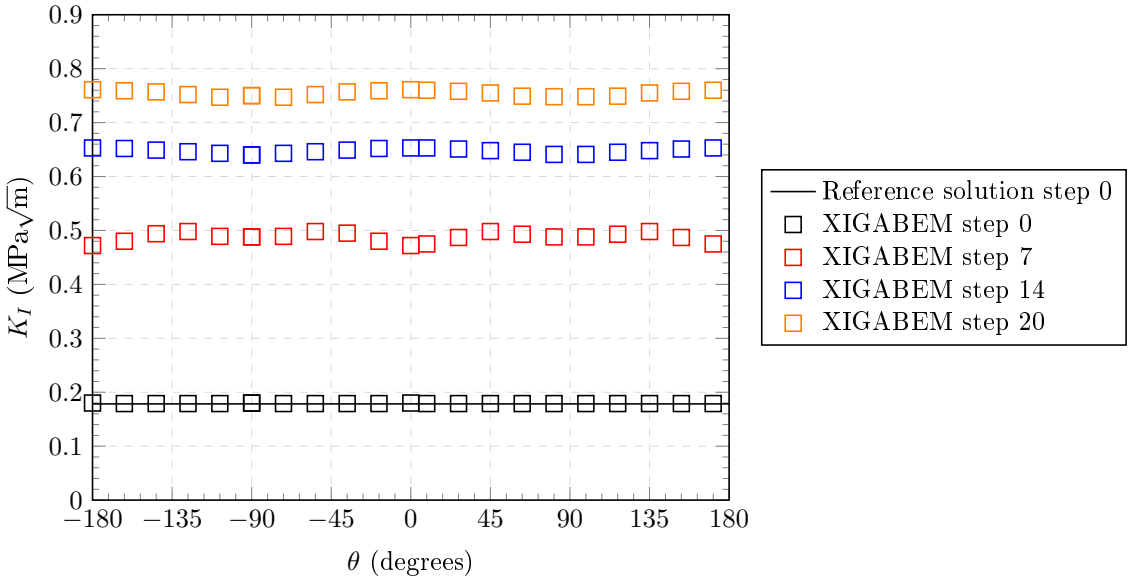

Source: The author.

Figure 93 – K_{II} distribution along crack front at steps 0, 7 and 14 for Schollmann criterion.

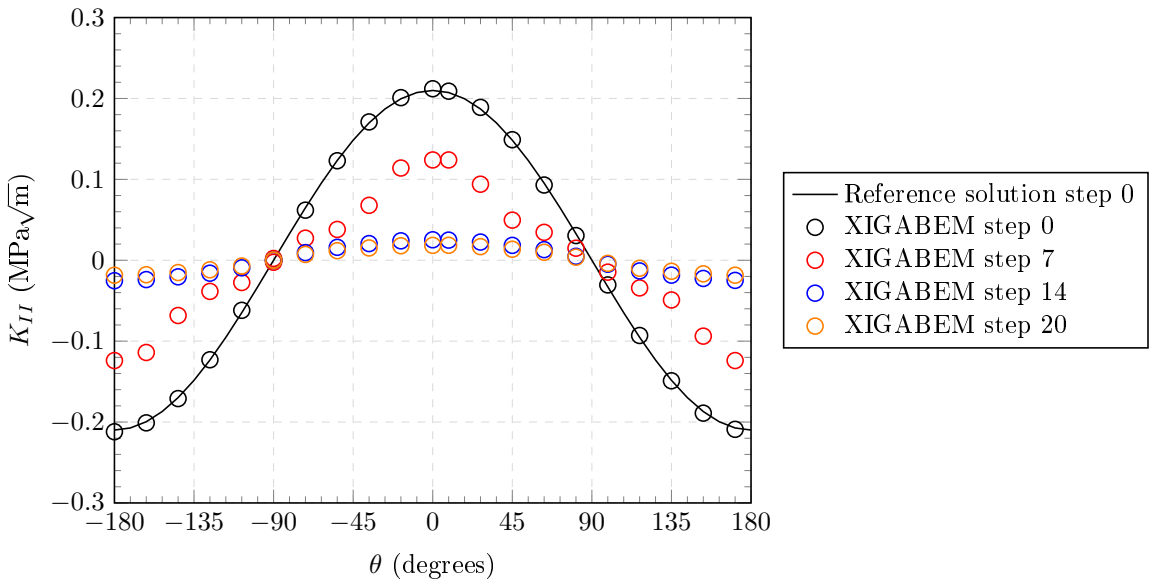

Source: The author.

Figure 94 – K_{III} distribution along crack front at steps 0, 7 and 14 for Schollmann criterion.

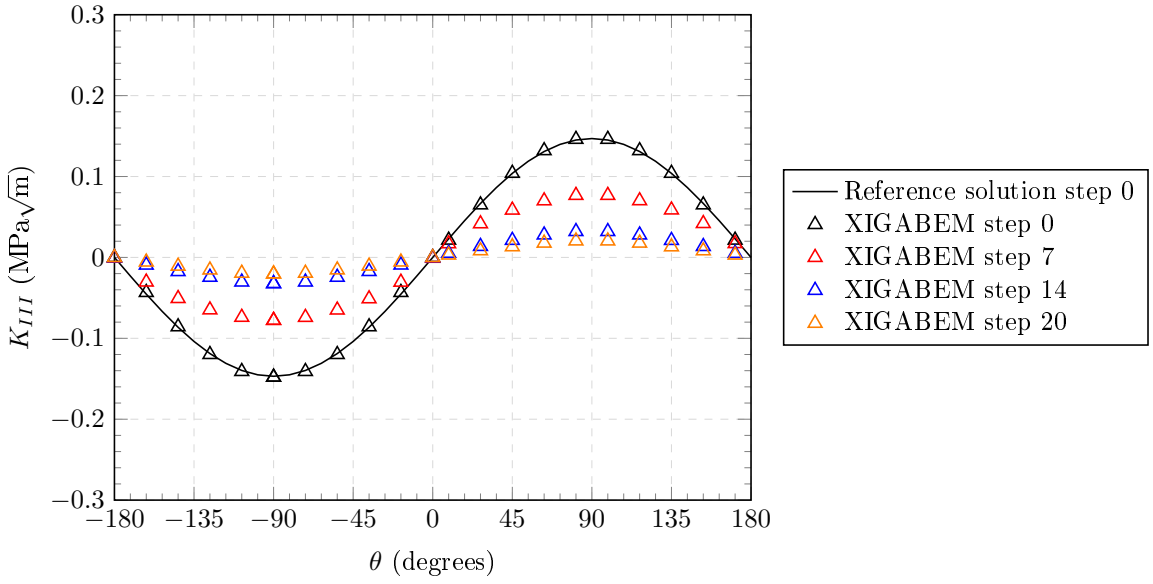

Source: The author.

Figure 95 – Fatigue life assessment of inclined penny-shaped crack.

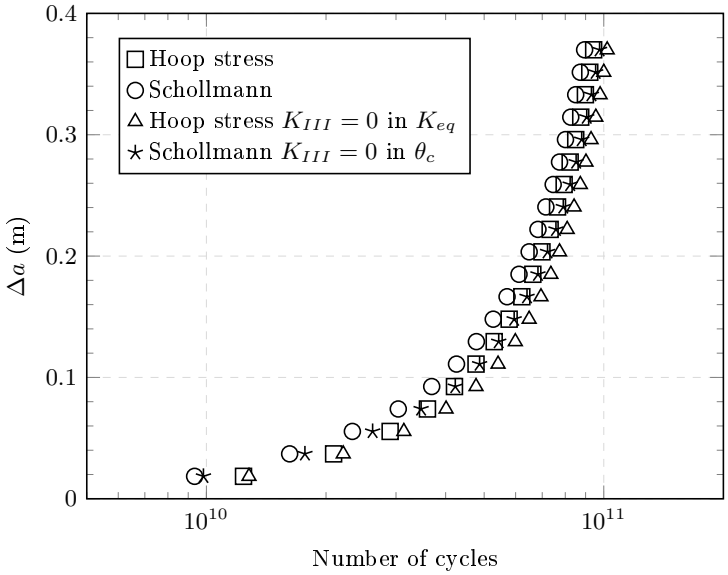

Source: The author.

6.5.3 Crack growth analysis of prism with edge crack under cyclic tensile load

The third application of this chapter comprises a fatigue analysis of a prism with edge crack under cyclic tensile load. The geometry and boundary conditions are presented in fig. 96, which are similar to the application in section 5.5.4. The cyclic load at the prism upper and lower faces assumes $\sigma_{\min} = 0$Pa and $\sigma_{\max} = 1.0$Pa. In addition, the material properties are $E = 100.0$Pa and $\nu = 0.0$ for the Young modulus and Poisson ratio. The isogeometric mesh consists of the same discretisation as shown in fig. 70(b). The enrichment strategy adopted at lateral faces is only the Heaviside function, which enables the use of a continuous mesh in these faces and using localised modification of the corresponding coefficients during crack propagation analysis. The Paris constants are $C = 10^{-13}$ and $m = 2.6$ in which the units are associated with the units for ΔK and da/dN to be Pa m$^{0.5}$ and m/cycle. The crack growth increment in this analysis is $\Delta a = 0.384615$m and the analysis stops after 3 propagation steps.

Figure 96 – Geometry and boundary conditions of prism with edge crack under cyclic tensile load.

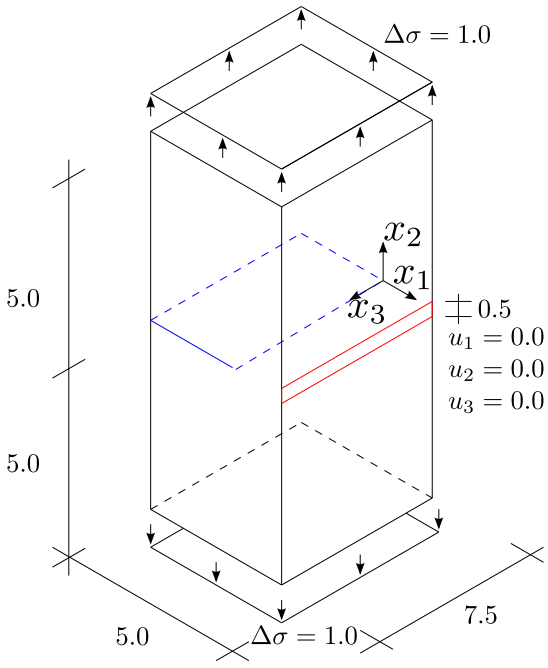

Source: The author.

This application focuses on the Heaviside function capacity in representing strong discontinuities in a crack growth scenario. Then, for simplicity, the crack advances in an uniform manner so that the next crack front is parallel to the previous. This allows a comparison of the numerical responses with the reference response for plane strain given by Tada, Paris and Irwin (2000), according to eq. (5.36). In this sense, fig. 97 presents the total displacements for each propagation step, which is a consistent displacement field during the whole analysis. Figure 98 presents the SIF K_I for each propagation step and directly extracted from the solution vector. In all steps, the numerical response is in agreement with the reference in the central region of the prism. At $z = 3.75$m, the relative difference between the XIGABEM K_I and the reference is 1.25%, 3.08%, 3.09%, and 0.41%, for steps 0, 1, 2, and 3, respectively. Besides, K_{II} and K_{III}

remain below 4.10^{-8}, which is expected from a pure mode analysis. Finally, fig. 99 presents a comparison of the fatigue life using the reference response in eq. (6.4) and the life cycle using the numerical SIFs. All these results attest for the success of the Heaviside enrichment in capturing the opening along the lateral faces without re-meshing them.

Figure 97 – Deformed shape of prism with edge crack under cyclic tensile load in all propagation steps.

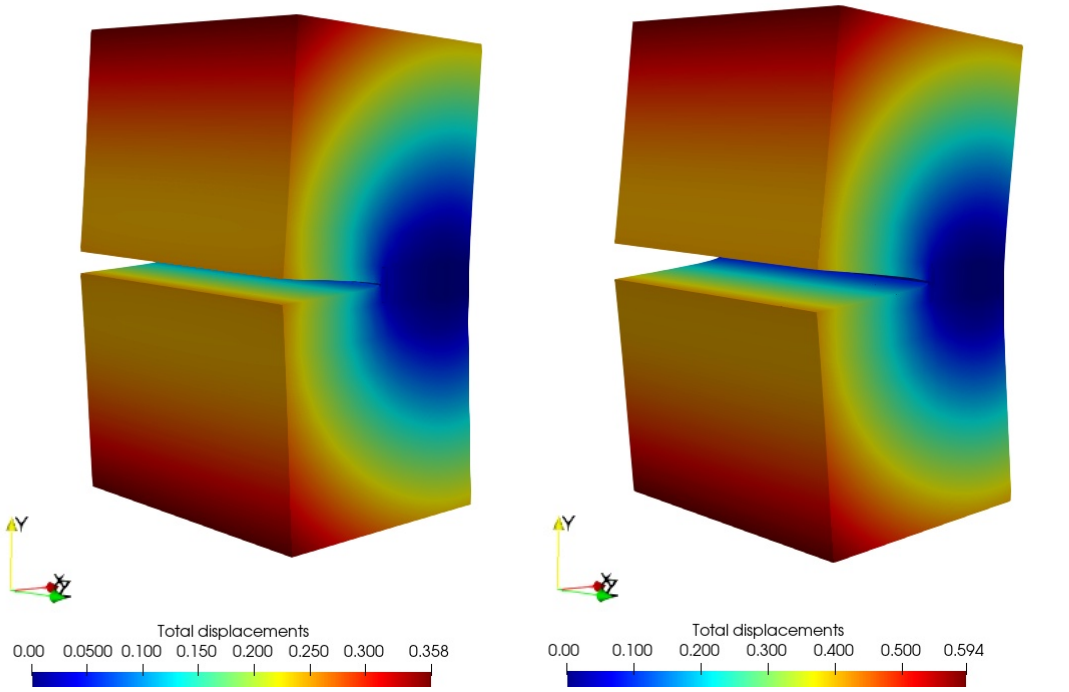

Step 0 Step 1

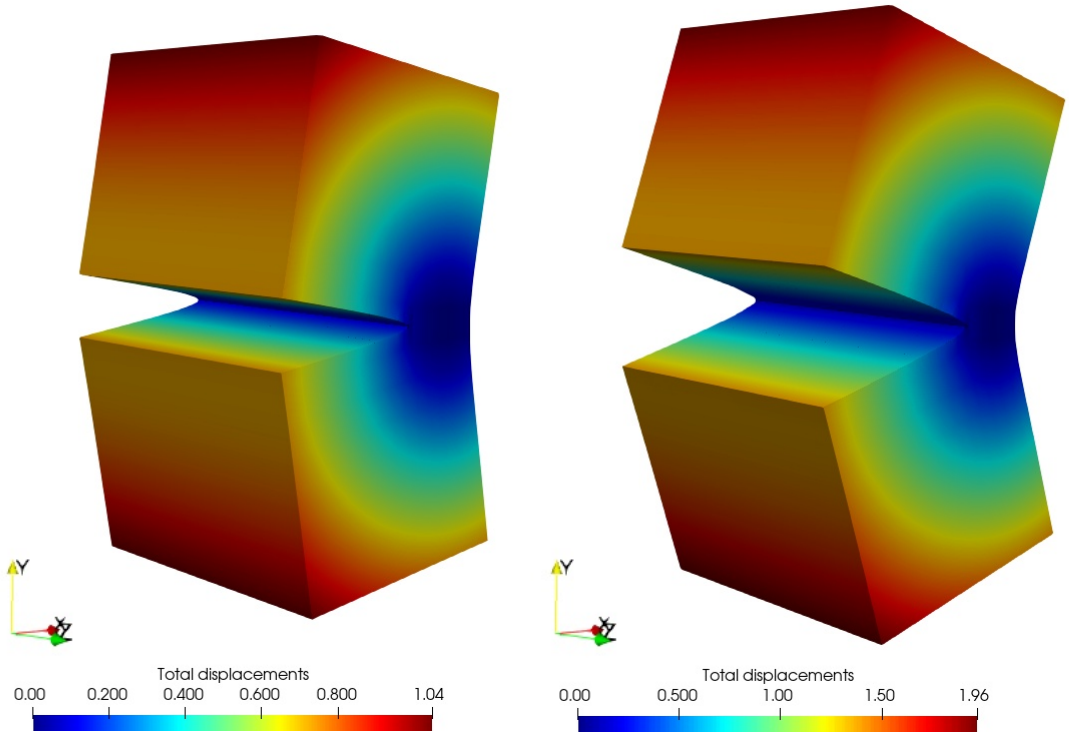

Step 2 Step 3

Source: The author.

Figure 98 – Prism with edge crack under cyclic tensile load: K_I through propagation steps.

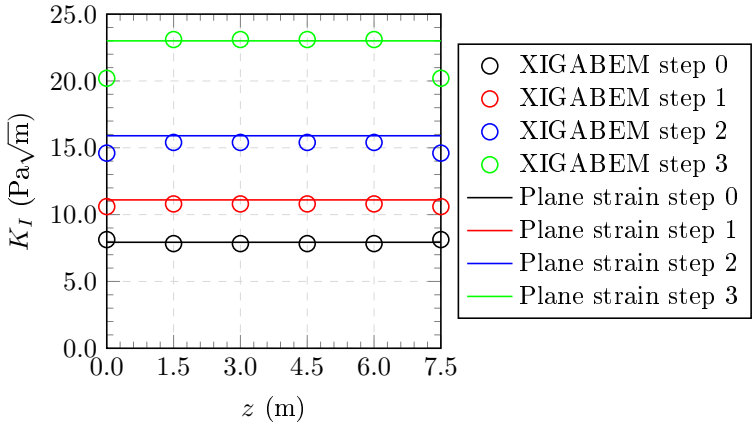

Source: The author.

Figure 99 – Prism with edge crack under cyclic tensile load: fatigue life.

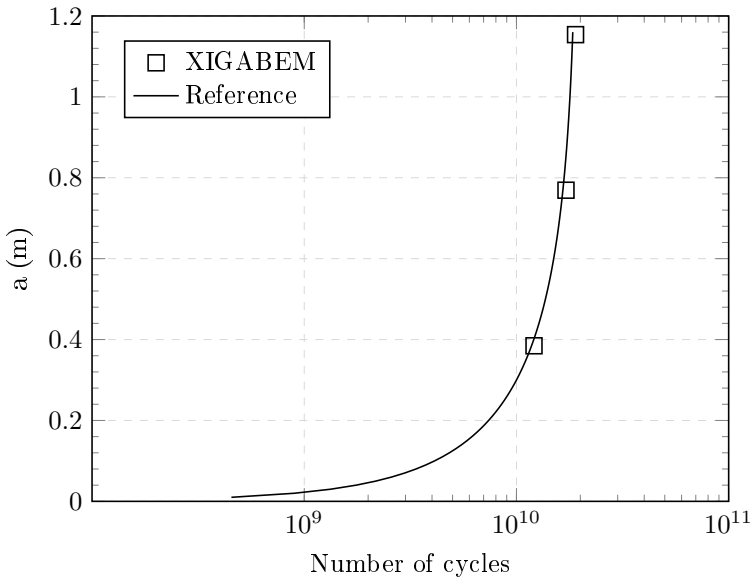

Source: The author.

6.5.4 Hook under cyclic loading

The third application of this study involves the fatigue analysis of a hook under loading service with an initial crack near its threaded notch. The geometry presented in fig. 100 contains various curved surfaces, which suggests an isogeometric three-dimensional formulation would be appropriate to analyse this problem efficiently. The notched region is common in crane hooks, and it normally induces stress concentration regions that become fatigue crack initiation sites. This behaviour aligns with the experimental results of fatigue propagation in a crane hook as studied by Kishore et al. (Kishore *et al.*, 2020) and shown in fig. 101. A uniformly distributed traction of $t_1^{\min} = 0.0$ and $t_1^{\max} = -8.0$ kN/cm^2 is applied to the grey region in fig. 100, which simulates the service loading of this hook, while the surface at $x_1 = 5.0$cm has all displacements clamped. The material properties are $E = 20,000.00$kN/cm^2 and $\nu = 0.27$ for the Young's modulus and Poisson ratio, and the fatigue properties are $C = 4.10^{-12}$ and $m = 2.7$. The units of the Paris constants consider ΔK and da/dN in kPa cm$^{0.5}$ and cm/cycle. The fatigue analysis comprises 9 propagation steps and a $\Delta a_{\max} = 0.2$cm. The crack propagation follows the maximum hoop stress criterion. This application serves as a benchmark for the capability of the proposed formulation to represent real, complex-shaped geometries.

The isogeometric model shown in fig. 102(a) has 38 NURBS surfaces of degree $p = q = 2$ defining the external boundary, while fig. 102(b) illustrates the crack description with four NURBS surfaces of $p = q = 2$, each modelling one side of the crack. The control points, weights, connectivity, and knot vectors are are provided in the supplementary material. The resulting IGABEM model undergoes two uniform knot insertions in both parametric directions on the notch and crack surfaces, resulting in a model with 738 collocation points, as shown in fig. 103.

Figure 104 presents the deformed shape of the hook under its maximum loading, considering different propagation steps and magnified 20 times. Step 0 represents the initial crack configuration. The displaced shape aligns with the expected behaviour for this geometry, which exhibits combined bending and tension. Additionally, the detailed view of the cracked region, with displacement magnified 100 times, demonstrates a smooth field along the crack surfaces. A gap in the external boundary mesh is evident at the intersection of this boundary with the crack front. This is expected, as this region is modelled using two independent, unenriched NURBS surfaces, with C^{-1} continuity between them. This gap is expected to have only a mild effect on the accuracy at the crack front since the enriched crack surfaces are responsible for SIF computation. In fig. 105, the crack front is seen to propagate faster at the edges than at its center, resulting in curvature loss during crack growth. The SIF distribution shown in fig. 106 for steps 0, 3, 6, and 9 indicates a dominant Mode I behaviour in this application. In addition, the higher values of K_I near the edges explain the faster crack growth in these regions compared to the middle of the crack front. At later propagation steps, K_I becomes more uniform along the front, however with higher values close to the edges. Finally, fig. 108 presents the fatigue life assessment of the hook under cyclic loading as a benchmark result for the literature. In summary, the XIGABEM formulation directly captures the SIFs, even for a complex geometry involving both the external boundary and the crack, and successfully analyses an industrial configuration.

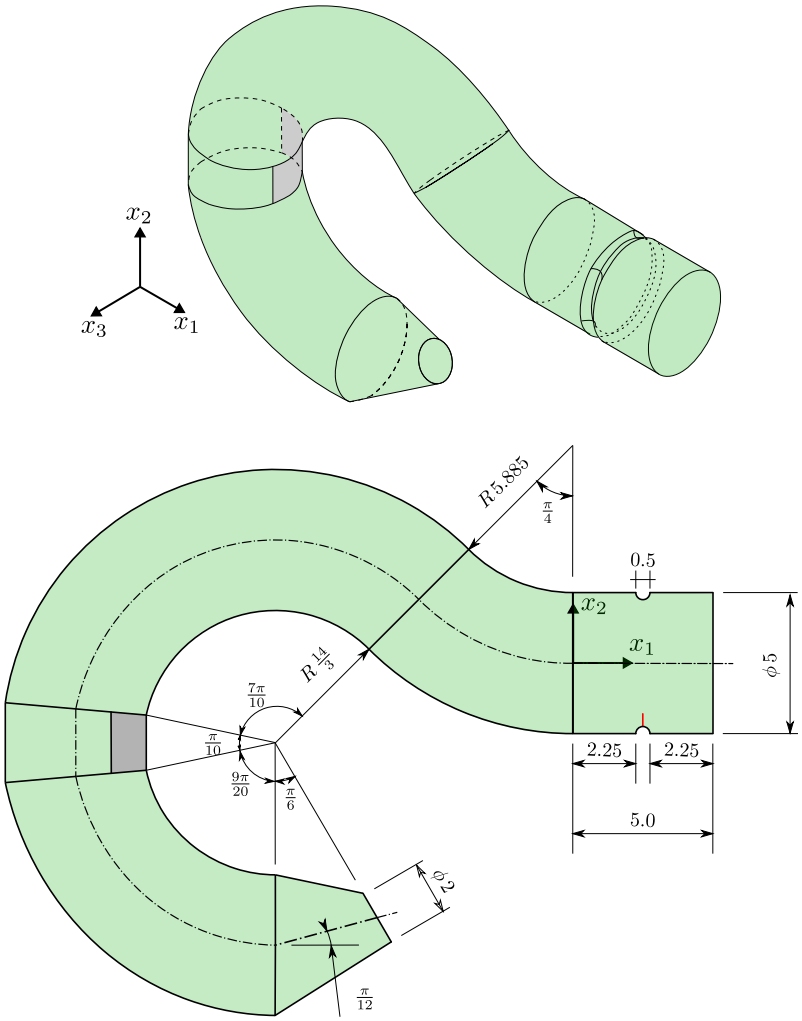

Crack detail at $x_1 = 2.50$

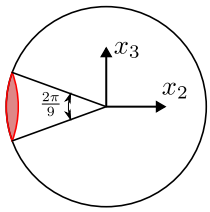

Figure 100 – Geometry of hook with initial crack, dimensions in cm.

Figure 101 – Fatigue crack location in crane hook experiment (Kishore *et al.*, 2020).

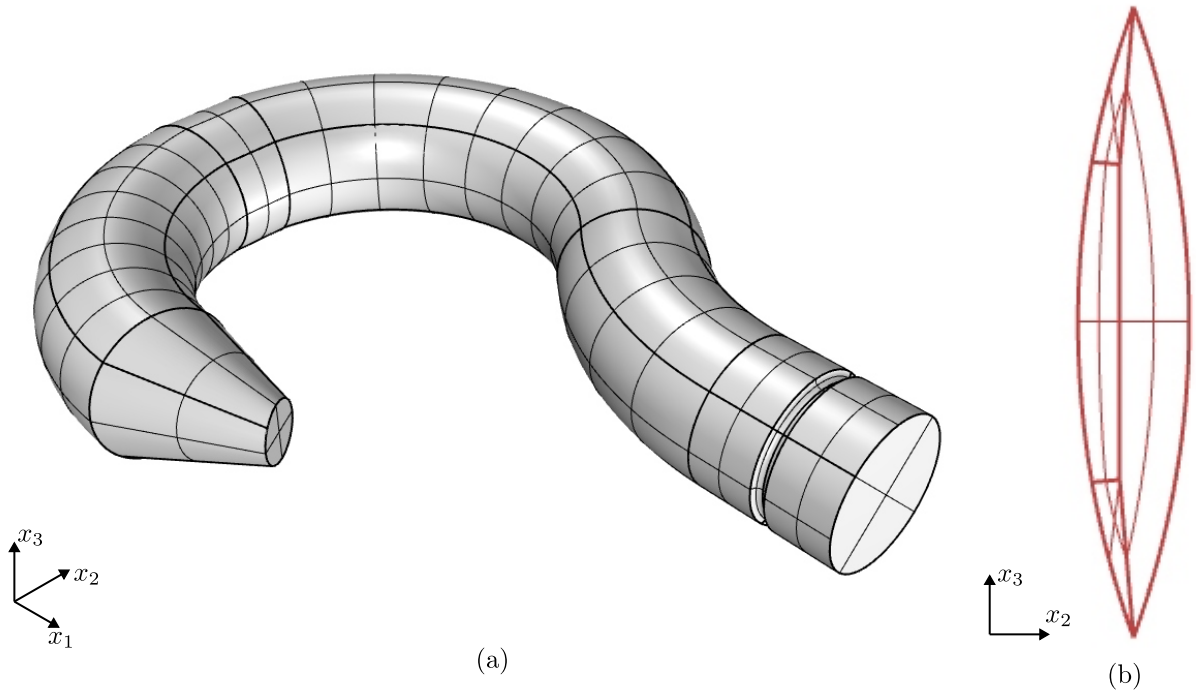

Figure 102 – Isogeometric model of hook with crack.

Figure 103 – Collocation points position for the XIGABEM model of hook with crack.

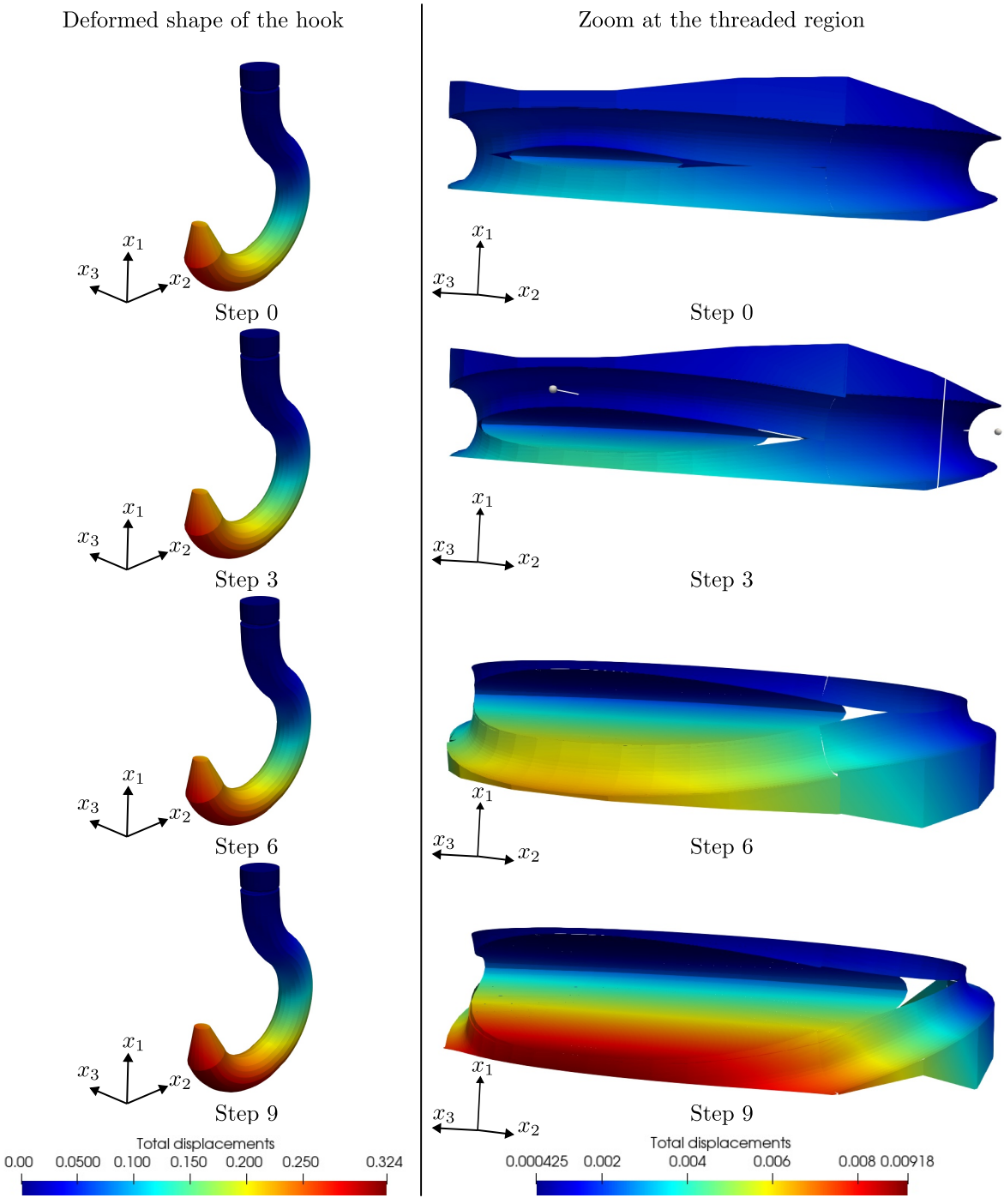

Figure 104 – Deformed shape of a crane hook under cyclic loading when the load reaches its maximum value for different crack steps.

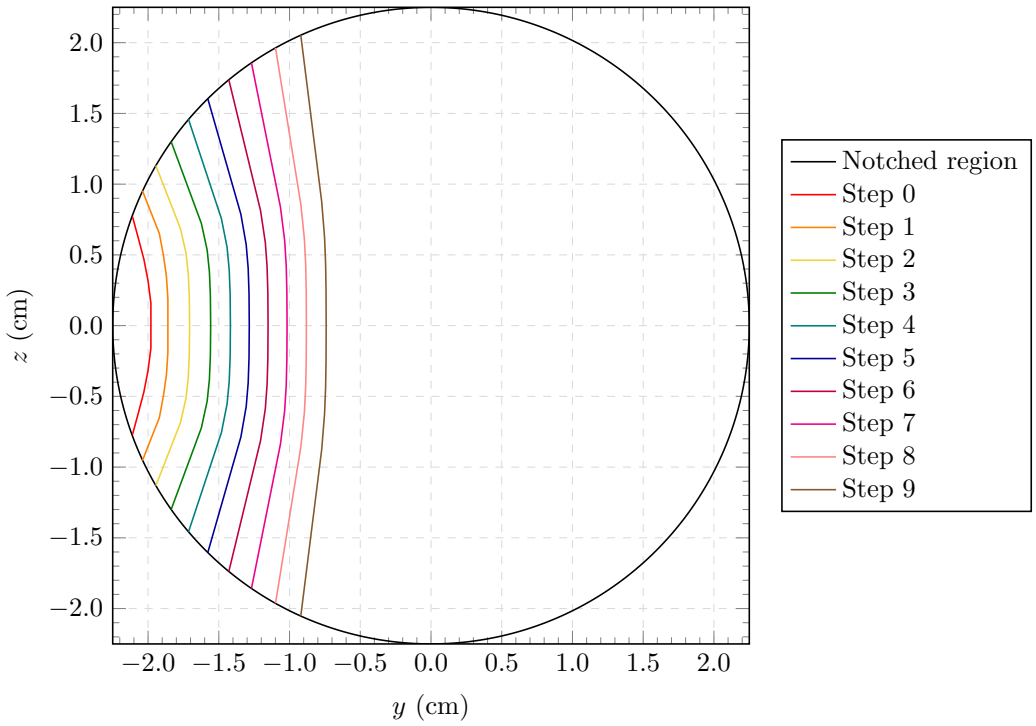

Figure 105 – Crack front evolution at the plane $x_1 = 2.5$ due to the cyclic loading on the hook.

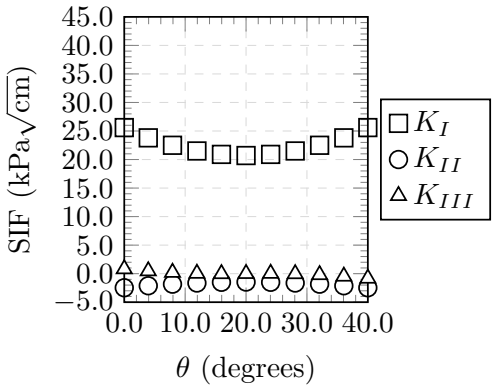

(a) Step 0

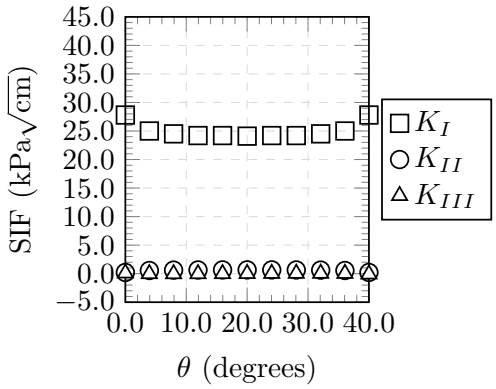

(b) Step 3

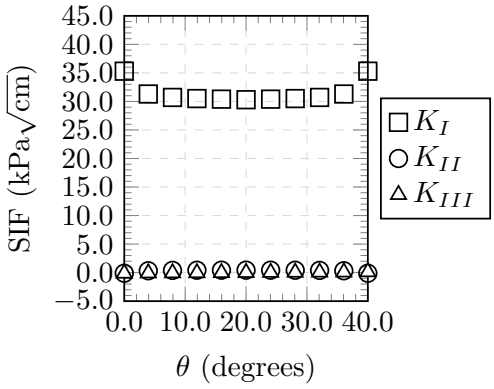

(c) Step 6

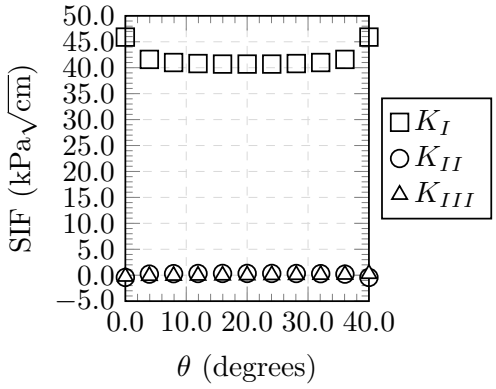

(d) Step 9

Figure 106 – Stress Intensity Factors' distribution along crack front during fatigue propagation on hook.

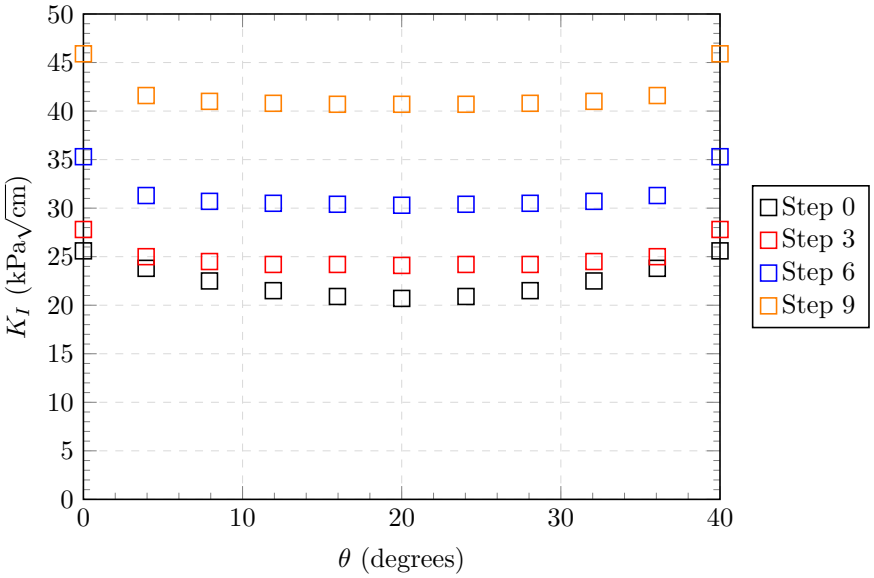

Figure 107 – Evolution of K_I during fatigue propagation of a at the threaded region of a hook.

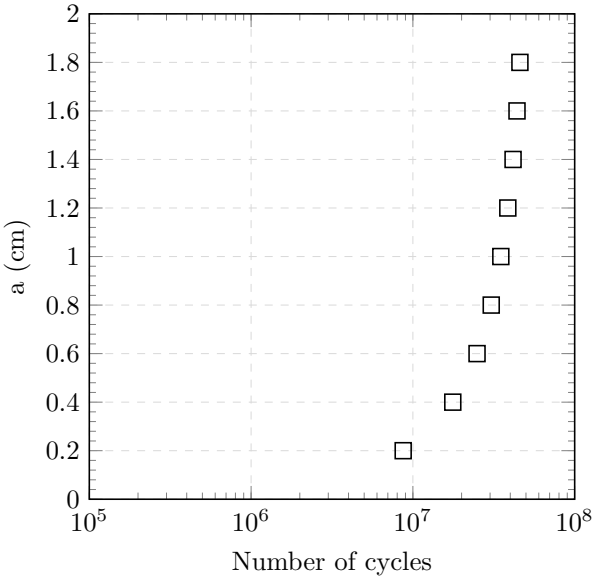

Figure 108 – Fatigue life assessment of hook under cyclic loading.

6.6 Partial conclusions

This chapter presents the high-cycle fatigue modelling of three-dimensional crack configurations with the XIGABEM. This formulation allows for the fatigue assessment of complex crack geometries, in which use of isogeometric basis functions is made for their accurate representation during propagation. In addition, the enrichment strategy gives rise to several advantages for the efficient determination of the mechanical solution throughout the incremental analysis with a small number of degrees of freedom. The enrichment functions introduce interpolation parameters that allow for the direct and accurate determination of the SIFs, which dismisses demanding post-processing tasks. Two crack growth criteria define the direction in which the crack advances: the hoop stress criterion and the Schollmann criterion. While the former has been applied in several research works using IGABEM for crack propagation analysis, this thesis promotes the first application of the latter. In addition, the Schollmann criterion includes the influence of mode III behaviour on the propagation angle. This study also proposes a novel strategy for the determination of the updated crack front, allowing for the NURBS curve weights to adjust during the crack growth. Also, the multi-patch modelling of the crack surfaces involves a fine-tuning algorithm for guaranteeing the required continuity between independent surfaces. Furthermore, the fatigue life assessment considers a linear interpolation of the SIFs in the Paris-Erdogan Law, permitting the use of larger crack increment lengths. Numerical applications have demonstrated that the formulation obtains accurate values for the SIFs during the whole crack growth process. This is particularly advantageous because the exponential behaviour contained in the Paris-Erdogan Law results in the accumulation of errors if a high level of accuracy in SIFs is not maintained.

7 FINAL REMARKS

This thesis proposed enrichment strategies for the isogeometric boundary element method in three-dimensional linear elastic fracture mechanics and linear fatigue analysis. Then, the eXtended Isogeometric Boundary Element Method was used for the numerical analysis of 3-D cracked bodies. Initially, this study focused on the incorporation of trimmed surfaces into the IGABEM formulation, to enable the analysis of more complex geometries without altering their original CAD models. However, this coupling had some limitations and it was not extended to cracked bodies. Subsequently, this study addressed the XIGABEM formulation for three-dimensional fracture and fatigue analysis. Two different enrichment functions were proposed for the first time within the 3-D IGABEM framework: the Heaviside function and the Williams solution-based function. The Heaviside enrichment represented strong discontinuities eliminating the need for mesh alignment between the external boundary and the crack. Furthermore, the Williams solution introduced the asymptotic behaviour to enriched patches. When applied to the external boundary, it can also introduce strong discontinuities. Its application to crack surfaces allowed the direct extraction of Stress Intensity Factors, eliminating the need for post-processing tasks. Finally, the XIGABEM formulation was coupled with a fatigue crack growth framework to model crack propagation under high-cycle loading condition.

In chapter 3, the incorporation of trimmed surfaces into the IGABEM enabled the direct import of original CAD models. This is advantageous because standard IGABEM formulations rely on the NURBS surface representation without accounting for trimming curves, which are common in CAD models. The method was successful in representing the mechanical behaviour of two numerical applications. The first application used the proposed collocation scheme for the singular version of the IGABEM with trimmed surfaces demonstrating the convergence behaviour of displacements as the number of integration points increases. The second application illustrated the capability of the trimmed IGABEM formulation to represent a more complex geometry, with circular details that are exactly represented by NURBS surfaces, as well as with two trimming curves at each end. However, the singular version of the trimmed IGABEM did not yield accurate results, which highlights a need for further investigation of this strategy. Moreover, implementation challenges in generalising this strategy prevented its application to cracked industrial components in this thesis. This provides scope for future studies.

Chapter 4 presented the Heaviside enrichment proposition for representing strong discontinuities in surfaces at the external boundary intersected by cracks. This provides an advantage by eliminating the mesh alignment requirement along the intersection, which facilitates the seamless integration of cracks into CAD models. As the numerical results have demonstrated, this strategy accurately represented the jump in the displacement field in the XIGABEM framework for a variety of crossed knot-spans, which demonstrated the effectiveness of the numerical integration of sub-cells and each strategy for supplementary equations. Additionally, this approach yields accurate results with fewer degrees of freedom in comparison to equivalent IGABEM models.

Notably, this approach introduced a novel contribution to three-dimensional IGABEM.

In chapter 5, the Williams solution-based enrichment function incorporated the asymptotic behaviour of fracture mechanics into the IGABEM framework. Its application to intersected faces enables the representation of the strong discontinuity induced by the crack, as the Heaviside enrichment does, while adding the $\sqrt{r^t}$ term in the displacement solution. When this strategy expands the displacement approximation of crack surfaces, the additional unknowns serve as interpolation parameters for the SIFs along the crack front. This represented a significant contribution of this thesis, since this enrichment eliminated the need for post-processing tasks in SIF assessment. For the SIF enrichment, a tying constraint equation was responsible for obtaining the supplementary equations to recover a square algebraic system. Furthermore, these equations enabled the XIGABEM formulation to remove a non-physical displacement discontinuity at the crack front that occurs in the Lagrangian BEM and IGABEM. Results indicated that XIGABEM exhibits an improved convergence rate compared to the standard IGABEM in various applications. Besides, the condition number growth did not jeopardise the overall quality of the numerical responses. In addition, it was possible to accurately extract the SIFs for problems containing straight and curved crack fronts directly using the additional unknowns introduced by crack front enrichment. The comparison with results from the literature also demonstrated improved accuracy in SIF determination.

The developments in chapter 6 involved applying the XIGABEM framework for the fatigue life assessment of three-dimensional components. The enrichment strategy eliminated the need for post-processing tasks by transforming the SIF parameters into system unknowns, which were directly solved along with the mechanical fields. The fatigue life assessment involved an alternative form of the Paris-Erdogan Law that enables larger crack growth increments while maintaining accuracy. The crack growth analysis considered two different criteria: the hoop stress criterion and the Schollmann criterion. While the former did not account for mode III in the crack propagation angle, the latter incorporated its effects. Additionally, this study proposed a novel strategy to define the updated crack front, which relied on a Least-Squares fitting approach that allowed the control point weights to vary during propagation. This is advantageous because it provides a better representation of curved fronts. Three numerical applications demonstrated the effectiveness of the XIGABEM formulation in computing the life cycle of different crack geometries subjected to pure mode and mixed-mode loading conditions. The accuracy of the SIF computation was demonstrated by the agreement between the obtained numerical results and reference solutions. Additionally, the XIGABEM formulation can model crack growth when the crack intersects the external boundary without requiring re-meshing, which is a significant advantage.

Finally, it is remarking the contributions of this thesis for the state of the art of the three-dimensional IGABEM formulations, as it introduces new scope of capabilities of the method by the enrichment approach.

7.1 Recommendations for future work

Firstly, this study addresses the incorporation of trimmed surfaces into the IGABEM to model more complex CAD geometries. This analysis yielded suitable results, yet for limited applications. In this context, further improvements are necessary to extend the capabilities of IGABEM. Applying global approaches to trimmed surfaces is one possible direction, as well as proper treatment of the trimming effect. Additionally, developing a general strategy to define the sub-cells on crossed knot spans is an important research aspect. Moreover, exploring alternative collocation strategies for trimmed patches in IGABEM is also a worthwhile topic.

This doctoral thesis extends the enrichment approach to three-dimensional fracture mechanics within the IGABEM framework for the first time. Naturally, the pioneering nature of this work allows for various enhancements both in the formulation and in new applications. For instance, the XIGABEM can be applied to other classes of problems, such as eliminating the need for re-meshing in the intersection between an interface and the external boundary in non-homogeneous materials. In this case, the step function could capture the derivative discontinuity in displacements at the external face in a manner analogous to how the Heaviside function captures the displacement jump in fracture mechanics.

There is room for improvement in the Heaviside enrichment. This study proposes an initial approach within the IGABEM formulation, and its extension to higher-order NURBS functions is a natural progression. To this end, alternative Heaviside functions, such as the linear Heaviside function, can serve this purpose. Consequently, blending elements emerge, and their proper treatment represents a significant advancement for XIGABEM.

The Williams solution-based enrichment strategy has been successful for problems in linear elastic fracture mechanics and fatigue analysis. Therefore, its extension to anisotropic problems could be considered. The main modification would involve adding more terms from the Williams solution to the enrichment function. Another aspect of investigation is its localisation to regions near the crack tip. This would reduce the computational cost associated with enriching the entire NURBS surface. In addition, mixed-mode crack propagation when the external crack intersects the external boundary is also a natural extension of this study.

In the context of fatigue crack growth, investigating the low-cycle fatigue phenomenon using the XIGABEM formulation is of great interest. In such cases, overload scenarios can extend the component's life cycle. Conducting this analysis within a three-dimensional framework would be beneficial for industrial applications.

Lastly, this study presents the XIGABEM formulation based on the collocation version of BEM. Since enrichment strategies in this type of formulation do not introduce additional equations to accommodate the enrichment parameters, alternative strategies to recover a square system become a challenge in this context. On the other hand, Galerkin-based approaches naturally introduce additional equations for the enrichment parameters, which circumvents this issue. Therefore, extending the enrichment propositions to the Symmetric Galerkin BEM (SGBEM) would constitute another contribution to the state of the art in computational mechanics.

REFERENCES

ALATAWI, I. **Extended Boundary Element Method approach for Direct and Accurate Evaluation of Stress Intensity Factors**. 2016. Tese (Doutorado) — Durham University, 2016.

ALATAWI, I.; TREVELYAN, J. A direct evaluation of stress intensity factors using the extended dual boundary element method. **Engineering Analysis with Boundary Elements**, Elsevier, v. 52, p. 56–63, 2015.

ALIABADI, M. H. **The boundary element method, volume 2: applications in solids and structures**. [*S.l.: s.n.*]: John Wiley & Sons, 2002. v. 2.

ALMEIDA, L. P. R.; ATROSHCHENKO, E.; LEONEL, E. D. Viscous-cohesive fracture parameters quantification by the coupling of 3d dipole-based bem formulation and bayesian updating model. **Engineering Structures**, v. 322, p. 119136, 2025.

ALMEIDA, L. P. R.; LEONEL, E. D. Dipole-based bem formulation for three-dimensional cohesive crack propagation modelling. **International Journal for Numerical Methods in Engineering**, v. 125, n. 17, p. e7535, 2024.

ALMEIDA, L. P. R.; LEONEL, E. D. The fracture failure modelling of three-dimensional structures composed of quasi-brittle materials subjected to different loading velocities rates by the dipole-based bem approach. **International Journal of Solids and Structures**, v. 286-287, p. 112595, 2024.

AMBATI, M.; GERASIMOV, T.; LORENZIS, L. D. A review on phase-field models of brittle fracture and a new fast hybrid formulation. **Computational Mechanics**, Springer, v. 55, p. 383–405, 2015.

AN, Z. *et al.* Implementation of isogeometric boundary element method for 2-d steady heat transfer analysis. **Advances in Engineering Software**, v. 116, p. 36 – 49, 2018.

ANDRADE, H.; TREVELYAN, J.; LEONEL, E. A nurbs-discontinuous and enriched isogeometric boundary element formulation for two-dimensional fatigue crack growth. **Engineering Analysis with Boundary Elements**, Elsevier, v. 134, p. 259–281, 2022.

ANDRADE, H.; TREVELYAN, J.; LEONEL, E. Direct evaluation of stress intensity factors and t-stress for bimaterial interface cracks using the extended isogeometric boundary element method. **Theoretical and Applied Fracture Mechanics**, Elsevier, p. 104091, 2023.

ANDRADE, H. d. C.; LEONEL, E. D. An enriched dual boundary element method formulation for linear elastic crack propagation. **Engineering Analysis with Boundary Elements**, Elsevier, v. 121, p. 158–179, 2020.

ANDRADE, H. d. C. e; LEONEL, E. D. The multiple fatigue crack propagation modelling in nonhomogeneous structures using the dbem. **Engineering Analysis with Boundary Elements**, Elsevier, v. 98, p. 296–309, 2019.

AREIAS, P. M.; BELYTSCHKO, T. Analysis of three-dimensional crack initiation and propagation using the extended finite element method. **International journal for numerical methods in engineering**, Wiley Online Library, v. 63, n. 5, p. 760–788, 2005.

BAZILEVS, Y. *et al.* Isogeometric analysis using t-splines. **Computer Methods in Applied Mechanics and Engineering**, v. 199, n. 5, p. 229 – 263, 2010.

BAZILEVS, Y. *et al.* Isogeometric fluid-structure interaction: theory, algorithms, and computations. **Computational mechanics**, Springer, v. 43, n. 1, p. 3–37, 2008.

BAZILEVS, Y. *et al.* Isogeometric fluid–structure interaction analysis with applications to arterial blood flow. **Computational Mechanics**, Springer, v. 38, n. 4-5, p. 310–322, 2006.

BAZILEVS, Y. *et al.* Isogeometric analysis: approximation, stability and error estimates for h-refined meshes. **Mathematical Models and Methods in Applied Sciences**, World Scientific, v. 16, n. 07, p. 1031–1090, 2006.

BÉCHET, É. *et al.* Improved implementation and robustness study of the x-fem for stress analysis around cracks. **International journal for numerical methods in engineering**, Wiley Online Library, v. 64, n. 8, p. 1033–1056, 2005.

BEER, G. The isogeometric boundary element method: A alternative approach to the analysis of trimmed geometrical models. **Computer Methods in Applied Mechanics and Engineering**, v. 436, 2025.

BEER, G. *et al.* Isogeometric boundary element analysis with elasto-plastic inclusions. part 2: 3-d problems. **Computer Methods in Applied Mechanics and Engineering**, Elsevier, v. 315, p. 418–433, 2017.

BEER, G.; MARUSSIG, B.; DUENSER, C. **The isogeometric boundary element method**. [*S.l.: s.n.*]: Springer, 2020.

BELYTSCHKO, T. *et al.* Arbitrary discontinuities in finite elements. **International Journal for Numerical Methods in Engineering**, Wiley, v. 50, n. 4, p. 993–1013, 2001.

BENSON, D. J. *et al.* A generalized finite element formulation for arbitrary basis functions: from isogeometric analysis to xfem. **International Journal for Numerical Methods in Engineering**, Wiley Online Library, v. 83, n. 6, p. 765–785, 2010.

BENTO, M.; PROENÇA, S. P. B.; DUARTE, C. Well-conditioned and optimally convergent second-order generalized/extended fem formulations for linear elastic fracture mechanics. **Computer Methods in Applied Mechanics and Engineering**, Elsevier, v. 394, p. 114917, 2022.

BERGARA, A. *et al.* Fatigue crack propagation in complex stress fields: Experiments and numerical simulations using the extended finite element method (xfem). **International Journal of Fatigue**, v. 103, p. 112–121, 2017.

BOOR, C. D. On calculating with b-splines. **Journal of Approximation Theory**, v. 6, n. 1, p. 50 – 62, 1972.

BOOR, C. D. **A practical guide to splines**. [*S.l.: s.n.*]: Springer-Verlag New York, 1978. v. 27.

BORDEN, M. J. *et al.* A higher-order phase-field model for brittle fracture: Formulation and analysis within the isogeometric analysis framework. **Computer Methods in Applied Mechanics and Engineering**, Elsevier, v. 273, p. 100–118, 2014.

BREBBIA, C. **The Boundary Element Method for Engineers**. [*S.l.: s.n.*]: Pentech Press, 1978.

BREITENFELD, M. S. **Quasi-static non-ordinary state-based peridynamics for the modeling of 3D fracture**. [*S.l.: s.n.*]: University of Illinois at Urbana-Champaign, 2014.

CARLSON, N. **NURBS surface fitting with Gauss-Newton**. 2009. Dissertação (Mestrado) — Luleå University of Technology, 2009.

CARRARA, P. *et al.* A framework to model the fatigue behavior of brittle materials based on a variational phase-field approach. **Computer Methods in Applied Mechanics and Engineering**, Elsevier, v. 361, p. 112731, 2020.

CARTER, B.; WAWRZYNEK, P.; INGRAFFEA, A. Automated 3-d crack growth simulation. **International Journal for Numerical Methods in Engineering**, v. 47, n. 1-3, p. 229–253, JAN 10 2000.

CHEN, L. *et al.* Structural shape optimization of three dimensional acoustic problems with isogeometric boundary element methods. **Computer Methods in Applied Mechanics and Engineering**, v. 355, p. 926 – 951, 2019.

CHEN, L. *et al.* An isogeometric approach of two dimensional acoustic design sensitivity analysis and topology optimization analysis for absorbing material distribution. **Computer Methods in Applied Mechanics and Engineering**, Elsevier, v. 336, p. 507–532, 2018.

CISILINO, A.; ALIABADI, M. Three-dimensional boundary element analysis of fatigue crack growth in linear and non-linear fracture problems. **Engineering Fracture Mechanics**, Elsevier, v. 63, n. 6, p. 713–733, 1999.

CISILINO, A. P.; ALIABADI, M. Dual boundary element assessment of three-dimensional fatigue crack growth. **Engineering Analysis with Boundary Elements**, Elsevier, v. 28, n. 9, p. 1157–1173, 2004.

COOX, L. *et al.* An isogeometric indirect boundary element method for solving acoustic problems in open-boundary domains. **Computer Methods in Applied Mechanics and Engineering**, Elsevier, v. 316, p. 186–208, 2017.

CORDEIRO, S. G. F. **Contribuições às análises de fratura e fadiga de componentes tridimensionais pelo método dos elementos de contorno dual**. 2018. Tese (Doutorado) — Escola de Engenharia de São Carlos, Universidade de São Paulo, São Carlos, 2018.

CORDEIRO, S. G. F.; LEONEL, E. D. Cohesive crack propagation modelling in wood structures using bem and the tangent operator technique. **Engineering Analysis with Boundary Elements**, Elsevier, v. 64, p. 111–121, 2016.

CORDEIRO, S. G. F.; LEONEL, E. D. Mechanical modelling of three-dimensional cracked structural components using the isogeometric dual boundary element method. **Applied Mathematical Modelling**, Elsevier, v. 63, p. 415–444, 2018.

CORDEIRO, S. G. F.; LEONEL, E. D. An improved computational framework based on the dual boundary element method for three-dimensional mixed-mode crack propagation analyses. **Advances in Engineering Software**, Elsevier, v. 135, p. 102689, 2019.

CORDEIRO, S. G. F.; LEONEL, E. D. Subtraction singularity technique applied to the regularization of singular and hypersingular integrals in high-order curved boundary elements in plane anisotropic elasticity. **Engineering Analysis with Boundary Elements**, Elsevier, v. 119, p. 214–224, 2020.

COTTRELL, J.; HUGHES, T.; REALI, A. Studies of refinement and continuity in isogeometric structural analysis. **Computer methods in applied mechanics and engineering**, Elsevier, v. 196, n. 41-44, p. 4160–4183, 2007.

COX, M. G. The Numerical Evaluation of B-Splines. **IMA Journal of Applied Mathematics**, v. 10, n. 2, p. 134–149, 10 1972.

DIEHL, P. *et al.* A comparative review of peridynamics and phase-field models for engineering fracture mechanics. **Computational Mechanics**, Springer, v. 69, n. 6, p. 1259–1293, 2022.

DING, J. *et al.* An adaptive phase field modeling of fatigue crack growth using variable-node elements and explicit cycle jump scheme. **Computer Methods in Applied Mechanics and Engineering**, Elsevier, v. 429, p. 117200, 2024.

DUARTE, C.; BABUŠKA, I.; ODEN, J. Generalized finite element methods for three-dimensional structural mechanics problems. **Computers & Structures**, Elsevier BV, v. 77, n. 2, p. 215–232, jun 2000.

DUARTE, C. *et al.* A generalized finite element method for the simulation of three-dimensional dynamic crack propagation. **Computer methods in applied mechanics and engineering**, Elsevier, v. 190, n. 15-17, p. 2227–2262, 2001.

DUFLOT, M. The extended finite element method in thermoelastic fracture mechanics. **International Journal for Numerical Methods in Engineering**, Wiley Online Library, v. 74, n. 5, p. 827–847, 2008.

ERDOGAN, F.; SIH, G. C. On the Crack Extension in Plates Under Plane Loading and Transverse Shear. **Journal of Basic Engineering**, v. 85, n. 4, p. 519–525, 12 1963.

FATHI, F.; BORST, R. de. Geometrically nonlinear extended isogeometric analysis for cohesive fracture with applications to delamination in composites. **Finite Elements in Analysis and Design**, Elsevier, v. 191, p. 103527, 2021.

FATHI, F.; CHEN, L.; BORST, R. de. Extended isogeometric analysis for cohesive fracture. **International Journal for Numerical Methods in Engineering**, Wiley Online Library, v. 121, n. 20, p. 4584–4613, 2020.

FATHI, F. *et al.* Extended isogeometric analysis of a progressively fracturing fluid-saturated porous medium. **International Journal for Numerical Methods in Engineering**, Wiley Online Library, 2022.

FENG, W.-Z. *et al.* An improved singular curved boundary integral evaluation method and its application in dual bem analysis of two- and three-dimensional crack problems. **European Journal of Mechanics, A/Solids**, v. 84, 2020.

FRENET, F. Sur les courbes à double courbure. **Journal de mathématiques pures et appliquées**, v. 17, p. 437–447, 1852.

GAO, X.-W. The radial integration method for evaluation of domain integrals with boundary-only discretization. **Engineering Analysis with Boundary Elements**, Elsevier, v. 26, n. 10, p. 905–916, 2002.

GARZON, J. *et al.* Improvements of explicit crack surface representation and update within the generalized finite element method with application to three-dimensional crack coalescence. **International Journal for Numerical Methods in Engineering**, Wiley Online Library, v. 97, n. 4, p. 231–273, 2014.

GERSTLE, W. H. **Finite and boundary element modelling of crack propagation in two and three dimensions using interactive computer graphics**. 1986. Tese (PhD thesis) — Cornell University, New York, 1986.

GHORASHI, S. S.; VALIZADEH, N.; MOHAMMADI, S. Extended isogeometric analysis for simulation of stationary and propagating cracks. **International Journal for Numerical Methods in Engineering**, Wiley Online Library, v. 89, n. 9, p. 1069–1101, 2012.

GHORASHI, S. S. *et al.* T-spline based xiga for fracture analysis of orthotropic media. **Computers & Structures**, Elsevier, v. 147, p. 138–146, 2015.

GREVILLE, T. Numerical procedures for interpolation by spline functions. **Journal of the Society for Industrial and Applied Mathematics, Series B: Numerical Analysis**, SIAM, v. 1, n. 1, p. 53–68, 1964.

GU, J. *et al.* An isogeometric bem using pb-spline for 3-d linear elasticity problem. **Engineering Analysis with Boundary Elements**, Elsevier, v. 56, p. 154–161, 2015.

GUIGGIANI, M.; GIGANTE, A. A General Algorithm for Multidimensional Cauchy Principal Value Integrals in the Boundary Element Method. **Journal of Applied Mechanics**, v. 57, n. 4, p. 906–915, 12 1990.

GUIGGIANI, M. *et al.* A General Algorithm for the Numerical Solution of Hypersingular Boundary Integral Equations. **Journal of Applied Mechanics**, v. 59, n. 3, p. 604–614, 09 1992.

GUPTA, P.; DUARTE, C. A. Simulation of non-planar three-dimensional hydraulic fracture propagation. **International Journal for Numerical and Analytical Methods in Geomechanics**, Wiley Online Library, v. 38, n. 13, p. 1397–1430, 2014.

GUPTA, V. *et al.* A stable and optimally convergent generalized fem (sgfem) for linear elastic fracture mechanics. **Computer methods in applied mechanics and engineering**, Elsevier, v. 266, p. 23–39, 2013.

HATTORI, G.; ALATAWI, I. A.; TREVELYAN, J. An extended boundary element method formulation for the direct calculation of the stress intensity factors in fully anisotropic materials. **International Journal for Numerical Methods in Engineering**, Wiley Online Library, v. 109, n. 7, p. 965–981, 2017.

HE, C.; PENG, X.; DING, C. Dual order-reduced gaussian process emulators (dorgp) for quantifying high-dimensional uncertain crack growth using limited and noisy data. **Computer Methods in Applied Mechanics and Engineering**, v. 417, 2023.

HELTAI, L.; ARROYO, M.; DESIMONE, A. Nonsingular isogeometric boundary element method for stokes flows in 3d. **Computer Methods in Applied Mechanics and Engineering**, Elsevier, v. 268, p. 514–539, 2014.

HONG, H.-K.; CHEN, J.-T. Derivations of integral equations of elasticity. **Journal of Engineering Mechanics**, American Society of Civil Engineers, v. 114, n. 6, p. 1028–1044, 1988.

HU, Y.; MADENCI, E. Peridynamics for fatigue life and residual strength prediction of composite laminates. **Composite Structures**, v. 160, p. 169 – 184, 2017.

HUGHES, T.; COTTRELL, J.; BAZILEVS, Y. Isogeometric analysis: Cad, finite elements, nurbs, exact geometry and mesh refinement. **Computer Methods in Applied Mechanics and Engineering**, v. 194, n. 39, p. 4135 – 4195, 2005.

ILIE, P.; INCE, A. Three-dimensional fatigue crack growth simulation and fatigue life assessment based on finite element analysis. **Fatigue & Fracture of Engineering Materials & Structures**, Wiley Online Library, v. 45, n. 11, p. 3251–3266, 2022.

JUNG, J.; SEOK, J. Mixed-mode fatigue crack growth analysis using peridynamic approach. **International Journal of Fatigue**, Elsevier, v. 103, p. 591–603, 2017.

KELVIN, L. Note on the integration of the equations of equilibrium of an elastic solid. **Cambridge and Dublin Mathematical Journal**, v. 3, p. 87–89, 1848.

KIENDL, J. *et al.* Phase-field description of brittle fracture in plates and shells. **Computer Methods in Applied Mechanics and Engineering**, Elsevier, v. 312, p. 374–394, 2016.

KIM, H.-J.; SEO, Y.-D.; YOUN, S.-K. Isogeometric analysis for trimmed cad surfaces. **Computer Methods in Applied Mechanics and Engineering**, Elsevier, v. 198, n. 37-40, p. 2982–2995, 2009.

KISHORE, K. *et al.* Failure analysis of a 24 t crane hook using multi-disciplinary approach. **Engineering Failure Analysis**, Elsevier, v. 115, p. 104666, 2020.

KOLK, K.; KUHN, G. The advanced simulation of fatigue crack growth in complex 3d structures. **Archive of Applied Mechanics**, Springer, v. 76, n. 11, p. 699–709, 2006.

KRISTENSEN, P. K.; MARTÍNEZ-PAÑEDA, E. Phase field fracture modelling using quasi-newton methods and a new adaptive step scheme. **Theoretical and Applied Fracture Mechanics**, Elsevier, v. 107, p. 102446, 2020.

KÜHNEL, W. **Differential geometry**. [*S.l.: s.n.*]: American Mathematical Soc., 2015. v. 77.

LABORDE, P. *et al.* High-order extended finite element method for cracked domains. **International Journal for Numerical Methods in Engineering**, Wiley Online Library, v. 64, n. 3, p. 354–381, 2005.

LAGRECA, R.; DANIEL, M.; BAC, A. Local deformation of nurbs curves. **Mathematical methods for curves and surfaces, Tromso**, Citeseer, p. 243, 2004.

LEONEL, E. D.; VENTURINI, W. S. Dual boundary element formulation applied to analysis of multi-fractured domains. **Engineering Analysis with Boundary Elements**, Elsevier, v. 34, n. 12, p. 1092–1099, 2010.

LEONEL, E. D.; VENTURINI, W. S. Non-linear boundary element formulation with tangent operator to analyse crack propagation in quasi-brittle materials. **Engineering analysis with boundary elements**, Elsevier, v. 34, n. 2, p. 122–129, 2010.

LEONEL, E. D.; VENTURINI, W. S. Multiple random crack propagation using a boundary element formulation. **Engineering Fracture Mechanics**, Elsevier, v. 78, n. 6, p. 1077–1090, 2011.

LI, C. *et al.* An advanced fast multipole dual boundary element method for analyzing multiple cracks propagation. **Engineering Fracture Mechanics**, v. 311, p. 110547, 2024.

LI, K.; QIAN, X. Isogeometric analysis and shape optimization via boundary integral. **Computer-Aided Design**, Elsevier, v. 43, n. 11, p. 1427–1437, 2011.

LI, S.; MEAR, M.; XIAO, L. Symmetric weak-form integral equation method for three-dimensional fracture analysis. **Computer Methods in Applied Mechanics and Engineering**, v. 151, n. 3, p. 435–459, 1998. Containing papers presented at the Symposium on Advances in Computational Mechanics.

LI, S. *et al.* Accelerating isogeometric boundary element analysis for 3-dimensional elastostatics problems through black-box fast multipole method with proper generalized decomposition. **International Journal for Numerical Methods in Engineering**, Wiley Online Library, v. 114, n. 9, p. 975–998, 2018.

LIAN, H.; SIMPSON, R. N.; BORDAS, S. P. Stress analysis without meshing: Isogeometric boundary-element method. **Proceedings of the Institution of Civil Engineers-Engineering and Computational Mechanics**, Thomas Telford Ltd, v. 166, n. 2, p. 88–99, 2013.

LIN, X.; SMITH, R. Finite element modelling of fatigue crack growth of surface cracked plates: Part i: The numerical technique. **Engineering Fracture Mechanics**, Elsevier, v. 63, n. 5, p. 503–522, 1999.

LIN, X.; SMITH, R. Finite element modelling of fatigue crack growth of surface cracked plates: Part iii: Stress intensity factor and fatigue crack growth life. **Engineering Fracture Mechanics**, Elsevier, v. 63, n. 5, p. 541–556, 1999.

LIU, W.; HONG, J.-W. A coupling approach of discretized peridynamics with finite element method. **Computer Methods in Applied Mechanics and Engineering**, Elsevier, v. 245, p. 163–175, 2012.

LO, Y.-S. *et al.* A phase-field model for fatigue crack growth. **Journal of the Mechanics and Physics of Solids**, Elsevier, v. 132, p. 103684, 2019.

LUYCKER, E. D. *et al.* X-fem in isogeometric analysis for linear fracture mechanics. **International Journal for Numerical Methods in Engineering**, Wiley Online Library, v. 87, n. 6, p. 541–565, 2011.

MARUSSIG, B.; HIEMSTRA, R.; HUGHES, T. J. Improved conditioning of isogeometric analysis matrices for trimmed geometries. **Computer Methods in Applied Mechanics and Engineering**, v. 334, p. 79 – 110, 2018.

MARUSSIG, B. *et al.* Stable isogeometric analysis of trimmed geometries. **Computer Methods in Applied Mechanics and Engineering**, v. 316, p. 497 – 521, 2017.

MCNEEL, R. *et al.* Rhinoceros 3d, version 6.0. **Robert McNeel & Associates, Seattle, WA**, 2010.

MESGARNEJAD, A.; IMANIAN, A.; KARMA, A. Phase-field models for fatigue crack growth. **Theoretical and Applied Fracture Mechanics**, Elsevier, v. 103, p. 102282, 2019.

MI, Y.; ALIABADI, M. Dual boundary element method for three-dimensional fracture mechanics analysis. **Engineering Analysis with Boundary Elements**, v. 10, n. 2, p. 161 – 171, 1992.

MI, Y.; ALIABADI, M. Discontinuous crack-tip elements: application to 3d boundary element method. **International journal of fracture**, v. 67, n. 3, p. R67–R71, 1994.

MIEHE, C.; HOFACKER, M.; WELSCHINGER, F. A phase field model for rate-independent crack propagation: Robust algorithmic implementation based on operator splits. **Computer Methods in Applied Mechanics and Engineering**, Elsevier, v. 199, n. 45-48, p. 2765–2778, 2010.

MOËS, N.; DOLBOW, J.; BELYTSCHKO, T. A finite element method for crack growth without remeshing. **International journal for numerical methods in engineering**, Wiley Online Library, v. 46, n. 1, p. 131–150, 1999.

MOLNÁR, G.; GRAVOUIL, A. 2d and 3d abaqus implementation of a robust staggered phase-field solution for modeling brittle fracture. **Finite Elements in Analysis and Design**, Elsevier, v. 130, p. 27–38, 2017.

NAGY, A. P.; BENSON, D. J. On the numerical integration of trimmed isogeometric elements. **Computer Methods in Applied Mechanics and Engineering**, Elsevier, v. 284, p. 165–185, 2015.

NARDI, D. C.; LEONEL, E. D. An extended lumped damage mechanics igabem formulation for quasi-brittle material failure. **Engineering Analysis with Boundary Elements**, v. 169, p. 105955, 2024.

National Transportation Safety Board. **Flight 243, Boeing 737-200, N73711, near Maui, Hawaii, April 28, 1988**. Washington, DC, 1989.

NETO, A. R. **Formulações numéricas baseadas no Método dos Elementos de Contorno Isogeométrico para a análise mecânica de solídos não-homogêneos reforçados tridimensionais**. 2023. Tese (Doutorado) — Universidade de São Paulo, 2023.

NETO, A. R.; LEONEL, E. D. One step forward towards the full integration of bem and cad software: An effective adaptive approach. **Engineering Analysis with Boundary Elements**, Elsevier, v. 143, p. 457–482, 2022.

NGUYEN, C. T.; OTERKUS, S.; OTERKUS, E. An energy-based peridynamic model for fatigue cracking. **Engineering Fracture Mechanics**, Elsevier, v. 241, p. 107373, 2021.

NGUYEN-THANH, N. *et al.* Multi phase-field modeling of anisotropic crack propagation in 3d fiber-reinforced composites based on an adaptive isogeometric meshfree collocation method. **Computer Methods in Applied Mechanics and Engineering**, Elsevier, v. 393, p. 114794, 2022.

NGUYEN-THANH, N. *et al.* An extended isogeometric thin shell analysis based on kirchhoff–love theory. **Computer Methods in Applied Mechanics and Engineering**, Elsevier, v. 284, p. 265–291, 2015.

ODEN, J. T.; DUARTE, C. A. Solution of singular problems using hp clouds. **Mathematics of Finite Elements and Applications**, Citeseer, v. 9, p. 35–54, 1996.

OLIVEIRA, H. L.; ANDRADE, H. d. C. e; LEONEL, E. D. An isogeometric boundary element approach for topology optimization using the level set method. **Applied Mathematical Modelling**, Elsevier, 2020.

OLIVEIRA, H. L.; LEONEL, E. D. Cohesive crack growth modelling based on an alternative nonlinear bem formulation. **Engineering Fracture Mechanics**, Elsevier, v. 111, p. 86–97, 2013.

OLIVEIRA, H. L.; LEONEL, E. D. A bem formulation applied in the mechanical material modelling of viscoelastic cracked structures. **International Journal of Advanced Structural Engineering**, Springer, v. 9, n. 1, p. 1–12, 2017.

O'HARA, P. *et al.* A two-scale generalized finite element method for fatigue crack propagation simulations utilizing a fixed, coarse hexahedral mesh. **Computational Mechanics**, Springer, v. 57, n. 1, p. 55–74, 2016.

PATHAK, H.; SINGH, A.; SINGH, I. V. Fatigue crack growth simulations of 3-d problems using xfem. **International Journal of Mechanical Sciences**, Elsevier, v. 76, p. 112–131, 2013.

PEAKE, M.; TREVELYAN, J.; COATES, G. Extended isogeometric boundary element method (xibem) for three-dimensional medium-wave acoustic scattering problems. **Computer Methods in Applied Mechanics and Engineering**, v. 284, p. 762 – 780, 2015.

PEAKE, M. J.; TREVELYAN, J.; COATES, G. Extended isogeometric boundary element method (xibem) for two-dimensional helmholtz problems. **Computer Methods in Applied Mechanics and Engineering**, Elsevier, v. 259, p. 93–102, 2013.

PENG, X. **Isogeometric boundary element methods for linear elastic fracture mechanics**. 2016. Tese (Doutorado) — Cardiff University, 2016.

PENG, X. *et al.* Isogeometric boundary element methods for three dimensional static fracture and fatigue crack growth. **Computer Methods in Applied Mechanics and Engineering**, Elsevier, v. 316, p. 151–185, 2017.

PENG, X. *et al.* Linear elastic fracture simulation directly from cad: 2d nurbs-based implementation and role of tip enrichment. **International Journal of Fracture**, Springer, v. 204, n. 1, p. 55–78, 2017.

PENG, X.; LIAN, H. Numerical aspects of isogeometric boundary element methods:(nearly) singular quadrature, trimmed nurbs and surface crack modeling. **CMES-COMPUTER MODELING IN ENGINEERING & SCIENCES**, TECH SCIENCE PRESS 871 CORONADO CENTER DR, SUTE 200, HENDERSON, NV 89052 USA, v. 130, n. 1, p. 513–542, 2022.

PEREIRA, J.; DUARTE, C. A.; JIAO, X. Three-dimensional crack growth with hp-generalized finite element and face offsetting methods. **Computational Mechanics**, Springer, v. 46, p. 431–453, 2010.

PERES, M. *et al.* Parallel isogeometric boundary element analysis with t-splines on cuda. **Computer Methods in Applied Mechanics and Engineering**, v. 432, 2024.

PIEGL, L.; TILLER, W. **The NURBS book**. [*S.l.: s.n.*]: Springer Science & Business Media, 1996.

POLITIS, C. *et al.* An isogeometric bem for exterior potential-flow problems in the plane. *In*: **2009 SIAM/ACM Joint Conference on Geometric and Physical Modeling**. [*S.l.: s.n.*], 2009. p. 349–354.

PORTELA, A.; ALIABADI, M.; ROOKE, D. P. Dual boundary element incremental analysis of crack propagation. **Computers & Structures**, Elsevier, v. 46, n. 2, p. 237–247, 1993.

PORTELA, A.; ALIABADI, M. H.; ROOKE, D. P. The dual boundary element method: Effective implementation for crack problems. **International Journal for Numerical Methods in Engineering**, v. 33, n. 6, p. 1269–1287, 1992.

PRICE, R.; TREVELYAN, J. Boundary element simulation of fatigue crack growth in multi-site damage. **Engineering Analysis with Boundary Elements**, Elsevier, v. 43, p. 67–75, 2014.

RABCZUK, T.; BORDAS, S.; ZI, G. On three-dimensional modelling of crack growth using partition of unity methods. **Computers & structures**, Elsevier, v. 88, n. 23-24, p. 1391–1411, 2010.

RANNOU, J. *et al.* Three dimensional experimental and numerical multiscale analysis of a fatigue crack. **Computer Methods in Applied Mechanics and Engineering**, v. 199, n. 21, p. 1307–1325, 2010. Multiscale Models and Mathematical Aspects in Solid and Fluid Mechanics.

ROCHA, M. **Análise da fratura coesiva com base em formulações enriquecidas do Método dos Elementos de Contorno tridimensional**. 2020. Dissertação (Mestrado) — Escola de Engenharia de São Carlos, Universidade de São Paulo, São Carlos, 2020.

ROCHA, M.; LEONEL, E. D. The fracture failure of three-dimensional concrete structures subjected to concentrated loadings using the boundary element method. **Revista IBRACON de Estruturas e Materiais**, SciELO Brasil, v. 15, p. e15504, 2022.

SALEH, A.; ALIABADI, M. Crack growth analysis in concrete using boundary element method. **Engineering Fracture Mechanics**, Elsevier, v. 51, n. 4, p. 533–545, 1995.

SANCHEZ-RIVADENEIRA, A.; DUARTE, C. A stable generalized/extended fem with discontinuous interpolants for fracture mechanics. **Computer Methods in Applied Mechanics and Engineering**, Elsevier, v. 345, p. 876–918, 2019.

SANCHEZ-RIVADENEIRA, A.; DUARTE, C. A simple, first-order, well-conditioned, and optimally convergent generalized/extended fem for two- and three-dimensional linear elastic fracture mechanics. **Computer Methods in Applied Mechanics and Engineering**, v. 372, p. 113388, 2020.

SANCHEZ-RIVADENEIRA, A. *et al.* A stable generalized/extended p-hierarchical fem for three-dimensional linear elastic fracture mechanics. **Computer Methods in Applied Mechanics and Engineering**, Elsevier, v. 364, p. 112970, 2020.

SAREGO, G. *et al.* Linearized state-based peridynamics for 2-d problems. **International Journal for Numerical Methods in Engineering**, Wiley Online Library, v. 108, n. 10, p. 1174–1197, 2016.

SAUTER, S. A.; SCHWAB, C. **Boundary element methods**. [*S.l.: s.n.*]: Springer, 2011.

SCHÖLLMANN, M.; FULLAND, M.; RICHARD, H. Development of a new software for adaptive crack growth simulations in 3d structures. **Engineering Fracture Mechanics**, Elsevier, v. 70, n. 2, p. 249–268, 2003.

SCHÖLLMANN, M. *et al.* A new criterion for the prediction of crack development in multiaxially loaded structures. **International Journal of Fracture**, Springer, v. 117, p. 129–141, 2002.

SCOTT, M. *et al.* Isogeometric boundary element analysis using unstructured t-splines. **Computer Methods in Applied Mechanics and Engineering**, v. 254, p. 197–221, 2013.

SERRET, J.-A. Sur quelques formules relatives à la théorie des courbes à double courbure. **Journal de mathématiques pures et appliquées**, v. 16, p. 193–207, 1851.

SHAABAN, A. M. *et al.* Shape optimization by conventional and extended isogeometric boundary element method with pso for two-dimensional helmholtz acoustic problems. **Engineering Analysis with Boundary Elements**, Elsevier, v. 113, p. 156–169, 2020.

SHI, J. *et al.* Abaqus implementation of extended finite element method using a level set representation for three-dimensional fatigue crack growth and life predictions. **Engineering Fracture Mechanics**, v. 77, n. 14, p. 2840–2863, 2010.

SILLING, S. A. *et al.* Peridynamic states and constitutive modeling. **Journal of elasticity**, Springer, v. 88, p. 151–184, 2007.

SIMPSON, R. *et al.* An isogeometric boundary element method for elastostatic analysis: 2d implementation aspects. **Computers and Structures**, v. 118, p. 2 – 12, 2013.

SIMPSON, R. *et al.* A two-dimensional isogeometric boundary element method for elastostatic analysis. **Computer Methods in Applied Mechanics and Engineering**, v. 209-212, p. 87–100, 2012.

SIMPSON, R.; TREVELYAN, J. Evaluation of j1 and j2 integrals for curved cracks using an enriched boundary element method. **Engineering Fracture Mechanics**, Elsevier, v. 78, n. 4, p. 623–637, 2011.

SIMPSON, R.; TREVELYAN, J. A partition of unity enriched dual boundary element method for accurate computations in fracture mechanics. **Computer Methods in Applied Mechanics and Engineering**, Elsevier, v. 200, n. 1-4, p. 1–10, 2011.

SOMIGLIANA, C. Sopra l'equilibrio di un corpo elastico isotropo. **Il Nuovo Cimento (1877-1894)**, Springer, v. 17, n. 1, p. 140–148, 1885.

SUKUMAR, N. *et al.* Extended finite element method for three-dimensional crack modelling. **International journal for numerical methods in engineering**, Wiley Online Library, v. 48, n. 11, p. 1549–1570, 2000.

SUN, F.; DONG, C. Three-dimensional crack propagation and inclusion-crack interaction based on igabem. **Engineering Analysis with Boundary Elements**, Elsevier, v. 131, p. 1–14, 2021.

SUN, F.; DONG, C. Effective elastic properties of three-dimensional multiple crack problems with the isogeometric boundary element parallel fast direct solver. **Engineering Analysis with Boundary Elements**, Elsevier, v. 155, p. 1104–1122, 2023.

SUN, S. *et al.* Structural shape optimization by igabem and particle swarm optimization algorithm. **Engineering Analysis with Boundary Elements**, Elsevier, v. 88, p. 26–40, 2018.

TADA, H.; PARIS, P.; IRWIN, G. The analysis of cracks handbook. **New York: ASME Press**, v. 2, p. 1, 2000.

TALEBI, H.; SILANI, M.; RABCZUK, T. Concurrent multiscale modeling of three dimensional crack and dislocation propagation. **Advances in Engineering Software**, Elsevier, v. 80, p. 82–92, 2015.

URAL, A. *et al.* Three-dimensional, parallel, finite element simulation of fatigue crack growth in a spiral bevel pinion gear. **Engineering Fracture Mechanics**, Elsevier, v. 72, n. 8, p. 1148–1170, 2005.

VERHOOSEL, C. V. *et al.* An isogeometric approach to cohesive zone modeling. **International Journal for Numerical Methods in Engineering**, Wiley Online Library, v. 87, n. 1-5, p. 336–360, 2011.

WALL, W. A.; FRENZEL, M. A.; CYRON, C. Isogeometric structural shape optimization. **Computer methods in applied mechanics and engineering**, Elsevier, v. 197, n. 33-40, p. 2976–2988, 2008.

WANG, Y.; BENSON, D.; NAGY, A. A multi-patch nonsingular isogeometric boundary element method using trimmed elements. **Computational Mechanics**, v. 56, n. 1, p. 173–191, 2015.

WANG, Y. *et al.* A 3-d conjugated bond-pair-based peridynamic formulation for initiation and propagation of cracks in brittle solids. **International Journal of Solids and Structures**, Elsevier, v. 134, p. 89–115, 2018.

WILLIAMS, M. L. On the stress distribution at the base of a stationary crack. **Journal of Applied Mechanics**, ASME International, v. 24, n. 1, p. 109–114, mar 1957.

WILLIAMS, M. L.; ELLINGER, G. A. **Progress Summary on Investigation of Fractured Steel Plates Removed From Welded Ships**. [*S.l.: s.n.*]: Ship Structure Committee, 1949.

WU, Y.; DONG, C.; YANG, H. Isogeometric fe-be coupling approach for structural-acoustic interaction. **Journal of Sound and Vibration**, v. 481, 2020.

YANG, B.; MALL, S.; RAVI-CHANDAR, K. A cohesive zone model for fatigue crack growth in quasibrittle materials. **International Journal of Solids And Structures**, v. 38, n. 22-23, p. 3927–3944, MAY-JUN 2001.

ZANG, Q. *et al.* Isogeometric boundary element method for axisymmetric steady-state heat transfer. **Engineering Analysis with Boundary Elements**, v. 160, p. 89 – 105, 2024.

APPENDIX A – B-SPLINES AND NURBS REPRESENTATION OF CURVES AND SURFACES

Computer-Aided Design (CAD) models utilize functions such as Bézier curves, Splines, and NURBS to describe complex geometries with high accuracy and few parameters when compared to the polynomial representation. In this sense, the isogeometric approach consists of using the same basis functions as the CAD models for the numerical analysis, which eliminates the mesh generation task of traditional numerical approaches relying on the polynomial approximation. Since this work uses the isogeometric approach of the BEM, this appendix presents the concepts and definitions about the parametric representation of curves and surfaces using B-Splines and NURBS basis functions, which can be found in Piegl and Tiller (1996).

A.1 B-Splines curves

A B-spline curve is a piecewise parametric curve throughout a space in which the separation between segments occurs from a break-point defined as a knot. The knot ordering in a non-decreasing vector results in the knot vector $\Xi = \{\xi_1,\ \xi_2,\ \ldots,\ \xi_k\}$, in which each segment $[\xi_i; \xi_{i+1})$ is a knot-span. The control points are the geometric parameters that permit the curve description in the $\mathbb{R}^2$ or $\mathbb{R}^3$ physical spaces as:

$$C_j(\xi) = \sum_{i=1}^{n} N_i(\xi) x_j^i \tag{A.1}$$

in which C_j represents the j-th direction coordinate of an arbitrary point on the curve associated with the ξ parametric coordinate, N_i is the i-th B-Spline basis function and x_j^i denotes the j-th direction of the i-th control point. The B-Spline curve possesses a p degree and an amount of n control points. An example of a B-spline curve is shown in fig. 109, having $p = 2$, $n = 7$ and a knot vector $\Xi = \{0.0; 0.0; 0.0; 0.3; 0.5; 0.7; 0.7; 1.0; 1.0; 1.0\}$. In addition, the knot multiplicity of 2 at the knot 0.7 results in the curve being C^0 at this knot.

This study applies the recursive formulae of Cox-de Boor (Cox, 1972; Boor, 1972; Boor, 1978) for the B-Spline basis function calculation because they are the most practical form for computational approaches. In this sense, the equation for $N_{i,p}$, the basis function corresponding to the i-th control point in a curve of degree p is:

$$\begin{aligned} N_{i,0}(\xi) &= \begin{cases} 1 & \xi_i \leq \xi < \xi_{i+1} \\ 0 & \text{otherwise} \end{cases} \\ N_{i,p}(\xi) &= \frac{\xi - \xi_i}{\xi_{i+p} - \xi_i} N_{i,p-1}(\xi) + \frac{\xi_{i+p+1} - \xi}{\xi_{i+p+1} - \xi_{i+1}} N_{i+1,p-1}(\xi) \end{aligned} \tag{A.2}$$

The recursive aspect of eq. (A.2) requires the basis function computing for all degrees prior to p. On the other hand, the B-Spline basis functions have local support, that arise from the $p = 0$ step function format. As a consequence, only the basis functions $\{N_{j-p,p}, \ldots, N_{j,p}\}$ are

Figure 109 – B-Spline curve representation: control points, segments and knots

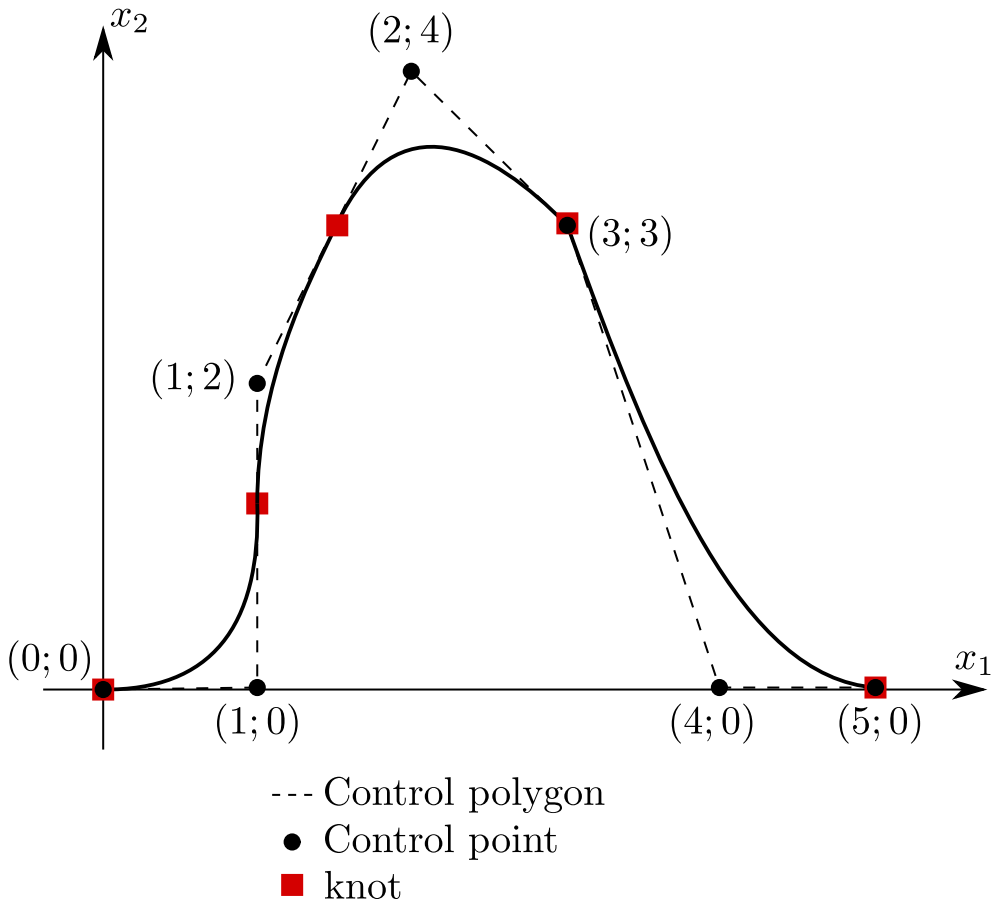

Source: The author.

non-zero for a given knot ξ such that $\xi_j < \xi < \xi_{j+1}$. This property enables reducing the number of calls for the previous basis functions in the recursive equation. Other notable properties of the B-Splines basis functions are their non-negativity, and Partition of Unity. Additionally, $N_{i,p}$ is infinitely differentiable (C^∞) inside its support and C^{p-z} at the knot, being z the knot multiplicity. In this study, all knot vectors are always open, or non-periodic. This characteristic causes a knot multiplicity of $p+1$ in both knot vector ends.

The B-spline basis function derivative performs an important role in the definition of other geometrical entities, such as normal and tangent vector, as well as in the numerical method context. The obtaining of the d-th derivative of $N_{i,p}$ is also recursive, being:

$$N_{i,p}^{(d)} = p\left(\frac{N_{i,p-1}^{(d-1)}}{\xi_{i+p} - \xi_i} - \frac{N_{i+1,p-1}^{(d-1)}}{\xi_{i+p+1} - \xi_{i+1}}\right) \tag{A.3}$$

It is worth mentioning that a $0/0$ term is common in the computing of both eq. (A.2) and eq. (A.3). In these situations, the procedure continues by assuming that $0/0 = 0$.

A.2 NURBS curves

The construction of a NURBS curve derives from open B-Spline curves in which each control point receives a weight w_i. This new parameter becomes part of the curve definition, which is now defined by the division between two functions. In this sense, the parametric representation of a NURBS curve is:

$$C_j(\xi) = \frac{\sum_{i=1}^{n} N_i(\xi) w_i P_j^i}{\sum_{k=1}^{n} N_k(\xi) w_k} = \sum_{i=1}^{n} R_i(\xi) P_j^i \tag{A.4}$$

in which all variables are similar to the ones in eq. (A.2). Also, the degree p is omitted in all other expressions. The NURBS curve basis function $R_i(\xi)$ takes its rational form as:

$$R_i(\xi) = \frac{N_i(\xi) w_i}{\sum_{k=1}^{n} N_k(\xi) w_k} \tag{A.5}$$

The relevance of the NURBS basis functions derivatives is analogous to that of the B-Spline counterparts. The d-th derivative of $R_i(\xi)$ is:

$$R_i^{(d)}(\xi) = \frac{w_i N_i^{(d)}(\xi) - \sum_{\ell=1}^{d} \left[\begin{pmatrix} d \\ \ell \end{pmatrix} \sum_{j=1}^{n} N_j^{(\ell)}(\xi) w_j R_i^{(d-\ell)}(\xi) \right]}{\sum_{j=1}^{n} N_j(\xi) w_j} \tag{A.6}$$

where:

$$\begin{pmatrix} d \\ \ell \end{pmatrix} = \frac{d!}{\ell!(d-\ell)!} \tag{A.7}$$

All the properties of B-Spline curves are present in NURBS curves, such as non-negativity, local support, and Partition of Unity. Additionally, NURBS curves are capable of exactly representing complex geometries as circles, spheres, and cones, among others.

A.3 NURBS surfaces

The NURBS surface parametrization consists of a bi-variate representation resulting from a tensor product of two univariate NURBS curves. Then, by taking two uni-variate NURBS curves, the first having basis functions N with degree p, number of basis functions n and knot-vector $\Xi_1 = \left\{\xi_1^1, \xi_1^2, \ldots, \xi_1^{n+p+1}\right\}$ in ξ_1 direction and the second with basis functions M with degree q, number of basis function m and knot-vector $\Xi_2 = \left\{\xi_2^1, \xi_2^2, \ldots, \xi_2^{m+q+1}\right\}$ in the ξ_2 direction, the parametric approximation of a point x_k is expressed as:

$$]x_k(\xi_1, \xi_2) = \sum_{\alpha=1}^{n^\gamma} \phi_\alpha^\gamma(\xi_1, \xi_2) P_k^\alpha \tag{A.8}$$

and the corresponding bi-variate NURBS basis function ϕ_α is:

$$\phi_\alpha(\xi_1, \xi_2) = \frac{N_i(\xi_1) M_j(\xi_2) w_{ij}}{\sum_{k=1}^{n} \sum_{l=1}^{m} N_k(\xi_1) M_l(\xi_2) w_{\alpha\beta}} \tag{A.9}$$

in which α refers to the NURBS surface local index associated to the indices i and j of each univariate NURBS function, and w_{ij} is the corresponding weight. Once NURBS surfaces derive from NURBS curves, they possess the notable properties mentioned for these curves. Figure 110 presents a NURBS surface representation and its corresponding parametric space.

Figure 110 – NURBS surface.

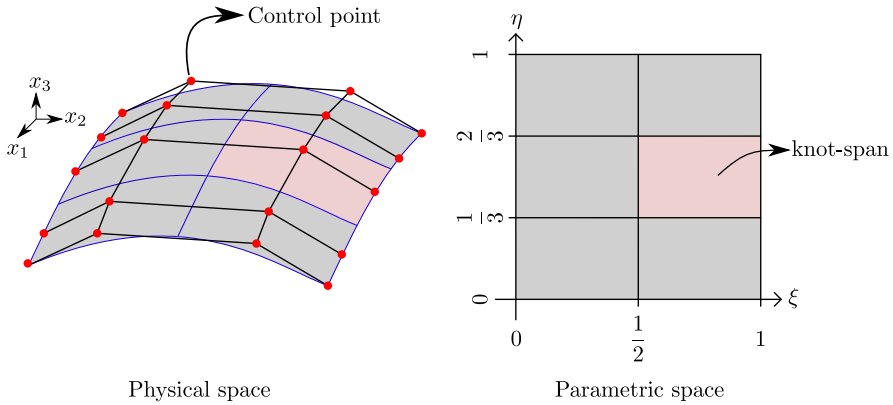

Source: Adapted from Cottrell, Hughes and Reali (2007).

The tensor product between the knot vectors of each parametric direction Ξ_1 and Ξ_2 generates a two-dimensional region in the parametric space such that each portion $[\xi_1^i, \xi_1^{i+1}] \times [\xi_2^j, \xi_2^{j+1}]$ is a knot span of the NURBS surface. In the IGABEM, the numerical integration takes place at each of these portions. Additionally, the knot insertion procedure is the equivalent in Isogeometric Analysis for the h-refinement, in which each knot vector of each univariate NURBS curve receives additional knots. This operation increases the amount of control points for the parametric representation, which is also responsible for increasing the amount of degrees of freedom and improving the numerical response precision. The convergence analyses of this study apply the knot insertion strategy.

A.4 Trimmed NURBS

The parametrisation of NURBS surfaces results from the tensor product of two uni-variate NURBS curves, and they typically represent large portions with four sides, or three when two edges collapse into one. However, CAD models often describe complex geometries with arbitrary topology, including holes and specific geometric details. Describing these surfaces using standard NURBS surfaces requires several patches. Alternatively, trimming allows the representation of these geometries with fewer patches by removing portions that do not belong to the model. For this purpose, trimming NURBS curves $C^{tr}(t)$ define the limits of the parametrisation. These curves have their own parametric space and knot vector, and their control points lie within the parametric space of the NURBS surface.

A closed set of trimming curves defines the removed or retained portion of the original NURBS surface. A set of trimming curves is classified as either inner or outer, depending on whether the removed portion is internal or external to the set, respectively. Consequently, the trimming operation introduces a classification of the basis functions and their corresponding control points into three categories: complete, trimmed, and void, as shown in fig. 111.. Complete basis functions are those whose support remains unaffected by trimming, while trimmed basis functions have the trimming curve within their support. Lastly, void basis functions are not crossed by any trimming curve, but their entire support is removed from the model. For void basis functions, the corresponding control point is unnecessary for the geometric description.

Figure 111 – Types of basis functions for trimmed surfaces.

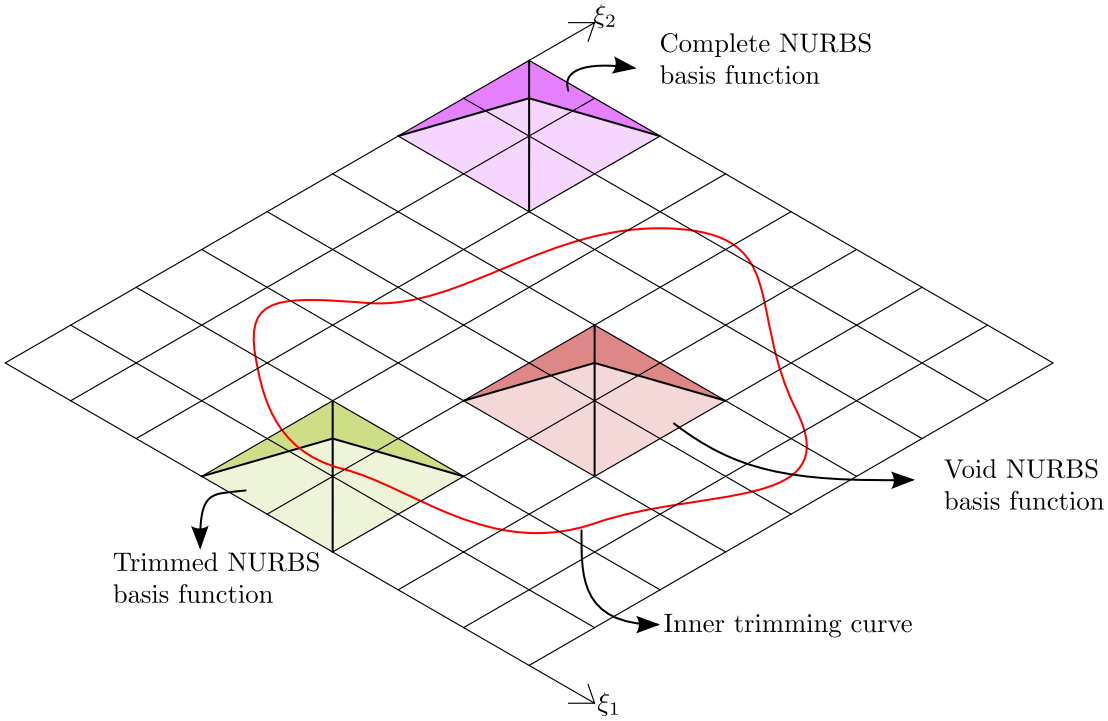

Source: The author.

APPENDIX B – GEOMETRICAL DATA OF ELLIPTICAL CRACK UNDER CRACK GROWTH

This appendix provides the geometrical data associated to the modelling of the coarse mesh of the section 6.5.1. Table 12 provides the control points coordinates and weights. Patches 1 to 6 have $p = q = 1$, with their corresponding knot vector being $\Xi_1 = \Xi_2 = \{0, 0, 1, 1\}$. All other patches have $p = q = 2$ and their knot vector are $\Xi_1 = \Xi_2 = \{0, 0, 0, 1, 1, 1\}$. Table 13 refers to the control point connectivity in each patch. The first 8 control points and the first 6 patches represent the prism.

Table 12 – Control points and weights for the coarse mesh of the elliptical crack modelling of section 6.5.1.

Control point	x_1	x_2	x_3	w
1	-24.0000	-48.0000	16.0000	1.00000000
2	24.0000	-48.0000	16.0000	1.00000000
3	-24.0000	48.0000	16.0000	1.00000000
4	24.0000	48.0000	16.0000	1.00000000
5	24.0000	48.0000	-16.0000	1.00000000
6	24.0000	-48.0000	-16.0000	1.00000000
7	-24.0000	-48.0000	-16.0000	1.00000000
8	-24.0000	48.0000	-16.0000	1.00000000
9	0.0000	0.0000	1.6000	1.00000000
10	2.4000	0.0000	1.6000	0.70710678
11	2.4000	0.0000	0.0000	1.00000000
12	-2.4000	0.0000	1.6000	0.70710678
13	0.0000	0.0000	0.0000	0.41421356
14	2.4000	0.0000	-1.6000	0.70710678
15	-2.4000	0.0000	0.0000	1.00000000
16	-2.4000	0.0000	-1.6000	0.70710678
17	0.0000	0.0000	-1.6000	1.00000000
18	0.0000	0.0000	-1.8000	1.00000000
19	0.0000	0.0000	-2.0000	1.00000000
20	-2.7000	0.0000	-1.8000	0.70710678
21	-3.0000	0.0000	-2.0000	0.70710678
22	-2.7000	0.0000	0.0000	1.00000000
23	-3.0000	0.0000	0.0000	1.00000000
24	2.7000	0.0000	-1.8000	0.70710678
25	2.7000	0.0000	0.0000	1.00000000
26	3.0000	0.0000	-2.0000	0.70710678
27	3.0000	0.0000	0.0000	1.00000000

Table 12 – Control points and weights for the coarse mesh of the elliptical crack modelling of section 6.5.1.

Control point	x_1	x_2	x_3	w
28	0.0000	0.0000	1.8000	1.00000000
29	-2.7000	0.0000	1.8000	0.70710678
30	0.0000	0.0000	2.0000	1.00000000
31	-3.0000	0.0000	2.0000	0.70710678
32	2.7000	0.0000	1.8000	0.70710678
33	3.0000	0.0000	2.0000	0.70710678
34	0.0000	0.0000	1.6000	1.00000000
35	-2.4000	0.0000	1.6000	0.70710678
36	-2.4000	0.0000	0.0000	1.00000000
37	2.4000	0.0000	1.6000	0.70710678
38	0.0000	0.0000	0.0000	0.41421356
39	-2.4000	0.0000	-1.6000	0.70710678
40	2.4000	0.0000	0.0000	1.00000000
41	2.4000	0.0000	-1.6000	0.70710678
42	0.0000	0.0000	-1.6000	1.00000000
43	0.0000	0.0000	1.8000	1.00000000
44	2.7000	0.0000	1.8000	0.70710678
45	2.7000	0.0000	0.0000	1.00000000
46	0.0000	0.0000	2.0000	1.00000000
47	3.0000	0.0000	2.0000	0.70710678
48	3.0000	0.0000	0.0000	1.00000000
49	-2.7000	0.0000	1.8000	0.70710678
50	-3.0000	0.0000	2.0000	0.70710678
51	-2.7000	0.0000	0.0000	1.00000000
52	-3.0000	0.0000	0.0000	1.00000000
53	0.0000	0.0000	-1.8000	1.00000000
54	0.0000	0.0000	-2.0000	1.00000000
55	2.7000	0.0000	-1.8000	0.70710678
56	3.0000	0.0000	-2.0000	0.70710678
57	-2.7000	0.0000	-1.8000	0.70710678
58	-3.0000	0.0000	-2.0000	0.70710678

Source: The author.

Table 13 – Connectivity of the elliptical crack model of section 6.5.1.

Patch	Control points								
1	1	2	3	4					
2	4	2	5	6					
3	1	3	7	8					
4	4	5	3	8					
5	1	7	2	6					
6	7	8	6	5					
7	9	10	11	12	13	14	15	16	17
8	17	18	19	16	20	21	15	22	23
9	17	14	11	18	24	25	19	26	27
10	9	12	15	28	29	22	30	31	23
11	9	28	30	10	32	33	11	25	27
12	34	35	36	37	38	39	40	41	42
13	34	37	40	43	44	45	46	47	48
14	34	43	46	35	49	50	36	51	52
15	42	53	54	41	55	56	40	45	48
16	42	39	36	53	57	51	54	58	52

Source: The author.

PPG
SET

EESC • USP